Modelling rock slope behaviour and evolution with reference to Northern Spain and Southern Jordan

Nelis, Simon Brett

MODELLING ROCK SLOPE BEHAVIOUR AND EVOLUTION WITH REFERENCE TO NORTHERN SPAIN AND SOUTHERN JORDAN

VOLUME 1

SIMON BRETT NELIS

Ph.D. THESIS 2004

Modelling rock slope failure and evolution with reference to northern Spain and southern Jordan

Simon Brett Nelis

Department of Geography

University of Durham

Thesis submitted for the degree of Doctor of Philosophy

August 2004

Declaration

I confirm that no part of the material presented in this thesis has previously been submitted by me or any other person for a degree in this or any other university. In all cases, where it is relevant, material from the work of others has been acknowledged.

Signed:

Date:

Abstract

The geomorphological behaviour of steep jointed rock slopes has been studied using distinct element computer models. In order to model steep slopes effectively, methodologies need to be combined from the studies of environmental modellers, geomorphologists and engineers. The distinct element method is ideal for the study of the development of jointed rock masses, where the failure is controlled by the nature of the discontinuities.

Theoretical modelling identified that block size is a key control affecting the deformation of rock masses. Deformation of rock masses with smaller block assemblages is greater than for rock masses composed of larger block sizes. This is due to the increased magnitude of joint normal closure. Catastrophic failure is less likely in slopes with smaller block sizes because the shear strength is greater in a closely jointed rock mass. These slopes are more likely to undergo gradual deformations. Block-size effects are also responsible for influencing the failure mechanism of rock masses. As block size decreases, the magnitude of block rotation increases and the failure mechanism changes from sliding to toppling. The effect of slope scale on the deformation properties of the rock masses has also been investigated.

Two field locations, the Picos de Europa mountains, northern Spain and Wadi Rum, southern Jordan, have been chosen to provide a link between the theoretical modelling and classic rock landforms which are controlled by the discontinuity geometry. Given the sporadic and infrequent occurrence of failure events at the field sites, a computer modelling approach has been adopted to analyse slope behaviour. In the Picos de Europa, slope deformations are deep-seated, with sliding and toppling being the dominant modes of failure. Much of the slope deformation in these mountains is a result of post-glacial rock-slope deformation. The sandstone inselbergs of Jordan show a range of morphologies from rounded hills to vertical cliffs. The morphology of the inselbergs is related to the intact rock strength; stronger Red Ishrin sandstone forms vertical slopes, whereas the weaker Disi sandstone forms rounded domes. Jointing in the area is sub-vertical with horizontal bedding and computer simulations have shown that toppling is the dominant mode of failure in these inselbergs.

Comparison of computer model output suggests that different failure mechanisms have distinct failure signatures. Catastrophic, deep-seated failures are characterised by a long period of acceleration as the failure propagates through the rock mass and infinite velocity is reached. Non-catastrophic slope movements, such as self-stabilising topples, are characterised by short periods of acceleration followed by small creep movements at a constant velocity.

Computer modelling has indicated that scale effects do exist in the modelled rock masses from the Picos de Europa and particularly Wadi Rum. In areas where jointing is constant, the relative block size of the rock mass decreases as slope scale increases. The greater number of blocks along with greater *in situ* stresses influence the failure of the slope.

Cosmogenic dating was used to temporally constrain UDEC model output and provide a better understanding of rock slope failure mechanisms in the Picos de Europa and Wadi Rum. Dating indicated delayed paraglacial adjustment was the triggering mechanism for slope failure in the Picos de Europa, whereas failures in Wadi Rum appeared to be closely linked with wetter climatic conditions.

Acknowledgements

The research in this thesis has only been made possible by the help and guidance which I have received from numerous sources over the last three years. First of all, I would like to thank my mother and father for providing the constant support throughout my various geographical exploits. Without their help and encouragement over the years, this thesis would not have been possible. Second, I would like to thank my supervisors, Professor Bob Allison and Dr Nick Cox. Bob has been a constant source of enthusiasm and ideas throughout my studies. Without his help and inspiration it would not have been possible to undertake this research in Wadi Rum. It was Bob in the first instance who inspired me to embark upon this research. Thanks are extended to Nick for his constant attention to detail and statistical input, which has greatly improved the quality of this thesis. I used several of his programs, especially for fitting and graphical testing of Weibull, gamma and lognormal distributions, for calculation of L-moments and nonlinear least squares fitting of the model discussed in Chapters 7 and 8.

The fieldwork for this thesis was based in the Picos de Europa mountains, northern Spain and in Wadi Rum, Jordan. I would like to thank Mike and Lisa Stuart for providing me with free food, accommodation and most importantly beer, while undertaking my research in the Picos de Europa. Use of a free landrover and transportation of rocks back to the U.K is very much appreciated. I would also like to thank Mike for taking me climbing to gain a more detailed appreciation of some of the slopes studied as part of this work. I would also like to thank the countless people who staff the mountain refuges in the Picos de Europa. Their help and advice in navigating the complex topography was invaluable.

The fieldwork in Jordan was undertaken in Wadi Rum. In Amman, the Centre for British Research in the Levant provided a welcome base from which to start and return and also allowed for the hire of field equipment, which made life in the desert much more comfortable. In particular I thank Dr Bill Finlayson, Mohammed and Nadja, who were incredibly supportive and helpful throughout my fieldwork.

Valuable assistance in the field was greatly appreciated. I would particularly like to thank Dr Nick Rosser for his help in Jordan. Without him and the 'chariot' this research would have been very much harder.

In Durham, the staff and students of the Department of Geography have been a constant source of help and support. I am indebted to the Department of Geography for providing my studentship over the past three years. In the laboratories, Derek Coates, Frank Davies, Eddie Million, Brian Priestley and Neil Tunstall have all been excellent. The staff in the department office, in particular Derek Hudspeth and Christine Bones, have been invaluable in helping to arrange fieldwork in Jordan. I would also like to thank the Department of Engineering for providing support, advice and laboratory space for the rock testing program used in this thesis. I have benefited greatly from working and living in a vibrant postgraduate community. A particular mention goes to Nick Rosser, Duncan Wishart, Allison Scott, Damien Laidler and Toru Higuchi.

I have had the opportunity to discuss my research with many people outside of Durham. I thank Professor Andrew Goudie at the IAG, Tokyo, 2001, for first suggesting that Wadi Rum would make an ideal site for my research. I would like to thanks Mark Christianson of ITASCA and Rajinder Bhasin of the Norwegian Geological Institute for giving up their time to provide me with ideas for this thesis. I would also like to thank N. Lemmens for his invaluable advice on non-destructive materials testing.

Contents

List of Tables

Chapter 6

Chapter 7

Chapter 8

List of Figures and Plates

The figures in this thesis include output from the UDEC computer simulation software and from the laboratory testing of rock. The output consists of two-dimensional block plots and filled contour block plots. The labelled notation (*10^1) indicates that the axes need to be multiplied by 10. On all UDEC plots, the horizontal and vertical axes are in meters. The plot legend includes an indication of the type of output plot, model cycle count, model time and also the contour intervals. In plots with displacement vectors, the scale presented is in meters. The notation 1 E 1 on the scale means that the scale is 1*10 m long. The values of displacement relate to actual displacements in the rock mass in meters. Where plots of unbalanced forces are presented, the x-axis is model time (s) and the y axis is force (kg m s^{-2}).

Chapter 2

Chapter 4

List of Plates

List of Appendices

All appendices are to be found on the disk which is attached to the back cover of Volume 2 of this thesis. The appendices are chapter ordered and the filename corresponds to the appendix number. For the UDEC input files, where the letter '*v*' is used, values are varied for the different model runs.

Chapter 3

3.1 Basic program for calculating the angle of intersection between a joint plane and a UDEC mesh.

Chapter 4

4.1 A FISH function to calculate strain accumulation at gridpoints.

4.2 UDEC input file for a 1 m sandstone rock mass with variable joint spacing. A '*v*' indicates that the block size parameter was varied.

4.3 UDEC input file for a 1 m limestone rock mass with variable joint spacing. A '*v*' indicates that the block size parameter was varied.

4.4 UDEC input file for a 1 m granite rock mass with variable joint spacing. A '*v*' indicates that the block size parameter was varied.

4.5 UDEC input file for a 10 m sandstone rock mass with variable joint spacing. A '*v*' indicates that the block size parameter was varied.

4.6 UDEC input file for a 10 m limestone rock mass with variable joint spacing. A '*v*' indicates that the block size parameter was varied.

4.7 UDEC input file for a 10 m granite rock mass with variable joint spacing. A '*v*' indicates that the block size parameter was varied.

4.8 UDEC input file for a 100 m sandstone rock mass with variable joint spacing. A '*v*' indicates that the block size parameter was varied.

4.9 UDEC input file for a 100 m limestone rock mass with variable joint spacing. A '*v*' indicates that the block size parameter was varied.

4.10 UDEC input file for a 100 m granite rock mass with variable joint spacing. A '*v*' indicates that the block size parameter was varied.

4.11 UDEC input file for a 1000 m sandstone rock mass with variable joint spacing. A '*v*' indicates that the block size parameter was varied.

Chapter 8

List of Notations

A summary of the commonly used symbols used throughout this thesis is provided below. Other symbols are explained in the text as they are introduced. The corresponding SI unit for each quantity is given after the symbol. The notation after a symbol indicates that it is dimensionless.

R	Schmidt Hammer rebound number
g	gravitational acceleration (m s^{-2})
C_o	compressive strength (MPa)
E_s	static Young's Modulus (GPa)
E_d	dynamic Young's Modulus (GPa)
P	maximum load at failure (MPa)
A	cross-sectional area of rock core being tested (m^2)
$\sigma_1, \sigma_2, \sigma_3$	principle stresses (MPa)
ε_a	axial strain (%)
ε_l	lateral strain (%)
Δd	change in rock core specimen diameter (mm)
Δl	change in rock core specimen length (mm)
R_g	strain gauge resistance (Ω)
r	total resistance per meter of lead wire (Ω/m)
L	length of strain gauge lead wire (m)
F	supplied strain gauge factor (0, %)
F_o	corrected strain gauge factor (0, %)
τ	shear strength (MPa)
c	cohesion (MPa)
σ	normal, or axial stress (MPa)
ϕ	friction angle; both internal and surficial (degrees)
K	bulk Modulus (GPa)
G	shear Modulus (GPa)
ν_s	static Poisson's ratio
ν_d	dynamic Poisson's ratio
E_m	rock mass Young's modulus (GPa)
G_m	rock mass shear modulus (GPa)
K_s	joint shear stiffness (GPa)
k_n	joint normal stiffness (GPa)
γ	unit weight of rock (kg m^3)

Z	depth below ground surface (m)
λ	Lambda (1-velocity of failed mass)
$k\omega$	half-way time (model cycles)
t	time (UDEC model cycles)
ka	thousands of years
v	velocity (m s^{-1})

Chapter 1: Introduction

Chapter 1: Introduction

1.1 Research Objectives

The principal aim of this thesis is to examine the deformational behaviour and mechanisms of failure in jointed rock-slopes through computer simulation of theoretical and natural rock mass data. This study arises from the need for a more comprehensive geomorphological understanding of the behaviour and development of jointed rock-slopes and their associated landforms. Computer simulation techniques used widely for engineering design allow the study of slope processes on a timescale over which it is difficult to monitor in the field. To achieve a better understanding of rock-slope deformations, theoretical modelling is used to isolate important controlling parameters governing the deformational properties of slopes in jointed rock. Particular attention is given to the study of the Carboniferous Limestone slopes of the Picos de Europa mountains, northern Spain, and the Salib Arkosic, Red Ishrin and Disi Sandstones of the Al-Quwayra-Wadi-Rum region of southern Jordan. Dating the temporal evolution of landforms and thus providing a real-time constraint on computer simulations of rock slope development is attempted by using *in situ* cosmogenic isotopes to date past slope failures.

Sites in the Picos de Europa were chosen because the evolution of slopes in high mountain areas is poorly understood in comparison with slopes at lower elevations, given their remote location. The Picos de Europa are much more accessible than many other mountainous areas, making them ideal for study. Second, the mountains are formed in strong, brittle limestones, which are relatively well jointed. The area was glaciated during the last glaciation and this has produced oversteepened slopes where they have been truncated by glacial erosion. This contrasts with the field sites in Jordan, which are formed in weak, massively jointed sandstones that have never been glaciated. The slopes in the Picos are interesting because high slopes (100 to 300 m) are maintained in relatively well-jointed rock masses.

The Wadi Rum field sites were chosen for a number of reasons. First, the area is an excellent example of structural control on landscape development; joints and normal faulting are the result of plate motions along the Red Sea and Dead Sea. This affects the scale of the inselbergs, which increase in size towards the south, so that it is possible to assess the effects of slope scale on the deformation and failure

mechanisms of the sandstone inselbergs. Jointing is relatively consistent across the area because the sandstones have not been affected by folding. Second, the characteristics of the inselbergs provide a contrasting environment to the slopes found in the Picos de Europa. Whereas the Picos are located in a recently glaciated Alpine environment, with slopes formed in strong, brittle limestone, the Wadi Rum sites are located in an arid environment, with isolated rock masses formed in weak sandstones. In addition, little previous research has been undertaken to determine the geomorphological behaviour of these slopes.

The contrasting environments provide the opportunity to compare the frequency of rock slope failures in a recently glaciated environment and one where there is no history of glaciation. The suitability of *in situ* cosmogenic nuclide dating for dating rock slope failures in these two environments is also assessed.

The research uses the Universal Distinct Element Code (UDEC) computer software in a multidisciplinary approach based on geological, geomorphological and rock mass geotechnical properties. The data are combined in a single model to consider landform behaviour. The advantage of this approach is that a rock mass can be treated as an assemblage of blocks, with failure of a cliff face being modelled by the movement of the blocks along discrete joint sets. Field and laboratory data can be synthesised with model input, including joint geometrical information, rock strength properties and cliff morphometric data.

To address the main aim of the thesis a number of primary research objectives were identified.

1. Develop the UDEC computer simulation software as a geomorphological technique for the study of jointed rock slope landforms.
2. Investigate scale effects to improve geomorphological understanding of the deformation of rock slopes before failure and the parameters controlling the mechanisms of failure, through a theoretical modelling approach.
3. Collect appropriate field and laboratory data to determine the intact rock and rock mass geotechnical properties.
4. Investigate the controls on rock slope failure and evolution using computer simulation based on data from natural sites in the Picos de Europa, northern Spain and the Al-Quwayra-Wadi-Rum region of southern Jordan.

5. Application of *in situ* Terrestrial Cosmogenic Nuclides (TCN's) for dating of past rock slope failures in an attempt to provide a temporal framework for understanding UDEC model outputs of rock slope evolution.

1.2 Background and justification of thesis

Geomorphological research on rock slopes has concentrated largely on descriptions of failure magnitude and frequency (Brunsden *et al.*, 1984), slope retreat rates (Jones and Williams,1991) and failure products (Whalley, 1984). Jointed rock masses have received less attention than soft argillaceous sediments. Rock slope research is limited by the timescale over which behaviour needs to be monitored and the data-limited nature of the problem. The timescales over which rock slopes evolve are far greater than periods of monitoring that can be achieved in a human lifetime. Computer simulation offers the advantage of transgressing temporal boundaries. In rock mechanics research there has been an increase in the application of numerical modelling (Starfield and Cundall, 1988; Eberhardt, 2002; Hart, 2003; Eberhardt, *et al.* 2002) and the potential now exists for the use of advanced computer simulation codes in geomorphology (Kimber, 1998).

The study of landforms is increasingly making use of the advantages of adopting a multidisciplinary approach (Allison, 1997). Rock-slope research has advanced by the consideration of material properties jointly with processes and form (Allison *et al.*, 1993; Cooks, 1983). Rock masses contain structural discontinuities that significantly reduce the shear strength of the rock below that of intact material. This study considers jointed rock masses in which the deformational properties and failure mechanisms are influenced by the properties of discontinuities and intact rock. Others have studied the deformation of rock material by falls or avalanches (Azzoni *et al.*, 1995; Maharaj, 1994). Geomorphologists have previously accounted for discontinuities by using classification systems to assess the stability of landforms (Selby, 1980). However, the development of numerical codes that simulate the behaviour of rock masses allows the study of slopes in a more quantitative way, without the subjective weighting of data. The strength of the intact rock and discontinuities, discontinuity and slope geometry, and *in situ* stresses can all be accounted for in numerical codes.

The UDEC software uses physically-based calculation systems and allows for the synthesis of information in a rigorous scientific manner. The physically-based

calculations are gained from Newton's laws of motion, along with laboratory-derived data to described the deformation of the intact material and discontinuities. The UDEC code has been extensively verified in the field of rock mechanics. Only a small number of geomorphological studies have used the code to simulate the longer-term geomorphic behaviour of jointed rock slopes (Allison and Kimber, 1998; Kimber, 1998; Kimber *et al.*, 2002). These studies have provided an initial indication of the potential of the UDEC approach for improving the understanding of rock-slope behaviour.

The incorporation of the UDEC numerical code into a geomorphological study provides the opportunity to examine rock-slope behaviour and recurrence intervals of failure in two contrasting environments. The Picos de Europa mountains in northern Spain consist of Carboniferous Limestones uplifted by a series of nappe units. The area is Alpine in character and was glaciated during the Last Glacial Maximum (Crompton, 1964; Gale and Hoare, 1997; Smart, 1984). The study of Alpine slopes has generally lagged behind those in more accessible regions. The sandstones of the Al-Quwayra-Wadi-Rum region of southern Jordan occur in an arid environment and form a large assemblage of inselberg landforms. Initial studies suggest that the nature of failure is joint-controlled, but this work is mainly descriptive and concentrates on rock-fall debris (Goudie *et al.*, 2002). The numerical simulation approach provides the opportunity to asses the relative importance of joint geometry and other factors on the behaviour of slopes in both areas. No previous work has been undertaken to determine the mechanisms of failure, or assess landform evolution at either site.

An important issue in geomorphology is gaining an accurate assessment of the significance of high magnitude, low frequency events in landscape evolution (Cockburn and Summerfield, 2004). Rock slope failures are difficult to monitor because of their low frequency, but they may have a significant influence on the evolution of the landscape. Cosmogenic dating of slope failures is beginning to yield valuable insights into the recurrence intervals of slope failures and is also providing important quantitative data for hazard management.

Dating of rock slope failures has the potential to provide geomorphologists with more detailed information about the temporal evolution of the landform. Rock slopes often contain little organic material and conventional methods of dating, such as ^{14}C and luminescence, can only be used under favorable conditions where

organic material is contained within the failed material. Terrestrial Cosmogenic Nuclides (TCN's) have been successfully used to date rock slope failures (Ballantyne *et al.*, 1998). In an attempt to improve understanding of the temporal framework of rock slope failures, cosmogenic ages of past failures are used to provide an insight into the temporal patterns observed in the model output.

This research attempts to combine numerical modelling and cosmogenic dating to provide a better understanding of the recurrence intervals of rock slope failures in contrasting geomorphic and geological settings.

1.3 Background to UDEC

The most comprehensive, powerful and versatile discontinuum theory available is the distinct element method (Brown, 1987). The Universal Distinct Element Code (UDEC) is a two-dimensional numerical program based on the distinct element method for discontinuum modelling, originally developed by Cundall (1971). The modern UDEC code is proprietary software published by HCItasca. The version of the code used in this research is the latest release, UDEC v. 3.10.

UDEC simulates the response of a jointed rock mass, represented by an assemblage of discrete blocks, under loading from either gravity or external forces. UDEC runs by simulating the motions of blocks along discontinuities as governed by linear or non-linear force-displacement relations, for movement in the normal and shear directions solved by Lagrangian calculations. The program uses explicit time-marching to solve the equations of motion. UDEC has several built-in material models, for both intact rock and discontinuities. Blocks can be made deformable by sub-dividing into a mesh of finite difference elements. The code is able to simulate the flow of fluid through discontinuities, the transient flux of heat in materials, seismic loads, linear and non-linear joint behaviour and plastic behaviour of blocks (Lemos *et al.*, 1985).

UDEC is ideally suited to the long-term geomorphic study of the behaviour of jointed rock-slopes for a number of reasons. First, it is best used as a means of modelling the progressive failure of rock slopes where block size is a key control on stability. The code is ideally suited to investigate potential modes of failure directly related to the presence of discontinuities; it offers the advantage that there is no limit to the magnitude of displacement or rotation of blocks, meaning that progressive failure can be monitored. Second, the program allows the study of the effects of joint

geometry, joint parameters, loading conditions and anthropogenic activity such as excavation. Other codes assume that the intact properties of the rock and the stiffness of the joints play a negligible part in the deformation and failure of rock masses. Third, UDEC recognises new block-block contacts automatically as the calculation progresses and this allows for the modelling of large numbers of blocks whose interactions are not known in advance. Many other modelling approaches, concerned with short-term stability problems, are restricted to small displacements and do not address changes in force distribution that accompany displacement of blocks. UDEC has been extensively verified (Cundall and Strack, 1979; Lemos, 1990) and a number of studies have successfully applied the software to rock mechanics situations (Barton *et al.*, 1994; Pritchard and Savigny, 1991).

1.4 Organisation of the thesis

The text, table and references of this thesis are to be found in Volume 1. Volume 2 contains the figures and plates. The appendices are to be found on the accompanying CD-ROM, which is provided inside the back cover of Volume 2.

The thesis begins with a review of the study of jointed rock slopes and the geotechnical properties that need to be considered for this research. An outline of the field and laboratory methods required to determine relevant rock mass parameters is given.

Chapter 3 assesses the various approaches to modelling jointed rock masses that have been used in rock mechanics research. In modelling rock masses, the selection of the most appropriate modelling approach is critical for accurately representing a physical system. The various approaches for modelling rock masses that have been used include kinematic analysis, limit equilibrium analysis, finite element/difference, distinct element and hybrid finite / distinct element, and these are reviewed. The numerical basis and operation of UDEC is described.

Chapter 4 outlines the results of theoretical modelling and explains the relationships between outcrop scale, block size, lithology and the deformational/failure characteristics of rock masses. The chapter explains how the block size distribution controls the pre-failure deformation behaviour of the rock mass and also the failure mechanism. Outcrop scale (defined as the slope height) is also considered as a scale effect and its effect on rock mass behaviour is investigated. The chapter then

discusses the implications of the findings for the evolution and behaviour of slopes in the natural environment.

Chapter 5 begins by providing a geological and geomorphological background to the Picos de Europa field sites. The geotechnical properties of the landforms are then discussed for each site. The geotechnical data presented in this chapter form a direct input for the computer models and provide the link between field investigation and computer simulation.

Chapter 6 begins by providing a geological and geomorphological background to the Wadi Rum-Al-Quwayra field sites. The geotechnical properties of the landforms are then discussed for each site. The geotechnical data presented in this chapter form a direct input for the computer models and provide the link between field investigation and computer simulation.

Chapter 7 presents the results of numerical modelling using UDEC of the behaviour and mechanisms of failure of slopes in the Picos de Europa mountains, northern Spain. The significance of the model output for the evolution of each of the field sites is discussed. In the Picos de Europa, the main scale effect is related to block size vs outcrop scale. The size of the blocks tends to be small in relation to the size of the slope face. This has implications for the type of deformation and failure of the slopes. ^{36}Cl cosmogenic dates provide a temporal framework for the history of large slope failures on selected sites in the Picos de Europa. An attempt is made to provide a broad temporal framework that can be used to constrain the UDEC model output of rock slope evolution and provide an indication of the recurrence interval of slope failures.

Chapter 8 presents the results of UDEC modelling to investigate the behaviour and failure of the sandstone inselbergs found in the Al-Quwayra-Wadi Rum region of southern Jordan. The area is unique in that two scale effects related to the theoretical modelling are preserved in the natural landforms. First, outcrop scale of the sandstone inselbergs increases towards the south of the study area. Second, because joint spacing is constant across the area, as outcrop scale increases so the relative block size in relation to the landform decreases. This has implications for the nature of deformation and failure of slopes. ^{10}Be cosmogenic dates provide a temporal framework for understanding the history and recurrence interval of large slope failures on selected sites in the Wadi Rum region. An attempt is made to

provide a broad temporal framework that can be used to constrain the UDEC model output of rock slope evolution.

Chapter 9 provides a concluding synthesis of the findings of this research. The original contribution made in thesis is discussed and the advances made compared with previous research are outlined. In conclusion, recommendations for further study are made.

Chapter 2: The geomorphology and geotechnical properties of jointed rock masses

Chapter 2: The geomorphology and geotechnical properties of jointed rock masses

2.1 Introduction

The aim of this chapter is to present the background information necessary for this study. There are four main topics of discussion. The methodology used as part of this study raises general issues of how geomorphologists and engineers have dealt with slope development. Central to this are magnitude-frequency concepts and the timescale of study and how these are related to numerical modelling in geomorphology. Engineers and geomorphologists are often interested in different timescales and magnitude-frequency relationships. This sets the overall context of this study.

This study uses both the properties of intact rock and the discontinuities to examine slope development using numerical modelling. Therefore, a background of the issues associated with the measurement of both joint and intact rock properties used in this study forms parts two and three of the discussion. To study jointed rock masses, consideration needs to be given to the strength of the intact rock and movement of blocks along discontinuities. Thus, the final section gives a background to the study of the stability of rock masses by combining information upon intact rock strength and the discontinuities between blocks.

2.2 Background to slope studies in geomorphology

Much discussion has occurred within geomorphology regarding the link with other scientific disciplines (e.g. Fookes and Vaughan, 1986). Close synergy exists between slope studies undertaken by geomorphologists and engineers. For example, there is a desire in both to understand how the Earth works, at and close to the ground surface (Allison, 2001). It is believed that a more holistic view of Earth surface systems is possible by integrating the geomorphology and engineering approaches . At the same time, it has been suggested that there is too much study of processes and that more thought needs to be given to landform development in geomorphology (Ahnert, 1996).

Two main linkages can be identified between geomorphology and cognate subjects, such as geology and engineering (Allison, 2001) (Figure 2.1). First, there are studies of contemporary landforms at the surface of the earth, the processes which operate on the landforms and their earth materials – most specifically the geotechnical properties. Establishing interactions between landforms, processes and materials helps establish relationships, linkages and causal effects (Allison, 1996a). Second, there are studies of past environments through the palaeo-sedimentary record. Allison (2001) emphasises that a continuum exists between geomorphology, geology, engineering and engineering geomorphology, where contemporary studies and palaeoenvironmental investigations provide essential information to engineers.

An obvious distinction in slope stability studies is that engineers tend to study the behaviour of systems over short (< 100 years) timescales. The true distinction, however, lies in the objectives of analysis. Engineers are interested in stability assessments for specific slopes, which are likely to affect structures, whereas geomorphologists are interested in quantifying the role of failure mechanisms in slope evolution over long time-scales.

Accounting for the mechanical properties of landform materials is important for geomorphology and engineering studies. It is possible to define geomorphological research within a continuum with extremes focusing on form, processes and materials (Allison, 1996). Individual studies can be plotted relative to the importance of form, processes and material variables. Attention is given in this work to the development of rock slope form by considering processes affecting a rock mass and the strength of the rock mass material. A good understanding of the material properties of jointed rock mass landforms, particularly joint parameters, is necessary when studying rock slopes (Allison *et al.*, 1993; Gerrard, 1988).

2.2.1 Timescales of slope development in geomorphology

Space and time link all earth surface processes and landforms. Geomorphological systems work through space to modify landforms over time. At any point, a ratio exists between processes associated with tectonic activity and uplift, which generally increase relief, and weathering and erosion, which generally decrease relief. Time is important for a variety of reasons in geomorphology and engineering geology. Events with particular return intervals, such as the 100-year flood or 75-

year wave, are often part of engineering design criteria. In engineering, relatively short time intervals may be used as a basis for design or landscape modification. From a geomorphological perspective, even the shortest timescales fit into a larger picture.

At one end of the temporal spectrum is the long-term, characterised by changes to the earth's surface, which take place over millions of years. Examples include tectonic uplift, glaciation and variations in global climate. Davis (1892, 1899, 1930) suggested the cycle of erosion based on the systematic progression of landforms through time, initiated by uplift of the land surface. Penck (1925, 1953) argued that landscape form depends on whether the rate of uplift is increasing, decreasing or constant through time. A more complex understanding of slope development is evident in contemporary geomorphological thought, with the mode of slope evolution depending on the environment, morphometry and structure, as well as process (Chorley, 1964).

A second group of events are those within the 50 000 year timespan, which includes climatic variation such as glacial and interglacial cycles. At the 0 to 50 000 year time interval, issues of landscape response to specific events emerge. As landscapes respond to changes in their controlling variables, lag times develop, illustrated by slope form. For example, the Penck framework allows for the possibility of parallel retreat of slopes (Tuan, 1958). King (1957) showed that low-angled escarpment slopes in southern Africa had experienced parallel retreat. In some places the slope angle is over-steepened, exceeding that which might be expected for the prevailing conditions. Slope form must still be adjusting to reach equilibrium with processes which previously changed at a much faster rate than slope response. Slope failures may develop if the imbalance between slope form and processes is large enough to push the Factor of Safety below 1.0 (Allison, 2001). The implication is that slope form is inherently stable (Brunsden and Thornes, 1979, Thornes and Brunsden, 1977).

For each slope form, over-steepened, equilibrium and over-relaxed, the main issue is the balance between form, process and materials over thousands of years because of the landform response to time. The longer the timespan, the greater the likelihood of complexity. Engineering designs rarely account for the fact that landforms are in a state of flux between instability and equilibrium. An example is road engineering along the Karakoram Highway, where an already dynamic

environment, due to uplift and tectonic instability, was affected by road alignment, over-steepening many slopes that were already unstable.

2.2.2 Magnitude-frequency and return intervals of rock slope failures

The concept of magnitude, frequency and return intervals is central to geomorphology and should be of interest to engineers. At points in the temporal record, perturbations will occur driving the system away from stability. The potential for landform changes increases as the magnitude of the perturbations increases. The time-lag between the start of a high-magnitude event during which the energy available for modifying the surface of the Earth will increase, and the landform response by changing its form, can be considered to be its reaction time. The implication for engineering is that if the reaction time of a geomorphological system is known for events of a specific magnitude, it becomes possible to establish boundary conditions above which remedial works are necessary to prevent further landform change.

Once the total reaction time is reached, the system will begin to change. As the magnitude of an event increases, the degree of change will be greater. At the same time the frequency of that event in the temporal record will decrease (Brunsden, 1980; 1993). The total time period over which landform changes take place can be considered as the relaxation time, or the duration a landform takes to respond to a pulse of energy passing through the system.

An important issue in engineering geomorphology is gaining an accurate assessment of the significance of high magnitude-low frequency events in affecting slope behaviour and landscape evolution (Cockburn and Summerfield, 2004). Rock slope failures are difficult to monitor because of their low frequency, but they may have a significant influence on the evolution of the landscape.

Previous geomorphological research on rock slopes has concentrated largely on descriptions of failure magnitude and frequency (Brunsden *et al.*, 1984; Hungr *et al.*, 1999; Matsuoka and Sakai, 1999), slope retreat rates (Jones and Williams, 1991) failure products (Whalley, 1984), spatial differences in slope form (Weissel and Seidl, 1997), and structural control on slope form and failure (Cruden, 2003; Maharaj, 1994; Sauchyn *et al.*, 1998). Understanding the properties of intact material in accounting for cliff face development has been minimal (for example,

Douglas *et al.*, 1991). These studies have tended to focus on the observable features in the paleo-record to infer likely consequences of future events, as well as the magnitude-frequency of event occurrence. For example, Hinchcliffe and Ballantyne (1998) used the volume of accumulated rockfall deposits on the Isle of Skye to estimate that since deglaciation, 5.6 m of rockwall retreat has occurred. The main conclusion was that the frequency and magnitude of failure was greatest following deglaciation because the slopes were over-steepened. Present rates of retreat are much lower because of the lag-times involved since deglaciation.

New geomorphological approaches using cosmogenic dating of slope failures are beginning to yield valuable insights into the recurrence intervals of rock slope failures and also providing important quantitative data for hazard management on engineered slopes.

Ballantyne *et al.* (1999) studied post-glacial landsliding on the Isle of Skye to investigate the recurrence interval of rock slope failures. Cosmogenic dating of failed boulders put the failures to 6.5 ± 0.5 ka BP. This failure post-dates deglaciation by several thousand years and the failure was attributed to joint extension, rather than to periglacial effects, such as freeze-thaw. Post-glacial rock slope failures in the Swiss Alps at Köfels have been dated to 9800 ± 100 ka BP using cosmogenic ages (Ivy-Ochs *et al.*, 1998; Kubik *et al.*, 1998). It was concluded that paraglacial slope adjustment through stress redistribution was the most likely cause of slope failure.

Hermanns *et al.* (2000, 2001) used cosmogenic dating to provide age estimates for eight rock avalanches on the Puna Plateau in the central Andes. Dates ranged from 152 – 31 ka BP, to investigate the effect of active faulting on slope oversteepening and subsequent gravitational collapse. The return interval of seismic events in California and Nevada has been investigated by Bell *et al.* (1998) who dated precariously perched boulders, which would topple under seismic ground accelerations.

Cosmogenic dating of past failure events can also provide benchmark data for assessing modern rates of slope failure. In the Garwhal Himalaya, northern India, Barnard *et al.* (2001) compared estimates of the rates of modern slope failures with longer-term rates of failure dated using cosmogenic isotopes. They concluded that

modern rates of slope failure were much higher, with accelerations in slope failures being caused by anthropogenic activity, such as deforestation.

A complex geomorphological problem arises from trying to establish linkages, causal effects and relationships. The association of geomorphology and engineering in understanding the response to landscape change has considerable potential here, particularly in view of climate change. More recently geomorphological research has focused on the mechanisms of slope collapse in relation to paraglacial rock-slope modification (Augustinus, 1995, Ballantyne, 2002a; 2002b). These studies have identified steepening and debuttressing of the rock-slope through glacial erosion as important processes leading to failure. Such failures have been studied to a greater degree by geomorphologists because they have the potential to affect the processes operating in other geomorphological systems, such as fluvial systems. Three geomorphological responses of rock masses can be identified: (1) large-scale catastrophic failure; (2) progressive rock mass deformation; and (3) gradual slope adjustment by small-scale topples and slides. Each event has different magnitude-frequency intervals, lag-times and impact on the landform. Catastrophic events have a high magnitude and low frequency with a large lag-time and produce major landform change. These failures represent rapid adjustment to equilibrium form. Small-scale topples and slides are of low magnitude and high frequency, and change slope form gradually through time.

Progressive rock mass deformation is of particular interest to engineers and geomorphologists because of the timescale over which change takes place, and the magnitude of the failure event. Many of the progressive slope deformations tend to be deep-seated and have the potential to induce significant landform change and pose a considerable engineering hazard. Landforms produced by deep-seated deformations include 'bulging' toe slopes, ridge-top depressions and uphill-facing scarps (antiscarps). Such time-dependent deformations are important because they may be major factors in reducing the stability of rock slopes and promoting catastrophic failure (Chigira, 1992). Bovis (1982, 1990) examined the geomorphological evidence for deep-seated deformations on the slopes overlooking Affliction Glacier in southwest British Columbia. Geomorphological evidence for deep-seated deformations included tension cracks, antiscarps, and elongated graben indicative of tension in the near-surface zone. It is argued that down-wasting of Affliction Glacier by 100 m since the mid-19th century is the main process causing

deformation of the rock mass. Monitoring indicated that an estimated 3 x 10^7 m^3 of rock is undergoing time-dependent deformation (Bovis, 1990). These studies have argued that rock slope failure is mainly a response to changing stress regimes caused by deglaciation. In many cases it is difficult to estimate the timescale over which progressive low magnitude, high-frequency deformations lead to a high-magnitude low frequency event due to the crossing of a threshold.

A major geomorphological and engineering issue, therefore, is that as event size increases and its return interval increases, the frequency with which real-time observations can be made diminishes. A point is reached where the largest events for a landscape system have never been observed or recorded. One method often employed in both engineering geology and geomorphology when events are difficult to record, either due to their infrequent, short-lived and sporadic occurrence, or because of their size, is to develop models to predict change (Kirkby, 1994, Ahnert, 1996). Mathematical computer-based methods developed by engineers are increasingly used by the geomorphologist. Investigations of rates and mechanisms of cliff development relative to the displacement of rock mass block sequences using distinct element modelling is one example (Kimber *et al.*, 2002).

Engineering-based computer models are important because they require knowledge of the engineering properties of the landform, such as *in situ* stress, intact rock strength, discontinuity geometry and the shape of the landform. These are also of interest to geomorphologists because the response of landforms in jointed rock masses is dependent on the interaction of these factors. If the potential for linking geomorphology with engineering is considered, process, form and material associations are of equal importance.

Computer models have the potential to form the link between the geomorphological and engineering response of the landform. They require information regarding the intact rock strength and the discontinuity geometry and have the potential to investigate the process-form-material interactions relevant to the geomorphology of landforms in jointed rock masses. They have the advantage that magnitude-frequency relationships, return intervals and spatial and temporal patterns in activity rates can be investigated in an integrated geomorphological framework.

The remaining part of this chapter provides background on how appropriate intact rock strength parameters are gained and how this can be derived from testing

methods used mainly in engineering. Understanding material behaviour is crucial in providing data for numerical modelling. Most techniques of establishing intact rock strength and discontinuity properties are unfamiliar to the geomorphologist, but are critical to understanding and modelling landform behaviour because the response of the landform is dependent upon material properties. Moreover, these techniques are routinely used by engineers in assessing slope stability problems.

2.3 Intact rock strength characteristics

Stress-strain concepts are integral to a comprehensive understanding of how materials at the Earth's surface respond to the processes acting upon them and the resulting landforms (Allison, 1996b). It is important that the strength of intact rock blocks is known when studying landforms in jointed rock masses as it acts as a control on the failure of slopes. Intact rock strength properties are required by the modelling methodology used in this study. Rock resistance to deformation involves toughness, resilience, strength and elasticity (Deere, 1966).

A number of different laboratory and field tests exist to understand the links between stress, strain, shear and confining pressure. The resulting deformation may be volumetric and/or distortion-based (Brown, 1981; Goodman, 1980; Hoek and Bray, 1981). Types of tests include basic field estimates based upon Schmidt hammer testing, static laboratory stress-strain testing, dynamic sonic wave propagation and correlations with petrographic properties. The methods used to determine the intact rock properties and joint properties used in this study are described below.

Understanding the stress-strain response of Earth material's is important for creating realistic numerical models. The form of the stress-strain response of a material indicates whether the material is elastic or plastic. In elastic behaviour, all strain is recoverable after removal of stress, whereas plastic deformations are permanent. It is important to define the behaviour of the intact material in any numerical model by conducting laboratory experiments because assigning unrealistic models to the intact materials will produce inaccurate predictions.

2.3.1 Standard laboratory testing methods and material behaviour

Geomorphological consideration of material properties has used simple stress-strain relationships to estimate parameters associated with specimen failure or shear deformation (Selby, 1987). One of the most common strength parameters used by geomorphologists to account for differences in landforms is compressive strength (Allison *et al.*, 1993). The stress-strain response of Earth materials is critical for understanding the response of landforms to imposed stresses. Geomorphologically, strain is important because it usually occurs over a period of time in response to imposed stress. The rate of strain can be important in determining whether a rock will fail. Stress and strain are presented on the same diagram because strain is a function of stress.

Important parameters which describe the stress-strain response of a material to stress include compressive strength, Young's modulus, Poisson's ratio, friction angle and cohesion. These are required for numerical modelling of rock masses. Some account must also be made of the magnitude of *in situ* stresses. These parameters can be obtained from laboratory tests that replicate shear failure of rocks. Uniaxial and triaxial shear are used to derive values for these rock strength parameters used in this study.

Cut samples for uniaxial and triaxial testing are prepared from specimens recovered in the field. Samples are usually prepared to a diameter of 54 mm using a diamond-edged drill bit, with a length to width ratio of 2.0 to 2.5. It is important that sample ends are ground to a tolerance of ± 0.1 %, so that stress application is equal across the core, so that artificial failures are not produced in the test specimen. The unconfined compressive strength is requested nine times more often by engineers than the second most sought after property, triaxial strength (Bell, 2000). The compressive strength q_u is defined as the ratio of the maximum load at failure P to the cross-sectional area of the specimen A before the test (Goodman, 1989), namely

$$q_u = \frac{P}{A}. \qquad \textbf{Equation 2. 1}$$

A triaxial test varies a stress applied in the vertical direction σ_1 upon a sample at a chosen confining pressure applied horizontally σ_3 and represents a confined test. Tests can be conducted either at isotropic pressures, where all stresses σ_1, σ_2 and σ_3 are equal, or under deviatoric stress regimes, for which $\sigma_1 > \sigma_2 = \sigma_3$. Testing under deviatoric stress regimes is preferable, as it is the deviatoric stress components which produce deformation and failure of rock. Samples for testing are inserted inside a Hoek cell, where an impervious membrane applies a specified confining pressure. The confining fluid is hydraulic oil and the membrane is oil-resistant.

The shear failure of a rock specimen is normally analysed by the Mohr-Coulomb theory to derive the angle of internal friction, ϕ, which is due to the normal forces acting on the core and cohesion. Shear strength, τ, is related to cohesion, c, and normal stress, σ, by

$$\tau = c + \sigma \tan \phi. \qquad \textbf{Equation 2. 2}$$

By running at least three failure tests, the Coulomb failure criterion can be estimated by the Mohr graphical method. Cohesion is plotted against strength, with circles drawn as defined by σ_1 - σ_3. A line drawn tangent to all the Mohr circles representing specimen failure defines the failure envelope of the rock. The gradient of the line is the effective friction angle of the sample and the cohesion axis intercept of the envelope represents the apparent cohesion of the sample. However, there is often much variation in the results of a number of tests and the failure envelopes for most rocks lie between a parabola and a straight line (Goodman, 1989).

The stress-strain response, or deformation of material under uniaxial and triaxial compression, is measured with surface-bonded electric resistance strain gauges. A gauge bonded parallel to the specimen axis records axial deformation, $\varepsilon_{axial} = \Delta l/l$, while diametrical strain, $\varepsilon_{lateral} = \Delta d/d$, is recorded by a gauge bonded perpendicular to the longitudinal axis. The bonding agent should have similar deformation properties to the rock being tested, so that an accurate representation of specimen deformation is attained. It is important to attach the axial strain gauges at opposite ends of the core and at least 27 mm from the ends where the load is applied. This is because the loading frame can impart artificial strength at the ends of the core specimen, resulting in reduced deformation estimates.

Strain gauges are constructed by bonding a fine electric resistance wire or photographically etched metallic resistance foil to an electrical insulation base using an appropriate bonding agent and the attaching lead wires. The strain ε generated in a specimen subjected to stress is relayed through the base to the fine wire or foil, where expansion or contraction occurs. As a result, the fine wire or foil experiences a variation in electrical resistance. This variation is directly proportional to strain so that measured strain

$$\varepsilon = \frac{\Delta L}{L} = \frac{\Delta R_g / R_g}{F},$$

Equation 2.3

where ε = measured strain,

L = length of specimen,

R_g = gauge resistance (Ω),

ΔR_g = resistance change due to strain (Ω) and

F = gauge factor as shown on gauge packaging.

In the case of a 2 wire gauge system, as used in this study, the attachment of wires to the strain gauge using the quarter or half bridge method will result in an apparent deterioration of the gauge factor, because the resistance of the lead wire is in series with the gauge. The gauge correction factor, F_o, due to the lead wire in the case of a 2 wire system is given by two relationships:

The correction coefficient of lead wire is

$$A = \frac{R_g}{R_g + rL}$$

Equation 2. 4

and the gauge factor corrected K_o is then

$$F_o = \frac{R_g}{R_g + rL_w} K = AF,$$

Equation 2. 5

where F = gauge factor as supplied,

F_o = corrected gauge factor,

R_g = normal gauge resistance (Ω),

r = total resistance per meter of lead wire (Ω/m) and

L_w = length of lead wire (m).

The use of bonded strain gauges allows the full stress-strain curve to be analysed during loading, from which the deformation modulus E can be calculated. Deformability is the capacity of a material to strain under applied loads. Stress and strain may be theoretically related using Hooke's theory of linear elastic theory. For intact rock materials, static elastic properties can obtained from the gradient of the stress-strain curve over the elastic range (Deere, 1966). In the vertical direction, the stress-strain relationship of a specimen can be defined by

$$\sigma = E\varepsilon, \qquad \textbf{Equation 2. 6}$$

where σ = normal stress,

E = Young's modulus and

ε = normal strain.

Young's modulus is a good indicator of rock deformation under load, which has geomorphological importance when studying rock slopes (Allison, 1988; Augustinus, 1991). Young's Modulus is defined as the ratio of the axial stress change $\Delta\sigma$ to the change in axial strain produced by the stress change $\Delta\varepsilon_a$, namely

$$E = \frac{\Delta\sigma}{\Delta\varepsilon_a}. \qquad \textbf{Equation 2. 7}$$

In the horizontal direction, Poisson's ratio ν is the ratio of the lateral deformation to linear deformation in the rock core within the elastic limit and varies between 0 and 0.25 for a perfectly elastic body. Poisson's ratio can increase above 0.25, the theoretical limit for a perfectly elastic body, because of inelastic behaviour caused by the onset of microcracking. Elastic properties are meaningless unless the conditions under which the properties are obtained are specified. However, a

gradient of a stress-strain curve is not linear when testing rock samples because of the presence of pores and crack propagation. Brady *et al.* (1985) tested a closely jointed rock and showed that hysteresis can occur under loading, while the elastic properties were attained in the unloading phase. Ofoegbu and Currna (1991) suggested that structural defects such as microcracks cause the load-bearing capacity and elastic stiffness of rock to decrease.

All material models for deformable blocks assume isotropic material behaviour in the elastic range defined by two constants, bulk modulus K and shear modulus G. The elastic constants, K and G, are used in many numerical codes, rather than Young's modulus and Poisson's ratio, because it is argued that the bulk and shear moduli correspond to more fundamental aspects of material behaviour (Itasca, 2000). Bulk modulus and shear modulus are related to the more commonly attained elastic properties, Young's modulus and Poisson's ratio, by

$$K = \frac{E}{3(1 \times 2\nu)}, \qquad \textbf{Equation 2. 8}$$

$$G = \frac{E}{2(1+\nu)} \text{ and} \qquad \textbf{Equation 2. 9}$$

$$E = \frac{9KG}{3K+G}. \qquad \textbf{Equation 2. 10}$$

Conversely,

$$\nu = \frac{3K \times 2G}{2(3K+G)}. \qquad \textbf{Equation 2. 11}$$

An estimate of axial and diametrical strain is necessary to define material behaviour at different confining pressures from the shape of the stress-strain curve, Young's modulus and Poisson's ratio. Poisson's ratio ν is an elastic measure calculated by measuring the change in diameter, Δd, and the change in length, Δl, by

$$\nu = \frac{\Delta d / d}{\Delta l / l}. \qquad \textbf{Equation 2. 12}$$

2.3.2 Sonic wave propagation

An alternative method for the determination of the elastic properties of rock is dynamic wave propagation, used to determine the elastic properties of intact rock, namely Poisson's Ratio and Young's Modulus. The advantage of the method is that it is quick and relatively simple. However, it gives no information on the stress-strain behaviour of the material. Intact rock elasticity is useful in solving geomechanics problems in numerical modelling and has the advantage that it can be measured *in situ* (Davies and Salvudurai, 1996). The method was used in conjunction with conventional testing methods to provide the elastic properties of the intact rock required for the numerical modelling.

When a vibration is passed through a solid, four different types of velocity waves are generated: compressional *P* waves; shear *S* waves; Rayleigh and Love waves. The ability of a body to resist forces which tend to include compressive, tensional, shear or volumetric deformations is determined by its elasticity (Cooks, 1981; Selby, 1987). In practice, microcracks in the rock being tested have an influence, although this can be negated if porosity is considered (Goodman, 1980).

Allison (1988) used the Grindosonic device for measuring the speed of wave propagation through a rock sample, and the calculation of dynamic Young's modulus. The apparatus has been used in the field, with tests being conducted on the Napier Range, Australia. However, the test apparatus is bulkier and more expensive than the Schmidt hammer in conducting non-destructive field testing (Allison, 1991). Parameters such as mineralogy, texture, density, porosity, anisotropy, moisture content and temperature affect the propagation of waves (Augustinus, 1991). The dilation wave velocity increases with the state of stress, rock density and the closing of microcracks (Deere, 1966).

2.3.3 Schmidt hammer testing

A rapid estimate of the compressive strength of rock can be gained using the Schmidt hammer. This is useful in estimating the yield point of the rock. Although not as accurate as conventional laboratory testing, the method is useful in checking whether laboratory-based estimates of rock strength are accurate. For this study, only a limited number of samples could be taken for laboratory analysis, and the

Schmidt hammer was used in the field to gain a 'representative' estimate of rock strength. This was to ensure the data being used for the numerical modelling were representative of the site as a whole.

The Schmidt hammer measures the rebound distance of a controlled impact on the rock surface. The principle of the test is based on the absorption of part of the spring-released energy through plastic deformation of the rock surface, while the remaining elastic energy causes the actual rebound of the hammer. The distance travelled by the impacted mass, expressed as a percentage of the initial extension of the spring, is called the rebound number, *R* (Kolaiti and Papadopoulos, 1993). The elastic recovery of a rock surface depends upon the hardness of the surface. As hardness is related to mechanical strength, the rebound number gives a relative measure of surface hardness or strength (Day and Goudie, 1977). Hammer rebound readings are considered to be consistent and reproducible (Poole and Farmer, 1980; Goktan and Ayday, 1993; Amaral *et al.*, 1999).

Two types of Schmidt hammer exist, L and N-type, and reliable correlations have been achieved using both (Ayday and Goktan, 1992). The advantages of correctly using the Schmidt hammer are that it provides some useful indications of rock quality, it is cheap, and it is fast (Campbell, 1991). An advantage of the technique is that the *in situ* strength of the rock can be determined (Hucka, 1965), forming a direct link between the material properties of the landform and the numerical model.

There is no theoretical basis of relating Schmidt hardness measurements to other strength properties, but empirical relations can be made (Deere, 1966). In comparison with alternative, similar rock strength tests, such as the point load test, Los Angeles abrasion test and the slake durability tests, the Schmidt hammer provides the best correlation at unconfined compressive strengths of less than 150 MPa, but is not as good above this threshold (Cargill and Shakoor, 1990). Aggistalis *et al.* (1996) attempted to correlate the uniaxial compressive strength and Young's modulus of 63 gabbros and 30 basalts with the Schmidt hammer rebound value. Deere (1966) related Schmidt hammer rebound values to the ultimate compressive strength C_o and Young's modulus *E*. Twenty-four Schmidt hammer rebound values were recorded and the top 50% of values used in the correlation. More recently, Yilmaz and Sendir (2002) have related Schmidt hammer rebound values to unconfined compressive strength and Young's modulus in gypsum from the Sivas

Basin, Turkey, noting that it is impossible to derive a simple correlation that is applicable to all rock types.

Allison (1990) stated that the accuracy of Schmidt hammer tests has been questioned: a correlation of only 0.33 was observed with Hoek cell data from the Devonian limestone of the Napier Range, Australia. Campbell (1991) suggested that Schmidt hammer rebound data collected by Allison (1990) differed in accuracy from other, more sophisticated tests, arguing that the Schmidt hammer provided accurate estimates of *in situ* rock properties. Improvements to correlations by combining *R* values with ultrasonic pulse velocity or dry density have been recommended (Arioglu and Tokgoz, 1991). Stronger positive correlations have been recorded between Schmidt hammer rebound values multiplied by density and the uniaxial compressive strength (Augustinus, 1991; Xu *et al.*, 1990).

2.3.4 Representation and accuracy of intact rock strength tests

The material properties entered into numerical models should correspond as closely as possible to the actual strength of material in the natural rock slope. Laboratory experiments only partially reproduce the conditions under which rocks deform *in situ*. The sample dimensions are smaller than those in the field and drilling causes disturbance to the rock (Crïstecu, 1989). The presence of discontinuities in the model will account for most of the scaling effect on rock mass properties.

Intact rock blocks are said to be anisotropic as they have physical, dynamic, thermal, mechanical and hydraulic properties that vary with the direction of principal stresses. Not only is intact rock behaviour non-linear, but anisotropy is important when measuring rock parameters (Amadei, 1996). Chosen testing points and volumes for the measurement of rock mass properties can affect the results of laboratory tests (Cuhna, 1990). Anisotropy causes rocks to be 70% weaker parallel to the joints (Augustinus, 1991). The only sure way to evaluate the effects of anisotropy is by systematic laboratory testing of specimens drilled in a number of directions from an orientated block sample (Goodman, 1980). For the present study, samples were drilled according to their field orientation, so that the direction of principal stresses acting on the laboratory samples was the same as those acting *in situ*.

Some of the problems of sample representation, laboratory testing and anisotropy are overcome by the use of non-destructive field tests. However, they have the disadvantage that detailed material behaviour cannot be observed. One issue is how intact material behaves at different scales as confining and normal pressures are increased. By strain gauging samples at varying confining pressure, this study hopes to increase understanding of these properties and its significance for geomorphological evolution of rock masses, even though the stresses used are far greater than those found in most engineering and geomorphological situations.

2.4 Discontinuity characteristics

Numerical modelling of jointed rock masses requires that the characteristics of discontinuities are known. Understanding how these data are derived is important when designing models which capture the essential characteristics of the system being modelled. The following sections describe the importance of discontinuities in controlling the stability of rock slopes, how the discontinuity geometry is measured in the field, and how strength properties are assigned to the joints. Knowledge of spacing and the size of discontinuities in a rock mass is of considerable importance for the prediction of rock behaviour and the assessment of rock quality (Priest and Hudson, 1981; Priest, 1993). Geomorphologically, joint spacing is important in assessing rates of change in rock slopes because slopes with few joints are considered to be more resistant to failure than those with dense discontinuity networks.

2.4.1 Genesis

Rock masses contain many structural discontinuities, which reduce the shear strength of the rock mass below that of intact material (Hencher, 1987). It is crucial that these discontinuities be included in any stability assessment. A discontinuity can be defined as any significant mechanical break or fracture that possesses negligible tensile strength (Priest, 1993). The term makes no distinctions concerning age, geometry or mode of origin of the feature and includes bedding planes, faults, fissures, fractures, joints and other mechanical defects. The discontinuities can be classified into four groups of tension, shear, sedimentation and metamorphic, according to the mechanical or environmental processes

responsible for their genesis (Aydan and Kawamoto, 1990a; 1990b). For this study, joints and bedding planes are the most important class, and the term discontinuity is used throughout when referring to these features. Joint initiation depends upon the nature of the material and also pre-existing weaknesses such as cleavages and grain boundaries (Whalley *et al.*, 1982) and can it be deduced by analysing joint aperture and spacing (Narr and Suppe, 1991; Pascal *et al.*, 1997). Overburden pressures which cause rock masses to crack have been calculated by relating the average joint spacing to thickness of the bedding (Angelier, 1989).

2.4.2 Measurement and analysis

The engineering behaviour of a rock mass is controlled by the presence of discontinuities on a scale which can be measured (Attewell and Farmer, 1976). To understand the influence that discontinuities have on rock mass behaviour it is necessary to measure the relevant characteristics of the discontinuities that form the complex three-dimensional fabric of mechanical breaks (Priest, 1993). In the field, two geometrical properties of the discontinuity have to be measured using a compass-clinometer. The strike is the trace of the intersection of an obliquely inclined plane with a horizontal reference plane and it is perpendicular to the dip and dip direction of the oblique plane (Brown, 1981), and is measured from 0 to 180° with the compass. The dip is the maximum inclination of a structural discontinuity plane to the horizontal, measured from 0 to 90° with a clinometer (Hoek and Bray, 1981). Often, when measured on a rock mass as a whole, the line where the discontinuity plane intersects the rock face is measured, giving a result which is usually less than the true dip. These two parameters, together with an indication of the direction in which the plane is dipping, are all that are required for the three-dimensional representation of a plane. These parameters are required for numerical modelling of rock masses; they also allow rapid assessments of the potential failure mechanisms that may occur in a rock mass.

It is recommended that at each location at least 100 strike and dip measurements should be taken to quantify the joint network (Goodman, 1980). On exposed rock slopes, joints should be recorded using a scan-line, which usually consists of a 100 m tape measure laid parallel to the cliff face and each discontinuity recorded along this line. It is important to conduct a second scan-line, where possible,

perpendicular to the first, so that orientation bias is reduced. This was possible in all but three of the field locations used in this study.

Hemispherical projection is a method for representing three-dimensional data in two-dimensions (Goodman and Bray, 1976; Phillips, 1971; Priest, 1985). The method is often referred to as stereographic projection (Phillips, 1971). The method is useful in representing the individual planes as a great circle and analysing their relationships and intersections. The technique is not very useful for measuring trends in the discontinuity data (Swan and Sandilands, 1995). It is more convenient to plot points that correspond to the normals of each plane. This allows analysis of the data when plotted on an equal area net (Mauldon and Goodman, 1996). The pole of each great circle is the point which is the centre of the great circle on a sphere. By plotting the poles for each measured discontinuity on a stereoplot, statistical contouring methods can be used to identify pole concentrations (Priest, 1995). From this, mean joint set characteristics can be defined. The technique can be used to investigate the likely failure mechanism of the rock mass (Lana and Gripp, 2003; Yoon *et al.*, 2002). Statistical processing of large data sets is more rapidly accomplished by use of computer software, such as DIPS (Rocscience, 2002).

Other discontinuity parameters measured include spacing between parallel pairs of joints and the persistence of individual joint segments (Gabrielsen, 1990). Joint spacing is important because it governs the stress-strain response of the rock mass (Hoek and Bray, 1981). Three types of spacing statistics can be recognised (Priest, 1993):

1. the spacing between a pair of adjacent discontinuities, referred to as *total spacing*;
2. the spacing between a pair of adjacent discontinuities from a particular discontinuity set, measured along a line of specified location and orientation, referred to as *set spacing*;
3. the set spacing when measured along a line that is parallel to the mean normal of the set, referred to as *normal set spacing*.

It has been suggested that a log-normal or exponential statistical model is the most useful for summarising total joint spacing data (Mohajerani, 1989; Priest 1993; Tindall and Davis, 2003). Other reported distributions for joint spacing include

gamma and Weibull (for example, Kulatilake *et al.*, 1993; Rives *et al.*, 1992; Warburton, 1980; Bardsley *et al.*, 1990; Sen, 1993). Yet other research has indicated that many discontinuity properties exhibit power-law distributions and are fractal (for example, Barton and Larson, 1985, 1988; La Pointe, 1988; Marrett *et al.*, 1999; Roach *et al.*, 1993; Ehlen, 2000).

Many difficulties have been noted when measuring the joint geometry characteristics of a rock mass. Errors in determining the orientation of discontinuities result in uncertainty about slope stability (Cruden and Charlesworth, 1976). Most studies assume full persistence and bias is frequently introduced due to the sampling method used (Kulatilake and Wu, 1984). A major problem of measuring the persistence of discontinuities is that it is impossible to map the rock mass internally (Einstein *et al*, 1983; Einstein, 1993; Odling, 1997). Some studies have attempted to overcome this problem by using probabilistic analysis based upon joint shape, distribution of centroids and joint distribution to predict the three-dimensional joint orientation in an outcrop. Errors can also be caused by sampling bias of discontinuity orientation caused by the linear sampling technique using scan-lines (Park and West, 2002; Terzaghi, 1965).

2.4.3 Strength Properties

Joint properties are derived from laboratory triaxial shear tests of joints and a knowledge of joint stiffness is required under normal and shear loads (Swan, 1983). Values for normal and shear stiffness for joints can range from 100 MPa m^{-1} for joints with a soft clay filling, to over 100 GPa m^{-1} for tight joints in granite and basalt (Kulhawy, 1975). Approximate values of normal stiffness k_n can be calculated from information on the deformability and joint structure in the rock mass through the rock mass Young's Modulus E_m the deformability of the intact rock E and the joint spacing s (Itasca, 2000):

$$k_n = \frac{E_m E_r}{s(E_r \times E_m)}. \qquad \textbf{Equation 2. 13}$$

Joint shear stiffness, k_s is related to the rock mass shear modulus G_m the shear modulus of the intact material G_r and the joint spacing s by

$$k_s = \frac{G_r G_m}{s(G_m \times G_r)}.$$

Equation 2. 14

The nature of joint fill material is important in understanding the mechanics of joint deformation. Although the shear strength of infilled rock joints has been studied extensively, a complete understanding of the controlling parameters has never been gained (DeToledo and DeFreitas, 1993). Closure, shear displacement and dilation are the main joint strength parameters that dictate the performance of a rock mass (Bandis, 1993). Joint stiffness values are dependent on joint surface roughness, the strength of asperities and the infilling material. Representative data for the stiffness properties of rock joints can be found in Kulhawy (1975), Rosso (1976) and Bandis *et al.* (1983).

It is important to recognise that joint strength properties measured in the laboratory are typically not representative of those for real joints in the field due to variability of joint fill material, surface roughness and aperture of joint surface contact (Itasca, 2000). Often, the only way to guide the choice of appropriate parameters is by comparison with similar joint properties derived from field tests (Kulhawy, 1975).

2.5 Rock Mass Stability

The geometry and strength properties of rock joints decrease the strength of a jointed rock mass below that of intact rock. The mechanical behaviour of a rock mass will depend on the mechanical behaviour of the intact rock and of discontinuities and their orientation with respect to the applied load and confining conditions (Aydan and Kawamoto, 1990a, 1990b). The reduction in rock mass shear modulus because of the presence of joints tends to be greater than corresponding reductions in direct moduli and Poisson's Ratio (Gerrard, 1982).

Rock mass classification techniques are used to gain an appreciation of the strength of a rock mass, and have been employed in many studies to complement rock mass modelling (Cameron-Clarke and Budvari, 1981; Hoek, 1983; Price, 1993). Engineering classifications have also been modified for use in geomorphological studies. The rock mass strength (RMS) classification, first introduced by Selby

(1980) for the analysis of jointed rock slopes, was designed so that geomorphologists are able to make rapid field assessments of RMS in remote locations (Selby, 1987; 1993). The strength of intact rock, degree of weathering, groundwater and joint geometrical properties are all measured and a weighting applied for a classification of up to 100. The RMS classification values correlated well with slope angles for slopes in Antarctica and New Zealand (Moon, 1984; Selby, 1980). As a result, the concept of a strength equilibrium slope was developed as stronger slopes are more likely to be inclined at steeper angles.

The RMS and other classification schemes are limited because of the simplifications in measurement and the lumping of different parameters to give a single estimate of rock mass performance. All widely used rating systems have been developed from many years of engineering experience, but all suffer from the problem of assigning weighting factors (Price, 1993). In the field, different properties may exert differing influences on the stability of the rock mass, depending upon other properties of the slope. For instance, the angle of bedding may exert a large influence on steep slopes, but where the angle of the slope is low, the influence of bedding structures may not be so great. Advances in the understanding of slope behaviour can be made using the RMS classification, but the numerical modelling of slopes is based on a physical, deductive approach in a more rigorous scientific style. The advantage of using modelling approaches over such empirical classification schemes is that insights can be gained into failure mechanisms and how the slope changes through time. This is important in assessing long-term geomorphological behaviour of steep slopes.

The classification of jointed rock masses, based upon the incorporation of weakening of rock material by discontinuities, is a commonly used engineering method of gaining a comparative measure of rock mass strength (Goodman, 1980). The rock quality designation system (RQD) was developed by Deere *et al.* (1969) and classifies the rock as excellent, good, fair, poor or very poor, giving an indication of stability. The RQD overcomes some simplifications of the RMS classification system as it makes more reference to the discontinuity structure of the rock mass. The RQD can be related to velocity measurements (Sen and Kazai, 1984; Sen and Sadahah, 2003) and discontinuity spacing (Priest and Hudson, 1981), but it ignores factors of rock strength, joint character and environmental properties (Goodman, 1980).

The rock mass rating schemes have been widely used and developed for engineering purposes. Brown (1981) developed the NGI tunnelling quality index Q which is related to RQD:

$$Q = \frac{\text{RQD}}{J_n} \times \frac{J_r}{J_a} \times \frac{J_w}{\text{SRF}}, \qquad \textbf{Equation 2. 15}$$

where J_n = number of joints,

J_r = joint roughness number,

J_w = water reduction factor,

J_a = joint alteration number and

SRF = stress reduction factor.

Q can vary from 0.001 for poor quality rock to 1000 for very good quality rock. The application of the Q system was demonstrated by relating 38 categories to an excavation support ratio (ESR), which varies with the use of excavation and the extent to which some degree of instability is acceptable (Barton *et al.*, 1974). The RQD index has been used to predict the deformation of rock masses (Gökçeoglu *et al.*, 2003). Bieniawski (1978) developed an empirical relation for a modulus of rock mass deformation E_m from numerous field test results and a rock mass rating RMR:

$$E_m = 2(\text{RMR})100. \qquad \textbf{Equation 2. 16}$$

The RMR is a measure from 0 to 100 derived from the strength of the rock, drill quality, ground water, joint spacing, and rock mass characteristics (Bieniawski, 1973). Schultz (1996) analysed Mohr failure envelopes obtained from the RMR classification system and showed that rock mass cohesive strength, tensile strength and unconfined compressive strength can be reduced by as much as a factor of ten, relative to the values for an equivalent unfractured material. The most commonly accepted approach to estimate rock mass strength is the Hoek-Brown failure criterion. The major principal stress at peak strength

$$\sigma_{1s} = \sigma_3 + (m\sigma_c\sigma_s + s\sigma^2{}_c)^{1/2}, \qquad \textbf{Equation 2. 17}$$

where σ_3 = minor principal stress

m and *s* = constants dependent on the properties of the rock and

σ_c = uniaxial compressive strength of intact rock material.

2.6 Failure mechanisms in jointed rock masses

In hard rock slopes failure under gravity alone is possible only if the discontinuities permit easy movement of discrete blocks. In regularly bedded rocks, cut by joints, many possibilities may exist for block movement along planes of weakness (Goodman, 1980). Collapse of rock slopes involving movement of discrete blocks along discontinuities leads to three basic modes of failure under gravitational stresses: plane sliding, wedge sliding and toppling (DeFreitas and Watters, 1973; Goodman, 1980; Hoek and Bray, 1981). The orientation of discontinuities, relative to the free-face, determines the stability of rock blocks (Leung and Quek, 1995).

A plane slide forms under gravitational stress when rock blocks rest on an inclined plane which dips out of the free face of the slope (Figure 2.2). The failure plane must intersect the slope free face and dip more steeply than the angle of internal friction ϕ of the discontinuity. Often, the sliding block must overcome the frictional resistance of lateral margins of the slide zone. In hard rocks, such as limestone, plane sliding can only occur if there are other discontinuities or valleys transverse to the crest of the slopes releasing the sides of the block. Plane sliding can occur when the plane of potential movement is within 20° of the strike of the slope face (Cruden, 1985; Goodman, 1980; Sharma *et al.*, 1995). A plane failure is a comparatively rare failure mechanism in rock slopes because it is only occasionally that all the geometrical conditions required to produce such a failure occur in natural slopes. Observations made in Kananaskis Country, in the Front Ranges of the Rockies, suggest that rock-slides occur on overdip slopes along penetrative discontinuities (Cruden, 1988).

Wedge failures occur along the intersection of two or more discontinuities (Hoek and Bray, 1981) (Figure 2.2). The dip of the line of intersection must be greater than the angle of internal friction across the surface, but less than the dip of the free face. Wedge failures occur when two or more planes of weakness intersect to define a tetrahedral block. Failure can occur without any structural or topographical release features if the line of intersection of two discontinuities daylights at the slope face

(Goodman, 1989). The formation of wedge failure is dependent primarily on lithology and structure of the rock mass (Piteau, 1972). Rock masses with well-defined orthogonal joint sets or cleavages in additional to inclined bedding or foliation generally are favourable situations for wedge failure. Shale, thin-bedded siltstones, claystones, limestones, and slaty lithologies tend to be more prone to wedge failure development than other rock types. However, because wedge failures are 3-dimensional problems, it is difficult to assess their importance using 2-dimensional modelling approaches. For example, a slope stability assessment for an open pit in Canada showed that the 2-dimensional UDEC code could not model 2435 potential wedge failures (Carvalho, 2002).

Toppling is a more complex failure mechanism that has only been recognised for the last 30 years (Goodman and Bray, 1976), but it has been the main focus of engineering geomorphological studies. Toppling involves rotation when the centre of mass of a block overlies a pivot point (Figure 2.2). Failure may be instantaneous and catastrophic, or merely involve deformation of the slope. Toppling has been identified as an important failure mechanism, which involves a large volume of rock in steep slopes composed of layered, well jointed or foliated rock. Failures have been classified into flexural-toppling, block toppling and block-flexural-toppling (Goodman and Bray, 1976). In slopes with one discontinuity system, columns break in flexure as they deform. In harder rocks, such as limestone and sandstone, block toppling can occur due to the pressure exerted by surrounding rocks, when individual columns are divided by widely spaced bedding planes. Block-flexure-toppling occurs when harder rock columns are interbedded with chert and shale. Toppling may also occur as a secondary motion to sliding (Evans, 1981). Block topples and block-flexure topples have been identified on the sandstone and shale slopes of the Highwood Pass, Alberta, Canada (Cruden and Hu, 1994). The toppling mode is controlled by the ratio of joint spacing to bedding thickness, rock strength and topography. In a geomorphic study of toppling failures from the dolerite alpine cliffs on Ben Lomond, Tasmania, two modes of toppling have been observed depending upon the location of the contact with the clay base (Caine, 1982). Toppling only occurs where the cliffs have been over-steepened due to glaciation, which occurred more than 100 000 years ago. Large scale toppling failures have been observed on the slopes of Ben Attow, Scotland (Holmes and Jarvis, 1985).

2.7 Conclusions

Many previous slope studies have failed to recognise the importance of combining information on the *in situ* stresses of the rock mass, intact rock strength and discontinuity characteristics. The methodology for the determination of relevant rock slope parameters used as part of this research for modelling rock-slope behaviour has been outlined. This study uses triaxial and strain gauge monitoring of rock cores from samples collected in the field at a range of confining pressures to obtain appropriate elastic constants relevant for slope stability studies. To model the evolution of jointed rock masses, methodologies and techniques need to be combined from geomorphology, geology and rock mechanics to produce appropriate input parameters. It is difficult to consider the characteristics of jointed rock masses together, but this research uses numerical software codes, which offer the advantage that geomorphological, geological and rock mechanics data can be synthesised in a deductive, scientific manner

Chapter 3: Modelling approaches to rock mass simulation

Chapter 3: Modelling approaches to rock mass simulation

3.1 Introduction

This chapter begins by providing an outline of the general considerations and approaches to the numerical modelling of slopes. Only by understanding the purpose of a model can meaningful insights into landform evolution be gained. It then discusses numerical engineering approaches to simulating jointed rock mass behaviour. There are many engineering approaches for simulating jointed rock masses and it is important to understand how different approaches differ, because each has a different purpose. Three broad approaches are available to engineers in assessing rock-slope stability: continuum; discontinuum; or hybrid approaches. The chapter reviews the relative advantages, limitations and applications of these approaches. The chapter then outlines the Universal Distinct Element Code (UDEC), which was used to model slopes in this study.

3.2 Approaches to numerical modelling of geomorphological systems

Early geomorphological slope models were the product of field investigation and were based on classification. Models are now more composite in character and predict long-term slope development which cannot be validated in the field (Anderson and Sambles, 1988; Howes and Anderson, 1988). Computer simulation provides a rapid and efficient means to examine the validity of a range of possible relationships and it requires clarity of thought and precise specification and commitment (Howes and Anderson, 1988).

Slope development modelling in geomorphology has primarily analysed slopes with softer sediments. For instance, the SLOP3D model has been used to model landform changes as a response to changes in the gross rate of fluvial downcutting (Ahnert, 1988). SLOP3D used the concept of dynamic equilibrium in slope evolution, relating the rate of creep to slope angle (Howard, 1988). The program has been used to model gully and valley development, inselberg development and karst landforms (Ahnert, 1994; 1996).

One area of omission by slope modellers is that of rock-slope processes in regard to rock-slope controls (Anderson and Sambles, 1988). However, the difficulty of modelling jointed rock-slopes has been noted (Selby *et al.*, 1988). It is suggested that a full understanding of rock-slopes can only be achieved by exploiting all physical, numerical, geotechnical and schematic models. Such an understanding is now possible with sophisticated computer simulation packages.

The purpose of any numerical model needs to be clearly defined to avoid ambiguity with the explanation offered by model output. The relevant aspects of the real world and the level of detail required have to be identified. Modelling has been defined as a purposeful representation of whatever is being modelled (Starfield *et al.*, 1990). The modelling methodology used in this work differentiates between designing a model of a landform and designing a model which represents important landform features. No model can include enough detail to accurately represent a real landform, but it is possible to gain an insight into the controlling mechanisms of landform development. It is important to consider the level at which the joint geometry represented in a numerical model represents that of the actual rock-slope being modelled. The model geometry must represent the physical problem to a sufficient extent to capture the dominant mechanisms related to geologic structure in the region of interest. Another important theme is the theoretical modelling approach, by isolating parameters such as block size, to advance geomorphological understanding of system behaviour. By conducting sensitivity analyses important controls on landform behaviour can be identified. Often, even large uncertainties in conditions do not alter the general conclusions that can be drawn from the predicted response of a model.

Several important issues arise when modelling landforms. A balance must be struck between the collection of essential data relevant to the broad-scale evolution of the landform and the exclusion of irrelevant, micro-scale data, which result in computationally expensive simulations. Model design must also take into account the accuracy of data collected, because this constitutes the physical attributes of the modelled system. Measurement error may result in up to 70% inaccuracy in model output through algebraic operations (Alonso, 1968). As models become more complex, errors accumulate as data are processed through mathematical algorithms. When accurate data are readily available, complex models can be designed and executed, whereas a data-limited model must be considered inherently simple. The goal of data collection for any modelling exercise is to collect

enough relevant data to represent, in a simple manner, the main processes controlling landform evolution.

Simplification is a crucial aspect of numerical modelling. A balance must be reached between geological detail, engineering understanding and computational efficiency. Rock mass modelling, for example, is a data-limited system (Starfield *et al.*, 1990) because field data such as *in situ* stresses, material properties and geological detail will never be fully known. Despite these limitations, numerical models are still important in providing the geomorphologist with an insight into the mechanisms operating within a physical system (Starfield and Cundall, 1988). The goal of modelling is not to reproduce, in exact detail, the geological and geomorphological structure of a site, but to include enough information so that the general behaviour of the system can be simulated.

In contrast, it has been argued that geomorphological models have become more detailed, incorporating aspects of natural systems, reducing the number of generalisations and accounting for non-linear system dynamics (Anderson and Sambles, 1988). Geomorphological process domains are linked in time and space, which means that it is often difficult to define meaningful system boundaries for the investigation of system behaviour. Generally, there have been two main ways that geomorphologists have designed models: first, by assembling small, known and unknown, elements of a system, or second, by starting with a coarse representation of the system and quantitatively describing component interactions (Carson and Kirkby, 1972; Ahnert, 1996). The environmental modeller has to be aware of the problems associated with randomness to explain natural systems. Modelled slope profiles generated with randomly varied processes can result in a general similarity to natural landforms (Ahnert, 1994; Chorley, 1964).

The behaviour of environmental systems can be considered as scale-dependent. The type of landform change exhibited has implications for the modelling methodology employed to explain the change. As a landform increases in scale, the longer it lasts, or the older it is, and there are a greater number of processes acting on it (Ahnert, 1988). A general aim of geomorphological modelling is long-term simulation to explain change through time. However, as the timespan over which the model simulates increases, the potential for errors being multiplied through the model run increases (Anderson and Sambles, 1988). Numerical models are designed to aid engineers to assess short-term stability problems, yet this study is

concerned with the long-term simulation of rock-slope evolution. Scale effects can also be replicated in numerical codes because there is no mathematical limit to the size of the system being modelled.

Some attention must also be given to the problem of representing past events in models which are based on present environmental conditions (Douglas, 1988). Hillslope development may be characterised by extreme events, such as rock-slope failure, followed by a period of adjustment by modifying processes. The age and persistence of the landform adds to the complexity of the modelled slope system (Brunsden, 1993). Rock-slopes will contain stresses which are the result of previous failures and loading. However, unless the history of failures is known for natural rock-slopes, the modelling methodology has to acknowledge some limitation in representing the field situation.

Numerical simulations have shown that regolith evolution can reach a steady state, undergo complex or simple response cycles or behave in a chaotic manner, depending on the chosen rate of bedrock weathering and removal of erosional debris (Phillips, 1993). Chaotic behaviour has been observed in many natural environmental systems. Chaos can be defined as irregular and complex behaviour, which is regulated by a deterministic, but unexplained rule (Gleick, 1987; Thompson and Stewart, 1988). If chaotic behaviour is inherent in landform processes, very small differences in the initial parameter conditions can lead to very different outcomes (Lorenz, 1976). In rock-slopes, there appear to be two main sources of chaotic behaviour. First, the discontinuity geometry forces the system to choose, apparently at random, between two alternate outcomes. If the apexes of triangular blocks touch, for example, a choice in the direction of movement will exist and will depend on microscopic irregularities in geometric properties of the rock blocks or kinetic energy (Cundall, 1990). Second, a positive feedback process of 'softening' arises when one or more stress components in an element are able to decrease with increasing strain. A region that has undergone greater stress softens more, leading to a greater amount of strain (Cundall, 1990).

3.3 Development of engineering rock mass models

Computer models are increasingly being used to analyse the response of jointed rock masses (Senseny and Pučik, 1999). This has been attributed to three main reasons (Starfield and Cundall, 1988): the increasing availability of software (ISRM, 1988; Spink, 2002); greater ability of these packages to synthesise geological data; and an acknowledgement of the success of modelling geomechanics problems (Pastor and Tamagnini, 2003; Pavlović, 1996, 1998). However, the difficulty in predicting and simulating the behaviour of rock masses is derived from their discontinuous and highly variable nature. The engineering geomorphologist must make a decision based on the scale of the problem being modelled when choosing between a discontinuous and continuous modelling approach (Brown, 1987).

Purrer (1997) has demonstrated that some state of the art computer models are not capable of replicating appropriate failure mechanisms, as the numerical methods are fed with variations of rock parameters. The first step should be to analyse the rock mass qualitatively. The most suitable numerical approach is not a complete representation of reality, but may provide an insight into the general performance of the rock mass, and suggest areas where it may be useful to collect more information (Lemos, 1990). The ISRM (1998) and Spink (2003) have described various computer programs for modelling rock mechanics problems. Since rock mechanics modelling has developed for the design of rock engineering structures in different circumstances and different purposes, and because different modelling approaches have developed, a wide spectrum of numerical methods are available (Jing and Hudson, 2002). The three most common numerical methods used in rock mechanics are finite element, boundary element and discrete element methods (Pande *et al.*, 1990). The boundary element methods are mainly concerned with sub-surface rock mass problems, so are not relevant to this discussion.

In any rock mechanics approach, it is often desirable to use a range of techniques, a view crystallised by Chen (2000), who argues that due to the cost of insurance and the need to apportion blame, all available methods should be used so that engineers are not liable for injury or damage. In addition, slope engineers often employ a hazard appraisal or risk assessment during the design stage to address the projected consequences of slope failure or the probability of failure. Both of these require an understanding of the failure mechanisms so that spatial and temporal probabilities can be addressed. It is at this stage that the geomorphologists' input

can provide unique insights into slope development, undertaking temporal and spatial analyses, which extend beyond the physical engineering structures in both time and space.

The earliest rock mass simulations were physically-based models, which were scale representations and simplifications of real-world problems. Two main approaches have been employed for the physical representation of jointed rock masses. Base friction models use a set of physical blocks with gravity being simulated by the movement of a belt along the underside of the model (Bray and Goodman, 1981). Tilt tables have been used to simulate the toppling of blocks (Pritchard and Savigny, 1990) and to determine the friction angles of various rock types (Bruce *et al.*, 1989). However, physically-based models lack the ease, flexibility, and quantitative basis of other rock mechanics models and do not replicate *in situ* stresses (Pritchard and Savigny, 1990).

Conventional methods of rock-slope analysis can be generally divided into kinematic and limit equilibrium techniques (Table 3.11). A first step in any rock mechanics modelling approach is a detailed appraisal of the lithology and structure of the rock mass. From this, it is necessary to determine the discontinuity geometry and assess whether these joint sets are conducive to block detachment from the free-face. This assessment can be undertaken using stereographic projection techniques and kinematic analysis. For example, the computer software DIPS (Rocscience, 2002) allows the visualisation and determination of the kinematic feasibility of rock-slopes by employing friction cones, daylight and toppling envelopes, in addition to graphical and statistical treatment of the discontinuity properties. The user must recognise that such software can be used to provide information on the potential for sliding failure involving single discontinuities or discontinuity intersections. They are not suitable for failure mechanisms which involve multiple joints or joint sets or deformation / fracture of intact block materials. However, such discontinuity data can be imported into limit equilibrium codes to provide an assessment of the factor of safety against sliding failure. These programs often incorporate probabilistic tools, in which joint set properties and support measures can be assessed for their influence on the Factor of Safety.

Analysis Method	Critical Parameters	Advantages	Limitations
Physical Modelling	Representative material characteristics; appropriate scaling factors.	Mechanisms clearly portrayed and results of analysis are a useful constraint for numerical modelling; centrifuge models able to investigate the effect of time on failure mechanisms.	Simplistic groundwater simulation especially in rock; techniques do not allow for the effects of scale and *in situ* stress; centrifuges are expensive.
Stereographic and Kinematic	Critical slope and discontinuity geometry; representative shear strength characteristics.	Relatively simple to use; gives initial indication of failure potential; may allow identification and analysis of critical key blocks using block theory; links are possible with limit equilibrium methods; can be combined with statistical techniques to indicate probability of failure.	Only really suitable for preliminary design or design of non-critical slopes; critical discontinuities must be ascertained; must be used with representative discontinuity/joint shear strength data; primarily evaluates critical orientations; neglecting other important joint properties.
Limit Equilibrium	Representative geometry and material characteristics; soil or rock mass strength properties (cohesion and friction); discontinuity shear strength characteristics; groundwater conditions; support and reinforcement characteristics.	Wide variety of commercially available software for different failure modes (plane, wedge, toppling etc.); can analyse Factor of Safety sensitivity to changes in slope geometry and material properties; more advanced codes allow for multiple materials, 3-D, reinforcement and/or groundwater profiles.	Mostly deterministic producing a single Factor of Safety (but increased use of probabilistic analysis); Factor of Safety gives no indication of failure mechanisms; numerous techniques are available all with varying assumptions; strains and intact failure not considered; probabilistic analysis requires well defined input data to allow meaningful evaluation.
Rockfall Simulators	Slope geometry, rock block sizes and shapes; coefficient of restitution.	Practical tool for siting structures; can use probabilistic analysis; 2-D and 3-D codes are available.	Limited experience in use relative to empirical design charts.

Table 3.1: Conventional methods of slope stability analysis (adapted from Coggan *et al.*, 1998).

All limit equilibrium techniques are attempts to solve one problem, using a comparison of resisting forces or moments mobilised and the disturbing forces or moments, to calculate a Factor of Safety (FoS). Methods vary, however, in the numerical solution scheme adopted to achieve problem solution. Graphical

analyses using stereographic projections can also be carried out using block theory analysis to assess the stability of critical keyblocks, without reference to the forces which may initiate movement. Once the potential mode of failure is known, it is possible to evaluate the probability of failure, although only minimal reference is made to the material properties. The limit equilibrium method can be applied by approximating the slope as a series of columns (Cruden and Eaton, 1987; Goodman and Bray, 1976). The failure mode for each block is determined by solving two statics problems: one assumes block sliding and the other block rotation, with the higher resultant force determining the failure mechanism (Pritchard and Savigny, 1990). The approach is limited in that it does not allow for the assessment of blocks failing by a combination of sliding and toppling. The resultant force is then applied to the next block and continues to the toe of the slope. Due to the calculation procedure, the method is mainly suitable for slopes with very simple block geometries and very few interacting blocks.

Despite these limitations, considerable advances have been achieved in commercially available limit equilibrium codes in recent years. These include:

1. integration of 2-D limit equilibrium codes with finite element groundwater flow and stress analysis;
2. development of 3-D limit equilibrium codes;
3. development of probabilistic limit equilibrium techniques;
4. ability to allow for varied support and reinforcement;
5. improved visualisation and graphical representation.

Limit equilibrium models have been used extensively in geomorphology to study slope stability problems. Although of restricted value individually, when combined with the results of field surveys, they form an important component of decision-making (Nash, 1987). Carter and Lajtai (1992) compared two limit equilibrium methods for analysing the stability of rock masses. The deterministic approach evaluates the stability of a rock wedge through three-dimensional vector algebra, whereas the probabilistic approach evaluates the probability of failure for the whole rock-slope by computing the distribution of the factors of safety from all potential wedges. It has been suggested that the limit equilibrium method is restricted to the analysis of small-scale toppling, where the process is limited by a planar failure surface and facilitated by joint shear and separation (Pritchard and Savigny, 1990).

The kinematic basis of block theory can be applied to find critical blocks created by discontinuity intersections, which allow blocks to slide free (Shi and Goodman, 1981; Goodman and Shi, 1982; 1985). The critical blocks can liberate, by moving or detaching from the rock face, blocks which were previously restrained. The method was mainly developed to be used during the feasibility and design stage of excavation projects, with the purpose of determining either a stable orientation for the excavation, or the required stabilising forces. Many types of rock mass are not amenable to analysis by block theory or similar methods because the methods assume that instability is caused by identifiable 'key blocks' (Goodman, 1989; 1995). The method is intended to provide a stability assessment, rather than monitor change through time. It is now possible for computer software to determine key blocks automatically from joint maps of engineering sites.

Basic kinematic analyses of rock-slopes are often no more than computational versions of conventional stereographic projection techniques but they can efficiently analyse joint sets to identify blocks failing by plane sliding, wedge sliding and toppling (Leung and Kheok, 1987). The benefit of such analyses is that there is very little computational effort required. However, the technique is limited in simulating rock-slope change through time and the interaction of a large number of blocks. Previous geomorphological applications of the limit equilibrium method include the assessment of coastal cliff failure mechanisms along the Pembrokeshire Coast, Wales (Davies *et al.*, 1998).

Many rock-slope problems involve complexities relating to geometry, material anisotropy, non-linear behaviour, *in situ* stresses and the presence of several coupled processes, for example, pore pressures and seismic loading. Advances in computing power and the availability of relatively inexpensive commercial numerical modelling codes mean that the simulation of potential rock-slope failure mechanisms should form a standard component of rock-slope investigations (Eberhardt *et al.*, 2002; 2004).

Numerical methods of analysis used for solving rock mechanics problems may be divided into three approaches: continuum; discontinuum; and hybrid modelling (Table 3.2).

Analysis Method	Critical Parameters	Advantages	Limitations
Continuum Modelling (e.g. finite element, finite difference).	Representative slope geometry; constitutive criteria; (e.g. elastic, elasto-plastic, creep); groundwater characteristics; shear strength of surfaces; *in situ* stresses.	Allows for material deformation and failure (Factor of Safety concepts incorporated); can model complex behaviour and mechanisms; 3-D capabilities; can model effects of pore water pressures, creep deformation and/or dynamic loading; able to assess effects of parameter variations; computer hardware allow complex models to be solved with reasonable run times.	User must be well trained, experienced and observe good modelling practice; need to be aware of model and software limitations (e.g. boundary effects, meshing errors, hardware memory and time restrictions); availability of input data generally poor; required input parameters not routinely measured; inability to model effects of highly jointed rock; can be difficult to perform sensitivity analysis due to run time constraints.
Discontinuum Modelling (e.g. distinct element, discrete - element).	Representative slope and discontinuity geometry; intact constitutive criteria; discontinuity stiffness and shear strength; groundwater characteristics; *in situ* stress state.	Allows for block deformation and movement of blocks relative to each other; can model complex behaviour and mechanisms (combined material and discontinuity behaviour coupled with hydro-mechanical and dynamic analysis); able to assess effects of parameter variations on instability.	As above, user required to observe good modelling practice; general limitations similar to those listed above; need to be aware of scale effects; need to simulate representative discontinuity geometry (spacing, persistence, etc.); limited data on joint properties available (e.g. joint normal stiffness, joint shear stiffness).
Hybrid/Coupled modelling	Combination of input parameters listed above for stand-alone models.	Coupled finite-/distinct-element models able to simulate intact fracture propagation and fragmentation of jointed and bedded rock.	Complex problems require high memory capacity; comparatively little practical experience in use; requires ongoing calibration and constraints.

Table 3.2: Numerical methods of rock-slope analysis (adapted from Coggan *et al.*, 1998).

Differential continuum methods, such as the finite difference and element methods, require that approximations be made throughout the problem domain, whereas discontinuum methods require approximations to be made only at boundaries. The continuum, implicit approach uses a single effective medium which is designed to deform as an assemblage of blocks, whereas the discrete, explicit approach models motions between blocks and across joints independently (Senseny and Simons, 1994).

3.3.1 Continuum finite element approaches

The continuum approach includes finite element models where the problem domain is divided into discrete elements, which provide a physical approximation to the continuity of displacements and stresses and then the governing equations are solved for nodes (Brown, 1987). The method is most suited to the analysis of slopes that are composed of massive intact rock, weak rocks, or heavily fractured rock masses, which can be represented as continuous media. Most continuum numerical codes incorporate the ability to include discrete fractures such as faults and bedding planes, but are inappropriate for the simulation of blocky media. Finite modelling methods require that physical or mathematical approximations be made throughout a bounded region.

Many limitations of the limit equilibrium method are overcome by constitutive relations of the intact rock and joints being modelled more realistically (Pritchard and Savigny, 1990). Although rock-slope stability problems rarely meet the conditions relevant to that of a continuum, finite element numerical methods have the advantage of being able to efficiently model progressive and time-dependent failure mechanisms. Finite difference methods are also available, but are more widely used in solving dynamics problems and approximate numerical solutions are obtained to the governing equations at an array of points within the problem domain (Brown, 1987). However, such methods are restricted in a number of ways when attempting to simulate a discontinuous medium. First, the logic may break down when many intersecting discontinuities are used. Second, there may not be a numerical scheme for automatically detecting new contacts. Third, the formulations are limited to small displacements or rotations. For these reasons, continuum codes are restricted in their applicability for analysis of jointed rock-slope stability problems.

Geomorphological applications of the finite element method include modelling the state of stress in natural rock columns in the Chiricahua Mountains, Arizona (Hall, 1996). The state of stress in the columns suggested that failure along discontinuities, rather than tensile or compressional failure of the intact rock, was the main mode of failure. The finite element method has been used to model the toppling of rock-slopes due to the tensile breakage rock columns (Adhikary *et al.*, 1996).

3.3.2 Discontinuous discrete element approaches

Discontinuum methods treat the rock-slope as a discontinuous mass by considering it as an assemblage of rigid or deformable blocks. A discontinuous medium is distinguished from a continuous one by the existence of contacts or interfaces between the discrete bodies that compose the system of blocks. The analysis includes sliding along and opening and closure of rock discontinuities as controlled by the joint properties (normal and shear stiffness, cohesion, friction, surface roughness).

Discontinuum methods can be categorised by the way they represent contacts and by the way they represent the discrete bodies in the numerical formulation. Discontinuities can be accounted for by two numerical approaches. In the first, a soft-contact approach is used, where a finite normal stiffness is taken to represent the measurable stiffness that exists on a joint surface. In the second group, a hard contact approach is taken, where interpenetration of blocks is regarded as physically impossible and is automatically prevented by the code. It is suggested that the choice between the two contact assumptions should be made on the basis of physics, rather than on computational elegance (Itasca, 2000). These models must also account for the behaviour of the solid material that composes the blocks in the discontinuous system. This is achieved using either rigid or deformable blocks, the choice being dependent on the problem characteristics. Rigid blocks are most suitable in systems where most of the deformation occurs due to movement along the discontinuities.

Discontinuum modelling constitutes the most commonly applied numerical approach to rock-slope analysis, the most popular method being the distinct element method. These codes use a force displacement law specifying interaction between the deformable joint bounded blocks and Newton's second law of motion, providing displacements induced within the rock-slope. Discontinuum codes are particularly well suited to problems involving jointed media and have been used extensively in the investigation of rock-slope failure.

Although both continuum and discontinuum analyses provide useful means to analyse rock-slope problems, complex failure may involve mechanisms related to both existing discontinuities and the brittle fracturing of intact rock. Coupled finite-

/distinct-element codes are now available, which allow for the modelling of both intact rock behaviour and the development of fractures through adaptive remeshing techniques. These methods use a finite element mesh to represent either the rock-slope or the joint-bounded block coupled together with discrete elements able to model deformation involving discontinuities. If the stresses within the rock-slope exceed specified failure criteria within a finite element model, a crack is initiated. Adaptive remeshing allows propagation of the cracks through the simulated finite element mesh (Koenke *et al.*, 1998). Applications of the technique include the simulation of the 1991 Randa rockslide in the southern Swiss Alps, where the method was able to provide information on pre-failure deformations of the rock-slope and model the propagation of fracture networks just before failure in response to increased stress concentrations (Eberhardt *et al.*, 2004). Similar numerical methods are being developed based on representing the rock mass as an assemblage of discrete disks bonded together. Simulation of the failure of intact material is represented by separation of the discrete disks once stress concentrations have exceeded the prescribed strength of the bonds between the particles. However, codes based on these principles, such as PFC^{2D} and PFC^{3D} (Itasca, 2003), are still in their developmental stages, and have not been verified in rock mechanics investigations.

3.4 Numerical formulation of UDEC

The code used most extensively in this study is the discontinuous, two-dimensional distinct element code, UDEC. The numerical code is based on the distinct element method for discontinuum modelling, originally developed by Cundall (1971). The modern UDEC code is proprietary software published by HCItasca. The version of the code used in this research is the latest release, UDEC v. 3.10.

UDEC simulates the response of a jointed rock mass under loading. The motion of blocks along the discontinuities is governed by linear or non-linear force displacement relations for movement in the normal and shear directions solved by a Lagrangian calculation scheme. The program uses an explicit time marching scheme to solve the equations of motion directly. Intact rock blocks can be represented by one of several built-in material models, and can be made deformable by sub-dividing the intact blocks into a mesh of triangular finite difference elements. The code assumes a two-dimensional plane strain rate. This condition is associated

with structures with constant cross-section acted on by loads in the plane of the cross-section. Discontinuities are treated as planar features orientated normal to the plane of analysis.

In the distinct element method, a rock mass is considered as an assemblage of discrete blocks and joints are represented as interfaces between two distinct bodies (Hart, 1993). UDEC uses dynamic relaxation techniques to solve Newton's laws of motion to determine the forces between, and displacements of, blocks during the progressive, large-scale deformation of jointed rock masses (Brown, 1987). The forces and displacements at the joints in a stressed rock are related to the movements of blocks. These movements result from the propagation of strains through the rock mass in response to applied stresses. The speed of strain propagation is dependent upon the physical attributes assigned to the joints and intact material. The method is based on the concept that the timestep is sufficiently small that, during a single step, disturbances cannot propagate between one discrete element and its immediate neighbour (Hart, 1993). The dynamic behaviour is represented numerically by a time-stepping algorithm, in which the size of the timestep is limited by the assumption that velocities and accelerations are constant within the timestep. The timestep is unrelated to explicit time (Iofis, *et al*, 1990). For rigid blocks, the block mass and the joint stiffness between blocks define the timestep limitation (Itasca, 2000).

The task of the solution scheme is to determine a set of displacements that will bring all elements to equilibrium, or indicate the mode of failure (Cundall, 1987). The dynamic relaxation calculations performed in UDEC alternate between the application of a force displacement law at all joint contacts and Newton's second law at all blocks (Senseny and Simons, 1994). The force-displacement law is used to find contact forces from known displacements and Newton's second law gives the resulting motion from the known forces acting on them (Cundall, 1971). Each timestep produces new block positions which generate new contact forces. Resultant forces are then used to calculate linear and angular accelerations of each block. Block displacements are then determined by integration over time increments. Dynamic relaxation is physically more realistic than other available techniques, but requires more computational effort (Cundall, 1987).

With a mass being acted upon by a force dependent on time, $F = F(t)$, Newton's second law of motion can be written as

$$\frac{dv}{dt} = \frac{F}{m},$$ **Equation 3.1**

where v = velocity,

t = time,

m = mass.

The distinct element method uses a central difference scheme, where all calculations are ordered. The form of the following equations follows the tensor format. Tensors provide a natural and concise mathematical framework for formulating and solving problems in areas of physics such as elasticity and mechanics. Superscripts relate to the contravariant tensor and the subscript the covariant tensor. This mathematically distinguishes tensors which have different transformation properties. In the following equations, the contravariant tensor is related to time t and the covariant tensor is related to the block indices i, which is related to the Cartesian Coordinate frame. The superscript in no way indicates a power function in tensor format.

The force / displacement calculation is computed during a time instant, with velocities stored at the half-timestep point. Displacement, u, at the half timestep point is represented by

$$u^{(t+\Delta t)} = u^{(t)} + v^{(t+\Delta t/2)}\Delta t.$$ **Equation 3.2**

The central difference scheme is second-order accurate, that is the first order error vanishes from the solution, preventing long-term drift in a distinct element simulation. This is important when considering long-term geomorphological simulations, which require substantial run times.

For blocks in two dimensions which are acted upon by several forces, including gravity, the velocity is calculated by

$$u_i^{(t+\Delta t/2)} = u_{i\,m}^{(t-\Delta t/2)} + \left(\frac{\sum F_{i_m}^{(t)}}{m} + g_i \right) \Delta t,$$

Equation 3.3

and

$$\theta^{(t+\Delta t/2)} = \theta^{(t-\Delta/2)} + \left(\frac{\sum M^{(t)}}{i}\right)\Delta t,$$

Equation 3.4

where θ = angular velocity of a block around a centroid,

i_m = moment of inertia of block,

M = moment acting upon the block,

U_i = velocity components of the block centroid and

g_i = components of gravitational acceleration (body forces).

The indices i denote components in a Cartesian coordinate frame.

The new velocities, calculated in Equation 3.3 and Equation 3.4, are used to determine the new block location according to

$$x_i^{(t+\Delta t)} = x_i^{(t)} + u_i^{(t+\Delta t/2)}\Delta t$$

$$\delta^{(t+\Delta t)} = \delta^{(t)} + \delta^{(t+\Delta t/2)}\Delta t,$$

Equation 3.5

where δ = rotation of block about centroid, and

x_i = coordinates of block centroid.

UDEC has several built-in models of joint behaviour, ranging from the basic Coulomb slip model, to the more comprehensive continuously yielding, displacement weakening model used throughout this research. The continuously yielding joint model proposed by Cundall and Hart (1984) is intended to simulate, in a simplified fashion, the internal mechanism of progressive damage of joints under shear. As shear progresses, the shear strength of the joint is reduced to simulate progressive weakening caused by the damage of asperities and a reduction in joint surface roughness. The model includes a hysteretic damping function for dynamic solutions, by using a 'bounding surface' concept similar to that proposed by Dafalias and Herrmann (1982) for soils. Previous applications of the model include rock fault instability induced by seismic events (Cundall and Lemos, 1990). The continuously yielding model (CYM) is considered more realistic than the standard Mohr-Coulomb

joint model in that the CYM attempts to account for some non-linear behaviour caused by joint shearing damage, normal stiffness dependence on normal stress and increase in dilation angle caused with plastic shear displacement. The essential features of the model are:

1. The curve of the shear stress/shear displacement is always tending towards a 'target' shear strength for the joint, i.e. the instantaneous gradient of the curve depends directly on the difference between strength and stress.

2. The target shear strength decreases continuously as a function of accumulated plastic displacement (taken as a measure of damage).

3. The dilation angle is taken as the difference between the apparent friction angle (determined by the current shear stress and normal stress) and the residual friction angle.

As a consequence of these assumptions, the model automatically exhibits the commonly observed peak / residual behavior of rock joints. In addition, hysteresis is displayed for unloading and reloading cycles at all strain levels, no matter how small (Itasca, 2000). This is particularly important where rock joints are subjected to progressive loading or unloading cycles, as in the present numerical simulations. For the purpose of the present investigations, the CYM represents the most realistic joint model. The model is described as follows. The response to normal loading $\Delta\sigma_n$ is expressed incrementally as

$$\Delta\sigma_n = k_n \Delta u_n, \qquad \textbf{Equation 3.6}$$

where Δu_n = current normal displacement and

k_n = normal stiffness.

The normal stiffness k_n is given by

$$k_n = a_n \sigma_n^{e_n}, \qquad \textbf{Equation 3.7}$$

where a_s = joint shear stiffness,

σ_n = joint normal stiffness,

e_s = joint shear stiffness exponent,

representing the increase in stiffness with normal load and where a_n and e_n are model parameters.

For shear loading, the model displays irreversible, non-linear behaviour from the onset of shearing. The change in shear stress $\Delta\tau$ is calculated by

$$\Delta\tau = Fk_s \Delta u_s, \qquad \textbf{Equation 3.8}$$

where Δu_s is the current shear displacement increment and

Fk_s is a factor dependent on the stress-strain curve.

The shear stiffness k_s can be taken as a function of normal stress:

$$k_s = a_s \sigma_n^{e_s}, \qquad \textbf{Equation 3.9}$$

Damage to the joint surface under progressive shear is modelled by the determination of joint bounding strengths in each timestep:

$$\tau_m = \sigma_n \tan\phi_m \, \mathrm{sgn}(\Delta u_s) \qquad \textbf{Equation 3.10}$$

The parameter, ϕ_m, can be understood in terms of the friction angle that would apply if the joint were to dilate at the maximum dilation angle. As damage accumulates, this angle is continuously reduced according to

$$\Delta\phi_m = 1/R(\phi_m - \phi)\Delta u_s^p \qquad \textbf{Equation 3.11}$$

where ϕ = basic friction angle of rock,

ϕ_m = effective friction angle,

R = joint roughness,

U^p_s = plastic displacement.

The parameter R has the dimensions of length and controls the rate at which ϕ_m decreases with plastic displacement.

Joints, irrespective of constitutive model, are represented numerically as contact surfaces between block edges within UDEC (Cundall and Hart, 1992; 1993). With rigid blocks, contacts are created at block corners, while with deformable blocks, contacts are created at all gridpoints located along the block edge (Lemos, 1994). An unrealistic response can occur when block interaction occurs close to or at two opposing block corners as a result of the modelling assumption that block corners are sharp or possess infinite strength. In reality, crushing of the corners would occur as a result of a stress concentration. However, a realistic representation can be achieved by rounding the block corners so that they slide smoothly past each other. To reduce numerical inaccuracies imposed by the rounding process, the rounding length should be no more than 1 % of the representative block edge length in the model (Itasca, 2000). Contact points are updated automatically in UDEC as block motion occurs. Computational efficiency is maintained by using domains, which allow large numbers of blocks to be modelled. Problems therefore occur when blocks become detached from the rock mass as the domain structure is ill-defined. It is suggested that blocks which become disconnected from the main rock mass during the modelling process should be deleted (Itasca, 2000). This process can be time-consuming for failures involving large numbers of blocks. UDEC v.3.1 contains a built-in programming language, FISH, to enable the user to extend the capabilities of the original UDEC code by writing sub-routines.

Blocks may be defined as rigid or deformable in UDEC. The formulation represents rigid blocks as a set of distinct blocks, which do not deform in response to loading. Rigid blocks are most suitable for simulations where the behaviour of the rock mass is dominated by discontinuities and for which material elastic properties may be ignored. Such conditions are present in low stress environments, or where the material possesses high strength and low deformation characteristics (Senseny and Simons, 1994). The UDEC code contains seven built-in models for assigning behaviour models to the intact blocks, which can be arranged into null, elastic and plastic models. For this thesis, the Mohr-Coulomb failure criterion was used to represent the behaviour of the intact material. Blocks defined as fully deformable are discretised into a series of triangular elements. The iterative cycles are modified slightly in that the displacements of grid points within the block are linked to the

displacements of grid points forming the block boundaries (Pritchard and Savigny, 1990). The complexity of deformation of the blocks depends on the number of elements into which the blocks are divided. Plane-strain conditions are assumed and the equations of motion for each gridpoint are

$$\ddot{U}_i = \sum \frac{\sigma_i n_j ds + F_i}{m} + g_i, \qquad \textbf{Equation 3.12}$$

where s = the surface enclosing the mass, m, lumped at the gridpoint,

n_j = the unit normal to s,

F_i = resultant of all external forces applied to the gridpoint and

g_i = gravitational acceleration.

During each timestep, strains and rotations are related to nodal displacements in the same fashion as for the rigid blocks. The constitutive relations for deformable blocks are used in incremental form so that implementation of non-linear problems can be easily accomplished:

$$\Delta\sigma_{ij}^{e} = \lambda\Delta\varepsilon_v\delta_{ij} + 2\,\mu\,\Delta\varepsilon_{ij}, \qquad \textbf{Equation 3.13}$$

where λ, μ = the Lamé constants,

$\Delta\sigma^{e}_{ij}$ = elastic increments of the stress tensor,

$\Delta\varepsilon_{ij}$ = incremental strains,

Δ_v = increment of volumetric strain and

δ_{ij} = Kronecker delta function, δ_{ij} = 1 if $i = j$ and 0 otherwise.

Damping is used in the distinct element method to solve mechanical problems (Cundall, 1971). An elastic system would infinitely oscillate, so damping must be used for a steady state system to be approached (Cundall, 1987). The equations of motion are automatically damped to reach an equilibrium state under the applied stresses. The magnitude of the damping factor is proportional to the velocity of the blocks. The viscosity of the damping is a constant proportional to the rate of change of kinetic energy in the system, with the adjustment to the viscosity being made by keeping the ratio, R, equal to a given constant (Cundall and Strack, 1979):

$$R = \frac{\sum P}{\sum E_k},$$

Equation 3.14

where P = the damping power for a node and

E_k = the rate of change of nodal kinetic energy.

The velocity-proportional form of damping has the advantage that damping-induced body forces, which may erroneously influence the mode of failure, are reduced because the damping tends to zero as the system approaches a steady state. The solution scheme for the distinct element method is only stable at the end of a timestep. A limiting timestep is determined that satisfies both the stability criterion for the calculation of internal block deformation and that for inter-block relative displacement. The timestep required for the stability of block deformation computations is

$$\Delta t_n = 2\min\left(\frac{m_i}{k_i}\right)^{1/2},$$

Equation 3.15

where m_i = mass associated with the block node, i, and

k_i = a measure of stiffness of the elements surrounding the node, affected by the elastic properties of the material.

For the calculation of inter-block relative displacements, the limiting timestep is calculated as

$$\Delta_{tb} = (\text{frac})\ 2\left(\frac{M_{min}}{K_{max}}\right)^{1/2},$$

Equation 3.16

where M_{min} = mass of the smallest block in the system, and

K_{max} = maximum contact stiffness.

The term 'frac' accounts for the fact that a single block is in contact with several blocks. The controlling timestep therefore becomes

$$\Delta t = \min(\Delta t_n \times \Delta t_b), \qquad \text{Equation 3.17}$$

3.5 Operation of UDEC

UDEC is operated by a series of ordered and structured commands (Table 3.3).

Example Commands	Data file component
new	Clear the UDEC 'memory'.
block...	Create the UDEC 'proto-block'.
crack...	Create individual joints by dividing the proto-block into smaller sub-blocks.
jreg...	Specify a joint region and create joint
jset...	sets within the relevant region.
generate...	Create internal finite difference zones within rock blocks.
prop mat...	Assign material properties to the rock
prop jmat...	blocks and discontinuities.
boundary...	Assign boundary conditions to the edges of the model.
insitu...	Assign internal initial conditions (e.g.
grav...	virgin stresses) to zones and contacts within the model.
hist...	Select points in the model to monitor (e.g. deformation of a free-face)
damp...	Apply mechanical damping.
cycle...	Run the model.
step...	

Table 3.3: Basic structure for a UDEC input file.

The input command sequence commences with the creation of the rock mass morphology and joint geometry. The second stage assigns material properties and behaviour to the intact rock blocks and joints. The third stage invokes boundary and initial conditions by specifying stresses. The model is consolidated to mathematical

equilibrium under a fixed mesh, and finally desired model boundaries are released to allow rock mass failure to occur.

The creation of the problem geometry begins with the creation of a single block, which spans the physical region being modelled. This single block is then subdivided into discrete blocks, which can be deleted to create the model mesh form. The corners of the blocks are rounded to prevent large stress concentrations building up at block corners. To prevent this, a rounding length of 0.1 – 1 % of intact block length should be used (Itasca, 2000). An automatic joint set generator is then invoked to define the two-dimensional joint geometry across the model. A joint mesh is created across the whole model according to mean joint set statistics. Joint parameters required are dip angle from the horizontal, joint trace length, gap length between discontinuous joint segments and joint spacing normal to the joint planes. For each parameter, a maximum deviation from the mean can be assigned. If a parameter is not defined, a default value of zero is assumed.

Individual blocks and defined regions may be deleted to simulate the morphology of the problem being modelled. It is usual for a region on the left-hand side of the model to be deleted for analysing rock-slope problems, although this is by no means fixed. It is recommended that very small blocks, with a size less than 0.01% of the whole mass, be deleted to improve calculational efficiency (Itasca, 2000). For N blocks, or deformable gridpoints, the computation time is proportional to $N^{3/2}$. Very small blocks play little role in controlling the failure mechanism of a rock-slope and, in the field, such small blocks would be crushed due to the build-up of stress concentrations. In addition, it is numerically possible for such small, rounded blocks to overlap, so it is usual to delete them.

An issue encountered when using UDEC for rock-slope problems is the mapping of a three-dimensional joint set of planes to a two-dimensional mesh (Jing and Stephansson, 1994). The dip of a joint set represented by a concentration of poles on a stereographic projection is a value which is fixed by the dip direction in three dimensions. Unless the strike of the UDEC model profile is perpendicular to the strike of the joint set, then the dip value on the UDEC mesh is different (Kimber, 1998). For example, a real joint set may be dipping 45° to the south. If it is desired to model a cliff with a north-south profile, then the dip of the joint set on the mesh would be at 45° above the horizontal (Kimber, 1998). However, if the modelled cliff had an east-west profile, then the represented dip on the UDEC mesh would be

horizontal. A simple computer program (Kimber, 1998) can be used to transform joint sets defined by the stereographic strike and dip to a defined UDEC mesh (Appendix 3.1).

Once the UDEC mesh has been designed, material models can be assigned to the blocks and discontinuities. Different areas of the UDEC mesh can be assigned different material models. For most rock-slope problems, the default elastic model is appropriate. The required properties for this are density, bulk modulus, and shear modulus. Material models must also be assigned to all the discontinuities within the problem domain. The properties required for joint models are joint normal stiffness, joint shear stiffness, joint normal stiffness exponent, joint shear stiffness exponent, joint intrinsic friction angle and a joint roughness parameter. It is usual to leave the shear and normal stiffness exponents as zero for most rock-slope problems. If the specified stiffness values are too small, block inter-penetration can occur. However, if a very high stiffness is specified, the solution convergence will be very slow. The joint normal stiffness k_n and the joint shear stiffness k_s should be set to at most ten times the equivalent stiffness of the most rigid neighbouring zone, namely

$$k_n \text{and } k_s \leq 10.0 \max\left(\frac{K + 4/3G}{\Delta Z_{min}}\right), \qquad \textbf{Equation 3.18}$$

where ΔZ_{min} = the smallest width of an adjoining zone in the normal direction.

Once initial block cutting and material models have been assigned, boundary and initial conditions must be specified. For rock-slope problems it is usual to apply zero velocity boundary conditions to the sides and lower part of the model. It is important to ensure that the boundary conditions assigned are far enough away from the region of interest that they do not adversely affect the simulation of failure. Once the model has consolidated and reached equilibrium, it is possible to release one or more sides of the model, depending upon geometrical complexity, and allow failures to develop. Initial stresses must be specified for all blocks in the model as there is an *in situ* state of stress acting in any real world rock-slope. For a rock mass, the vertical stress component σ_v is calculated as

$$\sigma_v = g\gamma Z, \qquad \textbf{Equation 3.19}$$

where g = gravitational acceleration,

γ = unit weight of rock, and

Z = depth below the surface.

UDEC automatically calculates a stress gradient through the model, depending upon the relative position of a block within the model and relating a gravitational acceleration to the density of the block (Hart, 2003). It is important to note that when gravitational acceleration is defined in the model, stresses do not appear directly in the model; it simply causes body forces to act on all gridpoints of deformable blocks or centroids of rigid blocks (Itasca, 2000). Body forces correspond to the weight of the material surrounding each block. Given fixed boundary conditions, the model can generate its own gravitational stress component, but this is computationally inefficient, as many hundreds or thousands of timesteps may be required to reach equilibrium. It is more efficient to initialise stresses so that they satisfy both the equilibrium and gravitational gradients. The gravitational gradient can be defined by the gravitational acceleration g multiplied by mass density of material γ. The *in situ* horizontal stress is more difficult to estimate and can be considered in terms of gravity being applied to an elastic mass which cannot undergo lateral deformation. However, this condition often does not apply to the history of the landform, which may have undergone erosion or burial and been subjected to tectonic stresses (Fairhurst, 2003). It is often assumed that the initial horizontal stress is half the vertical stress component (Herget, 1988; Itasca, 2000). It is important to recognise that stress calculations are based on the assumption that the problem domain is represented by an unjointed material. However, it is difficult to assign stress gradients to jointed media because spatial heterogeneity occurs due to stress paths following the fractures.

Before fixed boundaries can be released to allow failures to develop, the UDEC model must be in a force-equilibrium state. To reach this the model is run for a user-defined number of iterations with all boundaries fixed, or a command line invoked, which cycles the model until out of balance forces are close to zero. The model has reached equilibrium when the net nodal vector force in each block centroid or finite difference triangle is zero. The maximum nodal vector force, called the unbalanced force, can be monitored to allow the user to determine when equilibrium has been achieved. The advantage of this approach is that UDEC can allow for landform history to some extent, by allowing the model to reach an initial equilibrium before movement is permitted, allowing the stresses acting between rock blocks to decrease and balance. The net effect of past events is to produce a

landform that is not in present equilibrium. By reaching an initial equilibrium, the out-of-balance force in the model is zero at the start, so that failures develop due to inherent instability, rather than by unnatural forces imposed by the initial boundary conditions.

When entering data into UDEC, it is important that consistent magnitudes and units are used. In all cases, SI units were used. Data are converted in metres for length, kg m^{-3} for density, Newtons for force, Pascals for stress, m s^{-2} for acceleration and Pa m^{-1} for stiffness. Commands can be entered directly into the UDEC dialogue screen or called in from assembled text files. Log files can be recorded for any UDEC session and subsequently edited into input files. Save files can be used to record the status of the model at any point, and can be later restored so detailed analysis can be made. Block plots can be produced to provide a visual representation of the model at any point where a save file has been created. For this thesis, save files were created every 10,000 iterations, so that model development could be closely monitored. History files can be produced which quantitatively record the response of specified variables at user-defined times throughout the model simulation.

3.6 Verification and previous applications

Code verification is a necessary part of the development of a rock mass modelling approach (Brown, 1987). To date, there have been relatively few comparisons of numerical results from UDEC (Lemos, 1990). Often, the only method of code verification is through comparison with physical tests. Field tests are not suitable in assessing material properties and boundary and loading conditions cannot be accurately controlled. Lemos (1990) compared the numerical and physical results of the deformation and failure of a block system and found that good agreement could be achieved, provided low stiffness values were specified to account for the lack of fit in the physical models.

Brady *et al.* (1990) confirmed that UDEC can represent discontinuous deformation of jointed rock and the continuous deformation of individual blocks. In a simple problem involving the loading of a block bisected by an inclined joint, the UDEC analysis provided stiffness results which were almost identical to the closed system solution. The code has been verified through comparison with base friction models

involving the toppling of blocks (Pritchard and Savigny, 1990). The limit equilibrium analysis performed by Goodman and Bray (1976) was repeated to demonstrate that UDEC can accurately reproduce the known solution for limiting stability. Agreement between UDEC predictions and laboratory measurements for joint shear displacement for the loading of a 2 m cube of Precambrian gneiss has also been achieved (Chryssanthakis *et al.*, 1991).

Modelling rock-slope failure using UDEC has improved understanding of rock-slope processes. Hsu and Nelson (1995) modelled weak rock masses with a single discontinuity set and related slope stability to slope height, angle, discontinuity dip and spacing. Theoretical models have also suggested that toppling failure can be influenced by the discontinuity density and friction angle (Jiang *et al.*, 1995). Joint geometry parameters such as density, ratio of joint to block size and joint orientation have also been shown to influence slope failure and deformation of rock masses (Kulatilake *et al.*, 1994). Recently slopes modelled with variations in rock mass strength, discontinuity orientation, discontinuity persistence and toe oversteepening using UDEC have shown two toppling mechanisms to develop: block toppling and flexural toppling (Nichol *et al.*, 2002). The choice of joint constitutive model on the stability of jointed rock masses has also been shown to be important (Souley and Homand, 1996).

An important application of the UDEC software in simulating real-world slopes involves the understanding of failure mechanism (Kimber, 1998). It has been shown that the failure mechanism for an assemblage of interacting blocks differs from that for single blocks (Kimber, 1998). Models using deformable blocks, despite the low stress environments, have proved to be effective in illustrating the type and mechanism of block displacement of undermined Loire Valley chalk cliffs near Saumur (Homond Eitenne *et al.*, 1990). The toppling of the Heather Hill Landslide, British Columbia, Canada has been simulated using the distinct element method (Pritchard *et al.*, 1990; Pritchard and Savigny, 1991). By allowing for the rotation of blocks, UDEC is able to simulate toppling failures. It has been used to simulate landslide toppling failures in strong granites and large flexural topples in metamorphic rocks showing slow deformations (Nichol *et al.*, 2002). In an investigation of failure mechanisms at the Delabole slate quarry, Cornwall, it was shown that a raised water table caused failure of the slope (Coggan and Pine, 1996). The possibility of toppling failure in horizontally bedded masses has also been identified using the UDEC approach and verified by field observations on the

Isle of Purbeck, Dorset (Allison and Kimber, 1998). UDEC has also been shown to be useful in modelling large-scale deep-seated slope deformations that do not show catastrophic behaviour (Barla and Chiriotti, 1995). The code is also able to simulate large-scale catastrophic failures, such as the Frank Slide at Turtle Mountain, Alberta, Canada, which involved 30 million m^3 of rock (Benko and Stead, 1998). Simulation of the gradual sliding deformation of the Åkerness landside at Stranda, West Norway using UDEC indicated that rises in pore water pressures may trigger catastrophic failure (Chryssanthakis and Grimstad, 1996).

Much application of the UDEC code has been related to problems of underground stability. Although different failure modes occur and the timescales are different from geomorphological research, such work verifies the successful applications of the code. Sensitivity analysis has been performed using UDEC to provide insights into the deformation mechanisms in a large cavern in the Himalayas (Bhasin and Hoeg, 1998). It was found that block size and joint friction angle were the most important controls on cavern failure. UDEC models have also been constructed for the proposed Sellafield radioactive waste repository (Barton *et al.*, 1992), the 62 m span Norwegian Olympic Ice Hockey Cavern at Gkovik (Barton *et al.*, 1994) and the twin Fjellinjen road tunnels under Oslo (Makurat *et al.*, 1990). The UDEC modelling approach was also used to assess the stability of a 30 m span power generation cavern in hydrothermally altered granite at the Pergau hydroelectric project in northern Malaysia (Varley *et al.*, 1999).

3.7 Conclusion

Data on the strength of intact rocks and discontinuities have been combined in the consideration of the stability of engineered slopes. Computer models now account for the majority of stability analyses, and a large number of commercial codes are available, driven forward by the increases in computing power. The UDEC code has been used for the majority of the analysis in this study, because it has been widely verified in the field of rock mechanics and has a strong mathematical and physical basis. The distinct element method is able to account for the presence of discontinuities and the control they exert on rock-slope stability. The time-marching solution scheme adopted by UDEC makes it possible to simulate the progressive collapse of rock-slopes. The main advantage for geomorphological modelling of slope evolution is that there is no limit to the magnitude of block rotation which can

take place. The program allows the study of factors controlling slope stability and failure mechanisms in a rigorous scientific framework. Previous applications of the code have provided useful insights into the possible geomorphological applications.

Given the background information concerning rock mechanics modelling and long-term simulation of geomorphic systems, this thesis uses a well constrained modelling methodology. Importance is attached to a theoretical parametric study designed to ascertain which geotechnical and slope morphology variables exert an important control on the behaviour of steep rock-slopes. UDEC has the modelling methodological advantage that its calculation procedure is based on rigorous physical principles. Empirically based models do not possess such explanatory potential (Kimber, 1998).

Chapter 4: Numerical simulation of scale effects in rock masses

Chapter 4 : Numerical simulation of scale effects in jointed rock masses

4.1 Introduction

This chapter presents the results of numerical simulations on the deformation properties of hypothetical jointed rock masses. The aim is to investigate the influence of scale on rock mass deformation through stress-strain relationships. There has been no geomorphological research into how rock-slopes of different scales behave. Two main scale effects are present in rock masses. First, block size is controlled by the regularity and spacing of discontinuities. Second, outcrop scale can vary by three or more orders of magnitude from 1 m to over 1000 m. Understanding the influence of scale on the behaviour of rock-slopes is important because this has implications for the magnitude and frequency of failures in rock slopes. A greater understanding of the processes and mechanisms involved in controlling the behaviour of slopes at different scales will provide greater understanding of the geomorphological evolution of rock-slopes.

4.2 Background

Theoretical considerations of scale issues in geomorphology have been widely discussed elsewhere, and a comprehensive review of these arguments is beyond the scope of this research (e.g. Phillips, 1988; Schumm, 1991; Blöschl and Sivapalan, 1995). The consideration of scale in geomorphology falls into three broad categories: the scale of variation in the landscape form; the scale of process action; and the scale of investigation. The scale(s) at which rock-slopes are studied is ultimately a balance between the detail of measurement required against the size of the slope outcrop. The scale boundaries used in this research are not exclusive and are by no means fixed. The hierarchy of scales simply provides a useful framework within which the various components of rock-slopes and their interactions can be understood. Processes at one scale can have a profound influence on the behaviour of the landform at another scale.

Scale effects in rock masses consist of two main elements. First, there is the outcrop scale of the rock mass and this relates mainly to the height of the slope face. Second, scale effects are apparent when the block size distribution of the rock

mass is considered. Block size is governed by joint spacing and is generally regarded as the most important feature controlling the behaviour of rock masses (Palmström, 2000). It has often been cited as an important mechanism controlling the evolution of geomorphic features such as bedrock canyons (Ehlen and Wohl, 2002). The spacing of discontinuities determines the geometrical properties of the block assemblage composing the rock mass. Although block size has been accounted for indirectly in engineering and geomorphological rock mass classifications, a quantitative assessment of its effects on the evolution of rock slopes has not been attempted (Bieniawski, 1973; Selby, 1980, Palmström, 1995). Such classifications are based on the concept of rock mass quality: slopes composed of massive unweathered rock blocks are assigned a high quality value and those with dense fracture networks assigned low quality values. This study uses the height of the rock mass and joint spacing (which determines block size) as scale effects.

Although the modelling approach is theoretical, several important links can be made with the natural environment. There is a continuum of slope scales in rock masses ranging from 1 m to 1000 m. Figure 4.1 illustrates how the theoretical scales chosen for numerical modelling are represented in the natural environment. At the 1000 m scale, slopes tend to occur in competent materials and are often formed through glacial truncation in high mountain regions or by tectonic processes. Slope failures at the 1000 m scale tend to be infrequent and of relatively large magnitude. For example, Hermanns and Strecker (1999) have identified 55 major rock-slope failures with volumes greater than 10^6 m^3 in the semiarid Puna Plateau, adjacent to the Eastern Cordillera, and Sierras Pampeanas of Argentina, which occurred between 35,000 and 25,000 years ago. No large failures have occurred since. In addition, understanding the behaviour of slopes between 500 and 1500 m is important because of the implications for large-scale failures in populated areas. Recent attempts in Norway have used UDEC to model the failure of a 700 m slope because of the recognised consequences of failure into a populated fjord region (Bhasin and Kaynia, 2004).

At the 100 m scale, natural slopes exist in a range of environments from alpine to desert and tend to be the product of glacial, fluvial or coastal erosion. Slopes at this scale have been most widely studied because they are often the most common and easily accessible rock-slopes. Much information regarding slope evolution at this scale comes from studies of the Colorado Plateau. Episodic rock-fall events

intersected by stability and talus accumulation are considered the main mechanisms of slope evolution at this scale (Koons, 1955). Volumes of failed material in such slopes can range from 10^3 to 10^5 m^3. At the 10 to 1 m scale, slopes are represented by small bedrock steps, which rarely produce large-scale failures. Individual block-detachment tends to be the dominant process on these slopes and the volumes of failed material tend to be relatively low.

Engineers have tended to focus on slopes in the 100 m range because these are most commonly involved in engineering design. However, awareness is increasing that slopes at different scales exhibit different deformational properties with implications for the occurrence of failure events (e.g. Coulthard *et al.*, 1992; Sjöberg, 1996, 1999). From a geomorphological perspective, understanding the behaviour of slopes at different scales will provide insights into the evolution of landforms.

An important concept for this research is slope deformation. In natural slopes, deformation often precedes catastrophic failure. It is important to understand the concept of deformation because of its role in controlling rock-slope behaviour. Deformation is defined as a change in shape (expansion or contraction) and occurs in response to stress, while deformability is the ease with which a material can be deformed. The opposite to this is stiffness and describes rock mass resistance to deformation. Deformability is recognised as one of the most important parameters governing rock mass behaviour (Deere *et al.*, 1967; Duffaut, 1968; Rocha and Da Silva, 1970; Singh *et al.*, 2002; Asef and Reddish, 2002). It has been suggested that deformation rather than stress be used as a basis for stability assessments of rock masses (Müller, 1974). The deformational response of a rock mass is governed by the properties of joints and the intact rock (Singh, 2000). Important characteristics include the orientation of joints relative to the direction of major principal stress, the *in situ* stresses and block size (Yoshinaka and Yamabe, 1986). Deformation of a jointed rock mass is greatly influenced by the deformability of discontinuities and the deformation moduli of rock masses decrease markedly in comparison with intact rock. The prediction of the magnitude of rock mass deformation and failure mechanism is of paramount importance in arriving at safe engineering design structures (Kulatilake and Ucpirti, 1994).

Rock mass deformation has often been estimated through large-scale block tests (for example, Chappell, 1974; Cramer *et al.*, 1994; Pratt, *et al.*, 1977; Hardin *et al.*, 1981). Other methods include using artificially fractured triaxial samples to simulate

the behaviour of jointed rock (Einstein and Hirschfield, 1973; Ramamurthy and Arora, 1994; Sridevi and Sitharam, 2000), numerical simulations (Kulatilake *et al.*, 1992; Huang *et al.*, 1995;) and comparison with classification systems such as the RMR (Palmström and Singh, 2001).

Despite widespread recognition among engineers of the effects of deformation processes on the behaviour of steep slopes, geomorphologists have failed to appreciate the importance of these processes in controlling landform behaviour. Where slope deformations have been recognised, they have only been inferred from morphological evidence such as grabens, tension cracks and anti-scarp formation (Bovis, 1990; Bovis and Evans, 1996; Holmes and Jarvis, 1985). There has been no reference to the mechanics of deformation or what influence this has for the behaviour and evolution of landforms at various geomorphological scales.

The increased complexity of numerical codes, such as UDEC, provides the opportunity to examine the deformational response of rock masses to applied stresses. For the geomorphologist, the code has the advantage that time-dependent deformation can be monitored in addition to the examination of failure mechanism. The code has been used successfully to predict the deformational response of a large underground powerhouse cavern in the Himalayas (Bhasin and Høeg, 1998) and was able to predict deformations to within 2 mm of those gained from instrumental monitoring (Bhasin *et al.*, 1996).

4.3 Methodology and model boundary conditions

Numerical simulations of rock mass deformation and stress-strain relationships were undertaken using UDEC. Block size and outcrop scale effects were investigated in three lithologies (granite, limestone and sandstone) to determine how intact rock strength affected the deformation moduli of rock masses. These lithologies were chosen because they represent a continuum of rock strength: sandstone is weak; limestone intermediate; and granite very strong. To investigate the effects of block size on the behaviour of the rock mass, two theoretical joint sets were cut dipping at 45 and 135 degrees. Initially, the spacing was systematically varied for a 1 m rock mass using six different spacings: 0.05 m, 0.1 m, 0.2 m, 0.3 m, 0.4 m and 0.5 m. All blocks were assigned deformable properties because stress-strain response depends on both the deformation of the intact rock and discontinuities, particularly

as outcrop scale increases. In all cases, blocks were specified to deform in a linearly-elastic and isotropic way.

The input parameters used to define model boundary conditions are presented in Table 4.1. The parameters chosen represent 'typical' values for limestone, sandstone and granite from various sources in the literature. This is justified because the purpose of the theoretical modelling is to improve understanding of slope process, rather than the detailed modelling of specific sites.

Parameters	Units	1	2	3	4	5	6	7	8	9	10	11	12
Lithology	---	limestone	limestone	limestone	limestone	sandstone	sandstone	sandstone	sandstone	granite	granite	granite	granite
Scale	m	1	10	100	1000	1	10	100	1000	1	10	100	1000
Joint A: angle (α)	degrees	45	45	45	45	45	45	45	45	45	45	45	45
Joint A: spacing (h) *	m	v	v	v	v	v	v	v	v	v	v	v	v
Joint B: angle (α)	degrees	-45	-45	-45	-45	-45	-45	-45	-45	-45	-45	-45	-45
Joint B: spacing (h) *	m	v	v	v	v	v	v	v	v	v	v	v	v
Bulk density	kg m^{-3}	2600	2600	2600	2600	2300	2300	2300	2300	2650	2650	2650	2650
Joint normal stiffness	GPa m^{-1}	7.08	7.08	7.08	7.08	1	1	1	1	1	1	1	1
Joint shear stiffness	GPa m^{-1}	5.88	5.88	5.88	5.88	1	1	1	1	1	1	1	1
Friction angle (ϕ)	degrees	35.2	35.2	35.2	35.2	29	29	29	29	46	46	46	46
Bulk modulus	GPa	1.56	1.56	1.56	1.56	0.9	0.9	0.9	0.9	1.2	1.2	1.2	1.2
Shear modulus	GPa	1.17	1.17	1.17	1.17	0.8	0.8	0.8	0.8	0.9	0.9	0.9	0.9
Cohesion	MPa	28.4	28.4	28.4	28.4	23	23	23	23	56	56	56	56
Tensile strength	MPa	10	10	10	10	6	6	6	6	9	9	9	9
Sigma 1 (σ_1)**	MPa	0.025	0.25	2.5	250	0.025	0.25	2.5	250	0.025	0.25	2.5	250
Sigma 3 (σ_3)	MPa	0.025	0.25	2.5	250	0.025	0.25	2.5	250	0.025	0.25	2.5	250

* Joint spacing was varied so that rock masses consisting of a range of block sizes could be constructed. Each joint set had the same spacing so that the edge length of each block was equal.

** These values represent the stress regime during consolidation. After this phase of the simulation has expired, σ_1 was incrementally increased, first up to 10 kPa (or equivalent, depending on scale) and then by units of 10 kPa until the end of the simulation. In all models, σ_3 remained fixed at the initial value

Table 4.1: Representative geotechnical data used to define model boundary conditions. A 'v' indicates that the parameter was varied between different model runs.

A Continuously Yielding joint Model (CYM) was used to simulate the response of joints to loading in all model runs. It was decided to use the non-linear CYM because the use of linear joint models with constant shear and normal stiffness and linear frictional properties is limited when stress changes of several MPa can take place. It is important that this model is understood because the type of joint model used can influence the deformational response of the rock mass and the numerical modelling of practical problems may take joints through complex load paths. The Continuously Yielding joint model proposed by Cundall and Hart (1984) is intended to simulate, in a simplified fashion, the internal mechanism of progressive damage of joints under shear. As shear displacements progress, the shear strength of the joint is reduced to simulate progressive weakening, caused by the damage of asperities and a reduction in joint surface roughness. The model also includes a hysteretic damping function for dynamic solutions, by using a bounding surface concept similar to that proposed by Dafalias and Herrmann (1982) for soils. The model often exhibits the commonly observed peak / residual strength behaviour of rock joints. In addition, hysteresis is displayed for loading and unloading cycles at all strain magnitudes, no matter how small (Itasca, 2000). This is important where rock joints are subjected to progressive loading or unloading cycles, as undertaken in the present numerical simulations.

Each model was run under a biaxial stress regime because this most accurately represents the situation in natural surface outcrops. Under a biaxial stress regime, sigma 1 (σ_1) is the major principal stress, sigma 3 (σ_3) the minor principal stress and sigma 2 (σ_2) is zero. Stress boundaries were imposed on the sides and top of the model, while a velocity boundary was imposed at the base of the model to fix the problem domain in space (Figure 4.2). Initially, the model was consolidated under a stress $\sigma_1 = \sigma_3 = 0.025$ MPa. These values were chosen because 0.025 MPa represents the maximum *in situ* stress that would develop at this scale. After equilibrium was reached, σ_1 was incrementally increased by 0.01 MPa every 30000 iterations while σ_3 was kept constant.

Strain was calculated by defining profile lines along the top and side boundaries of the model. Each profile line was defined to include 20 monitoring locations along its axis, with *x* and *y* displacements being recorded at each location. The average x and *y* displacements from all profile lines were computed to construct the stress-strain curves. It is also possible to produce contoured plots of total strain by

producing user-defined sub-routines, using FISH, the built-in programming language of UDEC. A sub-routine was written to produce averaged *x-y* strain plots, so that the development of strain zones could be monitored (Appendix 4.1). It was decided to use average *x* and *y* strains to produce a total plot of strain, because the deformational response of the rock mass depends on both vertical and lateral stresses.

To simulate the deformational response of rock masses at greater outcrop scales, models were designed to simulate rock masses with dimensions of 10, 100 and 1000 m, in addition to the 1 m scenario described above. Joint spacing was increased by an order of magnitude as outcrop scale increased, but the block size area as a percentage of total rock mass area remained constant over all scales. Stresses were also scaled, so that in a 100 m rock mass consolidation occurred under a stress of $\sigma_1 = \sigma_3 = 2.5$ MPa. The stresses are higher than would be found in natural surface outcrops, but were set higher than would be found in natural systems to induce failure more rapidly, therefore improving computation time.

The command input files for the UDEC computer simulation exercise are listed in Appendices 4.2 to 4.13. In total, 72 models were run to investigate block size and outcrop scale effects in determining the deformational response of the rock mass.

4.4 Results

The results from the numerical modelling exercise are discussed in relation to the geotechnical properties of rock masses and their significance for the geomorphological evolution of rock slopes. To interpret the failure mechanisms operating in the models, displacement vector plots were produced. The length of the vector is proportional to the magnitude of the displacement. Displacement vectors for deformable blocks are calculated by monitoring the gridpoint displacements of finite difference zones created when the intact blocks are defined as deformable bodies. This is considered more accurate than velocity plots used in previous studies because the absolute direction and magnitude of movement are recorded, rather than the maximum acceleration of the block.

4.4.1 1 m rock masses

Geomorphic features at this scale consist of features such as bedrock ramps and small bedrock scar edges (Figure 4.1). As a comparison, an unjointed model was run for all 1 m rock masses to determine how the stress-strain response of a jointed medium differed from that of an isotropic elastic material. All lithologies show the same stress-strain pattern (Figure 4.3). The stress-strain curves for all lithologies are characterised by an initial non-linear convex-upward response followed by linear elastic behaviour in the axial and lateral dimensions. Under the low stresses (<2 MPa) of the numerical simulations, axial strains were less than 0.5 % in all three rock types. The Poisson's ratio derived from the numerical simulations for limestone is 0.13, for sandstone 0.09 and for granite 0.13. This is within the range of published values for intact rock under uniaxial compression (Attewell and Farmer, 1977; Goodman, 1989).

Simulation of jointed rock masses was undertaken using the same material properties and loading scenario applied to the unjointed models. The stress-strain plots for 1 m sandstone, limestone and granite rock masses are presented in Figures 4.4 to 4.6. The stress-strain response of all 1 m rock masses is non-linear, indicating that a complex normal force displacement is operating in the rock mass over a range of block sizes. The stress-strain behaviour is characterised by an initial curvilinear response as the normal load is distributed throughout the rock mass. This represents elastic strain and is recoverable. Permanent plastic deformations occur as shear displacements occur along joint surfaces, indicating initial failure. Once shear leads to a displacement of 1% of the rock mass area, the propagation of failure ensues. Although the stress-strain response in all jointed models is non-linear, the precise nature of the response is determined by the size of the intact rock blocks composing the mass.

For 1 m sandstone rock masses, the non-linearity of the stress-strain response increases as block size decreases up to a deviatoric stress of 0.1 MPa. For models with a block edge length of 0.05 to 0.2 m the initial response is linear as load is applied to the rock mass (Figure 4.4). Initial shear displacements occur at a deviatoric stress of 0.02 to 0.04 MPa, marked by a kink in the lateral and axial curves. As deviatoric stress increases above 0.08 MPa, non-linearity increases, as marked by a second kink on the stress-strain curve. For models with a block edge length between 0.3 and 0.5 m, the response is slightly different. As with models run

with smaller block sizes, the curve is initially linear between 0.02 and 0.04 MPa. Above these stresses, the 0.4 and 0.5 m block size models show approximately linear behaviour (Figure 4.4). This is related to constant shear displacements along joint surfaces. The 0.3 m model represents a transitional state between the two types of behaviour. The model behaves similarly to those with smaller block sizes, with an upward convex response until a deviatoric stress of 0.1 MPa is reached. Above this stress, kinks in the curve indicate that the rock mass is undergoing translational shear.

The Poisson's ratio of a sandstone rock mass also varies with block size. For a model with a block edge length of 0.05 m, the Poisson's ratio varies from 0.87 at a deviatoric stress of 0 MPa to 1.06 at the end of the simulation, compared with 0.12 for an unjointed model. The increase in Poisson's ratio is caused by the mobilisation of shear along joint surface, which results in lateral strain being of a similar magnitude to axial strain, producing a Poisson's ratio of 1. As block size increases, the initial Poisson's ratio is almost identical to that of the intact material, but reaches a ratio of 1 as shear is mobilised. For example, the Poisson's ratio of a model with block edge length of 0.5 m is 0.35 under a deviatoric stress of 0 MPa, rising to 1.0 at the end of the simulation. Poisson's ratio is lower at the start of the simulation because shear displacements have not occurred. In addition, the greater number of joint surfaces in the closely jointed models results in the shear strength being mobilised even under consolidation.

The stress-strain response of the limestone models differs slightly from that in the sandstone models (Figure 4.5). A model run with a block size of 0.05 m shows linear behaviour with virtually no strain up to a deviatoric stress of 0.04 MPa. The model then exhibits linear behaviour up to a deviatoric stress of 0.1 MPa. The response of the rock masses becomes more linear as block size is increased. Only the 0.05 and 0.1 m models exhibit linear behaviour after initial strain has been taken up in the rock mass. In the simulations using block sizes larger than 0.1 m, the response is non-linear with an upward convex stress-strain response in the axial and lateral dimensions. This is because as the block edge length is increased above 0.2 to 0.3 m, the stress-strain response of the rock mass is increasingly governed by the properties of the intact material once shear has been mobilised.

The Poisson's ratio for a 1 m limestone rock mass shows the same block size dependency as in the sandstone models. In the 0.05 m model, the initial Poisson's

ratio is 0.39, rising to 1.05 at the end of the simulation, and for the 0.5 m model the initial Poisson's ratio is 0.13, rising to 0.99. The data show that for a limestone rock masses three groups of block edge lengths produce a similar deformational response. The 0.05 and 0.1 m models have initial Poisson's ratios of 0.39 and 0.35 respectively, whereas the 0.4 and 0.5 m models have initial ratios of 0.13. As for the sandstone models, those with larger blocks have an initial Poisson's ratio identical to that of the intact rock at 0.13.

The stress-strain response of a 1 m rock mass composed of granite differs considerably from those in sandstone or limestone (Figure 4.6). Above a block edge length of 0.05 m, all rock masses show non-linear convex upward behaviour. The model composed of blocks with an edge length of 0.05 m exhibits linear behaviour with zero strain up to a deviatoric stress of 0.1075 MPa. As deviatoric stress increases, the response becomes non-linear, marked by the initial kink in the curve. This is recording small shear displacements in the closely jointed model. In the sandstone and limestone models, this detail is not recorded because the small (< 0.5 %) shear displacements are damped out by the recording of higher strain magnitudes as the model fails. The kink in the axial and lateral curves in models with edge lengths between 0.1 and 0.5 m is caused by joint dilation as small shear displacements occur. The dilation is more pronounced in the granite rock masses because normal and shear stiffness of joints is much greater than in sandstone or limestone. Dilation of the joint is controlled by the presence of asperities, which cause joint walls to move apart as shear displacements on a rough surface force intact blocks apart, provided that the intact rock strength is high enough to resist damage to the asperities under shear (Barton and Bandis, 1990; Bandis, 1993).

The Poisson's ratio for a 1 m granite rock mass indicates that only the 0.05 and 0.1 m models undergo significant shear, with initial Poisson's ratios of 0.62 and 0.46. By the end of the simulation the Poisson's ratio for a 0.05 m model has increased to 1.11 and for the 0.1 m model to 0.62. Despite this, the values are still lower than those found in the sandstone and limestone models. Once block edge lengths increase to 0.3 m, all models have similar Poisson's ratios ranging from initial values of 0.11 to end values of 0.40. These lower values are present because the granite rock mass has a greater resistance to deformation than the sandstone and limestone rock masses as a result of higher joint normal and shear stiffness.

Comparison of the axial stress-strain curves shows that for the limestone and sandstone rock masses, smaller block sizes experience greater axial deformation than simulations with larger block sizes (Figure 4.7). Simulations using a block edge length of 0.05 m show greater axial strain than those run with 0.1, 0.2 and 0.3 m block edge lengths. This is due to greater magnitudes of joint closure and increased block rotation which occur in the 0.05 m models. As block size increases to 0.4 and 0.5 m, axial deformation increases as significant shear displacements occur. The 0.1 to 0.3 m models have small enough blocks to resist axial deformations due to stress redistribution along the joints, which has the effect of producing less axial strain. The pattern observed in the granite simulations differs from the limestone and sandstone models (Figure 4.7). The maximum axial strain is produced in the 0.05 m model, with strain magnitude decreasing with increasing block size. This is because the axial strain in the granite model is dominated by joint normal closure with very little shear taking place, which would cause dilation (Figure 4.8).

The significance for this in natural slopes is that rock masses composed of smaller block sizes in limestone and sandstone generally have a greater shear strength than rock masses composed of larger blocks. Sliding failures in such slopes are therefore likely to be less common than in slopes with large planar joints which create discrete surfaces. The importance of these results is more fully discussed in section 4.6.

Initial model simulations indicate that the stress-strain response of rock masses can be influenced by the block size distribution. This has geomorphological and engineering implications for the response of the rock mass to applied stresses. As block size is reduced, the stress at which the model fails increases (Table 4.2). For a 1 m limestone rock mass, the deviatoric stress at failure is > 0.15 MPa for a model run with a block edge length of 0.05 m, whereas for a model run with an edge length of 0.5 m, the deviatoric stress at failure is 0.105 MPa. Models run with a block size of 0.3 m represent a threshold or transitional state where the behaviour of the rock mass begins to change. This is indicated by the deviatoric stress at failure decreasing to 0.135 MPa. A similar pattern is indicated by the output run for sandstone lithologies. For models with a block size of 0.05 to 0.1 m the deviatoric stress at failure is 0.145 MPa. As block size is increased to 0.3 – 0.5 m, the deviatoric stress at failure is 0.085 MPa, reflecting the decreasing strength of the rock mass with increasing block size. For granite rock masses, the observed pattern is slightly different, with all models remaining stable at an applied deviatoric

stress of 0.15 MPa. This reflects the much greater strength of the granite rock masses compared with the limestone and sandstone models.

It is assumed that the deformational response of rock masses composed of different block sizes is controlled by the magnitude of joint normal closure (Bandis *et al.*, 1983). However, this assumption has been based on a physical modelling approach where the joint normal closure cannot be measured directly. The magnitude of joint normal closure for the 1 m limestone rock masses shows that as block size increases, the magnitude of closure decreases (Figure 4.8). Models with a block edge length of 0.05 m undergo 0.02 mm of joint normal closure, whereas the model with an edge length of 0.5 m experiences normal closure of 0.0026 mm. For the sandstone and granite models, joint normal closure is greatest for models with a smaller block size (Figure 4.8). A sandstone model with 0.05 m edge length has a joint normal closure magnitude of 0.046 mm, decreasing to 0.002 mm for a model with a block edge length of 0.5 m. For a granite rock mass, the maximum magnitude of joint normal closure for a 0.05 m model is 0.4 mm and 0.18 mm for a 0.5 m model. Models with a smaller block size experience greater joint normal closure because the applied stresses are acting over a smaller joint surface area causing a greater stress concentration at the joint contact. The total closure of the granite rock masses is greater than the limestone or sandstone rock masses because the granite rock masses have undergone less shear and therefore dilation at the joint surface.

The deformation modulus is an indication of rock mass resistance to deformation; the higher the deformation modulus, the stiffer the rock mass, resulting in less deformation for a given stress. For a 1 m limestone rock mass, the deformation modulus decreases with increasing block size (Figure 4.9). A model run with 0.05 m block size has a deformation modulus of 0.033 GPa. A rock mass with 0.5 m blocks is just over half as strong with a deformation modulus of 0.053 GPa. The pattern is slightly confused with the 0.1, 0.2 and 0.3 m models having a greater deformation modulus than the 0.05 m models. Analysis of model output does not indicate any obvious explanation for this. The deformation moduli for the sandstone rock mass also show block size dependence (Figure 4.9).

1 m rock masses Lithology and block size	Peak deviatoric stress at failure (MPa)	Joint normal closure (mm)	Deformation modulus (GPa)	Maximum block rotation (x°)	Failure mechanism
Limestone					
0.05	>0.150	0.02	0.033	2.8	rotational
0.1	>0.150	0.011	0.077	0.87	rotational
0.2	0.165	0.0041	0.102	0.87	rotational / shear
0.3	0.135	0.0042	0.109	0.004	translational shear
0.4	0.115	0.0038	0.085	0.001	translational shear
0.5	0.105	0.0026	0.053	0.002	translational shear
Sandstone					
0.05	0.145	0.046	0.009	10.50	rotational
0.1	0.145	0.036	0.018	4.21	rotational
0.2	0.105	0.038	0.025	0.29	rotational / shear
0.3	0.085	0.011	0.030	0.006	translational shear
0.4	0.085	0.002	0.016	0.006	translational shear
0.5	0.085	0.002	0.007	0.006	translational shear
Granite					
0.05	>0.15	0.404	9.000	1.64	rotational
0.1	>0.15	0.565	15.341	0.01	n/a*
0.2	>0.15	0.214	38.571	0.001	n/a
0.3	>0.15	0.214	61.363	0.001	n/a
0.4	>0.15	0.175	88.466	0.0001	n/a
0.5	>0.15	0.188	108.000	0.0003	n/a

*Failure mode not applicable because the model did not fail during the simulation and, therefore, could not be determined.

Table 4.2: Summary of important model output parameters for all numerical simulations on 1 m rock masses.

A sandstone rock mass with 0.05 m block size has a deformation modulus of 0.009 GPa, decreasing to 0.007 GPa for a 0.5 m model. The deformation moduli for the granite rock masses are much greater than the limestone and sandstone models due to increased joint and material stiffness (Figure 4.9). For a 1 m granite rock mass with a block size of 0.05 m, the deformation modulus is 9.0 GPa, and for a model with 0.5 m spacing 108.0 GPa.

The distribution and dissipation of strain in the rock mass in response to stress can be represented in UDEC using a user-defined sub-routine, which produces filled contour plots of total (x and y) strain displacement (Appendix 4.1). Strain zones tend to occur perpendicular to the direction of principal stress during the consolidation phase of the simulation, i.e. $\sigma_1 = \sigma_3$. As vertical stress increases, strain zones become aligned with the major planes of weakness. Understanding how strains propagate through a rock mass at different stress levels has important implications for stress-strain relationships in natural slopes, by increasing our knowledge of the development and propagation of failure surfaces.

Strain zone development in a 1 m limestone rock mass shows block size dependency (Figures 4.10a to 4.10f). A model run with 0.05 m block edge length shows a vertical stress distribution after 30,000 model iterations (Figure 4.10), with maximum strain occurring along the upper boundary of the model. As the simulation proceeds, the stress distribution becomes aligned with the discontinuities, with maximum strains occurring in the left- and right-hand corners of the model after 480,000 iterations. Given the 45° geometry of the discontinuities in the model, the strain zones represent shear band formation, where the rate of shear decreases with depth due to increased deviatoric stress. As the block size increases, the vertical stress distribution at 30 000 iterations is predominantly controlled by the intact material, rather than the joints. The critical block size for this is 0.2 m, as the intact material begins to deform under stress. The depth of strain distribution is also controlled by the block size distribution of the rock mass. As block size increases, the depth of the strain zone decreases by the end of the simulation at 480,000 iterations, because there are a limited number of surfaces over which displacement can occur.

The development of strain zones in a 1 m sandstone rock mass shows a similar pattern to the limestone models at 30,000 iterations (Figures 4.11a to 4.11f). However, as the simulation continues, differences occur. By 480,000 iterations in a

sandstone model with 0.05 m block edge length only two main strain zones exist, with mean strain of 4 % and 8 % (Figure 4.11a). This is caused by weaker discontinuities and intact material. As stress is applied and strain occurs in the rock mass, the material is less able to resist deformation and large-scale shear occurs. As block size increases above 0.4 m, the deformation of the rock mass is dominated by the intact material because the blocks undergoing shear have failed and exited the problem domain, no longer contributing to strain accumulation. The timing of failure in sandstone rock masses with larger block sizes occurs much earlier than those with smaller block sizes because strain is concentrated along fewer boundaries.

The strain propagation through a simulated 1 m granite rock mass shows a contrasting pattern to the limestone and sandstone models at all block sizes (Figures 4.12a to 4.12f). Significantly, the granite models do not show the development of shear strain bands indicating the onset of large-scale deformation and failure. The simulation using 0.05 m block edge length shows a similar strain zone pattern to the limestone and sandstone models at 30,000 iterations. By 480,000 iterations, some strain zonation has occurred, with the largest strain accumulations occurring in the upper corners of the model. Despite this apparent development of strain zonation, the magnitude of total strain accumulation is very small, reaching a maximum value of 0.004 % in a model with 0.05 m block edge lengths. A similar pattern of strain accumulation occurs during the simulation using a block edge length of 0.1 m. As block size increases above this value the deformation of the rock mass is increasingly dominated by strain accumulation in the intact material, rather than the development of shear bands.

The deformational response and mode of failure are also affected by the block size distribution of the rock mass. Analysis of the magnitude of shear displacement along the joints generally shows that the magnitude of shear increases as block size increases (Figure 4.13). In a 1 m limestone rock mass with 0.05 m block size, the total shear displacement at the end of the simulation is 4.79 mm, whereas for a model with 0.5 m block size, shear displacement increases to 85.3 mm. For a 1 m sandstone rock mass the same pattern is observed. A model with 0.05 m block size experiences 35.5 mm of shear by the end of the simulation and the 0.5 m model 529 mm. A 1 m granite rock mass experiences 0.1 mm of shear in the 0.05 m model. As block size is increased to 0.1 m and above, shear displacement is negligible, contributing little to the deformational response of the rock mass (Figure 4.13). The

results show that the magnitude of shear displacement increases as block size increases, suggesting that the failure mechanism operating in the rock mass is dependent upon block size.

Block plots of gridpoint displacements indicate that the mode of failure changes with block size (Figures 4.14a to 4.14b). For a 1 m limestone rock mass with 0.05 m block edge length, the displacement vectors in the top centre of the model are not parallel to the bedding, indicating that the blocks have started to rotate (Figure 4.14a). Towards the outer boundary of the model the displacement vectors are parallel to the bedding, indicating shear. A similar pattern is observed in the models run with 0.1 m block edge length; block rotation occurs in the centre of the model and shear displacements dominate the side boundaries of the model (Figure 4.14b). A slight suggestion of rotation is seen in a model run with 0.2 m block edge length (Figure 4.15a). As the block edge length increases to 0.3 m the displacement vectors show that the mode of failure is increasingly dominated by shear rather than rotation (Figure 4.15b). Displacement vector plots for models run with a block edge length of 0.4 and 0.5 m show that shear is the dominant failure mechanism (Figures 4.16a and 4.16b). Analysis of the magnitude of block rotation confirms the qualitative patterns indicated in the displacement vector plots. The simulation of a rock mass with edge length of 0.05 m shows the greatest block rotation of 2.8 degrees. As the block size increases, the magnitude of rotation decreases. For models run with 0.1 and 0.2 m edge lengths the maximum rotation was 0.87 degrees, decreasing to less than 0.005 degrees for models with edge lengths from 0.3 to 0.5 m. This confirms that translational shear is the dominant mode of failure in the simulated rock masses where block size accounts for more than 4 % of the total rock mass area. Similar patterns are observed in the sandstone rock masses. In the granite rock masses, no plots are included because the models did not fail.

Block size is an important parameter controlling the stress-strain response and deformational behaviour of the simulated jointed rock masses at the hypothetical 1 m scale. As block size decreases, the distribution of strain changes, with a number of shear bands developing in the models composed of smaller blocks. This is in contrast to simulations using larger blocks, where one or two shear bands dominate the deformational response of the rock mass. Models run with small block sizes, which failed by translational shear along a large number of discrete boundaries, exhibited a higher strength than rock masses composed of larger blocks. However,

the depth of deformation in rock masses composed of smaller blocks is greater, suggesting that deep-seated failures are more likely in closely jointed rock masses. A number of important summary points can be made with regard to the behaviour of hypothetical 1 m rock masses:

1. The stress-strain behaviour of the rock masses in the three lithologies investigated can be described as a convex load-deformation response, and is typical of a rock mass with diagonal discontinuities.
2. The shear components are largely responsible for the deformation of a rock mass with discontinuities orientated at 45 degrees.
3. If the models are run with horizontal joints parallel to the bedding, deformation will be dominated by normal joint closure and a concave load-deformation response. In this case, the shear components are absent and lateral expansion is negligible.
4. The deformation moduli show that granite rock masses are much stiffer than limestone, with sandstone being the weakest.
5. All deformation moduli show block size dependency at this scale. In the limestone and sandstone rock masses, the deformation modulus increases with decreasing block size, while in granite it decreases. This is caused by the greater joint normal closure in granite, associated with reduced joint dilation caused by the onset of shear.
6. The deformation modulus for a rock mass with smaller block sizes increases because of the greater number of shear surfaces present in the model.
7. The combined shear strength of many joint surfaces is greater than in those models where only a limited number of joint surfaces are present.
8. The applied stress is also distributed throughout the rock mass, allowing the accumulation of greater magnitudes of strain before brittle failure of the rock mass occurs in a well jointed model.
9. Plots of strain zone accumulation illustrate how block size can influence the evolution of strain / deformation in a rock mass.
10. The timing of failure in sandstone rock masses, for example, consisting of larger block sizes occurs much earlier than those with smaller block sizes because strain is concentrated along fewer boundaries.
11. Analysis of shear displacement magnitudes show that the failure mechanism is dependent on block size.
12. As block size increases the failure mechanisms change from rotational to translational shear.

4.4.2 10 m rock masses

To simulate the effects of outcrop scale on rock mass behaviour, the modelling exercise was repeated on a 10 m rock mass. Natural slopes at this scale consist of small scar features and small rock-slopes (Figure 4.1) Block size was scaled, so that each block covered the same area of problem domain as in the 1 m model. Stresses were increased to allow strains to develop, with consolidation at $\sigma_1 = \sigma_3 =$ 0.25 MPa.

For a 10 m limestone rock mass the stress-strain curves show the same non-linear concave upward loading response of the rock mass at all block sizes (Figure 4.17). Initially, all the curves are linear indicating strain accumulation in the rock mass but that substantial shear has not occurred. At a deviatoric stress of 0.4 MPa, the lateral and axial strain curves show that the rock mass is responding in a non-linear way as shear displacements and block rotations occur. The kink between 1.0 and 1.2 MPa seen in the 0.5 and 1 m models is recording shear and block rotation movements. The Poisson's ratio of the rock mass shows block size dependency, with higher initial values being recorded in the closely jointed models. For example, the initial Poisson's ratio after 30,000 iterations in a 10 m model with 0.5 m block edge lengths is 0.16. As block size is increased, the initial Poisson's ratio ranges from 0.03 for a model run with 2 m block edge length to 0.09 for a 5 m model. Similarly, the Poisson's ratio at the end of the simulation is greater for the 0.5 and 1 m models. For the 0.5 m model, the Poisson's ratio is 1.16 at the end of the model run and 1.45 for the 0.1 m model. Models run with all other block sizes show a Poisson's ratio of 1.0 at the end of the simulation. The end Poisson's ratio is greater for the 0.5 and 1 m models because strain is being accumulated through shear and rotation, allowing a greater accumulation of lateral strain.

The stress-strain response of the 10 m sandstone models differs from the 1 m models, although the general form of the curve is preserved (Figure 4.18). An initial linear response is followed by non-linear behaviour associated with shear displacements and failure of the rock mass. Linear behaviour occurs between a deviatoric stress of 0.2 and 0.4 MPa followed by a non-linear load deformation response. The stress-strain curve on the 5 m model has many kinks after a deviatoric stress of 0.6 MPa; this is caused by blocks failing and leaving the problem domain. The highest initial values for Poisson's ratio occur in the closely jointed models. The initial value for a simulation with 0.5 m edge length is 0.33, decreasing

to 0.07 for a 5 m model. End values show a minor increase in Poisson's ratio. The value for a 0.5 m model is 1.06 at 480,000 iterations and 1.00 for a 5 m model. As for the 10 m limestone models, the Poisson's ratio for the closely jointed models is higher because of the combination of block rotations and shear displacements, rather than purely translational shear.

The 10 m granite model produces a similar load deformation response to the 1 m model (Figure 4.19). A model run with a block edge length of 0.5 m shows an initially linear deformational response up to a deviatoric stress of 0.9 MPa, where non-linear behaviour is caused by initial shear and rotational displacements of the blocks. The 0.5 m model undergoes 0.5 % axial strain and 1.0 % lateral strain, which is much greater than for other block sizes, which undergo less than 0.1 % strain. This can be explained by small cumulative shear displacements and the rotation of blocks. Models run with block sizes 1 to 5 m produce a response, which resembles that produced by intact material, i.e. no large shear displacements occur.

For 10 m limestone and sandstone rock masses, the maximum vertical stress at failure increases with decreasing block size. For a limestone rock mass with 0.5 m spacing, the maximum vertical stress at failure is 1.85 MPa (Table 4.3). This decreases to 1.05 MPa as block edge length increases to 0.2 m and 0.95 MPa for block edge lengths larger than 0.4 m. A similar pattern is found for sandstone rock masses. The maximum stress at failure for a sandstone rock mass with 0.5 m edge length is 0.85 MPa and 0.65 MPa for a model with a block edge length of 5 m. This shows that at the 10 m scale, rock masses with smaller block sizes require a greater stress to induce failure than rock masses composed of larger block sizes. For the granite rock masses, the model run with 0.5 m block edge length undergo failure at a vertical stress of 0.85 MPa, while the other models did not develop failure surfaces at the applied stresses used in the numerical simulation. This suggests that in strong rock masses, small cumulative shear displacements and block rotations may be an important mechanism of deformation. The data indicate that the shear strength of the closely jointed models is greater than for models with widely spaced joints.

10 m rock masses Lithology and block size	Peak deviatoric stress at failure (MPa)	Joint normal closure (mm)	Deformation modulus (GPa)	Maximum block rotation (x°)	Failure mechanism
Limestone					
0.5	1.85	0.119	0.123	17.47	rotational
1	1.85	0.105	0.255	14.10	rotational
2	1.05	0.079	0.324	0.19	rotational / shear
3	1.05	0.068	0.348	0.002	translational shear
4	0.95	0.022	0.435	0.001	translational shear
5	0.95	0.022	0.367	0.001	translational shear
Sandstone					
0.5	0.85	0.114	0.031	16.60	rotational
1	0.85	0.116	0.053	23.04	rotational
2	0.65	0.089	0.066	0.190	rotational / shear
3	0.65	0.059	0.091	0.004	translational shear
4	0.75	0.009	0.078	0.005	translational shear
5	0.65	0.02	0.58	0.005	translational shear
Granite					
0.5	0.85	0.19	0.155	10.6	rotational
1	>1.85	0.02	33.70	0.01	n/a*
2	>1.85	0.01	75.00	0.001	n/a
3	>1.85	0.01	84.30	0.001	n/a
4	>1.85	0.01	135.0	0.0004	n/a
5	>1.85	0.01	135.0	0.0003	n/a

*Failure mode not applicable because the model did not fail during the simulation and, therefore, could not be determined.

Table 4.3: Summary of important model output parameters for all numerical simulations on 10 m rock mass.

The deformation moduli for a 10 m limestone rock mass indicate that the stiffness of the rock mass increases with increasing block size (Table 4.3, Figure 4.20). The deformation modulus for a 10 m model run with 0.5 m block edge length is 0.123 GPa, increasing to 0.367 GPa for a model run with 5 m block edge length. This is in contrast to the data presented on the maximum vertical stress at failure which show that smaller block sizes fail at a higher deviatoric stress. This can be explained by the magnitude of joint normal closure. For a 0.5 m model, the maximum joint normal closure between two joint surfaces is 0.12 mm (Figure 4.21). The models run with smaller block sizes contain more joint surfaces over which closure can occur. In addition, the magnitude of joint normal closure in a 5 m model is much less at 0.02 mm. Thus, although the deformation moduli show that models with larger block sizes are stiffer, they record indirectly the influence of joint normal closure. This is reflected in the higher deviatoric stress at failure of the closely jointed models.

The pattern of deformation moduli for the 10 m sandstone models shows that the deformation modulus initially increases up to a block edge length of 3 m, but then decreases with increasing block size (Figure 4.20). Simulations undertaken with block edge lengths of 0.5 and 2 m have deformation moduli of 0.031 GPa and 0.066 GPa. There is an increase in deformation modulus with block size because initial shear displacements have resulted in some joint dilation. As block size increases to 4 m, further shear displacements destroy asperities on the joint surface reducing the deformation modulus as dilation decreases.

The 10 m granite models show a similar block size dependency to the 1 m models when the deformation modulus is considered, in that the stiffness of the rock mass increases with increasing block size. A model run with 0.5 m block edge length has a deformation modulus of 0.155 GPa, compared with 135.0 GPa for a model with 5 m block edge length (Table 4.3, Figure 4.20). This in part reflects the reduced joint normal closure and the increasing dominance of intact material in governing the behaviour of the rock mass. The deformation moduli are high because a 10 m block of almost solid granite is very stiff. Joint normal closure magnitudes also decrease with increasing block size (Figure 4.21) A model run with 0.5 m block edge length undergoes 0.19 mm of joint normal closure and the 1 to 5 m models have a normal closure of $\leq$ 0.02 mm.

The propagation of strain zones in the 10 m rock masses shows similar patterns to the 1 m rock masses (Figures 4.22a to 4.22f). However, the strain zones tend to be

less defined and there is less vertical variation in strain. In a 10 m limestone rock mass with 0.5 m edge length, only four main strain zones have developed by 480,000 model iterations (Figure 4.22a). A similar reduction in the number of strain zones occurs in the model run with 1 m block edge length (Figure 4.22b). The reduced number of strain zones in these models reflects the higher stresses imposed on the rock mass as scale is increased. Fewer strain / shear zones develop because deformation of the rock mass is more advanced in the 10 m models because of higher imposed stresses. The deformation of the rock mass is more uniform because failure is more advanced and rotation is the dominant mode of deformation (Table 4.3). As block size is increased to 2 m, more shear bands have developed in the 10 m model than in the 1 m model (Figure 4.22c). This reflects the higher stresses in the 10 m model and the increased potential for shear surfaces to develop under these higher stresses. For the 4 m and 5 m models, the same number of strain zones occur at both 1 and 10 m scales, because of the number of blocks that are free to move (Figures 4.22e to 4.22f).

Strain zone development in the 10 m sandstone rock masses shows a similar pattern to the limestone. The same explanations may be invoked for the propagation of strain through the rock masses (Figures 4.23a to 4.23f). The main difference is that for the 5 m model, the strain zones are dominated by the behaviour of the intact materials because the failed blocks have completely left the problem domain, so that shear bands are no longer present (Figure 4.23f).

For a 10 m granite rock mass the propagation of strain is markedly different in the simulation run with a 0.5 m edge length compared with the 1 m model (Figure 4.24a). The strain zones have become aligned with the discontinuities, indicating that shear displacements have occurred. A model run with 1 m edge length shows that strain zones are beginning to become aligned with the discontinuities, but shear displacements have yet to occur (Figure 4.24b). All other granite models show similar vertical strain zonation, indicating that significant shear displacements along the joints have not occurred (Figures 4.24c to 4.24f).

Analysis of block rotations indicates that the failure mechanism is still dependent upon block size in 10 m rock masses (Figure 4.25). All rock masses show decreasing block rotation with increasing block size. For a 10 m limestone rock mass, the maximum block rotation for a 0.5 m block size is 17.47 degrees, decreasing to 0.001 degrees for 5 m block size. This can be related to the

magnitude of joint shear in the models. As block size increases and rotation decreases, the magnitude of shear displacements increases (Figure 4.26). For a 10 m sandstone rock mass, the maximum shear displacement in a 0.5 m model is 35.5 mm, increasing to 529 mm for a 5 m block size. Granite shows a pattern of decreasing shear with increasing block size. This may be related to the increase in shear strength of joints in granite that prevents initial shear displacements until their strength is exceeded.

The most important findings of simulating the behaviour of rock masses at 10 m scale are:

1. The total joint closure magnitude for a rock mass consisting of smaller block sizes is greater than for one with larger block sizes. This is because in a well jointed model, there are more surfaces over which closure can occur and is reflected in increased deformation moduli for rock masses with fewer joints.
2. Comparison of the three lithologies shows that granite rock masses have the highest deformation modulus, and sandstone the lowest, reflecting the differences in material properties.
3. At the 10 m scale, granite experiences the least joint normal closure. This is in contrast to the pattern found for the 1 m rock masses, where granite experiences the most joint closure. This pattern is caused by the increase in joint dilation without significant shear.
4. In the limestone and sandstone rock masses, shear has begun and dilation along joint surfaces is greater as asperities to move over each other under shear.
5. Initial shear displacements have an influence over the deformational properties of the rock mass.
6. As block size is reduced the failure mechanism changes from brittle translational shear failure to a more time-dependent, rotational and ductile response.

4.4.3 100 m rock masses

Slopes at this scale are by far the most common, occurring in a range of environments from Alpine, desert to coastal (Figure 4.1). Understanding the behaviour of slopes at these scales is important because most failures occur in

slopes at this scale in the natural environment due to their prevalence. Failures in such slopes have the potential to be relatively large.

The stress-strain response of a 100 m limestone rock mass with block edge lengths of 20 m and below is almost linear, with some non-linear behaviour occurring in models run with 30 to 50 m edge lengths (Figure 4.27). This suggests that significant shear displacements have not yet occurred in the closely jointed models. All models show a linear strain response up to a deviatoric stress of 3 MPa because the model is taking up initial strain along the joint surfaces and joint strength is mobilised, resisting shear displacements. As the deviatoric stress increases above 3 MPa, shear can occur along the joint surfaces as the mobilised joint shear strength is exceeded. Non-linearity is greatest in the models with larger block edge lengths because shear displacements are concentrated along a small number of joint surfaces, rather than distributed throughout the rock mass. The initial Poisson's ratio for the 1 m limestone rock mass increases with increasing block size, indicating that initial shear is greatest in models with larger block sizes. The initial Poisson's ratio for a 100 m limestone model with 5 m block edge length is 0.01, increasing to 1.13 for a model with 50 m edge length. However, the value for Poisson's ratio at the end of the simulation is greatest for models composed of a greater number of blocks. For the 5 m block model the Poisson's ratio at the end of the simulation is 1.23, while for a block edge length of 50 m it decreases to 1.0. This is because blocks are undergoing rotation rather than shear, resulting in more lateral deformation than vertical deformation due to block rotation. Models with larger block edge lengths undergo shear deformations so that lateral and vertical deformations are almost identical under the defined geometry.

The stress-strain behaviour for a 100 m sandstone rock mass is slightly different from that in limestone. The 5 and 10 m block models show an upward convex deformational response associated with block rotation rather than shear (Figure 4.28). All other models show non-linear responses but with kinks in the curve associated with the mobilisation of shear displacements (Figure 4.28), as seen in the Poisson's ratio for the rock masses. The initial Poisson's ratio for a 100 m sandstone rock mass with 5 m block edge length is 0.26, whereas for a 50 m model it is 0.05. This is different from the limestone model where the shear and normal stiffness of the joints is not as high. Under initial loading, shear strength along the many joint surfaces is being mobilised, whereas in the 50 m model, the blocks have

fewer degrees of freedom to move under small shear displacements as shear strength is mobilised.

The stress-strain response of the 100 m granite rock mass produces a similar response to the 1 and 10 m rock masses (Figure 4.29). The 5 m model shows an initial linear response, followed by an kink in the stress-strain curve at 7 MPa, indicating that initial shear displacements and block rotations have begun. For models with block edge lengths of 10 to 50 m, the model behaves similarly to the intact material, showing that shear displacements have not occurred. Values of the rock mass Poisson's ratio also indicate very little deformation of the rock masses. For the 5 m model, the initial Poisson's ratio is very low at 0.02, because vertical deformation caused by joint normal closure is more important than lateral strain caused by translational shear. The initial Poisson's ratio for models with a block edge length above 20 m is similar to the intact material. At the end of the simulation, the Poisson's ratio is around 0.30 for these models, showing that some joint shear mobilisation has occurred, although substantial shear has not.

The peak deviatoric stress at which failure occurs shows that a decrease in block size leads to a decrease in deviatoric stress at failure (Table 4.4). For a 100 m limestone rock mass, the deviatoric stress at failure for a model with 5 m block edge length is 9.5 MPa, increasing to 16.5 MPa for a 50 m model. A similar but less consistent pattern is found for the sandstone rock masses with the 5 m model failing at a deviatoric stress of 4.5 MPa and the 50 m model at 6.5 MPa. The reduced deviatoric stress at failure is caused by a decrease in the stiffness of the rock masses as block size decreases. However, the shear strength of the closely jointed rock mass is higher, as shown by the lack of significant shear in the closely jointed models. Much of the deformation is occurring through gradual rotation of the blocks under load.

100 m rock masses Lithology and block size	Peak deviatoric stress at failure (MPa)	Joint normal closure (mm)	Deformation modulus (GPa)	Maximum block rotation (x°)	Failure mechanism
Limestone					
5	9.5	0.59	0.962	10.59	rotational
10	9.5	0.57	1.243	10.38	rotational
20	4.5	0.42	2.499	0.24	translation shear
30	4.5	0.23	3.426	0.007	translational shear
40	6.5	0.21	5.152	0.004	translational shear
50	6.5	0.13	1.646	0.017	translational shear
Sandstone					
5	4.5	12.44	0.326	22.60	rotational
10	3.5	5.54	0.393	18.60	rotational
20	6.5	4.97	0.793	0.001	translational shear
30	6.5	3.56	1.078	0.001	translational shear
40	3.5	2.22	1.339	0.001	translational shear
50	6.5	2.30	0.584	0.004	translational shear
Granite					
5	>17.5	3.15	3.214	10.04	Rotational (inferred)
10	>17.5	0.23	135.0	0.01	n/a*
20	>17.5	0.11	168.7	0.002	n/a
30	>17.5	0.10	225.0	0.002	n/a
40	>17.5	0.09	225.0	0.002	n/a
50	>17.5	0.09	225.0	0.002	n/a

*Failure mode not applicable because the model did not fail during the simulation and, therefore, could not be determined.

Table 4.4: Summary of important model output for all numerical simulations on 100 m rock masses.

For the limestone, sandstone and granite models the deformation modulus increases with increasing block size (Figure 4.30). The exception to this is the 50 m models which show a decrease in stiffness because all the load is concentrated along a single discontinuity. Figure 4.65 also indicates that intact rock strength affects the deformation of a slope. The weakest material is sandstone, which experiences the greatest deformation for a given stress. Granite, the strongest material, undergoes the least deformation. The deformation modulus for a 100 m limestone rock mass with 5 m block size is 0.962 GPa, increasing to 5.152 GPa for a 40 m model. The sandstone model with block size of 5 m has a deformation modulus of 0.326 GPa increasing to 1.34 GPa for a 40 m model. The deformation modulus of granite is several orders of magnitude greater. For a 5 m model, the granite rock mass has a deformation modulus of 3.214 GPa increasing to 225.0 GPa for a 50 m model.

Much of the deformation in the closely jointed models is caused by normal closure along joint surfaces. The closely jointed models experience a greater magnitude of joint normal closure than do models with fewer discontinuities (Figure 4.31). A limestone model with 5 m block size produces 0.59 mm of joint normal closure and a 50 m model 0.13 mm. Similar patterns are repeated for the sandstone and granite models. However, the sandstone model experiences greater normal closure and granite the least. This is because the normal and shear stiffness of dry joints with no fill is dependent on surface roughness and strength of the intact material.

The mode of failure and deformation in the rock mass can be examined by looking at the magnitude of shear displacements along the joint surfaces. It is clear that closely jointed rock masses undergo less joint shear than widely spaced models and that rock masses composed of weaker material undergo greater deformation than those composed of harder materials (Figure 4.32). The maximum magnitude of joint shear in a limestone model with 5 m block size is 1.51 mm, increasing to 11.51 mm for a 50 m model. For a sandstone model the maximum shear with block size of 5 m is 2.76 mm, increasing to 27.28 mm for the 50 m model. The main difference occurs in the granite rock mass where shear decreases with block size. The 5 m granite model experiences 0.11 mm of shear decreasing to 0.0005 mm for the 50 m model. This is caused by initial closure of the joint surfaces and associated shear displacements that occur as the asperities interlock. The lack of significant shear shows the model has not failed.

The mode of deformation and failure in the 100 m scale rock masses can be linked to the magnitude of block rotation. The amount of rotation decreases as shear displacements increase, which is related to block size (Figure 4.33). For a limestone rock mass with a block edge length of 5 m, the maximum magnitude of block rotation is 10.59 degrees, decreasing to 0.017 degrees for a block size of 50 m. The same pattern is repeated for sandstone with the 5 and 10 m models showing much greater rotation of blocks than those with a larger block size (Figure 4.33). For the granite models, only the 5 m model shows major block rotation of 10.04 degrees (Figure 4.33). The 10 m model does not show major rotation because small shear displacements have yet to occur, which increase the number of degrees of freedom for the blocks, allowing rotation to occur. At the 20 to 50 m block sizes, sandstone rock masses show the lowest magnitude of block rotation. This is because failure of the rock mass is advanced and the centre of gravity of blocks at the model edge is falling outside the model boundary, increasing the magnitude of rotation during failure.

The development of strain zones in the rock masses shows similar initial patterns to the 1 and 10 m simulations, where strain decreases with depth. However, some differences exist as the models are run. For a 100 m limestone rock mass with 5 m joint spacing, four shear strain zones have developed by the end of the simulation at 480,000 iterations (Figure 4.34a). These shear bands illustrate that strain in the closely jointed models is more deeply seated than in models with wider joint spacings (Figures 4.34b to 4.34f). As block size is increased, the area of equal strain in the model increases, showing that fewer strain zones have developed because fewer shear surfaces are present. A similar pattern of shear band formation and strain distribution is present in the sandstone models and does not need to be described in detail (Figures 4.35a to 4.35f). For a 100 m granite model, only the model run with 5 m joint spacing shows the development of shear bands by the end of the simulation. This is reflected in the higher shear displacements present in the 5 m granite model. As block size is increased, there is much clearer zonation of strain compared with the 1 and 10 m models. This reflects the increase in applied stresses, leading to a slight deformation of the intact material (Figures 4.36a to 4.36f).

Although the essential behaviour of the 100 m rock masses is similar to those with a smaller outcrop scale, a number of important points can be made.

1. As block size is reduced, the maximum deviatoric stress at which failure occurs decreases. This is caused by the cumulative effect of small shear displacements and a consequent increase in block rotation.
2. As block size is reduced, the depth of deformation increases due to the greater number of shear surfaces present in the model. The intact material exhibits uniform strain, partly due to the linear elastic model applied and partly due to the absence of shear surfaces.

4.4.4 1000 m rock masses

Understanding the behaviour of slopes at this scale is important, particularly in recently glaciated areas (Figure 4.1). Slopes at this scale are not as common as those at the 1 to 100 m scales because the conditions required for the formation and maintenance of such slopes tend to be fairly limited. They are often confined to the strongest rock masses which have been truncated by glacial erosion. However, failure of such slopes could produce catastrophic geomorphological responses.

The stress-strain response of all 1000 m rock masses is markedly different from simulations undertaken at smaller outcrop scales. The most important characteristic of the stress-strain behaviour of the rock masses at the 1000 m scale is the apparent stabilisation of the rock masses under increased deviatoric stress and the relatively low (< 1%) strain accumulation.

For a 1000 m limestone rock mass with block edge lengths of 50 and 100 m, the load-deformation response is almost linear (Figure 4.37). The stress-strain response is less steep for the 100 m model, suggesting that shear is more important than in the 50 m model, particularly after a deviatoric stress of 100 MPa. In the models run with 200 and 300 m block edge lengths, the stress-strain curve indicates that no further strain occurs after a deviatoric stress of approximately 50 MPa in the 200 m model and 30 MPa in the 300 m model. More significant block rotations in the 200 m give rise to the initial portion of the stress-strain curve being upward concave, whereas shear in the 300 m model produces an initial linear response. Values of Poisson's ratio indicate that shear strength has been mobilised in the models and that small shear displacements have occurred, producing a Poisson's ratio of ≥ 1. For the model run with a 50 m block edge length, the initial Poisson's ratio is 0.21, increasing to 1.04 at the end of the simulation. In the simulation run

with a block edge length of 500 m, the initial Poisson's ratio is 0.14, increasing to 0.99 at the end of the simulation. In the models run with 400 and 500 m block edge lengths, the initial load-deformation response is linear, followed by kinks in the curve indicating initial shear displacements in the rock mass. This is supported by the rock mass Poisson's ratio. In the 400 m model, the initial Poisson's ratio is 0.13, which is similar to the intact material, but it increases to 0.98 at the end of the simulation because the shear strength along the joint surface has been mobilised.

The stress-strain response of a 1000 m sandstone rock mass differs substantially from the limestone rock mass (Figure 4.38). Simulations undertaken with block edge lengths of 50 to 300 m produce a load deformation response that indicate no further strain above a deviatoric stress of 20 MPa (Figure 4.38). Models run with 400 and 500 m block edge lengths show an almost linear load deformation response associated with translational shear. These models show a much larger magnitude of strain than models run with smaller block edge lengths. The 400 m model undergoes 1.5 % strain and the 500 m model 2.5 % strain. Values for Poisson's ratio indicate that in all models shear strength has been mobilised. The 50 m model has an initial Poisson's ratio of 0, increasing to 1.06 at the end of the simulation; the 500 m model has an initial value of 0.05, increasing to 0.99 by the end of the model run.

The stress-strain response of a 1000 m granite rock mass shows an initial upward convex response. However, at a deviatoric stress of 65 MPa, no further strain occurs in the model (Figure 4.39). This is thought to be caused by the increase in normal vertical stress applied to the model. As deviatoric stress increases across a joint surface, the shear resistance of the joint also increases, resulting in reduced shear strain. The relative deviatoric stress in the models between scales is constant, so that failure would not be prevented by the increase in confining pressure, as the ratio of σ_1:σ_3 is the same. Therefore, the increase in deviatoric stress across the joint surface is responsible for imparting stability to the models, with the increase in joint shear and normal stiffness of the granite rock masses.

The maximum deviatoric stress at failure for the limestone rock masses shows some block size dependency and confirms the pattern produced by the stress-strain curves. Models run with block edge lengths of 50 to 300 m fail at a deviatoric stress greater than 150 MPa, whereas models run with edge lengths of 400 and 500 m fail at 60 MPa and 50 MPa, respectively (Table 4.5). The same pattern is repeated for

the sandstone rock masses with the 400 and 500 m models undergoing initial failure, whereas models with smaller block edge lengths remain stable. For the granite models, all remain stable at the maximum deviatoric stress of 150 MPa applied during the simulations (Table 4.5). The increase in strength is a result of the deviatoric stress being distributed along many joint surfaces, rather than concentrated along one or two joints where high stress concentrations can occur, resulting in shear failure of the model.

The deformation moduli for 1000 m limestone rock masses show clear block size dependency, increasing with decreasing block size (Table 4.5, Figure 4.40). For a model run with 50 m block edge length the deformation modulus is 555.26 GPa, whereas for a 500 m model the value is 8.99 GPa. This shows that as block size decreases, the rock mass becomes more resistant to deformation. This is due to the greater shear strength of the closely jointed rock mass, as indicated by the decrease in axial and lateral strain with decreasing block size.

For a sandstone rock mass, a similar pattern of decreasing deformation modulus with increasing block size is present (Figure 4.40). The deformation modulus for a 1000 m sandstone model run with 50 m block size is 4.38 GPa, decreasing to 3.49 GPa with 500 m block size. The sandstone rock masses at this scale reflect the behaviour of sandstone rock masses at smaller scales in that they are more deformable than the limestone or granite rock masses. For the granite rock masses, the 50 m model is the stiffest with a deformation modulus of 1350 GPa (Figure 4.40). The deformation then remains stable at 1125 GPa for model runs with block edge lengths of 100 to 500 m, as indicated by the stress-strain response.

1000 m rock masses Lithology and block size	Peak deviatoric stress at failure (MPa)	Joint normal closure (mm)	Deformation modulus (GPa)	Maximum block rotation (x°)	Failure mechanism
Limestone					
50	>150	0.21	555.263	0.39	rotational
100	>150	0.53	193.410	0.16	n/a*
200	>150	0.52	134.660	0.06	n/a*
300	>150	0.67	32.809	0.04	n/a*
400	60	1.19	21.577	0.01	translational shear
500	50	1.31	8.995	0.03	translational shear
Sandstone					
50	130	0.86	43.853	7.58	rotational
100	>150	1.35	35.563	0.75	rotational
200	>150	1.5	29.639	0.004	rotational / shear
300	>150	1.84	16.406	0.002	translational shear
400	70	2.65	9.162	0.002	translational shear
500	30	2.76	3.491	0.002	translational shear
Granite					
50	>150	0.40	135	0.01	rotational
100	>150	0.31	1125	0.008	n/a*
200	>150	0.22	1125	0.005	n/a
300	>150	0.22	1125	0.005	n/a
400	>150	0.17	1125	0.005	n/a
500	>150	0.18	1125	0.005	n/a

*Failure mode not applicable because the model did not fail during the simulation and could not be determined.

Table 4.5: Summary of important model output for all numerical simulations on 1000 m rock masses.

The pattern of deformation in the 1000 m models differs from that observed at smaller scales. Models run at smaller scales showed that the stiffness of the rock mass increases with block size. The simulations at 1000 m show the stiffness decreases with increasing block size. Mechanically, this is difficult to interpret. This is reflected in the magnitude of joint normal closure, which increases as block size increases (Figure 4.41). In the 1000 m limestone rock mass with 50 m block size, the joint normal closure magnitude is 0.21 mm, increasing to 1.31 mm for 500 m block sizes. The same pattern is repeated for sandstone. In granite rock masses, a pattern of decreasing closure with increasing block size is observed, reflecting the response at smaller scales. In addition, the magnitude of joint shear observes the same pattern as for smaller scale slopes, with shear increasing as block size increases (Figure 4.42). The pattern of shear therefore cannot be invoked to explain differences in the pattern of deformation. It is likely that the increase in deviatoric stress across the joint surfaces is responsible for an increase in effective friction, preventing failure of the rock mass and producing the patterns observed for slopes of smaller scale. For real-world slopes, this suggests that the highest slopes will be found in rock masses with few discontinuities. This numerical work reflects the real-world situation of 1000 m slopes, which tend to be formed in rock masses composed of strong intact material or few joints.

The magnitude of block rotation in all models is low because substantial failure has not occurred (Figure 4.43). In general, all models show that block rotation decreases with increasing block size. The maximum rotation magnitude of 7.58 degrees occurs in the 1000 m sandstone model with 50 m joint spacing. All other models show a block rotation magnitude of less than one degree. Despite the low magnitude of block rotation, the pattern of decreasing block rotation with increasing block size seen at lower outcrop scales is preserved at the 1000 m scale. For natural slopes the failure mechanism operating on the slope is not affected by the increased stresses found in higher slopes.

The propagation of strain and the formation of shear bands in the 1000 m limestone rock mass are similar to that seen in models run at smaller outcrop scales (Figures 4.44a to 4.44f). More shear bands develop in the closely jointed models and the deformation of the rock mass is more deeply-seated than for models with larger block sizes. For a 1000 m sandstone rock mass the same relationship between strain distribution and block size is also seen, although the magnitude of strain is larger than in the limestone rock masses (Figures 4.45a to 4.45b). For the granite

rock masses, the strain distribution of strain zones at the end of the model simulation is almost identical to that of the start (Figures 4.46a to 4.46f). The main difference is that the strain zones at the end of the simulation have shown some rotation indicating that there is slightly more strain occurring at the model boundaries.

The most important findings from the numerical simulations undertaken for 1000 m rock masses are:

1. Sandstone rock masses with 400 and 500 m block edge lengths show an almost linear load deformation response associated with translational shear. This is in contrast to models run with smaller block sizes that exhibit self-stabilisation.
2. For natural slopes, the implication is that if shear surfaces daylight at the slope face, those with fewer planes are more likely to undergo failure due to the concentration of stresses in slopes in weak lithologies.
3. As block size increases the magnitude of joint normal closure increases, despite shear displacements increasing too. This is due to the increased concentration of stress along fewer discontinuities damaging asperities so that dilation under shear is prevented.
4. As block size decreases, stiffness of the rock mass increases. For natural slopes this suggests that due to the dissipation of stress and the greater shear strength of closely jointed models, slopes with smaller block sizes will be less prone to catastrophic failure.

4.5 Discussion

Numerical simulation of the stress-strain behaviour of rock masses has shown that the form of the stress-strain curves differs significantly compared with that for intact rock (Figure 4.47). Deformation of a discontinuous rock mass rarely produces the characteristic peak strength found for intact rock. Instead, additional stress is accounted for by fairly constant strain accumulation. Previous geomorphological studies have not considered this difference in behaviour between the rock mass and intact rock strength. Most previous studies have assumed the behaviour of the rock mass to follow a similar stress-strain response to intact rock (Allison, 1993). For understanding slope deformations, this implies that once failure has occurred, additional increases in stress have minimal impact on the behaviour of the landform.

The results from the numerical modelling exercise show that block size controls both the shear strength and deformational characteristics of the slope. Figure 4.48 shows a summary of the stress-strain response of rock masses composed of different block sizes. The solid line summarises the stress-strain characteristics of translational shear movements that occur when the block edge length is 30 % of the outcrop scale length (e.g. block size of 0.3 m in a 1 m model). Although the initial response is linear, kinks in the curve caused by shear displacements produce a non-linear response. The dashed curve indicates the characteristic stress-strain response of the rock mass where block rotation is the major failure mechanism. Initially, the response is linear indicating that shear displacements are occurring. As the degrees of freedom of each block increase, joint normal closure and rotation occur, leading to an upward concave response. This is followed by an increase in the linearity of the response caused by the blocks rotating at a constant rate. These findings can be observed in natural slopes. Bovis and Evans (1996) suggest that at most sites where deformations have been monitored in the field, small shear movements are the initial mode of movement, followed by or accompanied by toppling and toppling-induced sliding movements. This work confirms that this mode of deformation is an important mechanism controlling slope behaviour.

The stress-strain response of the rock mass shows that in situations where translational shear is the dominant failure mechanism, catastrophic failure is common, whereas in closely jointed rock masses, deformation is slower and time-dependent. The stress concentration along a small number of discontinuities is much greater than if the stresses are distributed throughout the rock mass along many joint surfaces. The stress-strain response of rock masses failing through translational shear is characteristic of brittle behaviour, whereas rock masses with smaller block sizes produce a more ductile response. The stress-strain curves also show that slopes in rock masses with more closely spaced joints will generally undergo greater deformation before failure and for a given stress than slopes in rock masses with widely spaced discontinuities. This is reflected in the stress-strain curves produced from the numerical modelling exercise.

The production of stress-strain curves for the rock masses suggests that for limestone and sandstone rock masses, the magnitude of strain decreases as block size decreases, although this relationship is far from ideal. Comparison of axial strain curves at a range of scales confirms that block size has an effect on the

accumulation of strain in the rock slope. For the purpose of this discussion, reference is made only to the graphs produced for the simulations undertaken on 1 m rock masses (Figure 4.7). The same relationships hold true for 10, 100 and 1000 m rock masses.

The reduction of axial strain with decreasing block size shows that in natural slopes composed of smaller blocks, the shear strength is greater than for a slope composed of larger blocks. These results confirm early physical models. A large jointed slab of granite consisting of two blocks produced a maximum friction angle of 59°, while for an 18 block model the maximum friction angle was 69° (Bandis *et al.*, 1981). A similar physically-based shear test indicated that a slope composed of smaller assemblages of blocks had a greater shear strength than a model with larger blocks (Bandis *et al.*, 1981).

Comparison of joint shear magnitude and block rotations indicate that block size affects the failure mechanism of the rock mass (Figure 4.49). Generally, the largest shear displacements occur in models with the largest block sizes (Figure 4.49a). At the same time, block rotations decrease with increasing block size (Figure 4.49b). This indicates that failure mechanism is dependent on block size; shear failures dominate rock masses with larger blocks, whereas rotational/toppling failures dominate rock masses composed of smaller blocks.

Slopes with more closely spaced joints have a greater shear strength because there are more joint surfaces over which friction can act to resist movement. The mode of deformation inferred from the stress-strain response is that slopes composed of smaller blocks will exhibit more gradual deformation patterns than those with larger block sizes that fail catastrophically through brittle shear. Slopes composed of larger blocks have greater continuous joint surface areas over which shear failures can develop. The opposite condition exists for granite rock slopes at all scales, with axial strain increasing with decreasing block size. This is because the axial strain is dominated by joint normal closure. Shear movements leading to joint dilation have not occurred in the granite models, so more surfaces over which closure can occur produce greater axial strain where shear displacements are absent.

Previous geomorphological investigations have suggested that the stiffness of a rock mass can produce morphological differences in slope profiles. Allison *et al.* (1993) argued that concave slopes with vertical cliffs were characteristic of a stiffer

rock mass with few fractures, whereas concavo-convex slopes were found in more fractured rock masses that are more deformable and may exhibit time-dependent deformation. The results of this study suggests that block size and intact material strength have a direct influence on the deformational behaviour of the rock mass and ultimately slope form. The link between the theoretical models and behaviour / form of natural slopes is presented in Figure 4.50. Slopes composed of smaller blocks produce ductile deformation patterns, resulting in bulging of the slope toe and the development of a concave antiscarp zone.

The numerical modelling confirms that slopes composed of larger blocks can support more vertical cliffs. However, the concept of 'stiffness' as defined by Allison *et al.* (1993) is more complex than previously assumed. Although the shear strength of rock masses increases with decreasing block size, the stiffness generally increases with block size up to a relative block size of 0.3 m at all scales. The deformation of rock masses with closely spaced joints is, therefore, higher than in slopes containing widely spaced joints. Plotting joint normal closure against deformation modulus shows that the decrease in deformation with block size can be explained by joint normal closure (Figure 4.51). A greater number of joint surfaces allow a greater magnitude of closure and therefore deformation. Models with block sizes of 0.4 and 0.5 m do not fit this trend and show a decrease in deformation with block size. This is due to large-scale shear occurring in the model.

Intact rock strength has been cited as a controlling mechanism on slope form (Allison *et al.*, 1993). The present research shows that intact rock strength exerts an important control on the deformational properties of the rock mass. For a 1 m rock mass, sandstone has the lowest deformation modulus (therefore lowest stiffness) and granite the highest, across a range of block sizes (Figure 4.51). A similar relationship holds true at the 10 and 100 m scales, with sandstone having the lowest deformation moduli and granite the highest (Figures 4.511). The strength of the intact material also affects the joint stiffness with weaker intact materials forming weaker joint surfaces that cannot resist deformation as much as joints in stronger material. In natural slopes, the effect of the strength of intact material is to determine the general deformational response of the rock mass, with weaker materials experiencing more deformation for a given stress.

The granite rock masses exhibit less deformation than the sandstone or limestone rock masses at all block sizes and will be more likely to form stable cliffs of high

elevation (Figure 4.51). Slopes in sandstone rock masses undergo much more deformation before failure than the limestone or granite models at all scales. The implication of this for slope evolution is that slopes in weaker rock masses will experience gradual deformation before failure. This gradual failure is a ductile response to stress, and is influenced by block size and intact material. Slopes that deform in such a way produce characteristic geomorphological features, such as a concavo-convex profile, where slopes undergo toe bulging with anti-scarp formation further up the slope. In addition, increased deformation before failure will result in slopes that are neither as steep nor as high as slopes in more competent materials.

Allison *et al.* (1993) argued that failures in rock masses with smaller block sizes and weaker material will be larger. This work confirms this contention through the examination of strain zone development throughout the rock mass. The contoured total strain plots shows that deformation appears to be distributed throughout a rock mass with more blocks. Geomorphologically, this suggests that in natural slopes, large-scale deformations (indicated by the formation of antiscarps) are characteristic of well-jointed rock masses. The plots also show that if large-scale catastrophic failure were to occur in a closely jointed rock mass, the failure would be much more deeply seated than in a rock mass with widely spaced discontinuities. In addition to the size of the failures, the work suggests that block size can affect the type of failure, with toppling occurring where the rock masses is composed of smaller blocks and translational shear with larger blocks. This response is similar to the response found by Nichol *et al.* (2002), who simulated flexural ductile toppling using UDEC. However, they argued that toppling in slopes with bedding, as in the present simulations, was characterised by brittle, catastrophic failure.

The stress-strain curves presented here show that block toppling induced by reducing the size of the intact blocks is characterised by ductile deformations due to the progressive rotation of blocks. The behaviour of the rock mass becomes brittle once rotation has proceeded beyond a critical point as the centre of gravity of the blocks falls outside the base. Catastrophic, brittle behaviour occurs because once rotations exceed a critical value, the normal force acting on the base of the blocks decreases.

The development and timing of failures in natural slopes is dependent, therefore, on block size and intact material. Slopes with smaller blocks and weaker material undergo greater deformation for a given stress than slopes with larger blocks

composed of stronger material. However, they are less likely to fail catastrophically. Slopes with smaller blocks and weaker material will generally be less steep and exhibit concave-convex profiles, due to gradual deformations and the lack of clear failure surfaces. The deformation will also be more ductile and time-dependent than in slopes with large blocks of strong material that fail suddenly in a brittle manner. Failures are brittle in slopes that fail through translational shear because failure occurs suddenly as the shear strength of the joint surface is exceeded. Small shear displacements and block rotations that occur in closely jointed slopes produce more ductile deformations. The results suggest slopes which undergo greater deformation before failure produce less steep cliffs than those in brittle materials, which undergo sudden failure. As a slope evolves, brittle failures will enhance the profile, maintaining a vertical profile in rock masses which undergo little deformation before failure. Gradual deep-seated deformations will tend to produce a slope profile that is less steep and more concave in nature.

The results gained from this modelling have implications for the frequency and magnitude of failures in rock slopes. In slopes composed of smaller blocks resistance to stress deformation will be less than for slopes composed of larger block sizes. The frequency of movement, therefore, will be greater in slopes which tend to continuously deform and are composed of smaller blocks. However, the frequency of actual failure events is likely to be reduced because of the increased shear strength of these slopes in comparison with slopes with larger blocks. Continuous deformations without the development of failure surfaces will cause the slope angle to decline through time, reducing the possibility of brittle failure of the rock mass. Slopes composed of larger blocks resist deformation to a greater degree but most of the stress is concentrated along a few continuous shear surfaces. Once the stress concentration has exceeded the strength of the joint surface, then brittle failure occurs. However, the magnitude of deformation / failure is likely to be less than for slopes with smaller block sizes as the depth of deformation is less deep-seated. These concepts require detailed field investigations to determine how important these processes are in controlling the behaviour of natural slopes.

4.5.1 Effect of outcrop scale

The effects of outcrop scale are important for the geomorphological response of landforms to stress. The stiffness of the rock mass decreases with scale, so that the stress required to induce landform change is greater as the scale of the slope increases. The deformation moduli presented here are higher than those presented in the literature because they are computed for the whole rock mass, rather than for a particular slope or tunnel face. Therefore, the stress required to deform the whole rock mass is greater than the stress required to induce deformation of a slope face.

For sandstone rock masses, the deformation modulus increases with outcrop scale. The deformation for a 1 m rock mass is much less than for a 1000 m rock mass. With a relative block size of 0.05 m, the deformation modulus for sandstone at 1 m is 0.009 GPa and for a 1000 m rock mass 43.85 GPa, giving several orders of magnitude difference (Figure 4.52a). The equivalent deformation moduli for 10 and 100 m rock masses are 0.031 and 0.328 GPa, respectively. At the 1000 m scale, the stiffness of the slope decreases with an increase in block size (Figure 4.52a).

For a limestone rock mass a similar pattern of increasing stiffness with scale is observed between 1 and 100 m (Figure 4.52a). The deformation modulus for a 1 m limestone rock mass is several orders of magnitude lower than for a 1000 m rock mass for a relative deviatoric stress. All curves produce a similar pattern of deformation that increases up to a relative block size of 0.1 m and then decreases. For a 10 m rock mass the deformation modulus increases from 0.12 GPa with a relative block size of 0.05 m to 0.25 GPa at 0.1 m. The stiffness then gradually increases for all other block sizes to 0.36 GPa for a 0.5 m relative block size. For a 100 m rock mass the deformation pattern is slightly different, with stiffness increasing from 0.96 GPa for a 0.05 m relative block size to 5.15 GPa for 0.4 m (Figure 4.52a). Failure of the 0.5 m model at 100 m scale reduces the deformation modulus to 1.64 GPa. The deformation pattern at 1000 m is one of decreasing stiffness with increasing block size, indicating that deformation appears to be scale dependent. For a relative block size of 0.05 m the deformation modulus is 555.26 GPa decreasing to 8.99 GPa at 0.5 m (Figure 4.52a). This is thought to be due to strength reduction of the joint surface under shear. Fewer shear surfaces leads to reduced shear strength and a reduction in stiffness of the rock mass due to concentrated stresses on single joints.

The deformation moduli of granite rock masses at different scales show an increase in stiffness with increasing block size (Figure 4.52a). At 1 m scale the deformation modulus with 0.05 m relative block size is 9 GPa, increasing to 108 GPa for 0.5 m relative block size. At 1000 m scale the deformation modulus with a relative block size of 0.05 m is 1350 GPa, decreasing to 1125 GPa at 0.5 m relative block size. This is caused by the increased normal and shear stiffness of the joint surfaces that are able to resist deformation under the applied deviatoric stress.

Different lithologies exhibit different deformation characteristics at different scales. In limestone, rock masses at the 1 to 100 m scale show a general reduction in stiffness with increasing block size after an initial increase (Figure 4.52a). At the 1000 m scale there is a approximately linear decrease in stiffness with increase in block size (Figure 4.52a). This is related to the shear strength of fewer joint surfaces being exceeded under higher stresses. Sandstone rock masses show the same deformation pattern of decreasing stiffness with increasing block size at the 1000 m scale (Figure 4.52a). A similar pattern occurs in the granite rock masses, although this is not as pronounced (Figure 4.52). In natural slopes, this seems to suggest that the behaviour of 1000 m slopes differs from the 1 to 100 m scale slopes.

The deformation of rock masses at different scales is in part controlled by the magnitude of joint normal closure, which tends to increase with scale (Figure 4.52b). The deviatoric stress acting over the joint surface is greater in higher slopes because of the higher *in situ* stresses. The increase in deviatoric stress resisting shear failure, increasing the shear strength of larger rock masses. This is one reason why the stress-strain curves indicate stabilisation of the 1000 m rock masses.

The implications of these findings for the behaviour of natural slopes are important. The data suggest that larger-scale slopes are more resistant to deformation than smaller slopes, requiring greater stress to produce deformations or promote failure. It is likely that higher slopes in any given lithology will be steeper than in smaller slopes because of the increased deviatoric stress limiting the amount of deformation that can take place. Much previous research has been conducted into the frequency-magnitude relationships of slope failures, and it is not the aim of this discussion to produce a comprehensive review of this material. For further discussions, the reader is directed to the comprehensive review by Gardner (1980)

and the more recent review by Crozier and Glade (1999). The present research suggests that the frequency of failures in large rock-slopes will be less than for smaller slopes which exhibit less resistance to deformation. However, the magnitude of failures in large rock masses is greater than for failures in smaller slopes. This is one potential geotechnical explanation why failures in larger rock masses are often less frequent and of higher magnitude than smaller rock masses. Although other causal mechanisms such as pore-water variations and seismic activity can control the frequency-magnitude relationship of failures, this work is a first attempt to improve understanding of the processes controlling failures at different scales.

4.6 Conclusions

It is the combination of all the results presented in this theoretical modelling exercise, rather than any individual data set, that provides the most comprehensive explanation for variations in slope behaviour. The methodology applied here highlights the understanding of rock mass behaviour which can be gained from detailed and well-defined numerical models. This work examines for the first time the effects of block size and outcrop scale on the geomorphological behaviour of rock slopes.

Several key points regarding the behaviour of slopes have been raised from this modelling exercise. Each simulation has provided insights into the geomechanical behaviour of rock slopes and has provided discussion of the possible implications for natural slope development. Block size and intact material properties have been shown to control the pre-failure deformational properties of the rock masses and influence the actual failure mechanism. Outcrop scale has also shown to be an important control relating to the frequency-magnitude relationship of potential failures. Rather than provide a definitive explanation of scale effects in rock masses, the work has suggested that they intrinsically influence the performance of the rock slope and should not be ignored during geomorphological investigations of slope development. Future research is required to investigate the suggested relationships more fully.

Chapter 5: The Geomorphology and Geotechnical properties of the Picos de Europa field sites

Chapter 5: The Geomorphology and Geotechnical properties of the Picos de Europa field sites

5.1 Introduction

The Picos de Europa were chosen for investigation for a number of reasons. First, the evolution of slopes in high mountain areas is poorly understood in comparison with slopes at lower elevations because of their remote location. The Picos de Europa are much more accessible than other mountainous areas, making them ideal for study. Second, the mountains are formed in strong, brittle limestones, which are relatively well jointed. The area was glaciated during the last glaciation and this has produced oversteepened slopes where they have been truncated by glacial erosion. This contrasts with the field sites in Jordan, which are formed in weak, massively jointed sandstones that have never been glaciated (Chapter 6). The slopes in the Picos are interesting because high slopes (100 to 300 m) are maintained in relatively well jointed rock masses. The area also provides a contrasting environment for assessing the temporal evolution and recurrence interval of slope failures using cosmogenic dating.

No previous investigations have been undertaken to determine the mechanisms of slope failure, despite recognition that rockfall is an important geomorphological process in this mountain region (Marquínez and Adrados, 2000). Previous descriptions of rockfall have attributed the process to freeze-thaw, but it is clear that the size of some slope deposits indicates large-scale instability, rather than individual block detachment.

The Picos de Europa mountains of northern Spain rise abruptly from the coastal lowlands 60 km west of Santander and are characterised by a steep and rugged alpine karst terrain, producing a complex topographic setting (Mitoke, 1968) (Figure 5.1). The mountains are composed of a resistant block of mainly carbonate strata on the northern edge of the Cantabrian Mountain chain. The elevation of the Range has been enhanced by intensification of an ancient centre of uplift north of Riano during the Alpine orogeny (Smart, 1986). The regional drainage of the Picos developed to the north and was superimposed on the Paleozoic strata from a Mesozoic cover, which still outcrops on down-faulted blocks. The Range reaches a maximum elevation of 2648 m at the summit of Torre de Cerredo in the Western Massif.

Fluvial incision has generally kept pace with the rate of uplift, resulting in the formation of deep gorges such as the Cares Gorge in the Western Massif and the Deva Gorge in the Eastern Massif, which are over 1500 m deep (Plate 5.1). The fluvial incision has resulted in the dissection of the Picos range into three distinct massifs: Macizo Occidental (Western Massif), Macizo Central (Central Massif) and Macizo Oriental (Eastern Massif).

The climate is strongly influenced by the mountains' proximity to the Atlantic coast, with an average precipitation of 2100 mm a^{-1} (Walker, 1989). Under the Köppen system of climatic classification the region is assigned *Cfb* – a warm temperate climate with sufficient rainfall. Despite this, the Picos are dry, with little surface water above 500 m, because most water flows through fissures in the limestone bedrock. The most stable weather is in September; July and August are characterised by convectional storms. The steep relief of the Picos between the valleys and peaks gives rise to large thermal differences which often lead to temperature inversions in the valleys. Snowfall usually begins in late September and can persist until late June, although in recent years substantial snowfall has not occurred until late October. Permanent snowfields persist on north-facing slopes and in nivation hollows at altitudes as low as 1250 m. Above 2000 m there is a periglacial climate. Until recently, it was thought that no contemporary glaciers existed in the Picos, but a small area of ice has been found on the north slope of Torre de Cerredo, covered by rock-fall deposits (Clark, 1981; Suárez and Alonso, 1996). However, it is not considered a glacier because of the absence of stratified layers or flow features, such as crevasses (Alonso and González, 1998).

5.2 Geology

The three massifs consist almost entirely of Carboniferous limestones deposited between 290 and 345 million years ago. In the Western massif, 1200 m of carbonates were deposited with very few impermeable horizons. A similar thickness of carbonate sediment was also deposited in the Central and Eastern massifs. Generally, six units of Carboniferous limestones are recognised in the Picos de Europa, described from oldest to youngest (Figure 5.2). The descriptions are based on the work by Wagner *et al.* (1971).

Groitte Limestone. This basal unit is a thin, red nodular limestone deposited over a considerable period of time during the Variscan-Lower Namurian (Truyols *et al.*,

1980). It is not seen in the Western Massif but does outcrop in east-west bands along the Cares Gorge, near the base of thrust sheets. Due to its limited outcrop, the Groitte Limestone has little influence on the geomorphology of the Picos de Europa.

Barcaliente Formation. The formation overlies the Groitte limestone and is a dark, banded formation which occurs at the base of the thrust sheets where the Groitte limestone has been faulted in the Western Massif. The Barcaliente Fm averages 300-350 m in thickness and thins towards the east: it is composed of laminated, thinly bedded dark grey limestones and mudstones (Colmenero *et al.*, 2002). The depositional setting has been a matter of debate. Sánchez de la Torre *et al.* (1983) suggest a shallow water environment prone to evaporate deposition, while Reuther (1980) concluded that the formation represents turbidites characteristic of deeper water. Recently, breccia features within the limestone have been interpreted as displaying karst and subaerial exposure features (Wagner and Winkler Prins, 1999). Geomorphologically, the formation is important because it produces almost vertical slopes. Thrust sheet movements have produced a highly fractured limestone.

Valdeteja Formation. A grey massive limestone with occasional chert beds. The boundary between the Baracliente and Valdeteja is transitional. The limestone dominates the region around Ario and Jultayu (Truyols *et al.*, 1980). The Valdeteja Formation forms the largest slopes and outcrops only on the highest slopes. Local faulting due to mineralisation has fractured these limestones in places. These limestones were deposited on raised platforms (Kenter *et al.*, 2002). This platform developed a thickness of 1000 m on the northeastern part of the Ponga Nappe Unit (Bahamonde, *et al.*, 1997).

Lower Picos de Europa Formation. The lower Picos de Europa formation consists of thinly bedded, occasionally bioclastic limestones. Occasional chert beds 1-10 cm thick may also be found (Maas, 1974). It generally outcrops in the Verdeluenga-Punta Gregoriana region.

Upper Picos de Europa Formation. The formation consists of massive white or pink limestones, which are locally bioclastic. The Picos de Europa Formations comprise a 600-900 m thick carbonate unit representing a steep fronted carbonate shelf (Colmenero *et al.*, 2002; Maas, 1974). These form the very highest peaks but because they have a limited outcrop above 2100 m, they have little

geomorphological influence relative to the more fractured limestones, which they overlie.

Lebeña Formation. This unit outcrops at Canchorral de Hormas. The succession consists of conglomerates of limestones, shales and calcareous mudstones. In the area of study, the conglomerate unit is 150-200 m thick, and consists of dark pseudonodular carbonate mudstones with intercalations of boundstones. The member is interpreted as flood-dominated alluvial and shelf lobes entering a restricted carbonate ramp (Colmenero *et al.*, 2002). The unit also records the gradual back-stepping of the detrital lobes and the establishment of normal carbonate sedimentation towards the top of the sequence (Villa and Bahamonde, 2001).

During the Carboniferous the Picos de Europa occupied a position favourable for sediment deposition on a carbonate platform. While adjacent regions experienced unstable tectonic conditions, the Picos de Europa remained relatively stable allowing continuous carbonate deposition over 55 million years (Senior, 1987). The region was bounded to the west by the Ponga Nappe Province and to the south by the Pisuerga-Carrion Province.

At the beginning of the Carboniferous, uniform marine conditions persisted throughout the Cantabrian Zone resulting in the deposition of 10 to 40 m of red, nodular limestones, interbedded with chert and shales, representing the Genicera Formation (Farias, 1982). The onset of the Namurian saw the deposition of 350 m of black, unfossiliferous, laminated limestones of the Caliza de Montana, but in the Ponga Nappe and Pisuerga-Carrion Province sedimentation became increasingly dominated by terrigenous material. Above, more massive, fossiliferous limestones developed, giving a total thickness of 500 m to the Caliza de Montana unit (Maas, 1974). However, in the Picos de Europa Province, carbonate sedimentation continued, resulting in the deposition of 600 m of massive, fine-grained white limestones interbedded with bioclastic limestones containing crinoids, foraminifera and brachiopods (Wagner *et al.*, 1971). Intraformational breccias and slumps provide the only evidence of tectonic instability during this depositional phase. Tectonic movements were initiated by the north-west movement of the African Continental plate towards the Eur-American plate, which resulted in the formation of the Variscan orogenic belt. Most carbonate deposition occurred during two phases of carbonate platform development, sedimentation being controlled by tectono-

eustatic effects. Sea level highstands encouraged the growth and nucleation of the carbonate platforms, whereas sea level lowstands in combination with terrigenous infill of basins terminated platform growth (Bahamonde *et al.*, 1997; Bahamonde *et al.* 2000). The termination of carbonate platform sedimentation reflected the combined effects of sea level fall, subaerial exposure, erosion and a rapid transgression which polluted the platforms with shales and mudstones, which are exposed in the Lebeña valley.

The main period of deformation in the Cantabrian Zone occurred during the Asturian Phase of the Variscan orogeny some 295 Ma ago (Martinez-Garcia, 1981). This resulted in the emplacement of a series of thrust sheets from the north-west, west and south-west. The Cantabrian zone represents an easterly directed foreland thrust and fold belt and is located in the core of the arc described by the Variscan Orogeny. The Picos de Europa Province was the last to be affected by tectonic deformation given its marginal position in the north-eastern margin of the Cantabrian Zone: the main period of deformation was in the Kasimovian (Senior, 1987).

Within the Cantabrian zone, two main thrust systems can be recognised: an earlier one in the west and a later one developed underneath. The second thrust system affected the Picos de Europa (which are made of a large number of thin, imbricated thrust slices involving only massive Carboniferous sediments) and the Pisuerga-Carrion Province. Nappe emplacement was from the west and south to east and NE, then from north to south (Maas, 1974). Rotation and folding of older structural units explains why nappes in the southern area, which are the oldest, are much more deformed than the younger nappe units to the north. Despite the small degree of folding, tectonic shortening is very important in this region and is currently estimated at 70 km (Perez-Estúan *et al.*, 1988). Each thrust sheet was emplaced over the preceding sheet to the south, which greatly increased the total thickness of the carbonate sequence. It has been estimated that the limestones moved at least 20 km, because the Pisuerga-Carrion facies is so different from that of the Picos de Europa (Maas, 1974).

At the end of the Carboniferous, north–south compression resulted in the formation of a complex series of folds and thrust sheets. The incompetent Genicera Formation occasionally forms the basal unit of the thrusts, but frequently planes of dislocation tend to transgress bedding structures and are traceable in the Picos de Europa Formation above (Smart, 1984).

In addition to thrust plane movements, sub-vertical faulting also developed, notably in the Eastern Massif. A major trend can be observed between 106° and 120° with orthogonal minor fault systems (Smart, 1984). A typical example is provided by the San Carlos fault, where two phases of movement can be recognised, a horizontal and a vertical component. The San Carlos fault is complex, with minor faults splitting from the main discontinuity which had the effect of reactivating pre-existing high angle thrust planes. A dextral shear component has resulted in uplift on the western side of the San Carlos fault.

During the Permian, Mesozoic and early Tertiary, a sedimentary sequence was deposited over the Picos de Europa formation (Senior, 1987). The prior cover is inferred from the presence of Permian sediments in down-faulted regions such as at Sotres (Marquínez, 1978) and from the present drainage pattern, which was superimposed on the Carboniferous limestones from a now eroded post-Variscan cover. Concurrently, possibly during extensional tectonic phases, Hercynian fracture systems acted as conduits for circulating hydrothermal brines which resulted in zinc and lead mineralisation of the Picos de Europa Province (Gomez-Fernandez, 2000; Gasparrini *et al.*, 2003; Grandia *et al.*, 2003).

Post-Variscan deformation was extensional in character with fault-bounded basins controlling the nature of sedimentation. In the late Eocene and early Miocene, northern Spain experienced a further period of north-south compression related to the Pyrenean Orogeny (Boillot *et al.*, 1979). Compression ceased about 38 Ma ago and is thought to have initiated the uplift of the Picos de Europa (Vegas and Banda, 1982). The main effect of the Pyrenean Orogeny on the Carboniferous limestones was largely confined to the reactivation of Variscan and post-Variscan fractures. The specific geological settings of the two areas examined, the Andara region and Vega de Liordes, are shown in Figures 5.3 to 5.4.

5.3 Geomorphology

The geologic, tectonic and Quaternary history of the Picos and surrounding Cantabrian Mountains had a profound influence on the geomorphology, producing a distinct landform assemblage. The most important landscape components are depicted in Figure 5.5. The north-south direction of folding led to the dominance of vertical south-facing slopes, backed by more gentle northern slopes. Where the

limestones lie on impermeable shales and slates, springs rise to the surface. The general geomorphology of the area is alpine and periglacial above 1500 m. Above 1500 m, mass movement events are restricted to the failure of jointed rock slopes due to a lack of surficial sediments. Many of the mass movements are deep-seated, sometimes with a rotational plane, and have great geomorphological effects (Gutiérrez-Elorza *et al.*, 2002). Although no dates exist for failures in the Picos de Europa mountains, a number of dates for landslides are known in the Cantabrian mountains, ranging from over 120 ka to the present day (González-Diaz *et al.*, 1999).

Field observations indicate that three failure mechanisms operate on these slopes: sliding, toppling and wedging. Sliding occurs along the bedding planes, which have been vertically tilted by north-south folding of the strata. Wedge failures also occur by sliding along the intersection of two planar discontinuities. On north-facing slopes some relict rock glaciers can be seen, fed by rock fall from gully systems. A good example occurs in the Vega de Liordes, flowing off the north slope of Peña de la Regaliz (Plate 5.2). The feature is relict, given its vegetated surface and the occurrence of solifluction. Large numbers of ploughing blocks can also be observed above 1500 m, indicating a periglacial process environment. Rock slope debris below free-faces forms extensive talus slopes at all altitudes. The dominance of gullies in the Picos means that failed material is transported downslope by large debris flow systems with fans consisting of coarse debris (Plate 5.3). Occasionally systems are complex, with tongues of rock supplying the main channel from large boulder field systems (Plate 5.4). Although no data exist as to the timing of scree formation from failure events, some work has been conducted to the east in the Pyrenees (Garcia-Ruiz *et al.*, 2000). Such studies have shown two main periods of scree formation related to slope failure. The first occurred during 25-20 ka BP and the second with deglaciation 15-13 ka BP (Garcia-Ruiz *et al.* 2000). Many lower slopes are degraded; where they have been covered by glacial deposits, gully erosion and slumping processes dominate.

The Picos de Europa massif is dominated by two gorges, the Deva and Cares. They were formed by fluvial incision of the Rio Deva and Rio Cares, respectively. The rate of incision kept pace with the rate of uplift and pre-Carboniferous rocks are exposed in some portions of the gorges. Failure of slopes results in the delivery of large amounts of coarse debris directly into the fluvial system. However, the river channels are confined, so braiding is not well developed.

The geomorphology of the region is characterised by a cavernous alpine glacio-karst terrain, consisting of ice-modified closed depressions bounded by rock slopes known locally as hoyos. Surface karst forms are mainly restricted to Rillenkarren formed as raindrops penetrate the boundary fluid layer of the limestone, permitting surface mineral reactions and propagation of the form (Ford and Williams, 1989).

The present geomorphology of the area is dominated by the cumulative effects of the Quaternary glaciations. In the Picos de Europa the glacial processes are linked with karstic landforms (Gale and Hoare, 1997; Martín-Serrano, 1994). Glacial landforms dominate the geomorphology, although glacial deposits are rare, with the exception of the Enol and Ercina tills, which lie at 1300 m in the Western Massif (Gutiérrez-Elorza *et al.*, 2002). To the northern edge of the Picos de Europa range, ice flowed down to 650 m, whereas the glacial landforms are only present above 800 m on the south-facing slopes, indicating local cirque and valley glaciation, rather than the development of an ice-sheet.

The cave systems may contain detailed sedimentary records, which could be important in elucidating the glacial history of the Picos de Europa mountains. In addition, cosmogenic isotope studies of weathering limits may help elucidate the extent of the former ice cover in these mountains.

The general chronology of glaciation for the Late Quaternary is derived from regional studies from the Pyrenees and NE Spain. It is difficult to obtain chronological data from the Picos de Europa due to an almost total lack of glacial deposits. The established chronology for the last glacial cycle includes the development of a maximum glacial advance between 55 ka and 45 ka, followed by a deglaciation phase between 45 ka and 13 ka, with periglacial conditions between 11 ka and 10 ka (Sánchez and Arquer, 2001).

At least five glacial episodes are recognised in the Picos de Europa (Gale and Hoare, 1997). The most extensive glaciation is thought to be early Quaternary in age and has been argued to have been one of the earliest Cenozoic glaciations identified in Europe (Gale and Hoare, 1997). The Picos de Europa represented the most important area of glacial activity in Spain, outside the Pyrenees, during the Pleistocene. The Western Massif was a centre of ice movement which was independent of the Central and Eastern Massifs, as evidence suggests radial ice

movement in all directions. This suggests that the Cares Gorge, which separates the Western and Central Massifs, was already a major feature by the time of the onset of Quaternary glaciations. In general, most glaciers developed on north- and south-facing slopes (Crompton, 1964). An indirect effect of the glaciations was to provide sufficient meltwater to deepen the gorges. For instance, the floor of the Cares gorge, at its highest point, is only 400 m above sea level, whereas the highest point of its confining ridge exceeds 1500 m. Many of the major valleys in the Picos do not display the typical U-shape associated with glacial action. The typical profile is V-shape, suggesting that fluvial modification of the landscape subsequent to glaciation has been profound. The main effect of the glaciations above 1000 m has been the formation of glacial troughs and cirques, which have resulted in over-steepened rock slopes whose morphology has been preserved by the subsurface nature of fluvial activity.

In the Eastern Massif, the Andara region acted as a local centre of ice accumulation. Ice accumulated mainly in regions of depressed topography, eventually over-riding their margins and forming two valley glaciers in the Valdiezmo and La Llama valleys (Smart, 1984). Evidence of the Llama glaciers former extent is provided by a large terminal moraine complex, while a marginal moraine provides evidence of the Valdiezmo glacier. Outwash deposits provide evidence of recessional phases of ice movement during which ice remained only in the depressions. The pattern of ice movement appears to be radial and dominated by cirque glaciers. A similar pattern of ice accumulation occurred in the Central Massif, where depressions such as the Vega de Liordes acted as local centres of ice accumulation, which then supplied valley glaciers such as Fuente De via icefalls.

5.4 Field site descriptions

Fieldwork was undertaken at a number of locations within the Central and Eastern Massifs of the Picos de Europa. Six sites were studied across an altitudinal range from 2000 m to below 1000 m. These included high mountain and valley environments. Site selection was undertaken on geomorphological and geological grounds. First, the limestones represent a stratigraphic succession, so differences in jointing pattern associated with different geological conditions may help to explain spatial differences in rock slope evolution. Second, the intact strength of different limestones may vary within the succession, influencing slope behaviour. A description of each field location is provided below.

5.4.1 Torre de Salinas

This site was chosen because field evidence suggested that the slopes were unstable and it occurred in the upper part of the Valdeteja Formation. Glacial erosion has over-steepened the slopes and produced a number of different free-face orientations in the same rock mass. This allows an assessment of the importance of free-face orientation in controlling slope stability to be made.

Torre de Salinas represents the eastern end of a spur which forms the cirque in the Hoyo de Liordes, gaining height westwards from 2200 m to reach the high point of Torre del Hoyo de Liordes at 2474 m (GR 349000E, 477900N) (Plate 5.5). The spur joins the main north-west trending ridge that connects Torre del Hoyo de Liordes with Torre de Salinas and continues for approximately 1 km. At this site it was possible to sample the south and west faces. Field measurements determined the height of the rock slope to be 250 m from the base of the cirque to its crest. The east face has a strike of 70° and a base plane angle of 80°, while the south face strikes at 170° with a base plane angle of 75°. From the toe of the rock slope, the average slope angle in the Hoyo de Liordes is 21° on the eastern face and 33° on the southern face. Slopes leading off the free-faces were frequently punctuated by vertical cave shafts and nivation/solutional hollows, resulting in a very irregular topography. This type of surface topography dominates everywhere in the Picos where slopes in limestone bedrock fall below 40°.

5.4.2 Pico de la Padierna

This site was chosen because the slope represents a glacially truncated ridge which has been oversteepened. Slope failures are occurring in the centre of the ridge, but there is no evidence for active failures on the eastern and western flanks. The site provides the opportunity to examine spatial controls on slope stability within the same rock mass.

Pico de la Padierna is located in the Vega de Liordes, where an inlier of Mesozoic shales gives rise to numerous springs (GR 351000E, 477970N). Huge south-west walls rise 400 m above the floor of the depression from 1920 to 2320 m (Plate 5.6). A geomorphological survey of this site indicated that the lowest sections of the slope

were massively bedded. The joint survey was conducted along two 50 m transects, as the slope was too hazardous to allow a single scanline. However, the transects were located within 100 m of each other and considering the size of this slope, this was not considered to be a substantial source of error.

The sampled slope forms part of a north-west to south-east trending ridge, 6 km in length. Geological maps suggest that the line of this ridge follows a fault and it may represent an ancient fault scarp (Figure 5.4). The strike of the slope is 128° with a base plane angle of 78°. The toe of the free-face is bounded by a large talus slope falling towards the Vega de Liordes at an average angle of 45°. The site provided an ideal contrast to the western slope of Torre de Salinas. The northern slope is consistent with the north-south direction of folding and is relatively gentle at around 25°.

5.4.3 Tiro Pedabejo

This site was chosen because field evidence suggested that it was one of the few sites in the Picos de Europa where slope failures on the north face could be identified. Evidence for failure on the north face was in the form of rock-fall deposits.

Located on the southern side of the Vega de Liordes (GR 35000E, 477850N), this site provided the opportunity to investigate failure mechanisms on a north-facing slope (Plate 5.7). In addition, the western and eastern slopes could be included in the discontinuity survey, as they were easily accessible. The southern face of Tiro Pedabejo included a vertical wall, 150 m in height, but was inaccessible. Unlike previous sites in the Vega de Liordes, this is a peak in its own right and does not form part of a continuous ridge, despite maps of the region suggesting otherwise. The slope is terminated to the west by the Canal de Pedabejo and in the east by a grassy col leading to the summit of Peña la Regaliz. On the north-face, a partially vegetated talus slope forms the deposition area for failed material. The presence of a talus slope on north face is unusual: north faces are rarely steep enough or have sufficient bedrock exposure to produce conditions conducive to rockfall. The strike of the north slope is 080°, with a base plane angle of 50°, as defined in the field. The average angle of the scree slope leading off the north face to the Vega de Liordes is 30°. Evidence of numerous ploughing blocks could be seen on this slope.

The south slope had a strike of approximately 120° and an angle of 80°. The scree slope leading down from the south face had an average angle of 33°.

5.4.4 Canchorral de Hormas

This site was investigated because it represents a highly unstable mid-altitude slope, formed in conglomerates. The site lies at approximately 1500 m and forms the toe of a ridge which undulates between 1600 and 1700 m (GR 365000E, 478520N). It resembles a glacial cirque with oversteepened headwalls (Plate 5.8). The slopes of the cirque form a bounding edge reaching topographic highs at the summits of Pico del Accero and Pico de las Agudinas. The cirque floor is composed of a complex block field, with some boulders being over 10 m high. The rock slopes are the source of this debris. Some of the largest blocks contain discontinuities and it is clear they have not been broken by separation from the main rock face. The rock-fall deposits provide a source for a large debris flow system where three gullies coalesce to form a single channel, the headwaters of the Rio de la Sorda. The lithology is markedly different here from any of the other sites examined. The limestones appear to represent a conglomerate, containing many large (>50 mm) clasts.

The strike of the sampled slope was 163° with a base plane angle of 88° and free-face height of 100 m, while at the toe of the slope an angle of 22° is maintained until the boulder field is reached. The average angle of the boulder field slope is 30°.

5.4.5 Los Montes, Deva Gorge

This slope represents a buttress and pinnacle form (Plate 5.9). The base of the slope occurs at 200 m above sea level with the crest rising to 350 m (GR 370800E, 4789090N). The slope was very unstable. Continuous rockfall during the measurement period and retaining nets provide evidence of slope instability. Some remedial engineering had been carried out to grade the lower portions of this slope, which were closest to the road running through the Deva Gorge. The strike of the west face was 165° with an average angle of 60° over horizontal distance of 197 m. The south face had a strike of 70° and an average angle of 63° over 168 m. The north slope could not be investigated: access was impossible given the inherent instability of this slope.

5.4.6 Allende

The sampled rock slope is part of a discontinuous ridge which flanks the upper slopes on the western bank of the Rio Deva. The ridge has a cuesta type morphology, gentle northern slopes and steep southern slopes. The rock slope investigated forms a prominent rock buttress, 400 m above the village of Allende, rising 316 m from a basal altitude of 700 m to a high point of 1016 m (GR 370800E, 4787020N) (Plate 5.10). The south face is steep in its upper part, relaxes slightly in mid-slope and then steepens again in its lower portion to the rockfall deposition area. At the toe of the rock slope, the angle relaxes and the slope continues down to the Rio Deva at an average angle of 31°. The slope is separated from the main ridge via a gully forming the west wall and leading to a grassy col.

5.5 Geotechnical properties of the rock masses

The geotechnical properties of the rock slopes in the Picos de Europa were established from field and laboratory data. Discontinuity characteristics were measured in the field using scanline surveys. Intact rock strength data were obtained using detailed laboratory testing of samples recovered in the field. The geotechnical properties of the rock masses are required for input into the UDEC models to simulate the behaviour of the slopes.

5.6 Discontinuity characteristics

If the discontinuity patterns of the six sites in the Picos de Europa are considered, an indication of rock slope stability begins to emerge. By contouring poles on equal area stereographic projections, mean joint set characteristics can be identified (Hoek and Bray, 1981; Priest, 1985). Production of contoured plots is greatly enhanced by computer packages designed for the statistical treatment of discontinuity data, such as DIPS (Rocscience, 2002). Equal area projections were chosen in preference to equal angle plots so that a constant area on the projection represents a constant area on the surface of the sphere, regardless of location on the sphere. This method reduces visual bias in the interpretation of joint sets in different parts of the sphere. Contoured stereoplots from sites in the Picos de Europa are presented (Figures 5.6 to 5.11). Generally, there is little variability of joint set orientation because at each site pole clusters tend to be concentrated.

Some indication of the spatial variability of joint geometry within the study area can be gained by comparing the representative data for joint sets at each site, (Table 5.1). All sites show a minimum of two joint sets, while Torre de Salinas, Pico de la Padierna and Canchorral de Hormas show three sets, in addition to bedding. Values can be subdivided into six joint sets which occur in this region of the Picos de Europa.

Site	Bedding	Set 1	Set 2	Set 3	Set 4	Set 5	Set 6
Torre de Salinas	23/155	83/181	79/241	86/120			
Pico de la Padierna	19/123	71/218	78/257	79/107			
Tiro Pedabejo	41/341		66/263	64/164			
Canchorral de Hormas	07/102	76/199	81/258	77/158			
Algobras, Allende	73/321				76/84	62/239	
Los Montes	45/177				69/96		46/347

Table 5.1: Representative values for the bedding and joint sets for sites in the Central and Eastern Massifs of the Picos de Europa. Data are listed as pairs. The first value is the dip (degrees: 0° to 90°) and the second value is the dip direction (degrees: 0° to 360°).

A clear altitudinal link throughout the various limestone units can be identified. Torre de Salinas occurs at the greatest altitude at approximately 2250 - 2300 m to the toe of the rock face, while Los Montes has the lowest altitude at 200 m a.s.l. to the base of the slope. At the three highest sites, Torre de Salinas to Tiro Pedabejo, bedding is moderately dipping at angles between 19° and 41°, and joint sets '1', '2' and '3' can be identified, although set '1' is absent from Tiro Pedabejo. This may be due to a sampling bias, as the west face was inaccessible, and so was not recorded intersecting the north, south and east free-faces. It is reasonable to assume that joint set '1' was present at Tiro Pedabejo, although as the west face is marked by a col on the main ridge, it was not included because it would play little role in the stability of the other faces. Set '1' strikes approximately east to west and is almost vertical, with joints dipping towards the south. Set '2' strikes north-north-west to south-south east, dipping 65° towards the west. Set '3' strikes approximately north-east to south west with dip angles greater than 60°, and dip direction to the east, but swinging to the south at Canchorral de Hormas. Bedding at Canchorral de Hormas dips at an average angle of 07° and is the lowest bedding angle recorded. The bedding dip may be related to the proximity of the site to the San Carlos Fault, where horizontal thrust sheet movements occurred. The vertical and sub-vertical fracturing is represented by sets '2' and '3'. Canchorral de Hormas is a mid-altitude site at approximately 1500 m, and these movements may not be represented in sites at different altitudes. Sets '4' to '6' are found at the two lowest sites in the

Deva gorge; 600 m to the toe of the slope at Algobras, Allende and 200 m to the base of the rock slope at Los Montes. Set '4' strikes approximately north to south, is almost vertical and dipping towards the east. Set '5' occurs only at Algobras, Allende and strikes north-west to south-east with a dip angle of 62° towards the west. Set '6' strikes approximately east-west at a moderate 46° angle towards the north. It is this joint set that controls the broad morphometry of the site, with a relatively gentle north slope and steep, almost vertical, south face.

A computer program, Geocalculator v 4.5, was used to calculate the angle of intersection between the bedding and joint sets in three dimensions (Holcombe, 2003). Such analyses are useful when attempting to gain an insight into discontinuity genesis (Angelier, 1989, Bergerat *et al.*, 1991, 1992). The results are presented in Table 5.2. The data confirm that the joint sets identified in Table 5.1 have been correctly assigned. For example, the angle of intersection between the bedding and joint set '1' for the three sites listed varies between 63° and 77°. For the two sites located at lower altitudes the angle of intersection between the bedding and set '4' varies from 64° to 69°. The variation is low, considering the structural complexity of the region, indicating that the joint sets belong to the same statistical population. The angle of intersection between the bedding and the various joint sets is shown to be consistent throughout the two massifs. The angle of intersection between the bedding and set '1' is similar to those for sets '2', '3', '4' and '5'. The data suggest that the *relative* joint geometries and intersection angles at the sites are similar but because of intense folding and faulting, rotation and displacements of the joint geometry have occurred, producing spatial differences in the actual joint geometries measured at each site.

Site	1/Bed	2/Bed	3/Bed	4/Bed	5/Bed	6/Bed	1/2	1/3	2/3	4/5	4/6
Torre de Salinas	63°	78°	67°				59°	61°	61°		
Pico de la Padierna	74°	89°	61°				38°	74°	38°		
Tiro Pedabejo		64°	75°						87°		
Canchorral de Hormas	77°	87°	73°				58°	40°	82°		
Algobras, Allende				64°	75°					48°	
Los Montes				69°		89°					88°

Table 5.2: Angle of intersection between joint set planes and bedding in three dimensions.

The geometry of the discontinuities and the intersection of joint planes has a major effect on the failure mechanism operating on the rock slope. Stereographic projection can be used to undertake kinematic analysis of rock slopes. The analysis is kinematic because there is no reference to *in situ* stresses. For each of the slope free-faces, kinematic analysis was undertaken to determine the potential mode(s) of failure and provide an estimate of the probability of failure. The analysis requires the estimation of the joint friction angle to determine the probability of failure (Rocscience, 2002). Two joint friction angles were assumed, 30° and 40°, encompassing the range normally found on limestone joints (Goodman, 1989). The lowest probability estimate corresponds to the 30° friction angle, where there is a difference. The results of the kinematic analysis are presented in Table 5.3. The probability of a particular mode of failure is given by the relative number of poles within a particular joint set which fall within the defined region of failure as a percentage of the total number of poles in that joint set.

A number of failure mechanisms are possible at each site, ranging from toppling, through sliding to wedge failure. The failure mechanism is dependent on the angle of intersection between the joint geometries and the free-face of the slope. Bedding is important in controlling the failure mechanism operating at each site. For example, bedding is responsible for the occurrence of planar sliding at all sites except Algobras, Allende. The probability of planar sliding failure along bedding varies from 5-20% on the south facing slope of Los Montes to 60–100% on the south face of Torre de Salinas (Table 5.3). The probability of toppling shows a clear separation between the high altitude sites, and those located on the valley fringes. For sites Torre de Salinas to Canchorral de Hormas, the probability of toppling does not exceed 40% on any face, whereas for Algobras and Los Montes, the probability of toppling on west to north-west facing slopes is greater than 80%. Different joint sets can also be responsible for different failure modes, depending on the orientation of the free face. At Torre de Salinas, set '1' is responsible for toppling failure on the south-facing slope, but planar sliding on the east facing slope. The same joint set can also be responsible for initiating a combination of failures on the same face. At Algobras, set '4' is responsible for toppling and sliding, indicating that a sliding-toppling failure mechanism may be responsible for slope collapse at this site. The analysis is useful in identifying the possibility of wedge failures, since these are three-dimensional problems and cannot be simulated using numerical code for two-dimensional problems, such as UDEC. Wedge failures generally involve failure along three intersecting joint sets, although it is not present at all

sites. However, the analysis is limited in that statistical estimates of probability of failure cannot be made for wedge failure.

Site	Failure Mechanism	Facing slope	Probability of failure	Joint sets responsible
Torre de Salinas	Toppling	South	28 %	1
	Toppling	East	17 %	1
	Toppling	North	21 – 40 %	2
	Planar slide	South	60 – 100 %	bedding
	Planar slide	East	55 – 100 %	1
	Planar slide	North	< 5 %	bedding
Pico de la Padierna	Toppling	South	< 5 %	---
	Planar slide	South	25 – 28 %	bedding
	Wedge	South	n/a	1, 2, 3
Tiro Pedabejo	Toppling	North	< 5 %	---
	Toppling	South	< 5 %	bedding
	Planar slide	North	13 – 46 %	bedding
	Planar slide	South	< 5 %	bedding
	Wedge	North	n/a	2, 3
	Wedge	South	n/a	1, 2
Canchorral de Hormas	Toppling	East	40 %	2
	Planar slide	East	41 %	bedding
	Wedge	East	n/a	1, 2, 3
Allende	Toppling	North-west	95 %	4
	Toppling	South	< 5 %	4, 5
	Planar slide	North-west	< 5 %	4
	Planar slide	South	< 5 %	4
	Wedge	North-west	n/a	bedding, 4, 5
	Wedge	South	n/a	bedding, 5
Los Montes	Toppling	West	80 – 89 %	4
	Toppling	South	26 – 47 %	6
	Planar slide	West	< 5 %	bedding
	Planar slide	South	5 – 20 %	bedding

Table 5.3: Summary of kinematic analysis of failure mechanisms for sites in the Picos de Europa.

Theoretical modelling showed that the failure mechanism and deformational response of a rock mass is dependent on block size as determined by joint spacing (Chapter 4). In the field, tapes were laid perpendicular to joint sets identified in the field and the spacings between individual discontinuities were recorded. Bedding was treated separately because it was apparent that bedding spacing was much larger than joint spacing. The analysis was undertaken in two stages. First, spacing data were treated as a single sample for each site; and second, they were subdivided by joint set. The first analysis provides an estimate of the overall block size distribution at each site and the second an estimate of the spacing of each joint

set for input into the numerical model. Summary statistics for the first analysis are presented in Table 5.4.

Site	n	Mean (m)	s.d. (m)	Min (m)	Median (m)	Max (m)	Skew.	Kurt.
Torre de Salinas	145	0.76	0.86	0.07	0.34	3.18	1.51	3.86
Pico de la Padierna	220	0.53	0.49	0.05	0.38	2.88	2.56	9.72
Tiro Pedabejo	216	0.71	0.68	0.10	0.43	2.83	1.46	4.06
Canchorral de Hormas	216	0.59	0.50	0.10	0.42	2.97	2.76	11.15
Algobras, Allende	218	1.04	0.84	0.10	0.68	2.97	0.89	2.36
Los Montes	218	0.73	0.81	0.10	0.39	2.94	1.62	4.03

Table 5.4: Aggregated joint spacing statistics for sites in the Picos de Europa.

The probability distribution of joint spacing can provide insights into the nature of joint formation (Rives *et al*, 1992). A random spatial distribution is indicated by an exponential distribution. A random distribution along a scan line implies a Poisson frequency of discontinuities along that line (Bardsley *et al.*, 1990). Comparison of joint spacing data from the Picos de Europa shows that joint spacing cannot be considered random (Figure 5.12). The exponential distribution does not provide a good fit to the data. Other distributions that can be tested include the Weibull (Bardsley *et al.*, 1990), log-normal or gamma (Huang and Angelier, 1989). Weibull and gamma distributions are both generalizations of the exponential. Comparison of the quantiles and histogram frequencies of joint spacing with a Weibull distribution is presented in Figure 5.13. The data show a much closer fit to a Weibull distribution than for the exponential case, indicating joint spacing is not totally random. The gamma distribution did not provide a good fit. A log-normal distribution provides the best fit for joint spacing data from the Picos de Europa (Figure 5.14). The distribution is what would be expected from a natural statistical population where a large number of small spacings are observed in comparison with fewer larger spacings (Mohajerani, 1989).

Understanding the probability distributions of joint spacing is important in considering how realistically UDEC models joint spacing. Analysis has indicated

that joint spacing in the Picos de Europa is lognormal. However, UDEC models joint spacing as a uniform probability distribution, with a standard deviation from a mean value. UDEC is limited in that it cannot represent lognormal, Weibull or gamma distributions. However, modelling inherently involves simplification and given the data-limited nature of rock mass simulation, this is not thought to significantly influence model behaviour.

By plotting the ordered spacing values for each of the six sites on the same graph, the difference in spacing between sites can be seen (Figure 5.15). On the whole, Allende has larger values of joint spacing, with 50 % of values above 0.68 m. Torre de Salinas has the smallest joint spacing values, with 50 % of spacings below 0.34 m.

The analysis of distributions of data from many sites can be problematic using conventional statistical approaches. A relatively new technique in geomorphology to quantify data distributions is to use L-moments. They are an alternative system of describing the shapes of probability distributions (Hosking and Wallis, 1997). L-moments have become popular tools for solving various problems relating to parameter estimation and fitting distributions. They provide measures of location, dispersion, skewness and kurtosis. The 'L' stands for a linear combination of order statistics. This method has been shown to provide more reliable population estimates from small sample sizes because it reduces the influence that one outlier has on the selection of the population type and parameters. This can be a major advantage when analysing extreme events (Hosking, 1990).

The order statistics of a random sample of size n are the sample values arranged in ascending order: $X_{1:n}$, $X_{2:n}$,..., $X_{n:n}$. L-moments (Hosking, 1990) are certain linear combinations of the order statistics from small samples that can be used to summarize the sample and the distribution from which the sample was drawn. The first four L-moments are the following expected values of linear combinations (Hosking, 1990). Here E signifies the taking of exponentials (i.e. arrays) over a variable.

$$\lambda_1 = EX_{1:1}$$

$$\lambda_2 = \frac{1}{2}E(X_{2:2} - X_{1:2})$$

$$\lambda_3 = \frac{1}{3}E(X_{3:3} - 2X_{2:3} + X_{1:3})$$

$$\lambda_4 = \frac{1}{4}E(X_{4:4} - 3X_{3:4} + 3X_{2:4} - X_{1:4}) \qquad \textbf{Equation 5.1}$$

The first L-moment is just the mean, and the second is a measure of the dispersion of the distribution and is analogous to, but not equal to, the standard deviation.

When estimated from a sample of size n, L-moments are most conveniently calculated by first calculating the quantities

$$b_0 = n^{-1}\sum_{j=1}^{n} X_j$$

$$b_r = n^{-1}\sum_{j=r+1}^{n} \frac{(j-1)(j-2)...(j-r)}{(n-1)(n-2)...(n-r)}X_j. \qquad \textbf{Equation 5.2}$$

The sample L-moments are then calculated by

$$l_1 = b_0$$
$$l_2 = 2b_1 - b_0$$
$$l_3 = 6b_2 - 6b_1 + b_0$$
$$l_4 = 20b_3 - 30b_2 + 12b_2 - b_0, \qquad \textbf{Equation 5.3}$$

so that l_r is the sample estimate of λ_r. The L-moment versions of the coefficient of variation, skewness and kurtosis are estimated respectively by

$$t = l_2 / l_1$$
$$t_3 = l_3 / l_2$$
$$t_4 = l_4 / l_2. \qquad \textbf{Equation 5.4}$$

These last measures are dimensionless and thus independent of the units of measurement of the data. They have values ranging from -1 to +1 (Hosking, 1986).

Ordinarily, four L-moments are calculated, giving measures of location, dispersion, skewness and kurtosis. Because L-moments involve only linear combinations of the

data, and do not require raising the data values to higher powers, they are less sensitive than the conventional moments to the numerical values of the most extreme observations. This and other advantages of L-moments have been demonstrated by several authors (Hosking, 1990, 1992; Royston, 1992; Vogel and Fennessy, 1993).

The L-moments were calculated in Stata 8.2, by a computer program written by Cox (2003).

L-moments of joint spacing for sites in the Picos de Europa are presented in Figure 5.16. The first two L-moments show that Allende has the largest average joint spacing of all the sites in the Picos de Europa, while Los Montes in the Deva Gorge has the smallest (Figure 5.16a). This is surprising given that these sites are located much closer to each other than to any of the other sites. There is no apparent explanation for this, but it may be one reason why slopes here were unstable, even during field measurement. There is a cluster of sites towards the bottom left of the graph, indicating that the average joint spacing at these sites does not show major differences. These sites include Torre de Salinas, Pico de la Padierna, Tiro Pedabejo and Canchorral de Hormas. These sites range in altitude from 1800 m at Canchorral de Hormas to 2100 m at Torre de Salinas. Although not located in the same lithology, it is likely that tectonic stresses forming the discontinuity network would have been similar at these sites.

The t_3 and t_4, skewness and kurtosis statistics, respectively, are plotted in Figure 5.16b. Los Montes has the least skewed distribution, while Torre de Salinas has the most skewed joint distribution (Figure 5.16b). The data contrast to those presented in Table 5.4, which suggest that Canchorral de Hormas has the greatest skewness. This is caused by outliers in the data from Canchorral de Hormas; L-moments are not as severely affected by the presence of outliers as more traditional measures of distribution. Figure 5.16b clearly shows that Pico de la Padierna, Tiro Pedabejo, Canchorral de Hormas and Allende cluster together, having similar skewness and kurtosis.

There is no clear relationship between joint spacings and altitude of the sites. Joint spacing is largely determined by the intensity of stress concentration during tectonic deformations, and the data here do not suggest any clear pattern. Bedding spacing does not conform to a lognormal or exponential distribution (Figure 5.17). This is

important because the spacing of bedding structures in the rock mass is not random (Priest, 1993). This is mainly due to a strong bimodal distribution of bedding spacings, which may reflect inherent diagenetic properties of the limestones, related to sedimentation rates under fluctuating sea levels.

The UDEC modelling approach allows a number of different joint geometries to be created in a single model, with prescribed deviations, so statistical treatment of individual joint sets is of more practical value than the lumped data approach. The results of statistical analysis of joint data by set for each site are presented in Table 5.5. On average, Allende has the most widely spaced joints with both sets having a mean spacing above 0.6 m (Table 5.5). From the analysis Torre de Salinas has the most closely spaced joints at around 0.3 m (Table 5.5). Mean bedding spacing is similar between all sites at around 2.0 m, with Pico de la Padierna and Los Montes representing end members at 1.97 and 2.41 m respectively.

Site / joint set	n	Mean (m)	s.d. (m)	Min (m)	Median (m)	Max (m)	Skewness	Kurtosis
Torre de Salinas								
Bedding	20	2.13	0.35	1.52	2.21	2.75	-0.27	2.07
Set 1	47	0.42	0.27	0.11	0.29	1.01	0.97	2.64
Set 2	35	0.35	0.19	0.11	0.31	1.00	1.38	5.29
Set 3	19	0.31	0.27	0.08	0.18	0.85	1.01	2.25
Pico de la Padierna								
Bedding	12	1.97	0.34	1.43	1.88	2.51	0.02	1.99
Set 1	57	0.37	0.18	0.12	0.33	0.90	1.21	4.08
Set 2	12	0.36	0.13	0.10	0.37	0.54	-0.44	2.76
Set 3	14	0.36	0.17	0.11	0.36	0.75	0.52	3.50
Tiro Pedabejo								
Bedding	44	2.17	0.38	1.41	2.28	2.83	-0.40	2.06
Set 2	57	0.31	0.15	0.10	0.27	0.66	0.61	2.57
Set 3	50	0.42	0.22	0.10	0.37	1.17	1.21	4.55
Canchorral de Hormas								
Bedding	22	2.12	0.42	1.30	2.25	2.97	-0.21	2.25
Set 1	9	0.40	0.15	0.22	0.40	0.65	0.25	1.83
Set 2	75	0.42	0.21	0.10	0.38	1.07	1.00	3.58
Set 3	45	0.47	0.22	0.15	0.40	1.13	0.86	3.30
Algobras, Allende								
Bedding	58	1.91	0.88	0.14	2.28	2.97	-0.84	2.27
Set 4	30	0.61	0.66	0.10	0.41	3.19	2.64	9.95
Set 5	25	0.62	0.44	0.21	0.48	2.10	1.69	6.21
Los Montes								
Bedding	46	2.41	0.26	1.68	2.42	2.94	-0.31	3.04
Set 4	46	0.32	0.16	0.05	0.30	0.79	1.09	4.54
Set 6	18	0.45	0.23	0.15	0.39	0.98	1.12	3.49

Table 5.5: Joint set spacing statistics for each site investigated in the Picos de Europa.

5.7 Rock strength data

Information regarding rock strength data was obtained by Schmidt hammer testing of *in situ* material in the field and detailed laboratory testing. Schmidt hammer rebound data were converted into unconfined compressive strength (UCS) and Young's modulus (E) using the conversion in Deere (1966). For laboratory testing, rock samples were collected in the field and extracted from cliff free-faces and their orientation relative to the free-face noted. Samples for triaxial testing were cut in the same direction relative to the free-face as the samples were found in the field. This was to ensure that testing was not biased by rock anisotropy and the strength values represented material behaviour in the field. Representative samples were collected to ensure that the relative material properties for each site could be determined. Sites composed of the same geology were assigned the same material values.

Laboratory data for material properties were obtained using Hoek Cell and unconfined testing of rock cores with strain gauges attached, to monitor material deformation (Plate 5.11). The Grindosonic apparatus was used to provide comparative elastic measures to those gained from Hoek Cell and uniaxial testing. The confining pressures used for strain gauge monitoring of material deformation represent the approximate stresses present in the rock slopes found in the Picos de Europa. Approximations of the vertical stresses were made assuming a slope height of 500 m, material density of 2500 kg m^{-3} and gravitational acceleration of 9.81 m s^{-2}, giving an approximate vertical stress of 13 MPa. Due to the difficulty in calculating horizontal stresses in the rock masses, because of the complex topographic setting, it was decided to use confining pressures of 0, 10 and 15 MPa for deformation monitoring of material. A confining pressure of 30 MPa completed the failure envelope. In engineering situations, these are the maximum stresses likely to be experienced (Franklin and Dusseault, 1989). For each set of tests, Mohr's Circles were constructed and a failure envelope fitted to the data. Most failure envelopes are non-linear but there are difficulties associated with calculating representative material properties based on a parabolic failure envelope (Jaeger and Cook, 1979). An alternative method for presenting strength data is to plot the results in σ_1 - σ_3 stress space and fit a linear Mohr-Coulomb failure envelope to the data. For comparison, both plot types are presented (Figures 5.18 to 5.21). A summary of the geotechnical properties of the various limestone units found at each site in the Picos de Europa is presented in Table 5.6.

Torre de Salinas and Pico Padierna were assigned the same geotechnical properties since they are in the same limestone formation, as are the sites in the Deva Gorge and Allende. Density ranges from 2443 kg m^{-3} at Torre de Salinas and Pico de la Padierna to 2545 kg m^{-3} at Canchorral de Hormas. Primary porosity was determined by drying, weighing, saturating and then re-weighing samples cut for Grindosonic analysis. Values range from 0.22 % at Tiro Pedabejo to 0.61 % at Canchorral de Hormas and lie at the bottom of the limestone porosity scale (Goodman, 1980). Primary porosity of the limestones is low because thin section analysis showed that they were largely composed of well cemented, densely packed biomicrites that reduce porosity of the rock. In addition, the porosity may be lower than published values for similar limestones because porosity of the samples was determined through saturation at standard, rather than high pressure. The low primary porosity of the limestones explains why this region is so highly karstified by the development of secondary porosity in the form of cave and fissure networks (Ford and Williams, 1989). Errors in determining the porosity are not significant for numerical modelling, as these values are not used in the models.

The Unconfined Compressive Strength (UCS) of the limestones ranges from 165.31 MPa in the Olistrome and turbidites of the Lebeña Formation in the Deva Gorge and Allende to 39.16 MPa at Torre de Salinas and Pico de la Padierna in the massive, grey limestones of the Valdeteja Formation. This is surprising given that the popular name for these limestones is the 'mountain limestones', as they tend to form the highest peaks and the largest cliffs. The low strength values obtained from unconfined tests are probably due to the presence of micro-fractures in the rock, leading to rapid crack propagation. During testing, it was observed that spallation of the rock occurred at the end of the core in response to the applied stress, and that failure then propagated through the core. The location of the failure planes often coincided with veins in the rock, particularly with the samples from Tiro Pedabejo. Compared with the UCS calculated from Schmidt hammer rebound data, it is clear that these strength data are probably too low (Table 5.7), even though they are in the expected range of 30-250 MPa for limestones given by Attewell and Farmer (1979). The UCS estimated from the field is thought to be more representative because many more measurements were taken and the material remained *in situ*.

Location	Rock type	Density (kg m^{-3})	Porosity (%)	Unconfined Compressive Strength (MPa)	Yield stress (15 MPa)	Estimated tensile strength (MPa)	Static Poisson's Ratio ν	Static Young's modulus E (Gpa)	Static Bulk modulus k (GPa)	Static shear modulus G (GPa)	Dynamic Young's modulus E (GPa)	Dynamic Bulk modulus k_d (GPa)	Dynamic Shear modulus G_d (GPa)	Dynamic Poisson's Ratio ν_d	Estimated Young's modulus, E_e from R (Gpa)	UCS estimated from R value (MPa)
Torre de Salinas	Massive Grey limestone of the Valdeteja Fm.	2443	0.36	39.16	217.58	7.04	0.095	98.41	40.49	41.34	63.88	35.48	26.61	0.20	48.98	126.32
Pico de la Padierna	Massive Grey limestone of the Valdeteja Fm.	2443	0.36	36.16	217.58	7.04	0.095	98.41	40.49	43.34	63.88	35.48	26.61	0.20	52.92	143.34
Tiro Pedabejo	Thinly bedded limestone of the Barcaliante Fm.	2534	0.22	43.51	156.65	4.78	0.024	31.67	11.10	15.11	70.53	45.21	27.55	0.27	56.13	159.91
Canchorral de Hormas	San Carlos conglomerate of the Picos de Europa Fm.	2545	0.61	43.51	169.71	9.41	0.015	40.50	15.00	18.41	61.49	39.42	24.79	0.24	55.87	156.73
Deva Gorge, Los Montes	Olistrome / turbidites of the Lebeña Fm.	2521	0.29	165.31	234.98	50.72	0.037	100.73	40.43	46.19	--------	--------	--------	------	59.01	180.96
Allende	Olistrome / turbidites of the Lebeña Fm.	2521	0.29	165.31	234.98	50.72	0.037	100.73	40.43	46.19	---------	---------	---------	------	50.76	127.86

Table 5.6: Summary geotechnical properties of the various limestone units found at each site in the Picos de Europa.

It has been shown that sampling disturbance can affect laboratory derived mechanical properties of brittle materials under uniaxial compression, resulting in a 36 % reduction in UCS (Eberhardt *et al.*, 1999). In the current situation, disturbance results from mechanical abrasion and vibration during the core drilling process and stress concentrations which develop at the drill bit–rock contact (Guessous *et al.*, 1984; Rathore *et al.*, 1989; Martin and Stimpson, 1994). Combined with the presence of veins in the rock the net effect is to produce planes of weakness in the core through which cracks may propagate leading to premature failure. Although careful inspection of the unconfined cores was undertaken, before selection for UCS testing, it is likely that micro-cracks have greatly reduced the unconfined strength. The net effect of this is to over-estimate friction angles and under-estimate the tensile strength of the limestones. Ideally, at least five unconfined tests should be conducted and the UCS be taken as the average of these five results. However, this was not possible for the present study given the number of samples. To reduce the error, Mohr's Circles and stress space data were re-plotted using the UCS data estimated in the field using Schmidt hammer data for Canchorral de Hormas, Torre de Salinas, and Pico de la Padierna. The strength data for Tiro Pedabejo were considered inaccurate because of the orientation of cracks in the core reducing the compressive strength of the material and were not converted.

Yield strength at 15 MPa confining pressure ranged from 156.65 MPa for Tiro Pedabejo (cracked core) to 234.98 MPa at Los Montes and Allende, and represents the maximum strength under the confining pressures expected near the surface.

The deformation moduli, Young's Modulus, Poisson's ratio, bulk modulus and shear modulus are important measures which describe deformational response to stress (Chapter 2). Data were obtained from static testing under uniaxial compression and from dynamic testing by sonic wave propagation using the Grindosonic apparatus. Data are computed from the stress-strain curves (Figures 5.22 to 5.25). For all stress-strain diagrams, the green curve corresponds to lateral strain, red to axial strain and black to volumetric strain. Although the Unconfined Compressive Strength is not regarded as accurate, the elastic moduli are, because these data are computed from the initial elastic range of material behaviour before crack propagation occurs. Poisson's ratio, ν, shows that all material in uniaxial compression is behaving in a brittle manner. Values range from 0.015 for Canchorral de Hormas to 0.095 for Torre de Salinas. For an ideal, elastic material, ν should be 0.25; brittle behaviour is indicated by values below this. For these

limestones, once compressed, very little strain is recoverable. Static Young's Modulus varies from 31.67 GPa to Tiro Pedabejo to 100.73 GPa for Los Montes and Allende. Static bulk moduli vary from 11.10 GPa at Tiro Pedabejo to 40.49 GPa at Torre de Salinas and Pico de la Padierna. Dynamic moduli are considerably different from static values. Dynamic Poisson's ratios range from 0.2 at Torre de Salinas to 0.27 at Tiro Pedabejo, indicating almost ideal elastic behaviour. Dynamic bulk moduli vary from 35.48 GPa at Torre de Salinas to 45.21 GPa for samples from Tiro Pedabejo, while shear moduli range from 24.79 GPa at Canchorral de Hormas to 27.55 GPa at Tiro Pedabejo. Dynamic Young's Modulus ranges from 61.49 GPa at Canchorral de Hormas to 70.53 GPa at Tiro Pedabejo.

An issue arises about how representative elastic moduli obtained from static and dynamic tests are. Allison (1989) argued that the dynamic moduli were a good indicator of the elastic properties of rocks because they are related to rock hardness and strength. However, the data here suggest that dynamically determined elastic constants underestimate bulk, shear and Young's modulus, while overestimating Poisson's ratio. A possible reason for this is that dynamic moduli do not account for crack and pore space closure in compression (Cook *et al.*, 1984; Korinets and Alehossein, 2002). The amplitude of the stress wave transmitted through the material during dynamic testing is insufficient to cause even partial closure of cracks or pore spaces. Also, the rate of strain application in a dynamic test, caused by excitation of the sample, is much more rapid than plate loading tests, such as uniaxial or triaxial testing rigs. Thus, the predicted deformations are likely to be less using dynamic tests as they do not account for non-recoverable deformation caused by pore and crack closure. This is reflected in the higher values of Poisson's ratio, which indicate that virtually all the strain is recoverable. It was decided to use static values of bulk and shear modulus for direct entry into UDEC, as these represent more realistic values than the dynamic tests.

5.7.1 Effect of confining pressure on material behaviour

The principal effect of low confining pressures is to increase the compressive strength of the rock. Understanding global rock mass behaviour requires simple treatment of the effect of confining pressures on material behaviour, particularly for material in the centre of the rock mass, which is partly responsible for governing the magnitude of slope deformations. To investigate the effect of confining pressure, material deformation was measured by attaching strain gauges to samples before

placing them in the Hoek Cell. Gauge failures due to confining pressure and snapping of lead wires were frequent and not all samples could be monitored at all confining pressures. Data for percentage axial strain during compression are presented in Table 5.7.

Site	0 MPa	10 MPa	15 MPa
Torre de Salinas	0.0532	0.027	
Pico de la Padierna	0.0532	0.027	
Tiro Pedabejo	0.0297	0.494	0.2037*
Canchorral de Hormas	0.0992	0.2483	0.2516
Deva Gorge, Los Montes	0.2183	0.2989	0.4438
Allende	0.2183	0.2989	0.4438

Table 5.7: Percentage axial strain of limestone samples at differing confining pressures. Data for Torre de Salinas and Pico de la Padierna are unavailable due to gauge failure under 15 MPa confining pressure. *The core was cracked during sample preparation along the natural failure plane of the specimen, resulting in a strain reduction.

Although the data are not perfect due to micro-cracking and cracking in the samples, it appears that the amount of axial deformation a sample can undergo before failure increases with confining pressure. For example, the Olistrome / turbidite limestones of the Deva Gorge and Allende undergo 0.2183 % axial compression before failure under unconfined conditions. At 10 MPa, the sample has undergone 0.2989 % compression before failure, and at 15 MPa, 0.4438 % axial compression occurs before failure. As confining pressure increases, the ability of the material to undergo strain increases before brittle fracture occurs. Axial strain curves indicate the full range of material behaviour until failure (Figures 5.26 and 5.27). Axial data show some interesting features. Samples from the Deva Gorge tested at 0 and 10 MPa confining pressures show virtually identical behaviour in compression up to approximately 130 MPa axial stress. After this, the specimen tested at 10 MPa shows less strain for a given stress than the unconfined sample. Testing at 15 MPa produces a surprising result, in that the strains produced are larger for a given stress than samples tested at 0 and 10 MPa. This is probably due to the presence of a micro-crack or void space on the axis of the strain gauge, even though the surface pre-treatments used should prevent this to some degree. Samples from Canchorral de Hormas show a clear relationship between the magnitude of strain and confining

pressure. Unconfined samples undergo more strain for a given stress than samples tested at 10 and 15 MPa. The discrepancy between maximum strain at 10 MPa confining pressure is probably due to crack initiation after an axial stress of 126 MPa, indicated by the small upward kink in the curve. The increase in axial strain after this is probably caused by crack extension until failure at 152 MPa. If the strain in Table 5.8 at 10 MPa is adjusted to account for this, the behaviour of the limestone is less anomalous. The strain behaviour of samples from Tiro Pedabejo is not considered realistic because of the cracking caused by core preparation. This is shown by large deviations in the axial strain curves.

Volumetric strain curves show clear hysteresis associated with specimen dilation in response to micro-crack formation as the rock is stressed. For some samples, dilation was not apparent from the volumetric strain curve, as indicated by an absence of the curve from all stress-strain plots. The volumetric strain curves show the importance of fracturing when considering the geomorphological behaviour of brittle earth materials, such as rocks. Planes of weakness develop in all samples well before the yield point of the material, and in a rock mass that would lead to stress redistributions, promoting the failure of intact material in regions of elevated stress. Many previous geomorphological studies have used peak strength estimates of rocks, such as the unconfined compressive strength, to explain geomorphological differences (for example, Allison *et al.*, 1993). This work suggests that the pre-peak strength behaviour of the material is important in understanding the stress-strain response to earth materials.

Confined materials in the centre of rock mass are able to undergo more deformation before failure than materials exposed at the free-face, due to an increase in confining pressure. Material behaviour is important in understanding the time-dependent deformational behaviour of rock masses. An issue arises whether material becomes ductile at these pressures. Ductile behaviour can lead to continued deformation without loss of strength. The limestones for the Picos de Europa do not behave in a ductile manner (Figure 5.28). Brittle behaviour is exemplified by comparison with Table 5.7, showing total strain for different confining pressures. Donath *et al.* (1971) regard material behaviour as very brittle if the total strain before failure is less than 1 %, brittle between 1 and 3 %, transitional at 3–5 % and ductile where axial strain is greater than 5 % before failure. Comparison of Figure 5.26 with Figure 5.28, showing an idealised deformation curve, confirms that the limestone is deforming in a brittle way. At confining pressures experienced in

normal engineering situations (0 to 15 MPa), the limestones behave in a brittle manner for the sites investigated in the Picos de Europa.

5.8 Conclusions

A number of important points can be made regarding the discontinuity geometry and the stress-strain behaviour of intact material from the Picos de Europa.

1. Kinematic analysis shows a range of failure mechanisms are possible at each site; from sliding, toppling to wedge failure. Bedding is important because it produces shear surfaces over which sliding can occur.
2. Depending on the orientation of the free face, the same joint set can produce different failure mechanisms.
3. Joint spacing is lognormal, indicating a random Poisson distribution, whereas bedding spacing is non-random and probably reflects the diagenetic properties of the limestones. This has implications for joint spacing representation in UDEC.
4. Application of L-moments to joint spacing clearly shows that certain sites group together. The technique improves on previous engineering approaches by introducing a spatial element to joint spacing analysis by allowing comparison of joint statistics from widely distributed sites.
5. The limestones of the Picos de Europa behave in a brittle manner, in uniaxial and triaxial compression at the range of pressures expected at the earth's surface. The limestones in the centre of the rock mass are able to undergo more strain before failure than materials close to the free-face.
6. Volumetric strain curves suggest that the pre-peak behaviour of rock is important in understanding landform behaviour.

The rock strength data collected here can be directly entered into UDEC to simulate the global behaviour of rock masses. Understanding material behaviour in compression and confinement is important, as UDEC calculates the strain of deformable blocks during cycling.

Chapter 6: The Geomorphology and Geotechnical properties of the Al-Quwayra-Wadi Rum field sites

Chapter 6: The Geomorphology and Geotechnical properties of the Al-Quwayra Wadi Rum field sites

6.1 Introduction

The Wadi Rum field sites were chosen for a number of reasons. First, the area is an excellent example of structural control on landscape development; joints and normal faulting are the result of plate motions along the Red Sea and Dead Sea. This affects the scale of the inselbergs, which increase in size towards the south, so that it is possible to assess the effects of slope scale on the deformation and failure mechanisms of the sandstone inselbergs. Jointing is relatively constant across the area because the sandstones have not been affected by folding. Second, the characteristics of the inselbergs provide a contrasting environment to the slopes found in the Picos de Europa. Whereas the Picos are located in a recently glaciated Alpine environment, with slopes formed in strong, brittle limestone, the Wadi Rum sites are located in an arid environment, with isolated rock masses formed in weak sandstones. This provides an ideal contrasting geomorphic and geological environment for assessing the return interval of slope failures using cosmogenic dating.

Jordan can be divided into seven physiographic provinces, of which the most important for this study is the Southern Mountainous Desert (Bender, 1975). The Southern Mountainous Desert occupies the area south of the west-northwest trending Ra's an Naqb escarpment and extends into Saudi Arabia. Between Al 'Aqabah and Al Quwayra, where igneous rocks of the Precambrian basement outcrop, the terrain is rugged and steep mountains rise to 1550 m. Further east, Palaeozoic and Mesozoic sandstones overlie the Precambrian basement. The sandstones form inselbergs throughout this area. Drainage in the western part of this area is towards the south, into the Gulf of Aqaba, and is presently cutting headward. In the eastern part, drainage is towards the southeast.

Wadi Rum is located in south-western Jordan, to the north of the Gulf of Aqaba and to the east of Wadi Araba, part of the Jordan Rift Valley (Figure 6.1). The area is composed of sandstones which begin to outcrop near Al-Quwayra and continue south into Saudi Arabia. The region covers an area of approximately 3500 square kilometres. Wadi Rum was given protected area status in 1998, under the

supervision of the Royal Society for the Conservation of Nature (RSCN), with the aim of promoting ecologically sustainable tourism with local community development. The area immediately east of Al-Quwayra to the head of Wadi Rum is not protected and irrigation-fed crops are cultivated, with varying degrees of success. As salinisation becomes more prolific, farms are relocating further towards the Wadi Rum area.

The most important geomorphic features in this area are the cliffed sandstone inselbergs, which rise over 800 m above the playas and sandflats of the surrounding desert. The inselbergs reach an altitude of 1754 m above sea level and are separated by large wadis, such as Jebel Rum, which is over 15 km long and 1 km wide. The spatial extent of the sandstone outcrops vary, so in the area around Al-Quwayra the landscape is relatively open and dominated by desert and isolated outcrops, whereas towards Jebel Rum the size of the outcrops increases so that the portion of desert floor relative to the inselbergs decreases. A geomorphological gradient exists whereby the spatial scale (areal extent and height) of the outcrops increases from Al-Quwayra towards Jebel Rum, continuing into Saudi Arabia. This is related to down-faulting to the south and east of Al Quwayra (Heimbach and Meiser, 1971).

The inselbergs display a variety of weathering forms ranging from case hardening, tafoni and large numbers of discrete rockfalls (Plates 6.1 to 6.2). Natural rock bridges are also a major morphological feature of the landscape in Wadi Rum (Plate 6.3). The inselbergs are fronted by ramps that rise above the desert floor, which is characterised by large playas, wadi beds and aeolian sand. The bedrock surface beneath this cover is irregular and in places may lie 200 m below the surface (Osborne, 1985). The central portion of the region is dominated by the Qa Disa and Qa Um Salab playas.

Climatically, the area can be classified as arid to hyperarid, with an annual rainfall less than 65 mm, with most rainfall occurring between December and April at Al-Quwayra (Rabba, 1991). Maximum monthly temperatures range from 32°C in July to 6°C in January and daily maximum temperatures in summer readily exceed 38°C. The mean annual humidity is around 40 %, with a prevailing wind direction of north-northeast (Rabba, 1991). Although the climate is classified as arid to hyper-arid, this has not always been the case, and there is much unresolved controversy and contradiction regarding the climatic history of the region. Several researchers

maintain that the area was cold and wet during the Last Glacial Maximum (LGM), and warm and dry during interglacial periods (Horowitz, 1979, 1992; Bowman, 1990; Neev and Emery, 1995). Others argue that cold glacial periods in Europe correspond with a cold dry climate in Jordan, while interglacial periods are characteristically warm and wet (Huckriede and Wiesemann, 1968). Recent work suggests that before the LGM (30-22 kyr), the climate was much wetter and can be classed as a Pleistocene Pluvial environment (Abed and Yaghan, 2000), while during the LGM a cold, dry climate was prevalent. However, most of the work has been restricted to the Jordan Valley and much opportunity for research exists within the Wadi Rum-Al-Quwayra region. Detailed isotopic, microfossil and dating studies of the playas may hold the key to resolving the climatic history of the area.

6.2 Solid geology of Wadi Rum and Al-Quwayra

The geological successions in Jordan have been influenced by three factors: the Tethys Sea transgressions; the Wadi al 'Arabah-Jordan geosuture, which separates the Palestine block from the Trans-Jordan block on the east; and the Nubian-Arabian shield in the southeast and south, which is where Wadi Rum is located.

The broad geological setting of the Wadi Rum–Al-Quwayra area is shown in Figure 6.2. A generalised vertical stratigraphy is presented in Figure 6.3. To the west of the Al-Quwayra fault, Late Proterozoic igneous rocks outcrop, and these form the bulk of the mountains bordering the Arava Valley. These rocks comprise plutonic granitoids, extrusive rhyolites and dykes of the Aqaba Complex, which were intruded in the form of basal/dolerite and microgranite 620 Ma ago (Ibrahim and McCourt, 1995). The deposition represents a significant period of crustal extension. The dykes can be traced across the whole area, but mainly outcrop in the eastern, northeastern and southeastern areas, where they are unconformably overlain by Early Palaeozoic sandstones. The plutonic granitoids form part of the Precambrian basement and are termed the Aqaba and Arabia complexes (Abedlhamid, 1990). The Wadi Rum–Al-Quwayra region represents a shield area of volcano-sedimentary sequences which have undergone deformation and metamorphism, and were later intruded by post-orogenic granitoids, with probable ages of 630-580 Ma (Brook *et al.*, 1988).

The Aqaba complex developed a peneplained surface, over which a sequence of continental sandstones were unconformably deposited, which relates to the Ram

sandstone group. A mature erosional peneplain formed during the erosional phases of the Precambrian, with sedimentation being controlled by isostatic uplift of the Nubian-Arabian Shield. The shield provided the source area for large amounts of fluvial material which were deposited in braided rivers under a humid climate in a gently subsiding foreland basin during the Cambrian and possibly the early Ordovician (Selley, 1972; Powell, 1988). The Ram sandstones belong to the Nubian sandstone series, which dip gently towards the east, with a total thickness of around 900 m (Abdelhamid, 1990). To the northeast, the area is bounded by the 200-350 m high Ras en Naqb escarpment, which is formed from Cretaceous limestones, sandstones, shales and marls. To the east, the area is underlain by Ordovician sandstones of the Khreim Group and Umm Sahm Formation, which gives rise to a change in topography. This marks a change in sedimentation that took place as a result of marine incursions into the area which transgressed from the northeast, resulting in sedimentation in an epeiric shelf sea environment throughout the Ordovician and Silurian (Powell, 1989).

The Ram Group of sandstones are the most important because these outcrop at the surface in the Wadi Rum-Al-Quwayra region. Geomorphologically, they are important because all the inselbergs are formed in the Ram Sandstones. The properties of these sandstones produces different inselberg forms. The group comprises, in an upward sequence, the Salib Arkosic Sandstone, the Burj Dolomite-shale, the Umm Ishrin Sandstone, the Disi sandstone and the Umm Sahm sandstone. The two most important sandstones are the Umm Ishrin and Disi Sandstones: most of the inselbergs are formed within these, although the Umm Sahm sandstone does outcrop on the summits of the larger inselbergs towards the south of the region.

The Ishrin sandstone Formation was deposited on a braidplain and tidal flat in response to periodic shifting of the active braidplain system. Re-working of the abandoned parts of the braidplain by tidal currents and subsidence led to repeated phases of marine incursions and the development of tidal flats during deposition of the sandstone (Makhlouf and Abed, 1991). The Umm Ishrin sandstone has a massive morphology and is densely jointed, with a major joint set trending NNW-SSE, and minor joints trending NNE-SSW (Rabba, 1991). It attains a maximum thickness of 320 m in the vicinity of Al-Quwayra (Powell, 1988). The sandstone can be distinguished from other rocks by its dark brown colour and massive bedding. Lithologically, the formation consists of red-brown, coarse grained sandstone, with

variable amounts of pebbles. The major (>95 %) constituent of the rock is sand with subordinate siltstones, so that the rock can be classified as a quartz-arenite. Cross-bedding is common, indicating deposition in a braided river. Measurement of cross-bedded features indicates deposition under a unimodal NNW-NNE palaeocurrent (Powell, 1989). Locally, the sandstone contains black ferruginous layers, which may represent palaeosol horizons. They are recognisable because they tend to be resistant to erosion and outcrop as benches on the inselbergs.

The Disi formation mainly outcrops to the east of the Quwayra Fault where it forms a landscape of large domes due to its weathering features. The Disi formation consists of whitish grey to pale white sandstone with scattered quartz granules and pebbles (Rabba, 1991). Large-scale planar and trough cross-bedding is a common feature, with siltstone clasts present in the base of scoured channels (Abdelhamid, 1990). The morphology of the cross-bedded structures is indicative of deposition within a N-NW flowing braided river. The sandstone varies in thickness from 300-350 m in the Jabal Umm Ishrin area to 265 m in the Quwayra area. *Cruziana* trace fossils indicate a Middle Cambrian to Early Ordovician age (Rabba, 1991).

Three periods of deposition can be recognised within the Disi sandstone unit (Rabba, 1991). In the lower sections (0-100 m), the sandstones are coarse-grained with abundant quartz pebbles and large-scale trough cross-bedding indicative of a high-energy fluvial regime. In the middle part of the formation, a lower energy environment is recorded by the change in grain size from coarse to medium. In the upper part of the formation quartz pebbles indicate a return to a higher-energy fluvial regime.

As the height of the inselbergs increases towards the south, the Umm Sahm Sandstone formation outcrops on the summits of the highest peaks, where incisive erosion has produced peaks with a distinctive pyramidal appearance (Abdelhamid, 1990). On these summits, only the lower 50-100 m of the formation is exposed, even though the total thickness of the unit has been estimated at 220-250 m, based on geological investigations in the Qa Disi–Sahl As Suwwan area, located to the east of the study region (Abdelhamid, 1990). The unit is typically well bedded and massive (Powell, 1989).

6.2.1 Structural Geology

The region is located 25-35 km east of Aqaba, close to the Rift zone. The Red Sea rift is a continuation of the African Rift zone, splitting into two branches south of the Sinai Peninsula: (1) the Gulf of Suez; (2) the Gulf of Aqaba (Elat). The Dead Sea rift is a transform fault separating the Levantine (Sinai-Israel) and NNE sliding Arabian plates (Bender, 1969). The transform was formed in the Cenozoic when the African and Arabian plates separated. In Wadi Araba, the structure is principally a major left lateral strike-slip fault with an estimated horizontal displacement of 110 km (Quennell, 1951, 1958, 1984; Hatcher *et al.*, 1981). The shear movement is thought to have proceeded in two distinct phases (Freund *et al.*, 1970), which have been dated through magnetic anomaly data in the Gulf of Aden (Girdler and Styles, 1974; Girdler, 1985). The first movement took place between 25 and 14 Ma ago and involved 60-65 km of displacement, while the second occurred 4.5 Ma ago, and involved 40-45 km of movement (Zak and Freund, 1981). The direction of shear along the Dead Sea was closer to the general trend of the rift (N15°E) during the earlier phase and 10° greater (N25°E) during the later stage. The area as a whole forms part of the Nubian-Arabian Shield which is tilted regionally towards the north and northeast in southern Jordan (De Sitter, 1962). Contemporary shear displacements along the Dead Sea Rift have been measured at 6 mm a^{-1} (Galli, 1999; McClusky *et al.*, 2003), with average Late Pleistocene rates of 2 to 6 mm a^{-1} (Klinger *et al.*, 2000). In addition to shear movements, extensional episodes are marked by tensional grabens, of which the most important is the Dead Sea Rift, reaching a minimum altitude of –400 m below sea level.

A series of major faults occur in the area and these are orientated parallel or sub-parallel to the NNE-SSW trending Wadi Araba / Dead Sea Rift (Rabba, 1991). The largest fault is the Al-Quwayra fault, which extends several hundreds of kilometres south into Saudi Arabia. The fault has a major influence on the topography of the area, forming a boundary to the Western Mountains and the sandstone terrain in the west (Rabba, 1991). Other major faults include the Jabal Qalkha fault and the Wadi Judaiyid fault, both of which trend NE-SW. Further south, the dominant direction of faulting is NNE-SSW, and this is expressed in the Wadi Rumman and Wadi Ram faults, which have been downthrown 300 m towards the west (Abdelhamid, 1990). Analysis of lineaments from Landsat images shows a dominance of NW-SE, NNE-SSW and NE-SW trends, although important lineaments also have an approximate westerly trend (Beicip, 1981; Rashadan, 1988). In Wadi Rum, the most important

fault is the NW-SE trending Wadi Rum fault, indicating a swing in the trend of major faults; recorded by a change in the alignment of the inselbergs. The faults have been important in controlling the segmentation of the sandstone massifs and the orientation of their individual components (Goudie *et al.*, 2002).

Structural control affects the geomorphology of the sandstone inselbergs. The scale of the inselbergs increases towards the south and east. Down-faulting of the sandstones to the east of Al Quwayra means that many inselbergs have been buried by aeolian sediment (Heimbach and Meiser, 1971).

6.3 Geomorphology

The general geomorphology of the region is principally controlled by faulting. In total, four main physiographic areas can be recognised within the southern desert:

1. the western mountains, west of the Al-Quwayra fault;
2. the sandstone inselberg country in the centre and the east;
3. the Ras an Naqab escarpment in the northeast;
4. the massive sandstone inselbergs in the south of the region.

Only the geomorphology of the regions containing the sandstone inselbergs will be described here, as these are the location of the present study. The extent of the inselbergs within the study area is shown in Figure 6.4. Information on the other regions is widely available (for example, Rabba,1991).

A simple landscape component model can be constructed showing how the major geomorphic features are linked (Figure 6.5). Most overland flow in the form of wadis originates from the Ras El Naqab escarpment. The escarpment is dissected in places so that large alluvial fans sweep downslope. The sediments in these fans have been reworked by periodic incision of the wadis during the pluvial period. Alluvial sands cover around 40 % of the area, and consist of medium- to coarse-grained deposits (Goudie *et al.*, 2002). The thickness of the sand increases towards the south and west. The colour of the sands reflects the sandstone which is locally exposed. Weathering of the Umm Ishrin Formation gives rise to red-brown sands, while the Disi Formation produces white sands. Towards the Ras an Naqab escarpment, exposures of Disi sandstones dominate, producing inselbergs with a

characteristic rounded morphology (Osborne, 1985). The sands form two distinct types of dune. Seif dunes develop along the edge of the playas where prevailing wind directions are effective, while hummocky sand hills form in the wadis, where air currents are more diverse. The growth of both dune systems is accelerated by sparse vegetation which has the effect of fixing their location. Away from the escarpment, the landscape gives rise to a topography dominated by sandstone inselbergs, where rockfall is a major geomorphic process acting on these slopes. Large playas dominate the lowest areas of the desert around Wadi Rum and are kept sand–free.

The sandstone inselberg country to the east of Al-Quwayra is dominated by three distinct types of inselberg, whose morphology reflects lithological variations in the Umm Ishrin Formation. Jabal al Mukhruq is characterised by inselbergs with relatively gentle slopes (40-45°) with numerous benches covered with debris (Goudie *et al.*, 2002). The benches of these hills are formed by ferruginous bands developed within the middle section of the Umm Ishrin sandstone. Iron-rich layers are more resistant to erosion than other surfaces, thus giving rise to a stepped-like appearance to these inselbergs, producing more gentle slope profiles. Similar morphologies are present on the north-east-facing slopes of Jabal al Muhaymi. Here, the benches are covered by scree, although deposition here is associated with a dyke, which cuts through the hill. Stepped profiles also occur on the lower slopes of Jabal al Mu'aysi.

The second morphological type is characterised by steep, almost vertical cliffs rising 150 m from the desert floor. The hills often have a very sharp piedmont angle and rather flat summit surfaces (Osborne, 1985). Slopes have developed in the upper sections of the Umm Ishrin sandstone, which is characterised by a massive morphology and bedding with a 10-15 m spacing (Plate 6.4). They show extensive case hardening and the development of tafoni weathering. The inselbergs in the Jabal al Mu'aysi region are characteristic of this morphology (Goudie *et al.*, 2002). Major rockfalls are common here, principally because erosion along lower bedding planes produces slope overhangs.

The third type of hill is composed of 'white' Ishrin sandstone, and includes dome-like hills with steeply sloping sides, with convex profiles (Osborne and Duford, 1981) (Plate 6.5). The beds are white from iron depletion. Hills in white Ishrin sandstone also tend to be relatively low, producing a morphology similar to that found on the

Disi Sandstone. Further geological control can be recognised in the field and is related to the regional NE dip of the sandstone (Goudie, *et al.*, 2002). It helps explain why stepped profiles are absent in the middle and northern part of the area and the slightly asymmetrical cross profiles of some inselbergs, particularly in the 'white' Ishrin sandstone. Cavernous weathering forms are preferentially developed on SW-facing slopes, producing frequent undercutting of the slope toe. In addition, the NW-SE elongation of the inselbergs in the southern part of the area is likely to be related to the regional structure (Goudie *et al.*, 2002).

Within the Al-Quwayra-Rum area, discontinuities play a major role in determining slope evolution. The rock masses are dominated by vertical joints, which divide the rock slopes into a series of pillars (Plate 6.6). These 'primary' joints are highly weathered, so that joint surfaces are separated by as much as 50 cm (Osborne, 1985). The spacing of these pillars is governed by the spacing between discontinuities, which may be hundreds of metres. Superimposed upon this pattern of jointing is another vertical joint set which is much more closely spaced (<10 m), is dominated by cross-bedding features, and imparts a blocky structure to the rock masses.

Bedding structures are important in determining the spatial distribution and type of failure operating within the inselbergs. The bedding structures tend to be dominated by impermeable shale bands around 50 cm thick, which outcrop at the base of most of the inselbergs. Shale bands are important because they cause groundwater sapping. Sapping is the process leading to the undermining and collapse of valley heads and side walls by weakening or removal of basal support as a result of enhanced weathering and erosion by concentrated fluid flow at a site of seepage (Laity and Malin, 1985). The sandstone inselbergs contain large reserves of water, as shown by the construction of dams within large fissures. The porosity of the sandstone enables the rock masses to act as isolated aquifer systems with vertical and horizontal groundwater flow. Once a shale band is reached, preferential erosion of the weakly cemented rock occurs, which eventually leads to large-scale undermining of the base of the slope. Erosion continues until the undercutting weathers back to a joint surface, or the tensional strength of the rock is exceeded and failure occurs. It is not clear which is the most important process governing the failure of these rock slopes. Laity and Malin (1985) suggested that disruption of surface exposures by salt crystal growth where seepage emerges and sloughing of thin sheets of the bedrock are the major sapping processes in massive sandstones,

and that sapping is usually concentrated in thin zones above less permeable boundaries (e.g. shale units), within or below more permeable rocks. Backwasting and undermining of the overlying sandstone then promotes the development of slab failures. Where undercutting of the cliff face is occurring due to seepage, the sandstone is highly weathered and friable, eroding through exfoliation. Previous work had suggested that salt weathering is an important process leading to accelerated basal undercutting of slopes in Utah, which can cause rock slope failure (Mustoe, 1983). Preliminary work has suggested that salt weathering may be an important process leading to the development of slope undercutting in Wadi Rum (Goudie *et al.*, 2002).

Where rockfalls have occurred, debris is deposited at the toe of the undercut slope. In the weaker Disi sandstones, much of the rock has powdered upon failure, because of its low strength, so that only larger blocks remain as basal debris. On most desert rock slopes, this coarse debris must be weathered and eroded before further failure can occur (Howard and Selby, 1994). Weathering leads to both spatial and temporal variations in rockfall activity within the Rum-Quwayra region. Given the low angles of the ramps bounding the slopes (1-8°) run-out distances tend to be relatively low, rarely exceeding 100 m in the Al-Quwayra region, but increasing to >200 m around Wadi Rum (Goudie *et al.*, 2002). This is because rock slopes are higher around Wadi Rum, so that upon failure the rockfall contains more energy and debris leading to greater run-out distances. The presence of rock-cut ramps in front of many of the free faces suggests a long history of rockfall activity and slope retreat in the Wadi Rum-Al-Quwayra region.

6.4 Methodology and data acquisition

In Wadi Rum, it was possible to identify a range of jointed rock mass landforms at a range of spatial scales. The scale of the inselbergs increases towards the south. Discontinuity data were collected by laying tapes parallel and perpendicular to the strike of the bedding at each field site. Recordings were made as each discontinuity intersected the survey base line. The strike, dip and dip direction of each discontinuity were recorded. The recommendations of Priest and Hudson (1981) were followed and measurements were taken from more than one face of the rock slope to gain a three-dimensional picture of the discontinuity geometry. Spacings between joint sets were recorded along transects orientated perpendicular to the

strike of the joint sets (Mohajerani, 1989; Qin Huang and Angelier, 1989). In the Wadi Rum area, discontinuity sets are continuous throughout the rock masses, especially where a three-dimensional view of a slope could be obtained. It was noted in the field that all joints were persistent.

Rock strength data were collected by two methods. First, rock hardness values were measured in the field using the Schmidt hammer. At each site, 150 measurements were taken along the same transects used for recording the discontinuity geometry. By moving the hammer across the rock surface problems of rock mass anisotropy can be overcome. The variability in rock hardness values within a particular geological formation can be investigated by testing a number of sites within the same formation. Second, *in situ* rock blocks were removed from the cliff free face along intersecting discontinuities, their orientation relative to the free face was noted and they were returned to the laboratory for analysis.

6.5 Geotechnical Properties of the rock masses

Field investigations were conducted in the Al-Quwayra and Wadi Rum region of southern Jordan to analyse the joint geometry, geotechnical properties of the main sandstone units and cliff morphometry in order to model the mechanisms of failure and behaviour of the cliffs in the sandstone inselbergs of the southern desert. A range of landform sizes were examined, 1–100 m, 100–500 m and over 1000 m, to determine whether landform scale exerted any control on slope behaviour. The scale of the landforms increases in a southerly direction, and three broad clusters can be identified: the area immediately south and east of Al-Quwayra; a central region between Wadi Rum and Al-Quwayra; and the region of Wadi Rum itself. In total, 17 sites were selected for investigation, with the sample points reflecting the scale of the landform.

6.6 Discontinuity geometry

An initial understanding of the mechanisms of cliff failure in the sandstone inselbergs can be gained by contouring of the pole positions on equal area stereographic projections (Figures 6.6 to 6.22). By contouring the poles, mean joint set characteristics at all sites can be identified (Hoek and Bray, 1981; Priest 1985).

By comparing the representative joint data of all sites, some appreciation of the spatial variability in joint geometry can be gained (Table 6.1). In total, nine joint sets can be identified, although most sites show only two joint sets in addition to the bedding. Almost all sites are characterised by the presence of either set 1, 2 or 3, in addition to bedding, suggesting these are the dominant joint sets in the region. Sets 4 to 9 are not as common, nor are they as consistent and are interpreted as cross-bedding structures (Abdelhamid, 1990). Joint set 3 occurs mainly in the central portion of the study region, being absent on the north (AL13-15) and in the south (AL15-16). The occurrence can be explained by these sites' proximity to NNE- to SSW-trending faults, parallel to the Wadi Arabia Rift. Joint set 1 can be related to the NE-SW direction of faulting and set 4 to the approximately E-W trending faults. Set 1 is related to the dominant structural trend of the area, expressed by the Wadi El Marasad, Wadi Rumman, Wadi Ram faults and associated sub-parallel lineaments. All joint sets are steeply dipping, with most sets ranging from 70 to 90°. Bedding is close to horizontal, ranging from 2 to 7°. The steep dip of the joints indicates that little folding of the sandstones has occurred since deposition. The bedding generally follows the N – S to NE – SW tilt of the Nubian Shield in southern Jordan (Bender, 1974).

Jointing in the Al-Quwayra–Wadi Rum region is structurally controlled and explains the relative consistency of jointing in the region. Cross-bedding structures caused by changes in the direction of flow during deposition lead to the superimposition of random joint sets on this regional framework.

To confirm whether the joints had been correctly assigned to their respective sets, a computer program, Geocalculator v 4.5, was used to calculate the angle of intersection between the bedding and joint sets in three dimensions (Holcombe, 2002). Intersection angles have proven useful in delimiting joint set data. The results are presented in Table 6.2.

	Bedding	Set 1	Set 2	Set 3	Set 4	Set 5	Set 6	Set 7	Set 8	Set 9
AL1	04/209	86/222		88/143						
AL2	05/309	89/232								
AL3	03/011	82/225					79/270			
AL4	07/211		73/213	85/172	72/090			68/021		
AL5	07/274	82/254		85/182	72/045					
AL6	07/247		75/216	80/124						
AL7	06/359	71/234		76/190		81/004				
AL8	03/251	85/257								
AL9	06/123	78/258		84/224					76/328	70/130
AL10	07/345	76/232			76/061					
AL11	05/168			81/128		86/015				
AL12	04/248	79/231	79/195							
AL13	06/158		81/213						79/303	
AL14	04/310	82/254					79/291			
AL15	02/311	80/262						40/342		56/166
AL16	05/227		73/206		73/072					
AL17	07/269	82/259				81/006				

Table 6.1: Representative values for the bedding and joint sets of the Wadi Rum sandstones, Jordan.

	1/bed	2/bed	3/bed	4/bed	5/bed	6/bed	7/bed	8/bed	9/bed
AL1	82		86						
AL2	88								
AL3	84					79			
AL4		66	80	76			68		
AL5	75		85	77					
AL6		71	84						
AL7	75		82		75				
AL8	82								
AL9	82		85					81	58
AL10	79			74					
AL11			82		90				
AL12	75	77							
AL13		78						84	
AL14	80					75			
AL15	79						42		58
AL16		70		80					
AL17	75				82				

Table 6.2: Angles of intersection between the joint sets and bedding for the Wadi Rum sandstones.

The data confirm that the joint sets have been correctly grouped. For example, the angle of intersection between bedding and set '1' varies from 75 to 88 degrees. Set '3' has a consistent intersection angle, with values ranging from 80 to 86 degrees. The joint sets identified as cross-bedding structures also consistently intersect the bedding. Set '9' identified at AL9 and AL15 intersects the bedding at 58 degrees. For sets '1', '2' and '3', which are structurally controlled, the intersection angles are similar, indicating that jointing is relatively uniform. The low standard deviation in the angle of intersection suggests that the faults have not been responsible for tectonic deformation. Most faults are strike-slip and so this is consistent with the interpretation presented. However, the *relative* dip and dip directions of the joints between sites are slightly different, mainly due to lateral movements along faults; for example, 5 km of sinistral lateral displacement along the Wadi Rumman fault (Abdelhamid, 1990). In addition, the emplacement of dyke complexes due to crustal extension may have led to the formation of local stresses and disturbance of the joint sets in some places (Bender, 1974). It has been suggested that rejuvenation of these faults may have led to the development of tension joints in the rock masses (Rashdan, 1988).

The joint geometry and angles of intersection can exert a major influence on the failure mechanisms operating within the rock masses. Stereographic projection can be used to undertake kinematic analysis of rock slopes. For each of the inselberg free-faces, kinematic analysis was undertaken to determine the possible mode(s) of failure and the probability of that failure occurring, using the joint geometrical data presented in Table 6.1. A friction angle of 43 degrees was assumed for kinematic analysis as this represents the average friction angle of the three rock types present in the area, as determined from geotechnical analysis. The probability of failure is given to one and two standard deviations. The lowest probability estimate corresponds to the 1 standard deviation estimate and the highest to the 2 s.d. estimate. The standard deviations are obtained by fitting variability cones to each joint set. The 1 s.d. is given as the highest pole concentration on the stereograph, whereas the 2 s.d. encompasses all poles in a defined joint set and accounts for more variability in joint orientation. Where only one value is given there was no difference between the one and two s.d. estimates of the probability of failure.

Results of kinematic analysis are shown in Table 6.3. Kinematic analysis indicates that at all sites toppling is the dominant failure mechanism. Most of the toppling failures are restricted to the north and south faces, with toppling being

predominantly controlled by sets '1' and '3', aligned in a N-S to NE-SW direction. Substantial probabilities (> 40 %) of planar sliding exist on the west faces of AL4, AL5, AL6, AL7 and AL15. There is no common joint set controlling planar sliding at these sites, with sets '1', '2', '3' and '7' all being involved, although sliding occurs more commonly on set '1'. Overall, wedge failures are not common on any of the inselbergs. Where there is no chance of wedge failure occurring, it is not listed in Table 6.3. Even sites where wedging is kinematically possible, e.g. AL5, AL6, AL7 and AL9, the probability of this occurring is less than 5 %. The result is not unexpected given that wedge failures involve failure along the intersection of two or more discontinuities that daylight at the slope face. The jointing is so regular in the sandstones that the planes of discontinuities rarely intersect.

Kinematic analysis has shown that toppling is the dominant failure mechanism, with planar sliding being significant at a small number of sites. However, kinematic analysis does not take into account *in situ* stresses, which can promote or inhibit failure. Analysis using rock mass geotechnical and geometrical properties is, therefore, required to advance understanding of long-term slope evolution.

Joint spacing is an important property governing the behaviour of rock masses and was determined by laying tapes perpendicular to joint sets identified in the field, and the spacing between individual discontinuities being recorded. Bedding was treated separately from joint spacing, as this was relatively consistent. As for the Picos de Europa, the analysis was undertaken in two stages: first, data were treated as lumped to provide a broad comparison of discontinuity characteristics between each site; second, spacing was determined for each joint set. Summary statistics for the lumped spacing data for all sites are presented in Table 6.4. Spacing in the sandstone inselbergs is large, and at many sites it was only possible to estimate discontinuity spacings from fewer than 20 measurements. However, the data are accurate, because in many of the exposed faces, the spacing between all the joints present was measured.

Site	Failure mechanism	Facing slope	Probability of failure (%)	Joint sets responsible
	Toppling	North	75-100	1
AL1	Toppling	South	5-40	1
	Toppling	East	16-33	3
	Toppling	West	50-66	3
AL2	Toppling	North	18-33	1
	Toppling	South	30-33	1
AL3	Toppling	North	66-91	1
	Toppling	West	6	1
	Planar slide	West	37-50	1
AL5	Toppling	North	30-38	3
	Toppling	South	50-71	4
	Toppling	East	100	1
	Toppling	West	28-42	4
	Wedge	North	< 5	1+3 / 3+4
AL6	Toppling	North	77-100	2
	Sliding	West	55-100	2
	Wedge	South	< 5	2+3
AL7	Toppling	North	85-100	1
	Toppling	South	85-100	5
	Toppling	East	71	1
	Planar slide	North	28	3
	Planar slide	South	80-100	3
	Wedge	West	< 5	1+5
AL8	Toppling	East	36-54	1
	Toppling	West	10	1
AL9	Toppling	North	100	3
	Toppling	South	25	3
	Toppling	West	100	9
	Wedge	East	< 5	8,1+3 / 9+3 1+9
	Wedge	South	< 5	1+9
AL10	Toppling	North	52-66	1
	Toppling	South	57-100	4
	Planar slide	South	23-33	1
AL11	Toppling	South	52-100	5
	Toppling	East	83-100	3
	Toppling	West	16	3
AL12	Toppling	North	75	1
AL13	Toppling	North	52-76	8
	Toppling	South	64-88	8
	Toppling	East	11-18	8
AL14	Toppling	East	48-71	6
AL15	Planar slide	North	50-100	7
AL17	Toppling	East	76	1
	Toppling	West	76-100	1
	Planar slide	West	20	1

Table 6.3: Summary of kinematic analysis on the sandstone inselbergs of Wadi Rum, Jordan. Only the failure mechanisms kinematically possible on each slope are listed.

Site	n	Mean (m)	s.d. (m)	Min (m)	Median (m)	Max (m)	skewness	kurtosis
AL1	10	24.75	22.06	3.45	23.79	78.00	1.44	4.45
AL2	26	11.98	6.37	2.31	10.97	25.80	0.76	3.16
AL3	18	5.73	4.99	1.05	3.45	17.58	1.35	3.81
AL4	29	10.34	9.27	1.20	7.61	40.00	1.49	4.85
AL5	20	5.31	3.96	1.75	3.95	17.80	1.81	5.98
AL6	37	3.51	2.05	1.15	2.64	7.87	0.89	2.52
AL7	21	14.62	17.51	1.30	5.40	51.60	1.15	2.60
AL8	19	21.49	22.27	3.20	13.55	70.00	1.13	2.88
AL9	18	11.74	13.59	1.36	6.22	48.00	1.92	5.48
AL10	22	6.09	5.74	1.33	4.92	24.90	2.10	6.96
AL11	27	6.94	5.15	1.50	5.30	26.19	2.04	8.16
AL12	10	9.81	7.50	2.61	8.30	26.60	1.19	3.49
AL13	16	10.99	7.96	1.20	9.20	30.40	1.22	3.71
AL14	32	7.59	8.42	1.00	4.02	42.00	2.43	9.82
AL15	10	5.77	3.14	1.40	5.91	10.56	0.02	1.83
AL16	63	24.30	66.44	1.02	4.50	472.00*	5.30	34.46
AL17	32	26.17	36.62	1.40	18.26	135.86	1.43	4.00

Table 6.4: Summary statistics for lumped joint data for all sites in the Al-Quwayra – Wadi Rum area of southern Jordan. *This was a large joint that had been weathered out. Only two of these were present in the AL16 rock mass.

Comparison of raw spacing data indicates that all sites show a wide spread of joint spacings (Figure 6.23). This is due to the superimposition of joint sets with narrower spacing on the 'master' discontinuity sets with wider spacings. A number of probability distributions for joint spacing are recognised, ranging from exponential (Priest, 1993), log-normal (Tindall and Davis, 2003), Weibull (Bardsley *et al.*, 1990) or gamma (Huang and Angelier, 1989) (see Chapter 5). Of the above distributions, only the exponential has theoretical support in that it arises under conditions of random location of discontinuities along a line. This random distribution implies a Poisson frequency of discontinuities per unit length. Comparison of the quantiles of spacing values from each site with the exponential shows that joint spacing in the Al Quwayra-Wadi Rum area does not fit an exponential distribution (Figure 6.24). Comparison of spacing data with a log-normal distribution shows a relatively good fit for all sites (Figure 6.25).

Comparison with more flexible distributions have also been made. Non-exponential distributions may arise from the fact that non-random discontinuity spacing must represent the effect of some physical process. The exponential distribution arises as a limit for where non-random spacing is only just evident. Of the standard distributions, only the Weibull and gamma include the exponential as a special case. Comparing joint spacing for all sites with a Weibull distribution indicates that joint spacings in Jordan are probably not totally random (Figure 6.26). The Weibull distributions goes through the centre of the joint spacing data, indicating a generally good fit. Deviation around the ideal distribution is not unexpected. Simulating a number of spacing distributions, with the same sample statistics as AL7, shows that a range of non-random distributions can be produced (Figure 6.27). The gamma distribution does not describe the joint spacing as well as the Weibull or log-normal (Figure 6.28). From this analysis, joint spacing in Jordan cannot be considered as totally random. More detailed structural investigation would be required to investigate the origins of joints in the Al Quwayra Wadi Rum region of Jordan.

The first two L-moments indicate three main discontinuity sets can be identified in the spacing data (Figure 6.29a). The first includes AL16 and AL17, which have much greater average spacing than any of the other sites. The result is not surprising since these two sites were located further south in Wadi Rum than the other sites. They were also the largest inselbergs to be surveyed; therefore, the opportunity for wider joint spacings to be represented in the data was increased. A second set can be identified in the centre of the data spread and includes AL1, AL7, AL8, and AL9. Three sites, AL7, AL8 and AL9, are located in the same region and it is not unexpected that the joint statistics are similar. AL1 is located much closer to the Al-Quwayra fault than the other sites and it is not clear why the joint spacings of these sites are similar. They are found in different lithologies, so similar geology cannot be invoked to explain this. AL7, AL8 and AL9 are located near a granitic intrusion, while AL1 is located close to the Al-Quwayra fault and crustal movements may have led to some similarities in joint spacing, even though they have a different mode of origin. The third group contains all other sites, which are located in the north and central region of the Al-Quwayra-Rum region. At all these sites, joint surveys were conducted in Red Ishrin sandstone, away from major faults and intrusions. There is no relationship between the size of the landform here and joint spacing, as the group contains sites ranging in height from <50 m to over 300 m. Nevertheless, the sites show similar distributions.

Figure 6.29b presents the L-skewness and L-kurtosis data for the sites. AL16 is an outlier, mainly because of the inclusion of a joint set with a spacing of 472 m. AL15 has the least skewed distribution, showing that jointing here is fairly regular. The regularity of spacing may be due to the relatively few number of joints present in the landform as a result of its small outcrop scale. Almost all the data are skewed to some extent, indicating that there are fewer joints with wider spacings.

The UDEC modelling approach allows a number of different joint geometries to be created in a single model, with prescribed deviations, so statistical treatment of individual joint sets is of more practical value than the lumped data approach. The results of statistical analysis of joint data by set for each site are presented in Table 6.5. Skewness and kurtosis were not included because of the low sample populations.

Site / joint set	n	Mean	s.d.	Min	Median	Max
AL1						
Bedding	4	10.04	1.93	7.87	9.97	12.36
Set 1	5	8.36	4.14	3.45	7.81	15.10
Set 3	5	73.42	1.93	7.87	74.42	12.36
AL2						
Bedding	3	9.80	0.75	9.15	9.64	10.60
Set 1	22	12.18	6.34	3.40	10.76	25.80
AL3						
Bedding	4	12.91	1.79	10.30	13.56	14.21
Set 1	5	8.19	5.42	2.45	6.67	17.00
Set 6	10	3.18	1.98	1.05	2.45	7.58
AL4						
Bedding	4	11.18	2.89	7.03	12.04	13.62
Set 2	5	9.09	1.03	7.61	9.65	10.10
Set 3	2	13.07	4.36	9.64	14.79	17.99
Set 4	5	9.02	6.46	2.64	7.21	19.20
Set 7	6	5.03	2.73	2.30	4.17	8.54
AL5						
Bedding	4	12.85	1.07	11.84	12.62	14.34
Set 1	8	4.73	1.87	2.20	5.00	6.70
Set 3	8	4.85	3.38	1.75	7.24	11.43
Set 4	8	4.45	2.12	2.12	4.03	8.17
AL6						
Bedding	7	10.49	1.04	9.27	10.23	12.60
Set 2	6	4.09	2.51	1.66	3.74	7.59
Set 3	14	2.72	1.37	0.70	2.55	5.40
AL7						
Bedding	3	8.30	1.04	7.15	8.59	9.16
Set 1	4	5.28	1.27	3.70	5.32	6.80
Set 3	3	38.65	11.27	31.05	33.31	51.60
Set 5	5	3.47	0.27	3.24	3.33	3.80
AL8						
Bedding	4	11.63	2.68	9.24	10.96	15.34
Set 1	14	17.95	15.77	3.20	13.50	47.00

AL9						
Bedding	3	10.86	1.48	9.82	10.21	12.57
Set 1	3	4.56	1.00	3.75	4.25	5.68
Set 3	2	7.87	6.75	3.10	7.87	12.64
Set 8	2	3.82	0.00	3.82	3.82	3.82
Set 9	1	45.00	0.00	45.00	45.00	45.00
AL10						
Bedding	3	10.96	1.35	10.01	10.36	12.51
Set 1	12	5.37	3.02	1.30	4.76	11.30
Set 4	6	2.59	1.30	1.68	2.10	5.20
AL11						
Bedding	4	5.98	2.08	3.35	4.86	8.24
Set 3	4	5.95	4.71	1.50	6.18	12.60
Set 5	19	6.15	3.57	0.60	4.75	12.31
AL12						
Bedding	2	12.15	2.38	10.47	12.15	13.84
Set 1	8	19.46	10.33	10.05	16.30	42.24
Set 2	4	4.07	0.56	3.60	3.94	4.81
AL13						
Bedding	2	13.8	2.04	12.36	13.80	15.24
Set 2	2	8.85	0.21	8.70	8.85	9.00
Set 8	10	18.6	7.65	12.00	17.25	36.00
AL14						
Bedding	4	10.75	1.06	9.87	10.38	12.27
Set 1	2	40.17	2.58	38.35	40.18	42.00
Set 6	23	7.76	6.15	2.35	3.95	20.94
AL15						
Bedding	2	9.8	0.79	9.24	9.80	10.36
Set 1	3	2.16	0.66	1.40	2.50	2.60
Set 7	8	5.86	2.56	2.05	5.91	8.95
Set 9	2	9.65	1.28	8.75	9.65	10.56
AL16						
Bedding	3	10.28	1.08	9.21	10.26	11.37
Set 2	29	14	20.31	0.60	2.30	72.20
Set 4	6	4.99	0.94	3.73	5.18	6.00
AL17						
Bedding	3	14.5	0.77	13.61	14.87	15.03
Set 1	12	35.79	41.97	4.60	15.32	121.50
Set 5	13	45.24	38.53	7.35	37.86	134.86

Table 6.5: Summary statistics for individual discontinuity set spacing at each site in the Al-Quwayra-Wadi Rum region.

On average, bedding is consistent between sites, ranging from 8.30 m at AL7 to 14.50 m at AL17. Most sites show a 'dominant' joint set which has a greater mean spacing than the other sets. For example, at AL7, set '3' is the dominant set with a spacing of 38.65 m. Superimposed on this pattern are joint sets '1' and '5', with mean spacings of 5.28 m and 3.47 m, respectively. At AL9, joint set '9' is dominant

with a spacing of 45 m. This pattern is repeated throughout and can be seen in the field as major joints tend to become preferentially weathered.

6.7 Rock strength data

Information regarding the intact material properties was gained through a combination of Schmidt hammer testing of *in situ* material and laboratory triaxial testing. Triaxial testing was undertaken at the same confining pressures as used for samples from the Picos de Europa, i.e. 10, 15 and 30 MPa. Deformation of samples during unconfined and confined tests was monitored by axial and radial strain gauges. Laboratory strength data were plotted using Mohr's stress circles with a linear Mohr–Coulomb failure envelope fitted to the results (Figures 6.30 to 6.32). *In situ* strength data were also gained for parts of the slope currently being eroded through slope sapping. Care was taken to ensure that the weathering rind was removed before impact testing. A summary of the geotechnical properties of the various sandstone units found in the study area is presented in Table 6.6.

Values of density range from 2443 kg m^{-3} for the Salib Arkosic and Red Ishrin units to 2534 kg m^{-3} for Disi sandstones. Porosity varies from 6.94 % for the Salib Arkosic sandstones to 5.70% for the Disi sandstones and is within the range expected from previously published values for sandstone (Goodman, 1980). In the field, porosity varies spatially in response to case hardening of the sandstones caused by cavernous weathering; these values represent unweathered estimates.

The unconfined compressive strength (UCS) of the sandstones ranges from 32.63 MPa for Disi sandstones to 58.73 MPa for Red Ishrin, showing an almost twofold range. UCS data give some insight into the mechanisms of slope development in the study area. Inselbergs formed entirely from Disi sandstone tend to be dome-shaped and rounded in profile without steep cliffs, whereas slopes formed in the Red Ishrin sandstone are almost vertical and in many cases over 200 m high. Since discontinuity characteristics are fairly similar across the region it appears that the compressive strength of the rock is a major factor in controlling inselberg form. Estimated UCS from Schmidt hammer rebound data generally agrees well with the laboratory tests. Schmidt hammer data indicate a UCS of 47.90 MPa for the Red Ishrin sandstones and 39.46 MPa for Disi sandstone. The slight reduction in strength from the Schmidt hammer data reflects the fact that the impact delivered

from the hammer is not great enough to lead to pore and crack closure, which is an important property governing the behaviour of rocks. In addition, the differences will also reflect natural variability in material strength and differences in the amount of rock weathering, even though the weathered surface was removed before testing.

Schmidt hammer data indicate that the UCS of the sandstones is reduced where the slope is undergoing basal erosion in response to slope sapping. The data represent the average UCS calculated for each site. The UCS of the area of the slope undergoing erosion is 33.71 MPa for Red Ishrin sandstone and 30.12 MPa for Disi sandstone. At least part of this reduction in strength is caused by loss of cohesion, as the cementing agents bonding the sandstones together are weathered out. In addition, water has also been noted at the base of the slopes, especially where shale bands are present. Saturation and partial saturation of sandstone can lead to a further 10 – 20 MPa reduction in strength (Bell and Culshaw, 1993; 1998). Hawkins and McConnell (1992) demonstrated that saturation could lead to a 25 – 50 % reduction in the strength of 35 sandstone types; those with the greatest quartz contents were most sensitive to moisture content. Bell and Lindsay (1999) found that for sandstones from Natal, South Africa, a typical reduction in strength of 1.2 to 4.8 %. Various arguments have been put forward to explain this reduction in strength. Hawkins and McConnell (1992) argued that the reduction in strength may be related to softening and possible expansion of the clay mineral content of the sandstones. Dyke and Dobereiner (1991) and Atkinson (1984) argue that the presence of water increases the velocity of crack propagation in the quartz material by replacing strong silica bonds with weaker hydrogen bonds within the mineral lattice, a process referred to as stress corrosion. The reduction in strength caused by elevated moisture contents at the base of the slope may explain the reduction in strength of the sandstones, as indicated by the Schmidt hammer data. For more precise information regarding the reduction in strength upon saturation, a detailed laboratory programme would have to be conducted, which is beyond the scope of the present investigation. Yield strength at 15 MPa confining pressure shows similar trends to the uniaxial data, with Red Ishrin sandstone having the greatest inherent strength at 187.06 MPa, and Disi the lowest at 108.79 MPa.

The tensile strength of the sandstones is important as field evidence indicates that tensile failure is locally important (Plate 6.7). Red Ishrin sandstones have the greatest tensile strength at 12.26 MPa (Figure 6.30). The tensile strength of the Disi

sandstone is 8.26 MPa (Figure 6.31). The reduction in the tensile strength is an additional reason why steep slopes cannot be maintained in the Disi sandstones.

The deformation moduli, Young's Modulus, Poisson's ratio, bulk modulus and shear modulus are important measures that describe the deformational response to stress. They were determined through static and dynamic testing methods. Young's modulus for the Red Ishrin sandstones is 28.07 GPa and for the Disi sandstones is 9.21 GPa, indicating that the Disi sandstone undergoes more strain for a given stress than either the Salib Arkosic formation or the Red Ishrin sandstone. The values of Poisson's Ratio indicate that the material behaves elastically and ranges from 0.18 for Red Ishrin to 0.32 for Salib Arkosic sandstone. From these measures of deformation, the Bulk Modulus K and Shear Modulus G can be computed and directly entered into UDEC. Bulk modulus for Red Ishrin sandstones is 14.62 GPa and 5.85 GPa for Disi sandstone. Data from dynamic testing indicate that the Grindosonic apparatus can underestimate material strength, by not allowing for pore and crack closure. Dynamic Young's modulus E_d for Red Ishrin is 14.85 GPa, representing a twofold reduction in resistance to deformation as a result of not allowing for pore and crack closure. The underestimation given by dynamic testing of the Disi samples is thought to represent spatial differences in the pore density of the sandstones.

Rock type	Density, kg m^{-3}	Porosity, %	UCS, MPa	Yield stress 15 MPa	Estimated tensile strength (MPa)	Static Poisson's Ratio, ν	Static Young's modulus, E	Static Bulk modulus, k GPa	Static shear modulus, G GPa	Dynamic Young's modulus, E_d	Dynamic Bulk modulus, k_d GPa	Dynamic Shear modulus, G_d GPa	Dynamic Poisson's Ratio, ν	Estimated Young's modulus, E_o from R, GPa	UCS estimated from R value MPa	UCS of eroded slope from R value MPa	Estimated Young's modulus, E_o of eroded slope from R, GPa
Salib Arkose Sandstone	2443	6.94	45.67	137.07	8.83	0.32	18.13	5.76	8.78	8.07	2.75	3.99	0.01	19.08	42.73	32.21	13.51
Red Ishrin Sandstone	2443	6.04	58.73	187.06	12.26	0.18	28.07	14.62	11.89	14.85	5.75	6.94	0.07	22.27	47.90	33.71	14.68
Disi Sandstone	2534	5.70	32.63	108.79	8.26	0.23	9.21	5.85	3.72	12.08	5.29	5.39	0.12	18.64	39.46	30.12	13.34

Table 6.6: Summary geotechnical properties of the various sandstone of Wadi Rum.

6.7.1 Stress-strain behaviour of intact rock

During uniaxial compression, all the sandstones behave in a plastic-elastic manner. In all cases, the initial part of the axial strain curve is concave upward, reflecting the closure of pores and micro-cracks (Figures 6.33 to 6.35). Once all the pore spaces have closed, the axial curve becomes linear, showing that the sandstones are behaving elastically before crack propagation occurs. Only the elastic portion of the curve is recoverable during an unloading cycle; plastic strain represents permanent deformation of the material.

The black curve on the stress-strain graph represents the computed volumetric strain of the material. It was not possible to plot a meaningful volumetric curve for each sample, mainly due to the lateral strain gauge failure. The net effect of crack extension is to produce a volumetric curve which is very similar to the axial curve and does not represent ideal behaviour. Volumetric strain is important in understanding the behaviour of earth materials and their response to stress. After initial compression of the specimen, there is an increase in volume, or dilation. The point at which dilation begins is indicated by the onset of hysteresis in the volumetric curve. The effect of dilation is to create space in the specimen during the latter stages of deformation, indicating the onset of crack propagation. The onset of dilation occurs at about 40 % of the yield strength of the sandstones in both confined and unconfined samples. The volumetric strain data show that the effect of confining pressure is to increase the linearity of volumetric strain in the lower portion, indicating a greater strength of confined samples.

The effect of the confining pressures on the sandstones is similar to that for the limestones described in the previous section. The axial stress-strain curves show the effect of increasing confining pressure during compression for all three sandstones. As confining pressure increases, the amount of axial strain that the rock can sustain before failure increases (Table 6.7).

Lithology	0 MPa	10 MPa	15 MPa
Salib Arkosic	0.244	0.751	1.113
Red Ishrin	0.096	0.627	0.615
Disi	0.172	0.635	1.181

Table 6.7: Total axial strain for all sandstone samples tested in triaxial and uniaxial compression.

At 0 MPa confining pressure, the Disi sandstone undergoes 0.172 % axial strain before failure, whereas at 15 MPa total axial strain is 1.113 %. A similar pattern occurs in the Salib Arkosic sandstones with a total axial strain of 0.244 % at 0 MPa and 1.113 % at 15 MPa. The Red Ishrin sandstone does not conform to this pattern, probably due to the presence of a pre-existing micro-crack in the core.

Figures 6.33 to 6.35 represent the total axial and lateral strain curves for the sandstones loaded under confining pressure. The curves suggest that the main effect of confining pressure (apart from increasing total strain before failure) is to extend the range over which plastic deformation occurs. Confining pressure is important in considering rock mass deformation. Material in the centre of a large rock mass under confining pressure can undergo irrecoverable plastic deformation, resulting in permanent deformation of the slope at relatively low (10–15 MPa) deviatoric stresses. The deformation of intact material is in addition to that caused by movement along the discontinuities. A plot of material behaviour indicates that under confining pressure the sandstones tend more towards ductile behaviour than the limestones (Figure 6.36). The graph indicates that the Red Ishrin and Salib Arkosic sandstones are at the transition between brittle and moderately brittle behaviour, whereas the Disi sandstone is behaving in a moderately ductile way, according to Figure 6.36. The Disi and Salib Arkosic sandstones can be classified as brittle on the basis of total axial strain before failure, i.e. 1 – 3 % axial strain before failure. The Red Ishrin sandstone is more brittle than the other two types of sandstone and therefore able to support more vertical slopes than the other two sandstones.

6.8 Conclusions

The discontinuity surveys and investigations into material behaviour have highlighted the importance of gaining a detailed understanding of the geotechnical properties of rock masses for understanding landform behaviour. A number of important points have been gained from this work.

1. Toppling is the dominant failure mechanism in the sandstones because of the vertical nature of the jointing.
2. Joint spacing in the sandstones is large. This meant at many sites fewer than 20 measurements of each joint set could be gained.
3. The difference in strength between the sandstones controls the overall morphology of the inselberg landforms found in the Wadi Rum region of Jordan.
4. Vertical slopes are found in the Red Ishrin sandstones that have a higher unconfined compressive strength than the Disi sandstones that form rounded inselbergs, with few vertical slopes.
5. The Red Ishrin sandstones are more brittle and vertical slopes can be maintained because there is less deformation of the intact material before failure than in the Disi sandstones.

To gain a full understanding of landscape evolution, this work has demonstrated the importance of undertaking detailed laboratory studies of material behaviour in compression under uniaxial and triaxial stress regimes. The data gained from the field and laboratory research can be entered directly into UDEC to simulate slope behaviour.

Chapter 7: The mechanisms of failure and behaviour of high mountain limestone rock slopes in the Picos de Europa, northern Spain.

Chapter 7: The mechanisms of failure and behaviour of high mountain limestone rock slopes in the Picos de Europa, northern Spain.

7.1 Introduction

This chapter presents the results of numerical modelling of the geomorphological behaviour of key sites investigated in the Picos de Europa, northern Spain. Slope failure is an important process controlling the evolution of the landscape in this Alpine environment. No previous investigations have been conducted into the mechanics of slope failure in the Picos de Europa. The Universal Distinct Element Code (UDEC) was used to simulate the stress-strain behaviour and failure mechanisms operating at the field sites studied in this research. The purpose of the simulations is to improve understanding of rock slope evolution in the Picos de Europa.

7.2 UDEC modelling strategy and input parameters

Appropriate model input parameters were assigned to models constructed for profiles through each field site based upon the data presented in Chapter 5. The modelling methodology simulates the geomorphological evolution of the rock slopes and uses the current cliff profiles as initial conditions. To begin with, all models are stable after consolidation and an equilibrium stress regime has developed under constrained boundary conditions. The models are based on the real cliff profiles and controlling rock mass characteristics from the sites at Torre de Salinas, Pico de la Padierna, Tiro Pedabejo, Canchorral de Hormas, Allende and Los Montes, so that conclusions can be made about the geomorphological behaviour of the rock masses. Relevant input parameters can be divided into various groups. Information regarding rock mass geometry, discontinuity characteristics and intact material properties has been gained from field and laboratory investigations. Importance is attached to model accuracy in parameters such as joint spacing, which controls block size and the dimensions of the cliff free-face. However, it is emphasised that some level of simplicity must be maintained to understand the modelling response; the meshes are not intended to be complete scale representations. A particular problem was that the block size was so small in some models that unrealistically large computation times were experienced. Therefore, for some models it was

necessary to increase the joint spacing, so that more acceptable computation times could be achieved. Care was taken to ensure that the block height : width ratio remained constant, because this can influence the failure mechanism (Kimber, 1998). A number of model runs with different joint spacings were analysed to ensure that the increase in spacing did not substantially change the behaviour of the rock mass. In all cases, the minimum block size vs. computation time was selected. Average model run times varied between 24 and 72 hours, depending on the number of blocks within the models and the complexity and size of the failures. Despite this, the models do replicate the important characteristics of each site.

Parameters entered into UDEC for each model run are listed in Table 7.1 and the input files can be found in Appendices 7.1 to 7.15. Some similarities exist between the inputs (Table 7.1). To permit comparison between sites, meshes were constructed perpendicular to the strike of the free-face. The three-dimensional nature of the landforms in the Picos de Europa required the construction of two or more profiles to accurately represent the behaviour of the landform. However, the dips of each joint set on the two-dimensional UDEC mesh have to be converted from those gained from field measurements, which have a dip defined at the bearing of the joint strike. Thus, the mean joint set data were run through a computer program based upon the intersection of two planes to convert the data into the appropriate dip on the UDEC mesh (Kimber, 1998). Standard deviations of the joint spacing data were entered for each input file as indicators of spacing variability. Accurate data were available in the literature for the joint stiffness parameters. The joint stiffness was kept constant for all model meshes, regardless of site, to reduce errors associated with using different stiffness values with no physical basis for doing so. Furthermore, previous work has indicated that the control exerted on the UDEC models by the joint stiffness parameters is minimal (Kimber, 1998).

Parameter	Units	TS 1	TS 2	TS 3	PP 1	PP 2	PP 3	TP 1	TP 2	CH1	CH2	LM 1	LM 1a	LM 2	AL 1	AL 2
Free-face height	m	250	356	230	270	120	270	356	306	100	150	380	380	440	300	360
Free-face angle	degrees	65	55	75	70	60	60	70	65	66	65	54	54	70	80	60
UDEC mesh bearing (dip direction)	degrees	202	080	300	290	320	290	080	330	192	220	352	352	108	342	268
Joint set 1: angle	degrees	71	79.76	71	70	71	70	66	41.27	26	55	68	68	-28	76	16
Joint set 1: spacing/s.d.	m	8.4/5.4	4.8/5.4	8.4/5.4	7.4/3.6	7.4/3.6	7.4/3.6	6.2/3.0	6.2/3.0	4.0/1.5	4.0/1.5	6.4/3.2	6.4/3.2	6.4/3.2	6.1/6.6	6.1/6.6
Joint set 2: angle	degrees	73	77.22	73	69	76	69	12.09	63.31	80	76	5.2	5.2	-42	61	42
Joint set 2: spacing/s.d.	m	7.0/3.8	7.0/3.8	7.0/3.8	7.2/2.4	7.2/2.6	7.2/2.6	4.2/2.2	8.4/4.4	4.2/2.2	4.2/2.2	9.0/4.6	9.0/4.6	9.0/4.6	6.2/2.2	6.2/2.2
Joint set 3: angle	degrees	86	0	86	15	70	15	------	------	68	75	------	------	------	------	------
Joint set 3: spacing/s.d.	m	6.2/5.4	6.2/5.4	6.2/5.4	7.2/3.4	7.2/3.4	7.2/3.4	------	------	4.7/2.2	4.7/2.2	------	------	------	------	------
Bedding: angle	degrees	17.3	22.5	17	4.5	5.7	4.4	7.74	40.47	7.0	6.0	5.0	5.0	-43	50	69
Bedding spacing/s.d.	m	7.0/5.4	42.2/7.0	42.6/7.0	39.4/6.8	39.4/6.8	39.4/6.8	21.7/3.8	43.4/7.6	21.2/4.2	21.2/4.2	48.2/5.2	48.2/5.2	48.2/5.2	19.1/8.8	19.1/8.8
Bulk density	kg m^{-3}	2443	2443	2443	2443	2443	2443	2534	2534	2545	2545	2521	2521	2521	2521	2521
Bulk modulus	GPa	40.49	40.49	40.49	40.49	40.49	40.49	11.10	11.10	15.0	15.0	40.43	40.43	40.43	40.43	40.43
Shear modulus	GPa	35.48	35.48	35.48	35.48	35.48	35.48	15.11	15.11	18.41	18.41	46.19	46.19	46.19	46.18	46.18
Joint normal stiffness	GPa	70.8	70.8	70.8	70.8	70.8	70.8	70.8	70.8	70.8	70.8	70.8	70.8	70.8	70.8	70.8
Joint shear stiffness	GPa	58.8	58.8	58.8	58.8	58.8	58.8	58.8	58.8	58.8	58.8	58.8	58.8	58.8	58.8	58.8
Joint friction angle	degrees	33	33	33	33	33	33	33	33	33	33	33	33	33	33	33

KEY:

TS1 = Torre de Salinas, north wall

TS2 = Torre de Salinas, central wall

TS3 = Torre de Salinas, southern wall

PP1 = Pico de la Padierna, western section

PP2 = Pico de la Padierna, central section

PP3 = Pico de la Padierna, eastern section

TP1 = Tiro Pedabejo, north-south profile

TP2 = Tiro Pedabejo, east-west profile

CH1 = Canchorral de Hormas, north-south profile

CH2 – Canchorral de Hormas, east-west profile

LM1 = Los Montes, east-west profile no road-cut

LM1a = Los Montes, east-west profile, road-cut

LM2 = Los Montes, north-south profile

AL1 = Allende, north-south profile

AL2 = Allende, east-west profile

Table 7.1: UDEC input parameters for meshes used to simulate the behaviour of slopes in the Picos de Europa.

Individual blocks were defined as deformable because the relatively high *in situ* stresses in some of the models may cause deformation of the intact material. Defining blocks as deformable has the disadvantage of greater computation times, but the advantage that strain zone development can be monitored. Intact rock properties for each model were taken from the laboratory and field data presented in Chapter 5. Joint friction properties were assigned the same angle for each model. It was not considered accurate to use the friction angle of the intact material gained from uniaxial testing of rock specimens, because in reality the friction angle of the rock depends upon fill material and surface roughness. Field observations indicated that joint fill was not important, so based on qualitative assessments of surface roughness, the joint friction angle was set to 33°. Gravitational acceleration was set at 9.81 m s^{-2} and the initial vertical stress gradient was set to simulate the overburden weight of surrounding blocks. Initial horizontal stresses were set to the recommended half of the value of the vertical stress at a point (Herget, 1988). However, by the time the model had been run to equilibrium, the stresses were mathematically balanced throughout the model.

At the beginning of each model run, a zero velocity boundary was applied in the *y* direction to allow the blocks to consolidate. The main purpose of the consolidation phase is to allow the stresses to reach equilibrium before the fixed boundaries are released, preventing failures initiated by the initial out-of-balance forces. For each model, the bottom section was defined as a rigid block with no joints, because the slope angles are so low (< 20°) that failure would not have occurred, and so it plays no part in the failure of the slope. The extension to the model was included to represent the whole landform, rather than just the free-face. If this part of the model were defined as deformable, unrealistically high stiffness and strength values would have to be assigned to prevent material deformation caused by the overburden weight of blocks. For each of the meshes, a model time of 10 000 cycles was allowed to achieve equilibrium, which was associated with an exponential decline in the magnitude of unbalanced forces towards zero.

To simulate the slopes at Torre de Salinas, three model meshes were constructed for each face of the cirque headwall (Plate 7.1). All meshes cut through the cirque headwall perpendicular to the free face. The mesh simulating the northern cirque wall bisects the free face at a strike of 202°, with meshes simulating the central and southern cirque walls cutting through at 080° and 300°, respectively. The meshes constructed to simulate the evolution of Torre de Salinas occur in an area where the

bedding dips at 23° to the south. After conversion, the bedding dips at 17.3° for the mesh simulating the behaviour of the northern cirque wall (Figure 7.1). All joint sets were converted in the same way, so that the correct dip was represented on the UDEC mesh. To simulate the behaviour of the northern cirque wall, the right- and left-hand sides of the mesh were fixed during consolidation. Once equilibrium was reached, both boundaries of the model were released to allow failures to develop. Two further models were constructed to simulate the response of the central and southern walls. After conversion, the bedding dips at 22° for the mesh simulating the central cirque wall. On the same mesh, joint set 1 dips at 79.76°, joint set 2 dips at 77.22° and joint set 3 dips at 0° after conversion. Both faces were fixed in the *x* and *y* directions to allow equilibrium to be reached and then released to permit failures (Figure 7.6a). For the mesh simulating the southern cirque wall of Torre de Salinas, bedding dips at an angle of 17°, with joint set 1 dipping at 71°, set 2 at 73° and set 3 at 86° after conversion. The left- and right-hand boundaries of the model were fixed to reach equilibrium. Once consolidation had occurred, the left-hand boundary was released to simulate failure of the free face. The right-hand face remained fixed as the summit ridge continues for over 1 km at the same height and it is not possible for this to fail in the field.

Pico de la Padierna represents a large fault-bounded ridge, rising in height towards the south-east with evidence for slope failure. To simulate the behaviour of the slopes composing the ridge, three meshes were constructed (Table 7.1, Plate 7.2). For the mesh constructed to simulate the evolution of the western section of the ridge, the bedding has a dip of 5.7° after conversion, with joint set 1 dipping at 71°, set 2 at 76° and set 3 at 70° (Figure 7.11a). The left- and right-hand boundaries of the model were fixed to reach equilibrium and then the left-hand boundary was released to simulate the behaviour of the ridge free-face. The top of the ridge includes an extensive flat area, so the right-hand boundary of the model remained fixed. The mesh constructed for the central part of the ridge has a bedding dip of 4.5° after conversion and was designed to simulate the full free face, stretching back into the ridge. Joint set 1 dips at 70°, set 2 at 69° and set 3 at 15° after conversion on the mesh (Figure 7.13a). On the mesh for the western edge of the ridge, the left- and right-hand boundaries were fixed to reach equilibrium. The left-hand edge of the model was released to simulate failure of the free-face and the right-hand boundary remained fixed. The mesh constructed to simulate the eastern part of the ridge has a free face height of 270 m, with bedding dipping at an angle of 4.4° after conversion. The profile is very similar to the mesh constructed for the central

portion of the ridge, as there was little change in profile. Joint set 1 has a dip of 70°, set 2 69° and set 3 15° after conversion (Figure 7.17a).

Two meshes were constructed to simulate the rock slopes at Tiro Pedabejo (Table 7.1, Plate 7.3). The first mesh is a north-south profile and is constructed so that the north face is on the left-hand side of the model and the south face on the right-hand side. Both north and south faces have a free face height of 356 m, with the angle of the north face averaging 55° and the angle of the south face 70°. After conversion, the dip of the bedding on the mesh is 7.74°, joint set 1 is 66° and set 2 is 12° (Figure 7.20a). The second mesh constructed for Tiro Pedabejo represents an east-west profile, constructed so that the left-hand boundary of the model represents the west face and the right-hand side the east face. The model has a free face height of 306 m at an average angle of 65°. The eastern boundary of the model marks a col, which defines the eastern limit of Tiro Pedabejo. The dip of bedding on the mesh is 40.47°, joint set 1 is 66° and set 2 is 12.09° (Figure 7.23a).

Two model meshes were constructed to examine the evolution of Canchorral de Hormas in the eastern massif of the Picos de Europa (Table 7.1, Plate 7.4). The site includes two main free faces with a large block field providing evidence of failures. The meshes are taken perpendicular to these two faces. The first mesh represents the north-south profile of the rock mass, which is the slope field evidence suggests to be the source of debris for the block field at the toe of the slope. The south-east face of the model is on the left-hand side and the north-west face on the right-hand side. The mesh has a free face height of 150 m, at an average angle of 65°. The bedding dips at 7.0°, joint set 1 at 26°, joint set 2 at 80° and joint set 3 at 68° after conversion (Figure 7.26a). The slope at the toe of the south-east face represents the block field area, and has an average slope angle of 12° to the south. The second mesh is an east-west profile of the landform and is perpendicular to the second free face. The mesh has a free face height of 100 m and an average gradient of 66°. The free face then merges into a more gentle gradient, rising to a high point on the ridge. The model is constructed so that the eastern face is on the left-hand side and the western face on the right-hand side. The dip of the bedding on the mesh is 6.0°, joint set 1 dips at 55°, set 2 at 76° and set 3 at 75° (Figure 7.29a). The right-hand side of the model represents a continuation of the main ridge, with no major breaks of slope; the boundary remained fixed throughout the simulation to prevent artificial failure. After consolidation, the fixed boundary on the east face was released to allow failure.

Three meshes were constructed to simulate the behaviour of the landform at Los Montes in the Deva Gorge (Table 7.1). The first mesh simulates the east-west profile and has a free face height of 380 m at an average angle of 54 degrees (Plate 7.5). The right-hand side of the model represents the western edge of the rock mass and the left-hand side the eastern edge. On the mesh the bedding dips at 5.0°, joint set 1 at 68°, set 2 at 5.2° (Figure 7.32a). The eastern edge of the landform merges into the main slope, and the vertical boundary remained fixed throughout the simulation. The slope on the east face which is not vertical was released after consolidation, as this represents a small free face at an angle of 72° rising to the crest of the slope. The western face was released after equilibrium had been reached, to allow failure to occur.

The second mesh simulates the same east-west profile as the previous mesh, but a theoretical road cut is defined at the toe of the west face (Table 7.1, Figure 7.35a). This was included because at present the toe of the rock slope terminates in the valley bottom, where the current road runs. Constructed in the 1950s under the orders of General Franco, the road is the only one which runs through the Lebeña valley and is of vital economic and social importance to the area. Increased tourism means that the road is over-used and too small for coaches, so a road widening scheme has been proposed, plans of which were available from the council offices in Potes. The model is constructed to simulate the road widening by including a road cut 50 m wide and 50 m high. The road would be substantially widened because there is no room to expand away from the slope as the road is bounded by the Rio Deva. The cut was included to investigate its effect on the geomorphological behaviour of the slope. All other parameters, such as joint and bedding dip, were the same as in the first mesh.

The third mesh represents a north-south profile through the landform and is constructed so that the south face and the Deva Gorge are located on the right-hand side of the model and the north slope on the left-hand side (Figure 7.37a). The bedding dips at -43° on the mesh, i.e. out of the south face, joint set 1 dips at –28° and set 2 at -42° (Table 7.1). The converted discontinuities suggest that the rock mass is anisotropic, with the weakest plane being orientated perpendicular to the south face. The landform merges with the main valley slope and the vertical part of the northern edge of the model remained fixed throughout the simulation. After initial equilibrium had been reached, the right-hand side of the model was released to allow failure.

The final two model meshes constructed for the Picos de Europa were designed to simulate the geomorphological evolution of the slopes at Allende (Table 7.1, Plate 7.6). The first mesh simulates an east-west profile through the landform: the left-hand side of the model represents the west face, and the right-hand side the east face (Figure 7.39a). The bedding dips at a converted angle of 50° on the mesh, joint set 1 at 76° and set 2 at 42°. The free face of the west face has an average gradient of 80°. The east face has an average gradient of 80° and has a free face height of 300 m. A second mesh was constructed to investigate the behaviour of the north-south profile of the landform so that the north face is on the left-hand side of the model mesh and the south face on the right-hand side (Figure 7.42a). The bedding dips at a converted angle of 69°, with joint set 1 dipping at 16° and set 2 at 42°. All model boundaries were fixed in order to reach equilibrium, and the right- and left-hand boundaries released to allow failures to develop.

7.3 Results

During discussion of results the term *strain* is used to describe zones of the rock mass subjected to displacement. This is because those areas undergoing the most displacement are those under the greatest strain. *Displacement* is used when describing the magnitude of movement, whereas *strain* is used when describing the distribution of displacements in the model.

Results from the models run to simulate the evolution of the field sites in the limestone rock slopes of the Picos de Europa were plotted at important stages during modelling to show the type of failure occurring and the mechanisms responsible for the failure. Block plots were produced for each mesh at key stages in evolution. Displacement plots were produced so that the failure mechanism could be clearly identified. The plots monitor the movement of the finite difference gridpoints created when the blocks were assigned deformable properties. The evolution and distribution of strain zones in the rock mass was investigated by producing plots summarising the horizontal displacement of blocks in the model. Where blocks move towards the left on the UDEC mesh, the displacement is assigned negative values on the UDEC mesh. Displacements to the right are assigned positive values. This is related to the way in which UDEC calculates displacements in a Cartesian co-ordinate system. During the discussion of the results, all values are quoted as positive, regardless of their notation on the UDEC plots.

7.3.1 Torre de Salinas

The initial model mesh for the northern cirque wall of Torre de Salinas at equilibrium is plotted in Figure 7.1. The south face is on the left-hand side of the mesh and the north face on the right-hand side. An indication that the model has reached an equilibrium state with respect to unbalanced forces is given by a plot of unbalanced forces for the first 10 000 iterations (Figure 7.2). The plot shows that by 10 000 iterations the magnitude of out-of-balance forces is almost zero. The displacement vectors are vertical, indicating that the rock mass is stable and that forces are in equilibrium (Figure 7.1). Once the cliff faces are released, failure occurs through the detachment of rock blocks. By 100 000 model cycles, failure of the south face is beginning to propagate (Figure 7.3a). Detailed investigation of the failure mechanism indicates that blocks are moving by rotational sliding on the south face. A similar movement pattern is occurring on the north face, although the displacement vectors show a much smaller magnitude of block movement. The sliding failure is predominantly controlled by joint set 1, which dips at a converted angle of 71° out of the south face. Block plots without displacement vectors at 100 000 cycles indicate that anti-scarp features have begun to form on the north face in response to block sliding out of the south face and flexural toppling on the north face. This reflects the field situation: a number of bedrock steps had to be climbed when investigating the north face (Plate 7.7).

By 200 000 cycles, the displacement vectors show that failure on the south face is more advanced and a zone of secondary toppling has developed at the toe of the south face (Figure 7.3b). This is in response to blocks which have failed by sliding, moving down the bedrock ramp. The vectors also show that displacements on the north face are decreasing in magnitude and that stabilisation of the face is occurring. The principal deformation mechanism operating on the north face is flexural toppling. This is predominantly controlled by joint set 3, which dips at 86° and is indicated by a buckling of the rock mass on the north face, particularly towards the crest. By 350 000 cycles, sliding and secondary toppling on the south face have caused block detachment from the free face (Figure 7.3c). The zone of toppling on the north face has not changed substantially, indicating that the deformation on this face is time-dependent and less catastrophic over the same timescale than the failure operating on the south face. This strengthens the results gained from theoretical modelling, which suggests that toppling failures are more ductile than brittle sliding failures, which tend to be more catastrophic (Chapter 4).

Once the model reaches 600 000 cycles, the magnitude of toppling displacements on the north face has decreased markedly, in response to the reduced weight of surrounding rock caused by the sliding failure on the north face (Figure 7.3d). Secondary toppling caused by block sliding on the south face is also evident. Large amounts of debris are beginning to accumulate on the bedrock ramp and some blocks are continuing to slide over and past the bedrock ramp.

Filled contour plots for *x*-displacements were produced to examine how displacements develop in the rock and how this affects the geomorphological evolution of the landform. The plots form a direct link to the theoretical modelling and the evolution of strain zones in rock masses. Areas undergoing the greatest displacement are those which are under the greatest strain. When interpreting the plots, note that a given colour on plots does not necessarily represent the same magnitude of displacement. This is because UDEC automatically colours the plots based on strain magnitude and these cannot be changed by the user. At equilibrium no clear strain zones have developed and the distribution of stresses through the rock mass is fairly uniform (Figure 7.4a).

By 100 000 cycles, clear strain zones have developed with the maximum displacement at the surface of the south face (Figure 7.4b). The rotational distribution of strain associated with the rotational sliding failure of the south face can be seen. The north face also shows a similar rotational distribution of strain, but this is related to flexural toppling mechanism, rather than rotational sliding; cyan marks the zone of maximum toppling displacement. Also, the depth of failure is greater for the toppling failure on the north face than for the sliding failure on the south face; this may be one reason why toppling on the north face is more time-dependent and ductile. At 200 000 cycles, four strain zones can be identified, which are related to the sliding failure on the south face, with a maximum displacement of 40 m occurring near the surface (Figure 7.4c). The maximum displacement associated with toppling on the north face has slightly decreased, indicating that the north face is beginning to stabilise. At 350 000 cycles, the strain zones are almost homogeneous on the north face, reinforcing the pattern suggested by the displacement vectors that the north slope has stabilised (Figure 7.4d). On the south face, the depth of displacement associated with the sliding failure has increased in response to both secondary toppling and the failure propagating further into the rock mass. By 600 000 cycles, six strain zones have developed on the south face, indicating that failure is well advanced (Figure 7.4e). The strain zones show less

rotational movement than earlier phases in the model, as the increase in the degrees of freedom of blocks allows blocks to slide along joint set 1.

The total history of unbalanced forces shows that initially the unbalanced forces in the model are high, but that an exponential decline in forces occurs as equilibrium is reached (Figure 7.5). The landform shows pulsed events of activity; three main periods are apparent from the model output. Initially, activity is high as the model boundaries are released, and it continues until 180 000 cycles. The second phase of reduced activity then begins and continues to 400 000 cycles, when the third phase of low activity begins.

The second mesh represents an east-west profile of the central cirque wall of Torre de Salinas. The west face is on the right-hand side of the model and the east face on the left-hand side. Displacement vector plots are presented for 10 000 cycles at equilibrium (Figure 7.6a), 100 000 cycles (Figure 7.6b), 250 000 cycles (Figure 7.6c) and 500 000 cycles (Figure 7.6d). The first image shows the central cirque wall of Torre de Salinas at equilibrium by 10 000 cycles (Figure 7.6a). At 100 000 cycles, the displacement vectors show deep-seated flexural toppling on the west face (Figure 7.6b). The failure mechanism cannot be described as block toppling because major rotation of individual blocks has not occurred. Joint sets 1 and 2 dipping at 79.76° and 77.22°, respectively, are controlling this toppling failure. The displacement vectors at 250 000 cycles are almost identical to those found for the model at 100 000 cycles, and the zone of flexural toppling remains constant (Figure 7.6c). At 500 000 cycles the displacement vectors indicate that flexural toppling is still the dominant failure mechanism (Figure 7.6d). Any change in the orientation of the vectors would have suggested a change from ductile flexural toppling to a more brittle block toppling mechanism. A block plot produced at 500 000 cycles without displacement vectors shows a zone of buckling associated with flexural toppling and the formation of anti-scarps on the west face. Antiscarps are often the only geomorphological evidence of ductile deformations in hard rock mountain slopes.

Displacements in the rock mass are directly related to the mode of failure operating within the rock mass. At equilibrium a uniform strain distribution has developed, with no clear organisation (Figure 7.7a). At 100 000 cycles, seven main strain zones associated with the flexural deformation can be identified, producing a displacement of 14 m (Figure 7.7b). By 250 000 cycles the number of strain zones has decreased to four, reflecting the increased depth and propagation of failure in the model, with a

maximum displacement of 40 m (Figure 7.7c). The situation persists until the end of the simulation with no further shear band development or accumulation of flexural displacements (Figure 7.7d). UDEC modelling has suggested that flexural toppling exhibits self-stabilisation (Nichol *et al.*, 2002). The present work adds weight to this contention through demonstrating the self-stabilisation effect in natural mountain slopes.

The total history of unbalanced forces recorded throughout the simulation shows a generally low level of geomorphic activity compared with the forces for the northern cirque wall, which underwent a brittle rotational sliding failure. Five major peaks in geomorphic activity can be resolved, indicating pulsed activity in the rock mass (Figure 7.8). Activity is moderate until 200 000 cycles, when the level of activity decreases to almost zero, giving further support for the contention that slopes which deform through flexural toppling are characterised by self-stabilisation.

The final model mesh constructed to model the geomorphic evolution of Torre de Salinas is the east-west profile of the southern wall, taken perpendicular to the free face. The east face is located on the left-hand side of the model and the western face, which continues into a large ridge, is situated on the right-hand side of the mesh. A block plot of the rock mass geometry at equilibrium is presented in Figure 7.9a. Initial movements can be detected by 200 000 cycles and indicate that sliding is the major failure mechanism (Figure 7.9b). By 400 000 cycles, the displacement vectors show that sliding is the predominant failure mechanism but that secondary toppling is occurring at the toe of the slope, shown by a re-orientation of the displacement vectors from vertical to sub-horizontal (Figure 7.9c). A similar pattern is shown at 800 000 cycles, but the failure is beginning to show rotational movements caused by the unloading of the toe by the movement of failed material towards the bedrock ramp (Figure 7.9d). The zone of secondary toppling has also increased compared with that at 400 000 cycles. Sliding of the rock blocks has caused a series of terraces to form close to the crest of the west face, and although no field evidence could be found for this at Torre de Salinas, tentative evidence (e.g. uphill-facing bedrock steps), for anti-scarp formation was found during a climb of the south face of Peña Santa de Castilla in the Western massif.

The development of strain zones in the model shows an interesting pattern. At equilibrium no strain zones have developed (Figure 7.10a). By 200 000 cycles, six strain zones can be identified on the western face associated with sliding failure

(Figure 7.10b). The strain zones show rotation associated with the development of rotational sliding in the model. Away from the west face, very little displacement is occurring. By 400 000 cycles, increased rotation has occurred in the distribution of strain caused by blocks beginning to be pushed out and away from the free face along the bedding (Figure 7.10c).

7.3.2 Pico de la Padierna

The initial model mesh for the western section of the truncated ridge of Pico de la Padierna at equilibrium is plotted in Figure 7.11a. By 530 000 cycles no failures have developed and the displacement vectors show no preferred orientation (Figure 7.11b). Plots of strain distribution at equilibrium show that no strain zones have developed. By 530 000 cycles, five strain zones have developed, producing a maximum displacement of 1.6 m near the surface of the south face (Figure 7.12). The magnitude of displacement decreases with distance from the free face. The model confirms field observations which suggest that large failures have not occurred on this face (Plate 7.2c).

The initial mesh for the central section of the ridge of Pico de la Padierna at equilibrium is plotted in Figure 7.13a. By 150 000 cycles, the displacement vector plot shows that a sliding failure has developed, indicated by the vertical, downward orientation of the vectors (Figure 7.13b). The sliding failure is controlled by joint sets 1 and 2, which dip at 71° and 76°, respectively, towards the south. Re-orientation of the vectors has also occurred towards the toe of the south face because failed blocks are beginning to move down the ramp in front of the free face. The displacement vectors plotted at 550 000 cycles indicate that the sliding failure is still continuing but that the failure only involves the blocks which originally failed (Figure 7.13c), with little movement occurring away from the free face. A block plot without displacement vectors taken at 550 000 cycles shows that those blocks which failed by vertical sliding have undergone translation to a horizontal sliding movement as blocks slide over the failed debris at the base of the slope (Figure 7.14). The mode of failure on this slope represents a rock slump (Goodman and Kieffer, 2000; Kieffer, 1998). The failure describes a mode of backward rotation of hard blocks as they move from their original free face position. The sequence of displacement plots shows how the successive slumping of multiple blocks produces a scar resembling that of a classical soil slump. However, the internal anatomy of the failure is

different with independent back rotated blocks and large tabular apertures. The degree of block slumping changes according to block stiffness and the degree of cross-jointing (Goodman and Kieffer, 2000).

Plots of strain zone development in the model were taken at equilibrium, 150 000 cycles, 250 000 cycles and 550 000 cycles. At equilibrium, although no movement has taken place, the zone of greatest strain is concentrated near the surface of the south face, producing a maximum displacement of 1.5 m (Figure 7.15a). By 150 000 cycles, two strain zones have formed in the active zone of sliding (Figure 7.15b). The outer shear zone has produced 25 m of displacement, while the inner shear zone has undergone 20 m of displacement. As the failure becomes more advanced, the number of shear zones increases and by 550 000 cycles four main shear bands have developed with displacement magnitudes ranging from 100 to 40 m (Figure 7.15c). As the failure progresses, the displacement zones indicate that the number of shear surfaces increases, because of friction between the detached rock blocks. The contoured displacement plots show that surface movements are more than twice those at depth. The depth of deformation in this sliding failure is shallower than for the toppling failures at Torre de Salinas. The total history of unbalanced forces at 530 000 model cycles shows that, although the level of geomorphic activity is relatively high, there has been an exponential decline (Figure 7.16). The level of activity recorded at the end of the simulation is caused by continuing sliding of failed blocks, rather than the development of new failure surfaces.

The third mesh constructed to simulate the geomorphological evolution of Pico de la Padierna is a north-south profile of the eastern part of the ridge. The south face is located on the left-hand side of the model and the northern slope on the right-hand side. A block plot of the model mesh at 10 000 cycles after consolidation is presented in Figure 7.17a. By 500 000 cycles, the displacement vector plot shows that no failures have developed (Figure 7.17b). Despite the lack of failure, displacements have developed in the model, even though the maximum displacement is less than 80 cm (Figure 7.18) Although the rock mass is in equilibrium with the present geometry of the slope, the geomorphological implication is that the surface of the free face is most highly stressed, making the face more susceptible to environmentally induced stresses, such as weathering or rainfall input. Weathering could promote large-scale failure through a reduction in the strength of the discontinuities. The total history of unbalanced forces at 500 000

cycles shows that, after an initial period of activity the out-of-balance force has declined to zero after 20 000 cycles (Figure 7.19).

7.3.3 Tiro Pedabejo

The initial north-south profile showing the model after consolidation at 10 000 cycles is plotted in Figure 7.20a. By 500 000 cycles no failure surfaces have developed and the displacement vectors show that the discontinuity network is not conducive to the development of failures and that the landform is in stress equilibrium (Figure 7.20b). A plot of the total history of unbalanced forces at 500 000 cycles confirms that no failures have developed (Figure 7.21). Despite this, analysis of strain zone development in the rock mass can indicate how the landform may evolve in response to environmental stress. Displacement contours at equilibrium show that the model is stable and no shear surfaces have developed (Figure 7.22a). By 500 000 cycles, ten strain zones have developed suggesting that small shear displacements have occurred (Figure 7.22b). A maximum displacement of 2.5 m has occurred on the south face (right-hand side) of the model. Despite initial displacements, blocks have not become detached from the free-face. The geomorphological implication of the pattern of strain distribution is that as weathering becomes more advanced, block detachment will occur from the south face in response to the additional stress and loss of strength in the landform. The maximum displacement that has developed on the north face is 1.5 m. This confirms field evidence suggesting that block detachment caused by weathering is more important on the south face.

A second model simulates the geomorphological behaviour of the east-west profile of Tiro Pedabejo. The initial mesh at equilibrium is plotted in Figure 7.23a. By 20 1000 cycles, the displacement vectors are orientated parallel with joint set 2 on the west face, indicating that sliding failure has begun (Figure 7.23b). No failures have occurred on the eastern free face; the displacement vectors are of low magnitude and orientated almost vertically with respect to joint set 2. Kinematic analysis does not indicate failure of the west face, because the transformation of joint surfaces on the UDEC mesh represents the geometry of the slope more accurately (Chapter 5, Table 5.3). After 351 000 cycles, the sliding failure on the west face is more advanced and blocks have become detached from the free face (Figure 7.23c).

The magnitudes of the displacement vectors on the east face indicate that the face is stable with respect to the natural stresses present in the rock mass. Anti-scarps have formed at the crest of the sliding mass, indicating that in the field, sliding displacements could be recognised from geomorphological evidence. Towards the base of the sliding zone and away from the main failed mass, the displacement vectors show sliding is occurring along the bedding. Sliding along the bedding is in response to the weight of overburden from overlying blocks and unloading of the face increasing the potential for sliding along the bedding. By the end of the simulation at 610 000 cycles a similar situation exists, but the sliding failure is more advanced (Figure 7.23d). A zone of rotation is present towards the toe of the slide in response to block sliding along joint set 2 and then along the bedding in response to unloading. The dip of the bedding out of the west face is crucial. Without bedding blocks sliding along joint set 2 would remain stable without any surface over which translational movements could occur.

Development of the strain zones clearly indicates the pattern of stress-strain in the rock mass associated with the development of failures. At 201 000 cycles, four strain zones have developed on the west face in response to the sliding failure (Figure 7.24a). The maximum surface displacement of the slide is 20 m, but decreases to 4 m at depth. The development of the rotational zone of translational shear along the bedding is clearly identified by the yellow displacement zone and also by the sharp boundary of light green indicating zero displacement (Figure 7.24a). On the east face, displacement magnitudes are fairly homogeneous, varying between 0 and 2 m, which shows that the instability suggested by the displacement vectors is correct. At 351 000 model cycles four main strain zones are present on the west face, producing a maximum surface displacement of 50 m, decreasing to 10 m at the base of the sliding zone (Figure 7.24b). The translational shear zone is still present, but has become stepped because of an increase in the magnitude of sliding and increase in the degrees of freedom of each block at the toe of the slope in response to unloading of the face. The strain zones at the end of the simulation at 610 000 cycles show a maximum displacement of 80 m in the sliding mass which is not in 'free-fall' (Figure 7.24c). Increased rotation of the strain zones has occurred towards the base, in response to further unloading of the free face and continued translational shear along the bedding, rather than the development of a true rotational failure. No further displacement has occurred on the east face, indicating stability.

The unbalanced forces for the east-west profile show pulsed but nonetheless high levels of activity in the rock mass (Figure 7.25). Three main periods can be identified. The first period occurs after the release of the model boundaries, continues until 20 000 cycles, and is followed by a period of relative inactivity. The second phase begins at 70 000 cycles and continues until 430 000 cycles, with levels of activity increasing towards the end of this period. This ends suddenly; activity does not resume until 500 000 cycles and then continues until the end of the simulation at 601 000 cycles. The level of activity increases towards the end of the simulation, indicating that blocks on the west face, away from the initial failure at depth are beginning to move. The plot indicates that although the sliding is relatively brittle, the development of translational movements means that sliding is not continuous, as would be expected for a purely planar slide.

Field evidence suggested that the north face of Tiro Pedabejo was unstable because of the presence of rock-fall deposits. However, the modelling suggests that the west face is unstable, and the source of debris on the north face. The geometry of the sites means that it is possible for failed debris on the west face to be transported on the north face.

7.3.4 Canchorral de Hormas

Two model meshes were constructed to simulate the important characteristics of the San Carlos conglomerate limestones which outcrop at Canchorral de Hormas. The first model simulates a north-south profile through the rock mass. The south-east face of the model is on the left-hand side and the north-west face on the right-hand side: the initial mesh after consolidation is plotted in Figure 7.26a. Once both faces have been released, failure on the south-east face occurs by sliding and then secondary rotation of basal debris. By 100 000 cycles bulging occurs at the toe of the south-east face indicating that shear displacements associated with sliding failure have begun, shown by the horizontal orientation of the displacement vectors (Figure 7.26b). By 250 000 cycles the displacement vectors clearly show that sliding is the dominant failure mechanism, as they are orientated parallel to joint set 2, which dips at 55° to the south (Figure 7.26c). Anti-scarps have developed towards the crest of the failing mass, suggesting that the deformation is time-dependent rather than catastrophic. The anti-scarps are formed by differential displacement along joint set 2, which increases the number of degrees of freedom of

each block, allowing small rotations to occur towards the north. The rotations are controlled by joint sets 3 and 4, which dip at 75° and 76°, respectively on the mesh. A large cavity has also begun to form at the base of the failed material, caused by the sliding of blocks on to the top surface of failed material. By 500 000 cycles, a block plot shows that failure is still occurring and that material is flowing down, and beginning to accumulate on the bedrock slope at the toe of the rock slope (Figure 7.26d). The accumulation of failed material on the bedrock slope replicates the field situation very well; this is important because the model confirms that this area of slope is the source of material for the block field which in turn acts as a coarse sediment supply for a large debris flow system.

The development of stain zones shows how the strain distribution in the rock mass is related to failure mechanism. At 10 000 cycles, after consolidation, no distinct strain zones have developed (Figure 7.27a). By 100 000 cycles, six main strain zones have developed associated with the onset of failure on the south-east face. The distribution of strain shows rotation towards the toe of the slope and this is responsible for the basal bulge indicated on the vector plots (Figure 7.27b). The displacement has produced a maximum of 5 m of deformation towards the toe of the slope. By 500 000 cycles, eight strain zones have developed on the failing south-east face (Figure 7.27c). The formation of strain zones are caused by the gravitational acceleration of blocks and differential friction between the displacement zones which have developed. The maximum displacement at this stage of the simulation is 40 m. The distribution of strain follows joint set 2 and indicates that shear displacements are dominating the failure.

The total history of unbalanced forces indicates that movements are episodic, with four main periods of movement; the maximum level of activity is associated with the release of the model boundaries at 10 000 cycles (Figure 7.28). Throughout the simulation, levels of activity are relatively low, adding weight to the geomorphological evidence for time-dependent deformation, through anti-scarps, rather than catastrophic failure characterised by a 'burst' of geomorphological activity followed by relative inactivity.

The second mesh simulates the east-west profile of the west wall at Canchorral de Hormas. The east face of the rock mass is on the left of the model mesh and the west face on the right. The initial mesh at 10 000 cycles is plotted in Figure 7.29a. By 100 000 cycles the displacement vectors indicate that the east face of the rock

slope is undergoing failure by sliding, controlled by joint set 4, which dips at 68° to the east Figure 7.29b). A toe bulge has formed in response to the additional stress imposed by the sliding material. Away from the free face, the displacement vectors indicate very little movement, although some rotation of the vectors occurs at depth towards the free face, indicating that movement may occur if the face is unloaded. Failure is well advanced by 200 000 cycles and a rotational failure has developed and the failed blocks are moving over previously failed material (Figure 7.29c). The displacement vectors show that the level of activity away from the failure is very low, and that the failure is shallow, which is characteristic of sliding failures in brittle materials such as limestone. Material is beginning to move down the bedrock ramp at the toe of the slope by 500 000 cycles, under gravity and the weight of overburden from failed material (Figure 7.29d). Activity away from the free face is low, suggesting that once failure has occurred, the landform will be in equilibrium with respect to the internal stresses and discontinuity network, providing external forces do not lead to a substantial change in boundary conditions. The deposition of material on the bedrock ramp at the slope toe forms the block field observed in the field. The modelling results confirm field observations which concluded that it was very difficult to determine which face was responsible for the supply of debris to the block-field. The modelling exercise also provides clues on why the block field exists: the geometry of the bedrock ramp and the nature of the failure mechanism causes the blocks to 'flow' along the ramp rather than experience free-fall once they have become detached from the free-face. This results in failed material being relatively intact, so that the block field is composed of large (10 m) blocks.

The development and evolution of strain zones within the model is important because this gives information on the pattern of deformation within the rock mass. Once stepped to equilibrium at 10 000 cycles, no strain zones have developed (Figure 7.30a). By 100 000 cycles, five main strain zones have developed and are related to the onset of failure, producing a maximum shear displacement of 7 m (Figure 7.30b). The magnitude of displacement decreases with distance from the free face and contours indicate a displacement of 2 m. At 200 000 cycles, four strain zones have developed in the failed zone producing a maximum displacement of 25 m (Figure 7.30c).

The total history of unbalanced forces for the east-west profile at 500 000 cycles shows four main periods of activity (Figure 7.31). The greatest period of activity occurs at 100 000 cycles and can be related to the onset and propagation of failure.

Thereafter, rates of activity remain relatively low, and coincide with the decrease in the speed of failure. A slight increase in the unbalanced forces occurs between 250 000 and 300 000 cycles, which is related to the movement of failed material along the bedrock ramp, rather than the development of new failure surfaces.

7.3.5 Los Montes, Deva Gorge

Three model meshes were constructed to simulate the landform at Los Montes in the olistrome / turbidite limestones of the Lebeña Formation. The first simulates the east-west profile and the initial model mesh after consolidation is plotted in Figure 7.32a. The east face is on the right-hand side of the mesh and the west face is on the left. The west face is fixed because the landform merges into the valley slope. By 300 000 cycles, displacement vector plots show the development of a sliding failure on the west face (Figure 7.32b). Some buckling of the slope has taken place, and flexural deformations have begun. The displacement vectors are perpendicular to the east face, indicating potential for failure on the east face, where the main valley road runs. The failure on the west face is not considered to be representative of field conditions, because merger of the landform into the valley slope would prevent failure through buttressing the toe of the west face. The model was constructed in the way presented because of computational limitations and does not influence the development of buckling on the east face. Visual analysis of the model output suggests that the east face has stabilised because the magnitude of the displacement vectors is low.

The plot of unbalanced forces is misleading: it does not show a clear reduction in activity, due to the continuing failure on the west face. The failure of the west face would not occur in practice because the slope is bounded by a ridge (Figure 7.33). The contoured plot of horizontal displacement at 300 000 cycles shows a maximum displacement of 20 m on the west face in response to buckling of the slope (Figure 7.34). Analysis of previous plots shows that over 250 000 model cycles, only 5 m of displacement has occurred, indicating relative stability.

The second model mesh simulates the likely geomorphological impact that a road extension would have on the landform at Los Montes. A model simulating road extension was constructed because the previous model indicated that the geometry of the slope toe aided stabilisation of the slopes. The proposed extension of the

road would require a cut to be made in the toe of the east face, because the Rio Deva prevents eastward extension of the current road, and thus potentially de-stabilise the slope. The initial mesh, showing the road cut at 10 000 cycles, is plotted in Figure 7.35a. At 100 000 cycles, the displacement vectors are sub-horizontal showing that substantial deformation of the east face has occurred through a combination of flexural and block toppling (Figure 7.35b). The failure of the rock mass is a direct response to the unloading of the slope toe by the road cut. The failure is much more advanced at this stage of the simulation than in the previous model with no road cut. By 300 000 cycles the failure of the rock mass is more advanced and blocks have become detached from the east face and have been deposited in the area presently occupied by the Rio Deva (Figure 7.35c). Anti-scarps have also formed on the east face in response to the toppling failure.

The distribution of strain in the rock mass shows that five main strain zones have developed by 100 000 cycles, producing a maximum displacement of 60 m on the surface of the east face, but decreasing to 20 m at depth (Figure 7.36a). The deformation associated with the flexural and block toppling indicated by the displacement contours is deep-seated, in comparison with most sliding failures seen in previous models. The depth of the toppling zone is indicated by the formation of a shear surface (yellow) in the rock mass. By 300 000 cycles the number of strain zones associated with the failure has decreased to three, producing a maximum surface displacement of 80 m (Figure 7.36b). If the simulation were continued it is likely that the failed material would impart some stability to the rock mass through buttressing of the slope toe. The analysis of strain zone formation shows how the road cut has influenced the stress-strain response of the rock mass and its associated geomorphological behaviour. The deep-seated nature of deformation in this slope would make it very hard to implement remediation measures to prevent deformation if a road cut were made.

The third mesh for Los Montes simulates the north-south profile, with the south face located on the right-hand side of the mesh and the north face on the left-hand side. The initial mesh at equilibrium is plotted in Figure 7.37a. By 100 000 cycles a pronounced shear surface has developed along the bedding, which dips at 137° on the mesh and coincides with the break of slope of the north face (Figure 7.37b). The displacement vectors are parallel to the bedding, indicating that planar sliding is the dominant failure mechanism. By 300 000 cycles the sliding mass has developed two main shear surfaces and the position of the bedding controls the depth of failure

(Figure 7.37c). If the bedding did not outcrop at the toe of the slope, then the depth of failure would have been shallower.

Six main strain zones have developed in the sliding failure by 100 000 cycles, producing a maximum displacement of 16 m (Figure 7.38a). The shear surface is indicated by the light red homogeneous zone with a displacement of 2 m. There is a small zone of increased deformation above this, but below the main shear surface. Increased deformation occurs because elastic deformation of the rock blocks is produced by friction of the overlying sliding mass. The zone of increased deformation is similar to the ductile zone often associated with the development of shear surfaces in unconsolidated sediments. By 300 000 cycles, the number of strain zones associated with the failure has decreased to three, resulting in a maximum displacement of 50 m at the surface and 30 m at the shear boundary (Figure 7.38b). The reduction in the number of strain zones is related to the fact that the speed of failure is slowing and the rock mass is moving as blocks due to joint shear damage along the two main failure surfaces.

7.3.6 Allende

Two models simulate the geomorphological behaviour and evolution of the rock mass at Allende. The first mesh simulates the east-west profile and the initial geometry after consolidation is plotted in Figure 7.39a. The west face is on the left-hand side of the model and the east face on the right-hand side. The magnified plot shows the development of rotational displacements towards the toe of the east face by 100 000 cycles (Figure 7.39b). The rotational displacements are caused by the initial toppling of blocks increasing the number of degrees of freedom of surrounding blocks, and permitting sliding along joint set 2, which dips at 42°. At this stage, catastrophic failure has not occurred and the slope is deforming through flexural toppling. The displacement vectors are perpendicular to the toe of the east face indicating that some blocks are moving outwards.

By 250 000 cycles the model has undergone further flexural toppling on the east face, with the formation of anti-scarps (Figure 7.39c). The west face of the model has undergone some sliding failure, which is associated with shear along joint set 2. The displacement vectors show that the failure is deep-seated; almost the whole rock mass is affected by either sliding towards the west face, or flexural toppling on

the east face. The displacement vectors show a zone of divergence that indicates where the failure mechanism is changing from sliding to flexural toppling (Figure 7.39c). The divergent zone is marked on the plot by a yellow circle. This shows the importance of modelling the evolution of the whole landform, rather than individual free faces; this change in failure mechanism would not have been identified by modelling single faces. By 500 000 cycles, the model has developed a rotational slide on the west face and further flexural toppling has occurred on the east face (Figure 7.39d). The displacement vectors on the east face are of lower magnitude and the face is tending towards self-stabilisation. The development of the rotational slide is a secondary feature, caused by the cambering of joint set 1, dipping at 69° on the mesh, in response to the flexural deformations on the east face.

Displacement plots clearly show the development of strain zones associated with the two failure mechanisms and their divergence. On the east face, four strain zones have developed and are associated with the development of the flexural topple at 100 000 cycles (Figure 7.40a). The maximum magnitude of displacement is 25 m at the surface, decreasing to 10 m at depth. The light green and yellow colours indicate the transitional zone between the two failure mechanisms. On the west face, three main strain zones are present in response to the development of a rotational sliding failure, as indicated by the rotation in the strain zones. The maximum displacement associated with the rotational slide is 15 m. By 250 000 cycles, the number of strain zones associated with the flexural topple on the east face has decreased to three, with a maximum displacement of 30 m (Figure 7.40b). On the west face, five strain zones have developed as the rotational slide has become more advanced, producing a maximum surface displacement of 50 m. By 500 000 cycles, only one strain zone is present on the east face, indicating that the flexural topple is largely stable (Figure 7.40c). On the west face there has been a similar reduction in the number of displacement zones associated with the rotational slide (Figure 7.40c). Three main strain zones exist in the failed material, with a maximum displacement of 80 m. The yellow zone below the sliding mass has undergone deformation due to the sliding over the intact material: it represents the basal shear surface of the rock slide. The history of unbalanced forces at 500 000 cycles indicates a general decline in the activity of the rock mass through time (Figure 7.41). The peaks of activity are associated with movement in the rotational slide and are episodic in nature, showing that geomorphological activity in the rock mass is pulsed.

The second mesh simulates the geomorphological behaviour of the north-south profile at Allende. The north face is plotted on the left-hand side of the model and the south face on the right. The initial mesh at equilibrium is plotted in Figure 7.42a. The displacement vector plot shows that by 100 000 cycles sliding failure has begun along joint set 2, dipping at 42° out of the north face (Figure 7.42b). Some flexural deformations on the south face have also occurred, but these are relatively minor compared with the sliding failure on the north face. For the sliding failure, the displacement vectors indicate that the deformation of the rock mass is deep-seated. At 300 000 cycles, the sliding failure on the north face is more advanced and material has begun to move down the bedrock ramp at the toe of the slope (Figure 7.42c). The displacement vectors on the south face have decreased in magnitude, showing that the flexural deformations controlled by the 69° dip of the bedding have largely stabilised. By 401 040 cycles, the situation is broadly similar: the failure of the north face is more advanced and the magnitudes of the displacement vectors on the south face have decreased, indicating that the south face is virtually stable (Figure 7.42d). The model output was captured at 401 040 cycles because the UDEC simulation crashed, due to the number of falling blocks. Although UDEC is able to handle discrete blocks falling through space, it is not able to cope with dynamic problems involving large numbers of fast-moving blocks (Itasca, 2000).

Examining the development of strain zones in the rock mass provides greater information on the way in which failures develop in the rock mass. By 100 000 cycles, two strain zones have developed on the south face, associated with the flexural deformation, producing a maximum displacement of 10 m (Figure 7.43a). The light green colour, with a displacement of 5 m, indicates a zone of divergence in the mechanism of active failure. On the south face, three main strain zones have developed in response to sliding, producing a maximum accumulated displacement of 15 m. Some rotation of the strain zones has occurred towards the toe of the slope, indicating that the development of the sliding failure is more complex than commonly assumed for planar slides. By 300 000 cycles, the analysis of strain zone development confirms that the flexural deformations on the south face have largely stabilised, with only one main strain zone producing a total displacement of 20 m, only 5 m more than at 100 000 cycles (Figure 7.43b). On the north face, 6 strain zones have developed as the sliding failure has become more advanced. The maximum surface displacement is 70 m, declining to 20 m at depth. As the sliding failure has developed, the strain zones have become orientated towards the bedding, which controls the sliding failure. The rotation of the strain zones is caused

by material failing on to the bedrock ramp, which slightly alters the pattern of strain distribution in the rock mass. The analysis of strain zone development in the whole landform at Allende has shown how displacements associated with different types of failure develop in the rock mass.

7.4 Comparison of numerical simulations

Numerical simulations of the geomorphological behaviour of limestone rock slopes in the Picos de Europa have shown the important characteristics of rock mass failure. The models allow an assessment of the development and distribution of strain zones associated with different failure mechanisms. Detailed numerical simulations of rock slope behaviour in the Picos de Europa have shown a range of failure mechanisms, including deep-seated catastrophic topples, relatively shallow slides and self-stabilising flexural deformations. The dominant failure mechanisms for each model are summarised in Table 7.2.

The dominant failure mechanism is sliding, caused by the steeply dipping joints and bedding in the Picos de Europa caused by folding of the strata. Sets 1 and 2 dictate the shear surfaces of the sliding failures, but also the height of blocks in the toppling failures. Kinematic analysis suggested that bedding was the dominant control on sliding failure, but set 1 and 2 dip more steeply on the UDEC meshes after conversion controlling the occurrence of sliding failures.

Site / Model	Dominant failure mechanisms	Responsible joint set
TS1	Sliding and flexural toppling	Sliding = set 1 Topple = set 3
TS2	Flexural topple	Sets 1 and 2
TS3	Sliding with secondary toppling	Set 1
PP1	Stable	n/a
PP2	Stable	n/a
PP3	Sliding	Sets 1 and 2
TP1	Stable	n/a
TP2	Sliding	Set 3
CH1	Sliding with secondary toppling	Set 3
CH2	Sliding	Set 2
LM1	Self-stabilising flexural topple	Set 4
LM1a	Flexural topple	Set 4
LM2	Planar slide	Set 4
AL1	Rotational sliding / flexural toppling	Set 5
AL2	Rotational sliding / flexural toppling	Set 5

Table 7.2: Summary of the dominant failure mechanisms determined from the UDEC model output. The joint sets correspond to those assigned in Chapter 5, rather than the UDEC input parameters given in Table 7.1. Notation is that given in Table 7.1.

Analysis of strain zone plots has shown that in many cases, sliding failures are initiated as rotational slides, which then develop into planar/translational slides more commonly associated with rock masses. Modelling the development of rotational slides in rock masses is important since these failures are more commonly associated with unconsolidated sediments. The development of those failures in rock slopes reinforces the theoretical modelling (Chapter 4), indicating that block size exerts an intrinsic control on the type of failure occurring in rock slopes. The discontinuity spacings in the Picos de Europa limestones are all below 2.5 m, which produces block sizes that are very small compared with the size of the landform (Chapter 5, Table 5.5). Rotational failures occur because the rock mass behaves as

a granular rather than blocky mass when block size is small compared with the size of the failure (Hoek and Bray, 1981).

For comparisons between sites, a more general approach to analysing the failures is needed than the detailed site-by-site model outputs presented earlier. One approach to summarising the behaviour of the rock slopes is to analyse the pattern of failure. Analysis landslide movement can provide insights into the processes occurring during failure (Terzaghi, 1950). Landslide movement patterns have previously been examined by plotting the acceleration of failures in λ-t space, where $\lambda = 1/v$, t is time and v is velocity (Petley *et al.*, 2002). The velocity is taken to be the rate of displacement of the landslide over time. Petley *et al.* (2002) found that most movement patterns produced non-linear asymptotic non-zero trends related to crack initiation and propagation during failure.

For the current simulations, UDEC had difficulty in replicating the λ-t space relationship, so it was decided to plot λ as$1/\rho$, where ρ = horizontal displacement against time t.

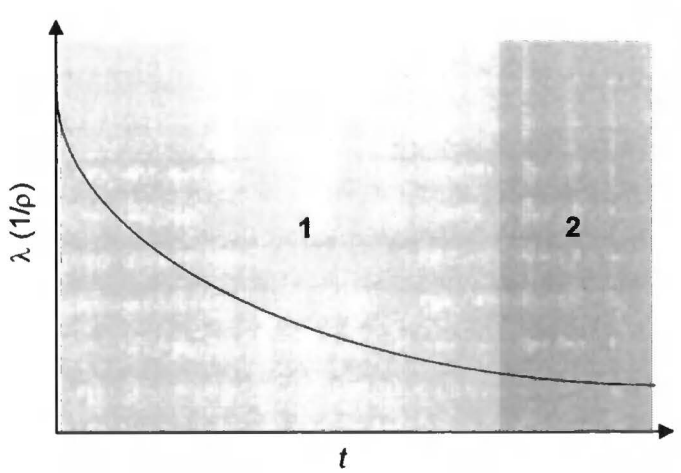

Figure 7.44: Schematic diagram of a the development of failure, plotted in λ-t space.

As failure begins, small movements occur and displacements increase. In Figure 7.44, this is indicated by a decline in λ, because $\lambda = 1/\rho$ (phase 1). This indicates that failure is being initiated as displacements occur. As the curve flattens out and λ approaches zero, this indicates that failure has occurred and no further displacements are occurring (phase 2). The plots provide a more detailed insight

into the patterns of movement associated with the failure of the rock mass. From a geomorphological perspective it is useful to be able to compare the relative speed of failures. It is possible to fit an asymptotic curve to the data to produce comparative statistics to compare the speed of failure.

For the simulations presented in 7.3.1 to 7.3.6, t is the number of UDEC model iterations, and ρ is the monitored displacement magnitude, of known points within the failure. Points away from the surface of the failing mass were used because strains can occur within the failing mass that are not translated into surface movements. Most models tend towards an asymptotic non-zero value, so it was not appropriate to fit an exponential decay model to summarise the data as has been employed in the past (Ahnert, 1994). Consider a variable y changing over time t from an initial state y_1 to a final state y_2. The curve

$$y = y_1 \exp(-t/\omega) + y_2 (1-\exp(-t/\omega)) \qquad \textbf{Equation 7.1}$$

where: y = x-displacement at t
t = model iteration
y_1 = initial x-displacement
y_2 = final x-displacement
ω = half-way time.

describes an exponential approach to the final state (Cox, pers. comm., 2003).

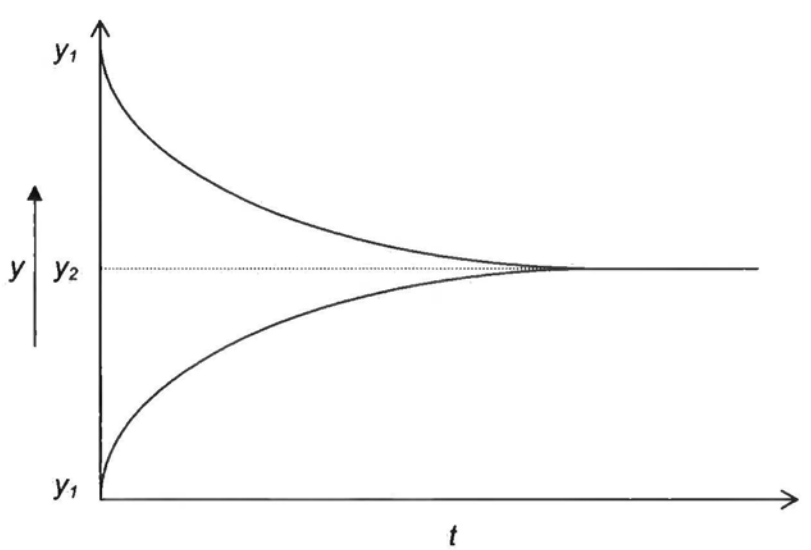

Figure 7.45: Schematic representation of equation 7.1.

The time curve is asymptotic, as the system never actually reaches y_2, but just gets closer and closer as time increases. ω is a characteristic time, interpreted as follows. At $t = \omega$,

$$y = y_1 \exp(-1) + y_2(1-\exp(-1)), \qquad \textbf{Equation 7.2}$$

(Figure 7.45),

and so expressing constants (to 3 decimal places)

$$y \approx 0.368y_1 + 0.632y_2; \qquad \textbf{Equation 7.3}$$

or, in words, after time ω the system has moved $1 - \exp(-1) = 1-e^{-1} \approx 63.2\%$ of the way from its initial state to its final state. ω is thus a little awkward to talk about or think about. It is more convenient to work with a half-way time, which can be thought of as an analogue of the half-life familiar from radioactive decay. A half-way time $k\omega$ can be calculated using the form $\exp(-k\omega/\omega) = 0.5$ so that $k = \ln 2 \approx 0.693$.

In practice this curve is fitted to the failure phase of the model. y_1, y_2 and ω are parameters to be estimated. The curve was fitted by nonlinear least squares using a program by Cox (2003). Once ω has been estimated $\omega \ln 2$ is calculated as the half-way time. It thus gives a handle on the time scale over which major change takes place, as it gives the time to go half-way from y_1 to y_2.

A summary of all model runs is presented in Table 7.3.

Site	y_1	y_2	ω	R^2	rmse	half-way
TS1	1.066	0.017	25072	0.991	0.010	17379
TS2	0.771	0.024	30025	0.992	0.008	20811
TS3	3.263	0.045	30018	0.994	0.029	20806
PP1	-------	-------	-------	-------	-------	-------
PP2	-------	-------	-------	-------	-------	-------
PP3	0.648	0.015	34675	0.987	0.010	24035
TP1	-------	-------	-------	-------	-------	-------
TP2	0.897	0.014	59513	0.973	0.010	41251
CH1	2.282	0.044	22727	0.950	0.067	15753
CH2	0.961	0.026	72113	0.984	0.029	49985
LM1	0.293	0.012	31008	0.922	0.020	21493
LM1a	0.693	0.036	12502	0.992	0.007	8665
LM2	0.889	0.029	23253	0.945	0.029	16118
AL1	0.490	0.010	12054	0.792	0.005	8355
AL2	0.394	0.018	39755	0.980	0.011	27556

Table 7.3: Summaries of halfway time and associated statistics for all model runs. Models with no data remained stable during the simulation. Notation is that given in Table 7.1.

A plot of the half-way time by site clearly shows that the failure in CH2 takes the longest time to develop; half-way time = 49985 model cycles (Figure 7.46). The development of catastrophic failure in TP2 where the half-way time takes the second longest time to develop. CH2 and TP2 are characterised by catastrophic, deep-seated failures that involve large volumes of rock. Both failures involve sliding along a bedrock ramp, which slows the speed of failure. The failures involving large volumes of material have a occur over a greater period of time than smaller failures. Similarly, the halfway time for CH1 is 15753 and involves a sliding failure where the displacement is limited to some extent by a bedrock ramp fronting the slope toe. The speed of failure propagation in LM1a is very rapid; the half-way time = 8665. LM1a simulates the east-west profile of Los Montes, without a road-cut, and exhibits self-stabilisation, with small creep movements dominating deformation after initial movements. The half-way time suggests therefore that the initial failure is relatively small and non-catastrophic.

The halfway time can be considered as analogous to the geomorphological concept of relaxation time because it indicates that the landform is moving towards a new state of equilibrium (Brunsden and Thornes, 1979; Brunsden, 1980, 1993). The half-way time gives an approximation of the time taken for the slope to move from an initial equilibrium to a new state of equilibrium after the failure event. Out-of-balance forces and an unstable slope geometry cause the slopes to fail. The initial condition of instability is followed by failure and the time taken for the failure/instability to propagate through the landform and reach a new equilibrium is equivalent to relaxation time; indicated by the half-way time. Once the failure has stabilised, the landform has reached characteristic form time (Brunsden, 1986). The magnitude-frequency of the out-of-balance forces, or reaction time, of the landform influences the relaxation time. Models with higher magnitudes of unbalanced forces typically head towards catastrophic failures, which are characterised by a greater half-way time.

Summary statistics provided by the fitted exponential asymptotic model suggest that large, catastrophic failures are characterised by greater half-way times. However, an examination of displacements in the model gives more detailed information regarding movement patterns during slope failure.

For Torre de Salinas, all curves show the same pattern of movement, despite differences in the failure mechanism (Figure 7.47). In all models, the curve is beginning to flatten out by 200 000 model iterations indicating failure has occurred and further displacements have ceased. Even for failures which are time dependent, such as flexural toppling, the movement pattern is characterised by initially rapid displacements (Figure 7.47).

At Pico de la Padierna, displacements are only available for the mesh constructed to simulate the central part of the ridge, because this was the only model to undergo failure. Displacements increase until 60 000 cycles when there is a temporary pause in failure until 80 000 cycles (Figure 7.48). This is followed by an increase in the magnitude of displacements until approximately 200 000 cycles, where displacements continue due to small creep movements.

A similar pattern is observed for Tiro Pedabejo, where three main periods of temporary stabilisation of the sliding mass can be seen (Figure 7.49). The first occurs between 121 000 and 141 000 cycles; the second between 151 000 and 171

000 cycles and the third between 221 000 and 251 000 model cycles. A number of further minor steps can be resolved from 300 000 cycles, but these are considered to be creep related displacements associated with stress redistribution within the failed mass.

Displacements associated with the modelled failures at Canchorral de Hormas also show that displacements are discontinuous (Figure 7.50). For the north-south profile, at least seven periods of temporary stabilisation of the failure can be recognised (Figure 7.50a). The plot of displacements for the east west profile show one main period of temporary stabilisation. However, this is followed by a decrease in the magnitude of displacements as failure has occurred and the rock mass is moving towards equilibrium (Figure 7.50b). By 200 000 cycles displacements are negligible indicating that failure has occurred and that the mass has stabilised. Further displacements are caused by creep.

For Los Montes, displacement plots show similar patterns to those described above, with temporary periods of stabilisation, even though failures are still active (Figure 7.51). The most interesting case is for the east-west profile with simulated road-cut, where movement ceases between 20 000 and 60 000 cycles (Figure 7.51c). The failure mode in this model is controlled by sliding along a bedding structure and the temporary stabilisation may be associated with shear strength being mobilised along the bedding. Further displacements continue once the shear strength of the bedding has been exceeded. Continued displacements occur, but these tend to be relatively small.

Displacement for Allende are plotted in Figure 7.52. A similar pattern of temporary cessation of movement can be seen for the flexural toppling failure on the east-west profile of Allende, where three main periods of zero displacement occur (Figure 7.52b).

This research indicates that displacements within failing masses are not continuous and are frequently characterised by periods of temporary stabilisation. There are several implications of these findings, particularly for monitoring slope failures in jointed rock masses. Geomorphologically, the results indicate that slope failures are discontinuous, particularly where the slope is continuing to adjust to new stress regimes imposed by glaciation. Movements are not continuous through time, suggesting that geomorphic activity occurs in a series of pulses, with the lag time

being dependent on how quickly stresses propagate throughout the rock mass. Periods of instability are followed by short periods of high-energy geomorphic activity as failure continues. The suggestion that periods failure of a rock mass involves periods of temporary stabilisation followed by periods of activity is important when considering timescales of slope development and failure propagation. From a geomorphic perspective, it is often assumed that failures are almost instantaneous in time in rock masses and that slope deformations dominated by creep movements are more representative of the long-term condition but rarely leading to catastrophic failure. However, numerical modelling suggests that catastrophic failures can take a considerable period of time to develop, partly caused by stress redistribution and partly caused by temporary stabilisation.

From the results presented here, no clear mechanism can be invoked to explain the apparent temporary stabilisation exhibited in the numerical models. Comparison with the plots of unbalanced forces suggests that periods temporary stabilisation may be related to periods when the out of balance force is close to zero. However, there is no conclusive evidence for this. In addition, periods of temporary stabilisation do not appear to be related to self-stabilisation of the global rock mass. Global stabilisation of the rock mass on the plots presented is indicated by λ approaching zero. The main periods of stabilisation occur before this point has been reached, while rock mass failure is still active. This suggests that temporary stabilisation of the failing mass is an inherent feature of some failures. More research is required to explore these relationships more fully to determine which mechanisms may be causing temporary stabilisation.

Where monitoring indicates that an initially moving mass has stabilised, the results should be carefully considered in the light of the movement patterns produced by the numerical models. These results suggest that monitoring of landslide movements should continue for a period after the data indicate that the failing mass has stabilised. Unfortunately, it is difficult to assess the time period over which monitoring should continue from the results presented here and requires more research.

It is difficult to assess how the model output compares with the field situation of each site, because modelling transgresses temporal boundaries, which cannot be assessed from field observations. However, some features apparent in the model output can be identified at some field sites. Anti-scarp formation is the most notable

example of how model output mirrors the field situation. These features are located all around the Picos mountains and indicate time-dependent deformation of the slopes. One of the best examples is at Pena Remona, where a back-tilted block is associated with the gradual deformation of the slope caused by rotational sliding (Plate 7.8). The features can be recognised in the field by breaks of slope in the large walls comprising the main peaks. As these features are present throughout the Picos, slope deformations indicated by the model output can be considered as representative of a dominant geomorphic process in these mountains. For the models run to simulate the behaviour of Canchorral de Hormas, the output indicated how failed material supplied a block field with debris for gradual down-slope re-distribution. In the field it was difficult to observe the failure mechanism operating on many slopes because of the large outcrop size and marginal vegetation.

7.5 Temporal evolution of the rock slopes

Suggested causes of rock slope failures in Alpine environments include glacial oversteepening, elevated water pressures in discontinuities under periglacial conditions or during deglaciation and progressive failure following deglaciation due to shearing along joints. Although UDEC modelling has indicated the mechanics of failure, evaluation of possible causes and triggers of rock slope failure is hindered by a lack of dating evidence. To improve understanding of the triggering mechanisms and temporal evolution of the rock slopes in the Picos de Europa, cosmogenic ^{36}Cl dating was carried out on samples extracted from large failures at sites chosen for UDEC modelling.

7.5.1 Background to Cosmogenic Chlorine-36 dating

Cosmogenic exposure age dating, which relies on the measurement of rare isotopes produced in near surface rocks by cosmic-ray bombardment, can be used to date bare rock surfaces (Cerling and Craig, 1994). Organic debris is absent from the deposition zone of failed material, so dating methods such as ^{14}C cannot be used to date the timing of slope failure. Cosmogenic nuclide accumulation is a function of exposure time, geographic location, and the abundance of target elements in a sample (Zreda *et al.*, 1991).

To date the limestone boulders of the Picos de Europa, the cosmogenic isotope used was chlorine-36 (half-life = 301500 yrs). The isotope is one of several

cosmogenic isotopes (i.e. ^{10}Be, and ^{26}Al). Unlike other isotopes, ^{36}Cl does not require silica to be present in the rock for its production making it ideal for application on carbonate geologies.

The production rate of ^{36}Cl is heavily dependent upon rock chemistry. The nuclear processes that produce cosmogenic ^{36}Cl in rocks are spallation, neutron capture and muon capture (Swanson and Caffee, 2001). The first two processes dominate surface production by cosmic ray-induced reactions with ^{35}Cl, ^{39}K and ^{40}Ca. Below approximately 1 m depth, muon production of ^{36}Cl in calcium (^{40}Ca) and potassium (^{39}K) become important production pathways (Gosse and Phillips, 2001). The decay of radioactive uranium (U) and thorium (Th) can also contribute to the production of ^{36}Cl in a rock by neutron capture (Bentley *et al.*, 1986). This subsurface ^{36}Cl, generally in secular equilibrium (Swanson and Caffee, 2001), is not produced through interaction with cosmic rays and must be subtracted from the total accelerator mass spectrometry (AMS) measured ^{36}Cl to determine the cosmogenic component (Phillips *et al.*, 1986).

The production rate of cosmogenic ^{36}Cl in rock exposed at the earth's surface is dependent upon its calcium, potassium and chloride content, expressed by

$$P = \psi_{ca}(C_{ca}) + \psi_k(C_k) + \psi_n\left(\frac{\sigma_{35}N_{35}}{\sum \sigma_i N_i}\right), \qquad \textbf{Equation 7.4}$$

where ψ_k = total ^{36}Cl production rate due to potassium;

ψ_{ca} = total ^{36}Cl production rate due to calcium;

C_k = elemental concentration of potassium;

C_{ca} = elemental concentration of calcium;

ψ_n = the thermal neutron capture rate.

The thermal neutron capture rate, ψ_n, is determined by the fraction of neutrons stopped by the effective cross-sections of ^{35}Cl(σ_{35}) and all other absorbing elements, $\Sigma\sigma$ and their respective abundances, N_{35} and N_i, determined by:

$$^{35}Cl\left(\frac{\sigma_{35}N_{35}}{\sum\sigma_i N_i}\right). \qquad \textbf{Equation 7.5}$$

The interpretation of cosmogenic ^{36}Cl measurements is directly dependent upon the accuracy of production rates (Gosse and Phillips, 2001). Many studies have been undertaken to assess production rates over a diverse range of geographic and geological settings (Table 7.4). The lack of consistency between the various production rates reflects the numerous physical and geological processes affecting the production of ^{36}Cl. At present, this is the main limitation of ^{36}Cl exposure dating.

Author	Path-target-nuclide	Exposure age ka	Production rate (atom g^{-1} target a^{-1})
Yokoyama et al. (1977)	P_s, Ca ^{36}Cl	Calculated	99.0 ± 20
Masarik and Reedy (1995)	P_s, Ca ^{36}Cl	Calculated	64.6
Phillips et al. (1996)	P_s, Ca ^{36}Cl	55.0 to 2.1	73.6 ± 5.0
Swanson (1996)	P_s, Ca ^{36}Cl	15.2	44.2 ± 1.4
Stone et al. (1996)	P_s, Ca ^{36}Cl	11.0 to 17.0	48.8 ± 3.4
Phillips *et al.* (2001)	P_s, Ca ^{36}Cl	2.1 to 55	66.8 ± 6.8
Swanson and Caffee (2001)	P_s, Ca ^{36}Cl	14.9 to 16.2	91.0 ± 5
Swanson (1996)	P_k, Ca ^{36}Cl	15.2	73.8 ± 5.0
Stone *et al.* (1996)	P_k, Ca ^{36}Cl	11.0 to17.0	185.0 ± 15
Phillips *et al.* (1996)	P_k, Ca ^{36}Cl	2.1 to 55	154.0 ± 10
Phillips *et al.* (2001)	P_k, Ca ^{36}Cl	55.0 to 2.1	137.0 ± 60
Swanson and Caffee (2001)	P_k, Ca ^{36}Cl	14.9 to 16.2	228.0 ± 18
Phillips *et al.* (2001)	$P_{f(0)}$	2.1 to 55.0	626.0 ± 105
Swanson and Caffee (2001)	$P_{f(0)}$	14.9 to 16.2	762.0 ± 28

P_s Ca is the spallation production of ^{36}Cl from calcium

P_k Ca is the spallation production of ^{36}Cl from potassium

$P_{f(0)}$ is the ground level secondary production rate in air inferred from thermal neutron absorption by ^{35}Cl (g air)$^{-1}$ a^{-1}.

Table 7.4: Comparison of ^{36}Cl production rates from various production pathways. Adapted from Gosse and Phillips (2001). All values have been normalised to production at sea level and high latitude.

7.5.2 Sample Collection

Samples for cosmogenic analysis were collected from three sites in the Picos de Europa: Pico de la Padierna, Tiro Pedabejo and Allende. At each site, two boulders were sampled where evidence suggested a discrete failure event had occurred. Sampling of material derived from periglacial freeze-thaw activity was minimised by sampling boulders larger than 2 m diameter. Based on geomorphic evidence from the field sites, freeze-thaw derived material tended to be < 0.5 m in diameter and was much more angular than the larger boulders which became detached from the free-face during large failure events. Also, the large failure events tended to have longer run-out distances.

Snow cover is present in the Picos de Europa above 1500 m from about September to April. By sampling boulders greater than 2 m diameter, the risk of shielding the boulders from incoming cosmic rays by snow was reduced. Boulders greater than 2 m in depth tend to resist snow accumulation due to wind acceleration over their upper surface preventing the snow from settling.

Samples were recovered using a selection of chisels and a hammer (Plates 7.9 to 7.11). The limestones of the Picos de Europa were very hard and the failed blocks contained few fractures. Therefore many of the samples were extracted by chiselling from the sides of the boulders. While this is not ideal (because of the potential for thermal neutron leakage) every effort was made to extract a sample at least 15 cm deep from the edge of the boulder so that samples for dating could be prepared in the laboratory from this furthest edge.

Samples were taken from boulders that showed minimal evidence of erosion since exposure. However, this is difficult because limestone is soluble and much of the evidence of weathering is carried away in solution. Evidence of excessive solution on limestone includes karren and solution pits. Most of the karren forms in the Picos de Europa are Rillenkarren – very sharp edged, fluted solution forms.

7.5.3 Chemical analyses

The production pathways of ^{36}Cl are heavily dependent upon rock chemistry. Major elemental composition of rock samples was determined by X-ray fluorescence (XRF) spectrometry, with an analytical uncertainty of < 2 % and a detection limit of

0.01 %. Since the limestones contain > 500 ppm of chlorine, it was possible to measure total chlorine content using XRF. The minor elements including boron and gadolinium (which have large cross-section areas for neutrons), uranium and thorium (the decay of which can produce non-cosmogenic ^{36}Cl) were measured using ICP Mass Spectrometry. Samples for ICP-MS were prepared using microwave acid digestion and measured according to the method outlined in Balaram and Gnaneshwar Rao (2003). Detection limits for ICP-MS were < 0.01 ppb.

7.5.4 Sample preparation and AMS analysis of ^{36}Cl

Sample preparation and AMS isotope analysis was carried out at the Purdue Rare Isotope Measurement Laboratory (PRIME LAB), Purdue University. The top 2.5 cm of each sample was used for analysis because this is the depth of rock with the greatest nuclide content. The sample preparation techniques of Stone *et al.* (1996) were specified. Briefly, chemical preparation was carried out as follows. Crushed and sieved rock was leached twice with 2 Molar HNO_3. After addition of 2-3 mg of ^{35}Cl carrier, the leached rock was dissolved with HNO_3, taking care to avoid foaming. Undissolved solids (generally clays and quartz grains) were separated by centrifugation. Cl was separated by AgCl precipitation. It was redissolved with NH_4OH, then $Ba(NO_3)_2$ was added to precipitate out sulphur (^{36}S interferes with ^{36}Cl AMS measurement). AgCl was centrifuged, rinsed, dried at 70 °C, then pressed into tantalum target holders.

7.5.5 ^{36}Cl production rate calculations

Chemical data used to correct for local ^{36}Cl production are presented in Table 7.5. Background production of ^{36}Cl from thermal neutrons by natural U and Th decay was calculated using the procedure described by Fabryka-Martin (1988). Production resulting from thermal neutron absorption by ^{35}Cl was treated using the equations in Liu *et al.* (1994), which are incorporated into recent calibrations of ^{36}Cl production rates (e.g. Stone *et al.* 1996; Phillips *et al.*, 2001; Swanson and Caffee, 2001). The ^{36}Cl data of Phillips *et al.* (2001) were used to compute the ages because the calibrated production rates span the approximate age of the samples from the Picos de Europa (2.1 to 55 ka BP).

The local production rate solution for a given reaction pathway was calculated using the CHLOE (Chorine-36 Exposure) program (Phillips and Plummer, 1996). CHLOE treats production of ^{36}Cl using the neutron production and diffusion model developed by Liu *et al.* (1994). Sample locations, topographic shielding and scaling factors used to correct for site-specific geometries, along with the ^{36}Cl site-specific production rate and exposure age estimate, are presented in Table 7.6.

Erosion rates entered in to CHLOE ranged from 0 to 20 mm/ka to permit erosion modelling (Figure 7.54). The maximum rate of 20 mm/ka is based on surface lowering studies on limestones in the Swiss Alps by Bögli (1961), in the absence of quantitative data for the Picos de Europa. The erosion rate of 20 mm/ka allows a minimum age of rock slope failure to be calculated (Figure 7.54).

Element	Units	Deva-B1	Deva-B2	Tiro-B1	Tiro-B2	Pico-B1	Pico-B2
Na_2O	% wt	0.2843	0.2844	0	0.43	0.2838	0.2856
MgO	% wt	0.0332	0.0507	0.0446	0.0398	0.0314	0.0361
Al_2O_3	% wt	0.0787	0.0935	0.0409	0.0319	0.0876	0.0953
SiO_2	% wt	0.1015	0.1749	0.0842	0.059	0.1546	0.148
P_2O_5	% wt	0.02	0.0239	0.0362	0.0238	0.0287	0.038
K_2O	% wt	0	0.0215	0.0217	0	0.0228	0.0219
CaO	% wt	30.168	29.661	29.589	31.366	30.712	30.54
Ti_2O_3	% wt	0	0	0	0	0	0
MnO_2	% wt	0	0	0.0339	0.0332	0.0339	0.0515
Fe_2O_3	% wt	0.1251	0.1318	0.1769	0.1068	0.1653	0.2106
Cl	ppm	262.8	330.5	341.1	221.8	299.1	267.6
B	ppm	5.959	2.943	5.83	5.87	0	0
Sm	ppm	0.01	0.001	0.003	0.003	0	0
Gd	ppm	0.01	0.002	0.003	0.003	0	0
U	ppm	0.259	0.792	4.822	4.822	0.518	0.417
Th	ppm	0	0	0	0	0	0

All chemistry data quoted are after chemical leaching.
Minor elements were measured to 1 ppb.

Table 7.5: Major and minor elemental concentrations for limestone samples selected for ^{36}Cl analysis.

Sample ID	Altitude (m)	Latitude (DD) °N	Longitude (DD) °E	Sample thickness (cm)	Q_s	Q_{th}	Q_{eth}	Q_μ	Topographic Shielding Factor[1]	$^{36}Cl/Cl$ (10^{-15})	Local production rate (atoms $^{36}Cl\ g^{-1}\ a^{-1}$)[2]	^{36}Cl age ± [1 σ][3]
Allende-B1	607	44.2916	6.7627	2.5	0.984	1.011	1.062	0.998	0.606	91.9 ± 9.0	59.817	6540 ± 636
Allende-B2	646	44.2061	7.0150	2.5	0.982	1.007	1.059	0.998	0.798	137.0 ± 5.0	100.582	6575 ± 242
Tiro-B1	1863	44.1116	7.3394	2.5	0.982	1.006	1.054	0.998	0.672	324.0 ± 16.0	221.810	7824 ± 403
Tiro-B2	1881	44.1288	7.4047	2.5	0.983	1.011	1.057	0.998	0.522	253 ± 7.0	118.408	7459 ± 214
Pico-B1	1939	43.5503	7.0683	2.5	0.983	1.007	1.053	0.998	0.657	284 ± 9.0	231.563	6054 ± 192
Pico-B2	1931	43.4692	7.3281	2.5	0.983	1.007	1.054	0.998	0.641	404 ± 12.0	202.446	8762 ± 259

Q_s = Thickness correction for spallation production.

Q_{th} = Thickness correction for neutron thermal production of ^{36}Cl.

Q_{eth} = Thickness correction for epithermal neutron production of ^{36}Cl.

Q_μ = Thickness correction for muogenic production of ^{36}Cl.

[1] Includes all topographic shielding effects, including snow depth correction, topographic shielding, boulder surface geometry and the associated changes in attenuation length.

[2] Averaged for sample thickness and includes total production from ^{40}Ca spallation, ^{39}K spallation, ^{35}Cl neutron activation and muon absorption by Ca and K.

[3] Assuming an erosion rate of 20 mm ka^{-1}.

Table 7.6: Sample locations, topographic shielding and scaling factors used to correct for site-specific geometries, along with the ^{36}Cl site-specific production rate and exposure age estimates.

7.5.6 Results and discussion of ^{36}Cl dating

The calculated ^{36}Cl ages range from 8762 ± 259 years BP for boulder one at Pico de la Padierna to 6054 ± 192 years BP for the second boulder sampled at Pico de la Padierna. The sampled boulders span a total time period of 2708 years (Table 7.6). The dates indicate that at Allende, in the Deva Gorge and Tiro Pedabejo, there has been one failure event. The consistency of ages can be seen in Figure 7.55. The fact that age estimates correspond well at Allende and Tiro Pedabejo suggests one major rock slope failure event.

The ^{36}Cl ages from Pico de la Padierna show more variation than the other two sites (Figure 7.55). If the age estimate errors are accounted for, this provides a minimum age difference between the boulders of 2257 years. Due to the consistency of ages between Allende and Tiro Pedabejo, it seems likely that the difference in age estimates is caused by analytical error, or by site-specific errors, such as inheritance of ^{36}Cl. Inheritance of 'old' ^{36}Cl can be caused by muogenic and thermal neutron production of nuclides at depth. If the boulder was located close to the crest of the slope or the free face before failure, then some inheritance of ^{36}Cl could have taken place due to production of the isotope at depth in the rock.

At Pico de la Padierna, there was no geomorphic evidence to suggest more than one phase of failure and it is likely that the contrasting dates reflect inheritance and analytical error. If an average of the two dates from Pico de la Padierna is taken, this produces an age estimate of 7408 ± 225 years BP for the failure. This fits in well with the average dates of failure of 6557 ± 439 years BP from Allende and 7641 ± 308 years BP at Tiro Pedabejo (Figure 7.55).

If the average dates are taken to be correct an overall age estimate for rock slope failures in the Eastern Massif of the Picos de Europa is 7202 ± 324 years BP. The good correspondence of ages within sites suggests that failures in the Picos de Europa were almost synchronous and represent one large rock slope failure at each site.

The dates of rock slope failure gained from Tiro Pedabejo and Pico de la Padierna correspond most closely. This is not surprising since they are both taken from south faces at elevations ranging from 1900 to 2100 m. The climatic conditions, therefore,

would have been very similar at these two sites throughout the Holocene. The site at Allende is located at a lower altitude: the south face is approximately between 700 and 1000 m. The ages obtained from Allende are younger than those at higher elevations indicating failures here occurred more recently than at Tiro Pedabejo and Pico de la Padierna. However, because of the error margin attached to the dates, it is difficult to say for certain whether the failures at Allende occurred after those at Tiro Pedabejo and Pico de la Padierna.

The dates of failure fall within the Holocene Climatic Optimum. In northern Spain the Holocene maximum was reached between 7 and 5 ka BP, during which climatic conditions were wetter than at any time during the Holocene (José Gil García *et al.*, 2002). The Holocene maximum was followed by more arid conditions from 5 ka BP. During this period, temperatures and rainfall were higher then present. This could have led to increased cleft water pressures as periglacial ice melted and higher rainfalls increased the water level in the slopes. González-Díez *et al.* (1999) dated slope failures in the Cantabrian Mountains and attributed those which occurred between 15 and 5 ka BP to increased rainfall following deglaciation. A number of other large rock slope failures, notably in Brez and Cordiñanes in the Eastern Massif, are also thought to date from this period, although dating evidence would be required to confirm this (González-Díez *et al.*, 1999). It is difficult, therefore to propose a single climatic cause alone for the synchronous timing of rock slope failures and the evolution of the slopes must be placed in a paraglacial context.

7.5.7 Paraglacial slope adjustment and rock slope evolution

The ^{36}Cl dates suggest that all three failures in the Picos de Europa represent paraglacial rock slope failure. Widespread paraglacial rock slope failure resulting from Late Pleistocene or Early Holocene deglaciation of mountain environments has been inferred by a number of authors, but the association is difficult because of the lack of dating evidence. For example, Gardner (1977, 1980) suggested most failures in the Canadian Rockies occurred in the immediate postglacial period. A major rock slope failure on Mount Rae has been attributed to glacial debuttressing by Gardner *et al.* (1983), noting that the slide occurred before the deposition of a tephra layer dated to 6.8 ka BP. Caine (1982) attributed toppling failures in Tasmania to a paraglacial response to Late Pleistocene deglaciation, noting that topples were absent from rock slopes which escaped glaciation.

The UDEC models for sites in the Picos de Europa indicate a gradual reduction in the magnitude of unbalanced forces through time, showing that residual stress release is an important initiation mechanism for rock slope failure at the sites investigated. The residual stresses are accounted for in the *in situ* stresses of the rock mass and the angle of free face relative to the discontinuities. Residual stress release and joint propagation following debuttressing were thought to be the main cause of failure on the Isle of Skye, where a large rock slope failure occurred 7000 years after deglaciation (Ballantyne *et al.*, 1998).

Cruden and Hu (1993) have proposed an exhaustion model to describe the temporal distribution of paraglacial rock slope failures. The basic argument of the model is that there are a finite number of potential failure sites following deglaciation and that each site fails once, allowing non-glacial strength equilibrium conditions to be attained. If it is assumed that: (1) the availability of potentially unstable material is the only constraint on paraglacial slope adjustment; (2) there are no further perturbations to the paraglacial rock slope system and (3) sediment supply is reduced through increasing stability of rock slopes as failures occur (Ballantyne, 2002).

The exhaustion model of Cruden and Hu (1993) provides a useful tool for conceptualising the progressive decline in the frequency of paraglacial rock slope failures, but it is difficult to assign a real time base to the model. The cosmogenic dates collected as part of this study allow the model to be compared with a more realistic timescale.

The rate of paraglacial rock slope failure through time can be approximated by

$$N_t = N_o e^{-\lambda t_g}. \qquad \textbf{Equation 7.6}$$

Here t_g is the time since deglaciation, N_t is the proportion of unfailed sites, N_0 is the initial number of potential failure sites at $t_g = 0$ and λ is the rate of failure. If $N_0 = 1.00$ at $t_g = 0$, the rate of failure is expressed as

$$\lambda = \ln\left(\frac{N_t}{-t_g}\right). \qquad \textbf{Equation 7.7}$$

The model implies that the rate of failure after deglaciation is dependent upon the proportion of remaining sites that can undergo failure. The approach adopted here constrains the decay curve using the average ^{36}Cl date of 7202 years BP for all failures in the Picos de Europa. Based on this approach, an estimation of the time period of paraglacial slope failures in the Picos de Europa can be made from Figure 7.56. The approach of Ballantyne (2002) is adopted and the cessation of paraglacial adjustment is assumed when the number of failures is less than 1 % of the initial number of failures. Figure 7.56 indicates that a period of 33 000 years is required for paraglacial adjustment of slopes in the Picos de Europa, but that more than 50 % failures have occurred within 5000 years of deglaciation. Also plotted on Figure 7.56 is the model calculated from Cruden and Hu (1993) from data for paraglacial slope evolution in the Canadian Rockies, which show more rapid failures than those in the Picos de Europa.

The data suggest that the paraglacial exhaustion model proposed by Cruden and Hu (1993) is a valid approximation of slope behaviour in the Picos de Europa. For example, comparison of unbalanced forces suggests a decline in the frequency of failure through time as failures occur and equilibrium stress conditions are established. For Tiro Pedabejo, the cosmogenic dates indicate large-scale slope failure at 7.6 ka BP. Analysis of the UDEC model output indicates that the slope is at strength equilibrium, given the present set of boundary conditions. For this site, the paraglacial exhaustion model provides a good approximation of the frequency of rock slope failure.

However, most UDEC modelling results indicate that readjustments of failed slopes are still occurring long after the initial failures, which occurred 7 ka BP. This suggests that slope evolution is more complex than the simple exponential decay model proposed by Cruden and Hu (1993). At Pico de la Padierna, for example, the UDEC models indicate paraglacial adjustment is still occurring, despite previous rock slope failures at the site. The UDEC models correspond well with the geomorphic evidence observed during a climb of the south face of Pico de la Padierna where the south face represents an overdip slope (Plate 7.12). The angle of slope and bedding is much greater than the friction angle of the intact material.

It is likely, therefore, that the failures dated at Pico de la Padierna (and others) record the initial paraglacial response of the rock masses to deglaciation. Renewed paraglacial response triggered by longer-term slope deformations causes stress

redistributions in the rock mass that lead, eventually, to catastrophic rock slope failures. A theoretical model of rock slope behaviour is presented in Figure 7.57 for the Picos de Europa, based on UDEC modelling, assessment of paraglacial exhaustion models and cosmogenic dating.

The speed of failure plotted in λ-t space can also be related to the delayed paraglacial adjustment of rock slopes in the Picos de Europa (Section 7.4). Failures in the Picos de Europa take 40 000 – 80 000 model cycles to develop. This slow deformation can be related to stress redistributions and elastic deformation of the rock mass, following deglaciation. Without the cosmogenic dates providing age estimates of failure, it would be difficult to provide such detailed interpretations of the rock slope failures.

7.5.8 Temporal constraint of UDEC model output

The cosmogenic ^{36}Cl dates indicate the failure of slopes in the Picos de Europa occurred approximately 8 ka BP after deglaciation, assuming deglaciation occurred around 15 ka BP. If it is assumed that failures occur, on average, every 7202 a, the next failures predicted by the UDEC models are likely to occur within 1000 to 2000 a. However, due to the mechanisms of slope evolution in the Picos de Europa, it would be invalid to propose that a particular number of model cycles can be related to real time, based on the dating evidence. This is because the failures are the result of processes acting under different climatic and stress conditions than exist at present. If paraglacial slope adjustment is the major cause of rock slope failure in the Picos de Europa, the frequency of failure will decline through time. Therefore, it would be erroneous in this environment to assume a steady-state failure model to constrain the temporal occurrence of future failures predicted by the UDEC models.

Without further chronological constraint on the frequency of failure at each site, it is difficult to propose a temporal frequency for future failures to a greater degree of accuracy than presented. All that can be argued is that future failure of the slopes is certain and that the interval between failures is likely to be greater than 7202 years.

Constraining UDEC model output using cosmogenic dating may be most applicable to sites where failures have the potential to span long time periods. In the Picos de Europa, all the failures dated are post-glacial and all occurred within a narrow time-span. Clustering of the cosmogenic dates suggests that in the Picos de Europa

paraglacial failures occur within a limited time period. The failures are principally controlled by stress-release, the speed of which is controlled by the degree of oversteepening of the slope and the orientation of the discontinuities. Therefore, the frequency of failures decreases through time, according to the paraglacial exhaustion model. Due to the clustering of failure ages from environments like the Picos de Europa, cosmogenic dating is most useful in constraining paraglacial exhaustion models, rather than time-marched models simulating future slope behaviour, such as UDEC.

Where slope failures occur within a restricted time period, it is difficult to gain any sense of return periods, especially if the frequency of slope failures decreases exponentially through time, as indicated by the paraglacial exhaustion model. In recently glaciated environments where the stress history is still influencing slope behaviour, a combined approach of UDEC modelling and the exhaustion model is most useful. Although the cosmogenic ages are not useful for constraining the future slope failures indicated in the UDEC output, they are useful in providing information on the actual causes of failure, such as paraglacial slope adjustment.

7.6 Conclusions

The modelling exercise carried out using the UDEC computer program has provided an initial understanding of the geomorphological behaviour of rock slope behaviour in the Picos de Europa mountains, northern Spain. The behaviour of high mountain slopes is relatively poorly understood in relation to more accessible, lower altitude slopes.

Rock slope failure is an important mechanism controlling the geomorphological behaviour in this region and its study contributes to knowledge of the evolution of mountain landscapes. The most common types of failure in the rock masses are sliding and toppling. Block size is an important control on the type of failure operating in the rock masses. The development of rotational failures is most clearly seen through the analysis of displacement zone development, which is related to stress distribution in the landform. Rock masses which exhibited flexural toppling also showed characteristic self-stabilisation under fixed boundary conditions.

The modelling has also provided insights into the deformation signature of the failures when plotted in λ-t space. Catastrophic failures are characterised by a long period of acceleration, whereas displacements which do not lead to failure are characterised by short periods of acceleration followed by long periods of creep movements. These patterns correspond well with the total history of unbalanced forces in the landform and may in future allow landslide prediction.

Cosmogenic dating of rock slope failures has indicated that delayed paraglacial slope adjustment is the principal cause of failure in the Picos de Europa. Oversteepened slopes were produced by glacial erosion. Slope failures in the Picos occurred, on average, 7.2 ka BP, 8000 years after deglaciation. Comparison of rock slope failures in the Picos with the paraglacial exhaustion model has indicated that slope adjustments are likely to occur over a period of 33 000 years. UDEC modelling indicated that initial paraglacial slope failures are followed by renewed periods of slope adjustment following deglaciation. The dating evidence also indicates that climate change may affect the timing of paraglacial rock slope failure in the Picos de Europa.

Chapter 8: The mechanisms of failure and behaviour of sandstone inselbergs in the Al-Quwayra Wadi Rum region, Jordan

Chapter 8: The mechanisms of failure and behaviour of sandstone inselbergs in the Al Quwayra-Wadi Rum region, Jordan.

8.1 Introduction

This chapter presents the results of numerical modelling of the failure mechanisms and geomorphological behaviour of the sandstone inselbergs of the Al-Quwayra-Wadi Rum region of southern Jordan. Slope failure is a key mechanism controlling the evolution of the sandstone inselbergs, which are the most dramatic geomorphological features of this desert region. No previous work has been undertaken to examine the processes controlling the geomorphological behaviour and evolution of the sandstone inselbergs. The UDEC code was used to simulate the failure mechanisms and stress-strain behaviour of the landforms.

Section 8.2 details how representative sites were selected for modelling, followed by a discussion of the model input parameters and mesh geometry in section 8.2.1. The results are discussed in outcrop scale order, ranging from the smallest inselberg, AL9, to the largest, AL17. This is to investigate scale effects that may exist in landform behaviour. Section 8.3.1 describes the model output from AL9 and AL12, which have a vertical outcrop scale of less than 50 m. Model outputs from AL2, AL3, AL7, AL10 and AL11, in the 100-500 m size range, are presented in section 8.3.2. The results are concluded by section 8.3.3, which presents the modelling results for AL17, an inselberg with a vertical height of over 500 m. A summary and comparison of model behaviour along with a discussion of scale effects is presented in section 8.4. Section 8.5 presents preliminary cosmogenic ^{10}Be dating results for the sandstone inselbergs and combines the dates with the UDEC model output in an attempt to provide a broad temporal framework for landscape evolution.

8.2 Sites selected for modelling

Theoretical modelling demonstrated that outcrop scale, defined as the vertical height of the landform, is an important control on the geomorphological behaviour of steep slopes in rock (Chapter 4). Until recently, the numerical modelling of slopes greater than 100 m in height was limited by available computing power. However, there is a

growing recognition that high rock slopes are important components of the landscape and pose a considerable social and economic risk should they fail (Bhasin and Kaynia, 2004). The Al-Quwayra-Wadi Rum region provides an ideal location for assessing how the outcrop scale influences the geomorphological behaviour of the landforms. The outcrop scale of the sandstone inselbergs increases from less than 50 m around Al-Quwayra in the north to over 500 m in the south towards Wadi Rum. After data analysis, similarities and differences can be identified between the field sites in the Al-Quwayra-Wadi Rum area. Based on the discontinuity geometry, all sites can be considered similar, being dominated by two sub-vertical joint sets and near-horizontal bedding (Chapter 6). At all sites, toppling and sliding are the principal failure mechanisms. The major differences are related to the strength of the intact material and the vertical scale of the landforms. The sites selected for modelling reflect differences both in outcrop scale and in the strength of the intact materials. Often, the two are linked; the landforms of smallest outcrop scale are composed of Disi sandstone, the weakest intact material forming inselbergs (Chapter 6). Theoretical modelling indicated that the strength of the intact material influences the deformation of rock masses; that smaller scale landforms are formed in the weakest materials is an important link (Chapter 4). In addition to outcrop scale, block size varies with respect to the scale of the landform. Joint spacing is relatively constant across the study area, so that landforms with an outcrop scale <50 m are composed of larger and fewer blocks with respect to the scale of the inselberg, compared with inselbergs of a larger outcrop size. This allows a tentative assessment of the importance of block size and its effect on landform behaviour.

On the basis of outcrop scale the sites selected for modelling can be divided into three groups (Table 8.1).

≤ 50 m	≥ 100 - ≤ 500 m	≥ 500 m
AL9	AL2	AL17
AL12	AL3	
	AL7	
	AL10	
	AL11	

Table 8.1: Sites selected for modelling and the outcrop scale of the landform.

A greater number of sites in the 100 – 500 m category are represented in the modelling study because these are the most common scale of landform in the Al-Quwayra-Wadi Rum region. Only one site greater than 500 m is presented because of the time taken in the field to gain appropriate geometrical data. In addition the modelling of large-scale rock masses requires unrealistic simplification if acceptable computation times are to be achieved.

8.2.1 UDEC model input

Appropriate input parameters were assigned to each model from the field and laboratory data presented in Chapter 6. The modelling methodology simulates the geomorphological evolution of the sandstone inselbergs and uses the current cliff profiles as an initial condition. Initially, all models are stable after consolidation and an equilibrium stress regime has developed under constrained boundary conditions. The constructed models are based on the real cliff profiles and controlling rock mass characteristics of the inselbergs. Data for construction of the model meshes regarding slope height and the profile of the inselbergs were gained through the analysis of scaled digital images of each site. Despite simplification of the meshes, the models replicate the major characteristics of each site. The sandstone inselbergs are three-dimensional landforms, so two models for each site were constructed, one representing the east-west profile and the other the north-south profile. All joint data used to construct the models were converted to represent the true dip on the UDEC mesh, as outlined in Chapter 7. Standard deviations of the joint spacing data were entered for each input file as measures of spacing variability. No data exist concerning the joint stiffness values of the sandstone inselbergs and, given the difficulty in obtaining estimates of stiffness properties in the field and laboratory, appropriate values for similar sandstones were used from the literature. The joint stiffness was kept constant for all model meshes, regardless of site, to reduce comparison error that would be associated in using different stiffness values without any physical basis. Field observations indicated that the surface roughness of the joints was low, and many of the joint surfaces relatively smooth; therefore it was decided to use the natural friction angle of the intact material to represent the inherent joint friction angle. A summary of the UDEC input parameters for each model is presented in Table 8.2. Data are presented in scale order, from smallest to largest. The UDEC input files are presented in Appendices 8.1 to 8.15.

Parameter	Units	AL9a	AL9b	AL12a	AL12b	AL10a	AL10b	AL11a	AL11b	AL3a	AL3b	AL2a	AL2b	AL7a	AL7b	AL17
Free-face height	m	30	30	30	30	100	100	110	110	196	196	200	200	270	270	650
Free-face angle	x°	90	70	70	30	70	60	43	50	70	60	75	70	85	85	80
UDEC mesh bearing (dip direction)	x°	131	220	271	218	140	232	100	230	094	220	140	228	120	270	350
Joint set 1: angle	x°	-72	66	-74	49	76	0	71	81	32	85	-63.4	89	58	60	82
Joint set 1: spacing/s.d.	m	4.56 /1.0	4.56 /1.0	19.46 /10.33	19.46 /10.33	5.37 /3.02	5.37 /3.02	5.95 /4.71	5.95 /4.71	8.19 /5.42	8.19 /5.42	12.8 /6.34	12.8 /6.34	5.28 /1.27	5.28 /1.27	35.79 /41.97
Joint set 2: angle	x°	45	15	79	64	-75	32	86	83	76	73	------	------	35	76	60
Joint set 2: spacing/s.d.	m	7.87 /6.75	7.87 /6.75	4.07 /0.56	4.07 /0.56	2.59 /1.30	2.59 /1.30	6.15 /3.57	6.15 /3.57	3.18 /1.98	3.18 /1.98	------	------	38.65 /11.27	38.65 /11.27	42.60 /38.31
Joint set 3: angle	x°	-75	51	------	------	------	------	------	------	------	------	------	------	60	81	------
Joint set 3: spacing/s.d.	m	3.82 /0	3.82 /0	------	------	------	------	------	------	------	------	------	------	3.47 /0.27	3.47 /0.27	------
Joint set 4: angle	x°	70	-70	------	------	------	------	------	------	------	------	------	------	------	------	------
Joint set 4: spacing	m	45/0	45/0	------	------	------	------	------	------	------	------	------	------	------	------	------
Bedding: angle	x	6.0	6.0	2.0	2.0	3.0	6.4	4.6	4.5	1.5	2.6	5.0	1.0	2.0	6.0	7.0
Bedding spacing/s.d.	m	10.86 /1.48	10.86 /1.48	12.15 /2.38	12.15 /2.38	10.96 /1.35	10.96 /1.35	5.98 /2.08	5.98 /2.08	12.91 /1.79	12.91 /1.79	9.8 /0.75	9.8 /0.75	8.3 /1.04	8.3 /1.04	14.5 /0.77
Bulk density	kg m^{-3}	2443	2443	2543	2534	2443	2443	2443	2443	2443	2443	2443	2443	2443	2443	2443
Bulk modulus	GPa	14.62	14.62	5.85	5.85	14.62	14.62	14.62	14.62	8.78	8.78	14.62	14.62	14.62	14.62	14.62
Shear modulus	GPa	11.89	11.89	3.72	3.72	11.89	11.89	11.89	11.89	3.72	3.72	11.89	11.89	11.89	11.89	11.89
Joint normal stiffness	GPa	20	20	20	20	20	20	20	20	20	20	20	20	20	20	20
Joint shear stiffness	GPa	4	4	4	4	4	4	4	4	4	4	4	4	4	4	4
Joint friction angle	x°	44	44	36	36	44	44	44	44	43	43	44	44	44	44	44

Table 8.2: UDEC input parameters for meshes used to simulate the behaviour of inselbergs in the Al-Quwayra Wadi Rum region. A denotes north-south profile, B the east-west profile of the inselberg. Where no indication is given, this is the east-west profile.

Individual blocks were defined as deformable because the outcrop scale of some of the inselbergs is large enough for *in situ* stresses to be high enough to allow the deformation of the intact material, affecting the stress-strain behaviour of the landform. The UDEC model meshes are orientated perpendicular to the trend of the free faces. In all the models, except AL3, the Salib Arkosic sandstone forms the base of the inselberg. In these slopes, the Salib Arkosic sandstone formed stable slopes due to their low angle (<10°). Thus, to reduce model complexity and computation time, the Salib Arkosic sandstones were modelled as a fixed rigid body with no joints. Such a simplification can be justified by running a set of scenarios and model accuracy is maintained as the important controls on rock mass stability are included. Although the sandstone inselbergs act as discrete aquifers, it was decided not to include water flow through the discontinuities for two reasons: first, it is almost impossible to obtain an accurate assessment of the water content of the rock masses and the rate of flow through the discontinuities; second, initial experiments suggested that the influence of water flow through the discontinuities for the modelled rock masses was negligible, mainly serving to double computational time.

Once the model mesh geometry and material properties were assigned, a gravitational acceleration of 9.81 m s^{-2} was set in addition to the *in situ* compressive stresses which were set to act vertically through the model based on the weight of overlying rock. A horizontal compressive stress gradient was set at the recommended half of the vertical value (Herget, 1988). However, by the time the model has reached initial equilibrium, stresses are natural throughout the rock mass. During the consolidation phase, the basal and vertical boundaries were fixed to nullify movement and allow the blocks to settle and consolidate under gravity. For each site, the model was run for 10 000 cycles to allow consolidation, which is indicated by the unbalanced forces approaching zero. After consolidation, the vertical boundaries representing the slope faces were released to permit block displacement and the development of failures. Blocks which became detached from the free face and reached an acceleration of 9.81 m s^{-2} were automatically deleted, because they have no further influence on the behaviour of the model. UDEC cannot accurately model material in free fall and by that point the failure mechanism and the development of displacements in the rock mass leading up to and during the failure are known. Over geomorphological timescales, the failed blocks resting on the Salib Arkosic ramps disintegrate relatively quickly and impart little stability at the toe

of the slope. Output from the UDEC simulations was logged and saved every 1000 to 10 000 cycles, depending upon the speed of model failure.

For sites with a vertical outcrop scale of less than 50 m, two sites were identified for modelling: AL9 and AL12. These were considered characteristic of the small inselbergs in the study area. Site AL9 represents a small rock mass outcrop of Ishrin sandstone in the central part of the study area, with a free face height of 30 m and evidence for failures on the north and south faces. (Plate 8.1). To simulate the behaviour of the inselberg, two models were constructed. The first mesh simulates the north-south profile of the inselberg, with the left-hand side of the model representing the north face and the right-hand side the south face. The model has four main joint sets in addition to the bedding. The converted angle of joint set 1 on the mesh is −72° south, set 2 has a dip of 45°, set 3 −75° and set 4 70°. The bedding dips at a converted angle of 6° out of the north face. A second mesh simulates the behaviour of the east-west profile and has a free face height of 30 m. The west face is plotted on the left-hand side of the mesh and the east face on the right-hand side. The elongated profile of the inselberg means that the east-west profile is much longer than the north-south profile. On the mesh, joint set 1 dips at 66°, set 2 at 15°, set 3 at 51° and set 4 at −70°. After conversion the bedding has a mesh dip of 6° towards the west.

To assess the geomorphological behaviour and evolution of AL12, two models were constructed. The landform is of similar scale to AL9, except that the inselberg represents an outcrop of Disi sandstone (Plate 8.2). The first mesh simulates the north-south profile of the model; the north face is plotted on the left-hand side of the model and the south face on the right-hand side. Three main joint sets can be identified. For the north-south profile, joint set 1 dips at −74° to the north and joint set 2 at 79° to the south. The bedding dips at a converted angle of 2°. A second mesh was constructed to simulate the east-west profile of the landform. The west face of the model is on the left-hand side of the model and the east face on the right-hand side. On the model mesh, joint set 1 has a converted dip of 49° to the west and set 2 dips at 64° to the west. The bedding has a mesh dip of 2° to the west.

Five models simulate the behaviour of the 100 to 500 m inselbergs, which are the most abundant landforms in the Al-Quwayra-Wadi Rum desert. The smallest landform in this group is AL10 with a vertical outcrop scale of 100 m (Plate 8.3). Two meshes were constructed to simulate the geomorphological behaviour and

evolution of the landform. The north-south profile has a free face height of 100 m and an average free face angle of 70° on the south face. The south face is represented on the left-hand side of the model and the north face on the right-hand side. Two main discontinuities can be identified, with joint set 1 dipping at 76° to the south and set 2 at –75° to the north. The bedding has a converted dip of 3° on the mesh. A second model simulates the east-west behaviour of the inselberg landform, with the west face on the left-hand side of the mesh and the east face on the right-hand side. Average free face angles for the west face are 50° and 60° for the east face. The east-west profile has a dip direction of 232°, producing a converted dip of 0° for joint set 1 and 32° to the west for joint set 2. On the mesh the bedding dips at an angle of 6.4°.

Two meshes were constructed to simulate the geomorphological behaviour of AL11, with a free face height of 110 m (Plate 8.4). The first mesh simulates a north-south profile through the landform, with the north face plotted on the left-hand side of the model. The UDEC mesh is perpendicular to the north and south faces and has a dip direction of 100°. The average slope angle on the north face is 40°, but represents a composite slope, with maximum angles between 50° and 90°. For the south face, the average angle of the main free face is 70°, with a 3 m undercut at the toe of the face produced by slope sapping. Converted joint dips on the mesh are 71° for joint set 1, 86° for set 2 and 4.6° for the bedding. All joint sets and bedding dip towards the north, which suggests the potential for toppling failures on the south face. A second mesh was constructed for the east-west profile of the landform. The west face is located on the left-hand side of the model and the east face on the right-hand side. The model was constructed with a free face height of 110 m, with an average angle of 50° on the west face and 25° on the east face. On the mesh, joint set 1 dips at an angle of 81°, joint set 2 at 83° and the bedding at 4.5°. Both joint sets and bedding dip towards the west.

AL3 is the only inselberg investigated to be composed entirely of Salib Arkosic sandstone (Plate 8.5). Field evidence suggests that localised normal faulting has resulted in the Salib Arkosic sandstone being uplifted. The first mesh simulates the behaviour and evolution of the north-south profile of the landform. The mesh has a free face height of 196 m, with an average slope angle of 70° on the north face and 50° on the south face. The dip direction of the UDEC mesh is 94°, producing converted joint dips of 32° for joint set 1, 76° for joint set 2 and 1.5° for the bedding. All joint sets and bedding dip towards the north, producing a potentially unstable

south face. A second mesh simulates the east-west profile of AL3, with the west face on the left-hand side and the east face on the right-hand side. The mesh is perpendicular to the east and west faces at a bearing of 220° with converted dip angles of 85° for joint set 1, 73° for set 2 and 2.6° for the bedding, on the mesh.

AL2 was the fourth model to be constructed to simulate the behaviour of the inselbergs at the 100 – 500 m scale. The inselberg is formed entirely from Red Ishrin sandstone, the bedrock ramp being formed from Salib Arkosic sandstone (Plate 8.6). The first model simulates the north-south profile of the inselberg and has a free face height of 200 m and UDEC mesh bearing of 228°. The average angle of the north and south faces is 60°. All discontinuities dip towards the north, with converted dip angles of -63.4° for joint set 1 and 5° for the bedding. The north face has been undercut by slope sapping in response to a shale band at the base of the notch leading to horizontal flow seepage. A second mesh was constructed to simulate the behaviour of the east-west profile of AL2. The west face is plotted on the left-hand side of the model and the east face on the right-hand side. The UDEC mesh has a bearing of 228° perpendicular to the east and west faces. On the mesh, joint set 1 dips at 89° and the bedding at 1°. The average angle of the west face is 70° and 60° for the east face.

The last two models in the 100 to 500 m scale range simulate the behaviour of AL7, which has a free face height of 270 m (Plate 8.7). The north-south profile of the landform is dominated by four columns which have formed by preferential weathering of joint set 3, dipping at 60° on the UDEC mesh. The rock mass is further fractured by joint set 1, which dips at 58° on the mesh. Joint set 2 has a dip of 35° on the mesh and the bedding dips at 6°. The south face is plotted on the left-hand side of the model and the north face on the right-hand side. The south face has an average free face angle of 80°, while the right-hand tower on the north face attains an average angle of 83°. A second model simulating the east-west profile was constructed after field observations indicated that the main tower was unstable in all directions. The west face is plotted on the right-hand side of the model and the east face on the left-hand side. The UDEC mesh is perpendicular to the cliff faces at a bearing of 270°. This produces a converted dip angle of 60° for joint set 1, 76° for joint set 2, 81° for set 3 and 6° for the bedding. The slopes leading to the toe of the tower have average angles of less than 45°, so that failures would not occur on these faces. The west face of the modelled tower has an average angle of 65°, while the east face has an angle of 85°.

The final model was constructed to simulate the geomorphological behaviour of rock masses with a vertical outcrop scale greater than 500 m. Only one model at this scale was constructed due to computational limitations. AL17 is located in the Barra Canyon, with the West face showing evidence of large past failures (Plate 8.8). The west face has been oversteepened due to fluvial incision by a large ephemeral channel which runs through the canyon (Plate 8.9). Although debris at the toe of the slope is present, it was decided not to include this in the model for two reasons. First, it would be difficult to include the debris in the UDEC model. Second, it would be difficult to define a model timescale over which the debris should be removed to simulate weathering. The only mesh constructed for the site is an east-west profile through the landform. This is because the longitudinal profile of the inselberg is almost 5 km long, producing a large model and consequently very long computational times. Moreover, there was no geomorphic evidence for past failures on the north and south slopes; this is supported by kinematic analysis (Chapter 6). The model has a vertical outcrop scale of 650 m, with the profile taken at a bearing of 350° perpendicular to the east and west free faces. The east face has an average angle of 50°, while the west face has an angle of 80°. Converted dips on the mesh are 82° for joint set 1, 60° for set 2 and 7° for the bedding. The two ramps leading to the main free faces represent the average gradient of the desert floor.

8.3 Results

Outputs from the models run to simulate the characteristics of the sandstone inselbergs at key field sites in the vicinity of Al-Quwayra and Wadi Rum were plotted at important stages. A block plot was created for each site after the model had consolidated, and the mesh was re-plotted at various model cycles for each simulation. It was not considered appropriate to plot the meshes at the same number of model cycles to permit direct comparison: the speed of failure varied so much between the different sites that it would have been difficult to monitor the failures occurring in some of the models. Once the boundary constraints had been released, displacement vector plots were produced so that the failure mechanism and deformation could be monitored. Contoured plots of horizontal displacements were produced at key stages, so the propagation and distribution of displacements associated with failure could be monitored. The maximum displacements occur in regions of the rock mass under greatest strain.

8.3.1 Simulation of inselbergs at the ≤ 50 m scale

The initial north-south profile of AL9 at 10 000 cycles after consolidation is plotted in Figure 8.1. The history of unbalanced forces at 10 000 cycles indicates that the model reached equilibrium before 10 000 cycles (Figure 8.2). The block plot shows that because joint spacing is between 5 and 10 m, block sizes are large compared with the outcrop scale of the rock mass (Figure 8.1). At 15 000 cycles, the displacement vector magnitudes are greatest towards the top of the blocks on the north face, indicating the onset of toppling failure (Figure 8.3a). The mechanism of failure is block-toppling as opposed to flexural deformations observed in larger scale slopes (Chapter 7). The failure is more advanced by 17 000 cycles and the limit of toppling is controlled by a shear surface along joint set 2, which dips at 45° to the north on the mesh (Figure 8.3b). A small sliding failure involving three blocks is occurring on the south face, but this is minor compared with the failure of the north face. By the end of the simulation at 40 000 cycles, the displacement vector plots show that that the model has largely stabilised because of the accumulation of failed debris at the slope toe (Figure 8.3c). Stabilisation of the model is confirmed by analysis of the total history of unbalanced forces at 40 000 cycles (Figure 8.4). The plot indicates relative stability until 15 000 cycles, when the propagation of failure begins. The block-toppling failure mechanism can be considered relatively brittle and catastrophic, indicated by the high magnitudes of unbalanced forces over a short period of time. By the end of the simulation at 40 000 cycles, the unbalanced forces are approaching zero, indicating that the model has stabilised.

The development of displacement zones in the model shows that, at equilibrium, no displacements have developed because the model boundaries are constrained (Figure 8.5a). By 15 000 cycles, the displacement zones clearly show the development of block-toppling along a shear surface caused by joint set 2 (Figure 8.5b). A maximum displacement of 3.5 m occurs on the upper left of the toppling zone, decreasing to 0.5 m along the shear surface. By the time the model has reached 17 000 cycles, there has been greater displacements as the failure has advanced (Figure 8.5c). The maximum displacement by this stage is 10 m on the outer edge of the toppling zone and 2 m along the shear surface. At the end of the simulation the maximum block displacement and runout distance of the failed material is 20 m (Figure 8.5d). The blocks which have not failed are situated below the toppling surface, and have undergone virtually no displacement.

The second mesh for AL9 simulates the east-west profile of the landform and the initial mesh at equilibrium is plotted in Figure 8.6a. The displacement vectors at 50 000 cycles are virtually zero in magnitude indicating that the model is stable (Figure 8.6b). The total history of unbalanced forces also indicate that no failures have developed (Figure 8.7). Three main peaks of activity can be identified throughout the model run. The first is associated with the release of the model boundaries and initial accumulation of strain along the discontinuities, leading to the displacement of a single block on the west face through a sliding failure. The second and third peaks are related to additional shear displacements of the failed block. The contoured displacement plot indicates that by 50 000 cycles no displacement zones have developed, apart from in the failed block, which has been displaced by 7 m.

The second site modelled to investigate the geomorphological behaviour of the inselbergs ≤ 50 m was AL12. The first mesh simulates the north-south profile and is plotted at equilibrium in Figure 8.8a. The south face is on the right-hand side of the mesh and the north face on the left. By 12 000 cycles, the displacement vectors show a sliding and toppling failure has begun on the south face. (Figure 8.8b). The toppling is induced by the presence of a notch at the base of the south face, caused by slope sapping. The shear surface of the sliding zone is controlled by joint set 1, dipping at −74° on the mesh, as indicated by the parallel alignment of the vectors along this joint surface. The displacement vectors indicate that the failure is not deep-seated, because the magnitude of the vectors is almost zero away from the failed zone. Toppling is indicated by the orientation of the displacement vectors out of the sliding zone. The failure is more advanced by 15 000 cycles; the zone of toppling has increased and the toppling blocks have wedged over previously failed blocks lying at the toe of the south face (Figure 8.8c). After 25 000 cycles, Figure 8.8d indicates that the toppling columns have failed. The failure is dominated by the rotational movements of blocks in topple. The virtual absence of displacement vectors away from the failed zone on the south face indicates that the model stabilises after failure. This suggests that, following failure, the landform would be in equilibrium until weathering changed the planform of the slope, promoting consequent failures through slope sapping along the bedding. The total history of unbalanced forces at 25 000 cycles shows that the activity in the landform is pulsed (Figure 8.9). The failure is catastrophic as indicated by the high and sustained activity in the rock mass throughout failure.

The plots of displacements shows that the failures are not deep-seated, and involve a relatively small volume of rock (Figures 8.10a to 8.10c). By 12 000 cycles, three main displacement zones have developed within the failure (Figure 8.10a). A maximum displacement of 2 m occurs at the top of the toppling zone, decreasing to 0.8 m along the shear surface of the sliding zone. By 15 000 cycles, four zones of displacement can be identified, with a maximum displacement of 8 m in the first toppling column (Figure 8.10b). The magnitude of displacement decreases towards the base of the shear zone, indicating that in toppling failures, rotation of the blocks can produce differential displacements. Away from the failure, the magnitude of displacement varies between 0 and 1 m, showing that most of the rock mass is relatively stable. The number of displacement zones in the failed zone has decreased by 25 000 cycles as the failure begins to stabilise (Figure 8.10c). The maximum run-out distance of the failed blocks is 20 m.

The second mesh constructed simulating the behaviour of AL12 is an east-west profile through the inselberg. The initial mesh is plotted at equilibrium in Figure 8.11a. By 100 000 cycles, the displacement vectors are pointing upwards, indicating the east and west faces are stable (Figure 8.11b). This reflects the field situation, with no evidence of past or present failures being found on these faces. By 100 000 cycles, some displacement has occurred on the west face (Figure 8.12). However, the magnitude of displacement is less than 8 cm, and is caused by small movements of blocks after the release of the model boundaries.

8.3.2 Simulation of inselbergs at the ≥ 100 to ≤ 500 m scale

The initial mesh for the north-south profile of AL10 at 10 000 cycles after consolidation is plotted in Figure 8.13a. The displacement vector plot indicates that by 13 000 cycles large-scale failures have begun on the north and south faces (Figure 8.13b). The failure mechanisms operating in the rock mass are complex. On the south face (left-hand side), the upper zone of failure is moving by sliding indicated by the orientation of the displacement vectors parallel to joint set 1 dipping at 76° on the mesh (Figure 8.13b). Below this zone, the vectors have re-orientated out of the slope face, indicating flexural toppling. Although not clear from the displacement vector plots, anti-scarps have formed in the zone of flexural toppling. On the north face, the development of flexural toppling at the toe of the slope has increased the degrees of freedom of each block behind, allowing sliding to occur

along joint set 2, dipping at -75° on the mesh. The zone of flexural toppling is controlled by the decrease in the spacing of joint set 1 in response to the large standard deviation of spacing of the joint set. This suggests that changes in joint spacing can influence the failure mechanism by altering the block size distribution. This is in contrast to previous research, which suggested that the variability of joint spacing exerts little control on the geomorphological behaviour of the rock mass (Kimber, 1998). By 15 000 cycles, the failures are more advanced and are deep-seated (Figure 8.13c). The magnitude of the flexural toppling has increased, mainly due to the stress exerted by the blocks above which are failing through sliding. This prevents the characteristic self-stabilisation shown for flexural topples in the Picos de Europa (Chapter 7). By 21 000 cycles, the additional stress imposed by the blocks overlying the flexural topple has caused the flexural topples to fail completely, changing the mode of failure to a block topple (Figure 8.13d). At this point large numbers of blocks are in free fall, so the simulation crashed. However, if the simulation were allowed to continue, then the accumulation of failed debris at the toe of the north and south faces would have imparted stability to the model.

The analysis of the development of displacement zones associated with the failure provides further detail on the response of the landform. By 13 000 cycles, two main displacement zones have developed on the north and south faces in response to the failure of the rock mass (Figure 8.14a). On the south face, the zone of flexural toppling is characterised by a maximum displacement magnitude of 10 m. The zone of sliding behind the toppling zone, represented by the red colour, shows rotation as sliding blocks begin to topple. The maximum magnitude of displacement in this zone is 5 m. An almost identical pattern occurs on the north face, with the toppling and sliding zones having accumulated 10 and 5 m of displacement, respectively. The boundary between the dark red and light brown marks the change in the direction of failure between the north and south faces. By 15 000 cycles, the toppling zone has undergone 20 m of displacement on both faces, with the zone of sliding experiencing 10 m of displacement (Figure 8.14b). There are no clear displacement zones by 21 000 cycles because many of the blocks are in free-fall, so that the accumulation of displacements does not follow any clear pattern (Figure 8.14c).

The total history of unbalanced forces at 21 000 cycles shows there are two main periods of activity associated with failure (Figure 8.15). During the first, the level of activity rises, associated with the increase in the development of the flexural topple.

The level then drops during the second as the topple self-stabilises, with activity rising as the increased stresses promoted by the weight of the sliding blocks causes catastrophic failure to develop.

The second mesh simulating the behaviour of AL10 represents an east-west profile through the landform. The mesh is plotted at 10 000 cycles after consolidation in Figure 8.16a. By 100 000 cycles, the displacement vectors indicate that the rock mass is stable, because they are all orientated vertically (Figure 8.16b). There has been very little accumulation of strain in the model by 100 000 cycles; a maximum displacement of 1.2 m occurs in the centre of the model (Figure 8.17). Throughout the rest of the model, the magnitude of displacements are less than 1 m, which indicates the east-west profile is stable with respect to the boundary conditions.

The second site chosen as representative of the landforms in the 100 to 500 m inselbergs was AL11. The first model simulates the geomorphological behaviour of the north-south profile. The initial mesh at equilibrium is plotted in Figure 8.18a. After 100 000 cycles, the displacement vectors show that virtually no failures have developed (Figure 8.18b). A sliding failure has occurred on the north side of the central tower of the insleberg, but this stabilised after the failed blocks reached the main surface of the inselberg. The displacement vectors also indicate the potential for toppling failures exists on the south face. However, given current boundary conditions, the geometry of the south face is not conducive to failure. The toppling failure will develop as the notch at the base develops through slope sapping. Analysis of the total history of unbalanced forces at 100 000 cycles indicates that no large failures have developed and the landform is in equilibrium (Figure 8.19). The early activity from 20 000 to 40 000 cycles represents the small sliding failure on the central tower. By 100 000 cycles, only three main displacement zones have developed, producing a maximum displacement of 2 m, indicated by the yellow contour in Figure 8.20. This is related to the small movements caused by initial topples, which then stabilised.

The second mesh for AL11 simulates the east-west profile and the initial mesh is plotted in Figure 8.21a. After the model boundaries have been released, displacement vector plots show the development of block toppling failures on the east face by 20 000 cycles (Figure 8.21b). Field evidence suggests that the failure has developed in response to sapping on the east face, which has created an unstable geometry. At 20 000 cycles, two zones of movement can be identified.

The first zone consists of toppled blocks which form rockfall debris at the toe of the east face. The second zone consists of an active area of block toppling further towards the west. By 40 000 cycles, the toppling of the second zone has almost finished because the accumulation of debris at the base of the east face has imparted stability (Figure 8.21c). Through time, further failures may develop as the basal debris is weathered away.

The development of displacement zones associated with the block toppling failure on the east face is presented in Figure 8.22a and 8.22b. At 20 000 cycles, two displacement zones are associated with the toppling failures (Figure 8.22a). The first has produced a maximum displacement of 25 m and the second 10 m. The plot indicates that the magnitude of displacement is greatest at the top of the toppling columns. There has been no development of a substantial shear surface over which the toppling is occurring at this stage. The magnitude of displacement away from the failure is up to 5 m, and indicates that the rock mass is stable in these areas. By 40 000 cycles, a clear shear surface has developed in the toppling zone, which is marked by the transition from light red to dark red (Figure 8.22b). The maximum run-out distance of the failed debris is 40 m. The total history of unbalanced forces at 40 000 cycles indicates that failure is pulsed, with at least 8 phases of activity (Figure 8.23). The reduction in the magnitude of the unbalanced forces towards the end of the simulation confirms that the accumulation of basal debris has prevented the development of further failures.

AL3 was the only inselberg investigated in the Al-Quwayra-Wadi Rum region composed entirely of Salib Arkosic sandstone. This is due to displacement along a local normal fault. Two meshes were constructed to simulate the geomorphological behaviour of the landform. The first mesh simulates the north-south profile of the inselberg; the initial mesh at equilibrium is plotted in Figure 8.24a. By 13 000 cycles, the displacement vector plot indicates that toppling failure is occurring on the south (right-hand side) face of the model (Figure 8.24b). The orientation of the vectors out of the south face shows that toppling, and not sliding, is the dominant failure mechanism. The toppling failure at this stage is flexural and block plots indicate that anti-scarp formation has occurred in response to the deformation of the rock mass. The flexural toppling failure is controlled by the natural variability of joint set 2, which dips at 76° on the UDEC mesh. This joint set has a standard deviation of 1.98 m, producing variability in the block size distribution of the rock mass; this

suggests that flexural topples occur in areas of rock masses consisting of smaller block sizes, because this allows the slope to deform in a more ductile manner.

The displacement vectors on the north face show sliding failure because the vectors are parallel to joint set 2, with a zone of secondary toppling at the toe, indicated by the orientation of vectors out of the free face. The zone of secondary toppling has developed because of the elevated stresses imposed by the sliding mass above the intact blocks at the base. The failures on both faces have become more advanced by 15 000 cycles (Figure 8.24c). The toppling on the south face is still flexural, with some blocks rotating through 45°, indicating that the south face is behaving in a ductile manner. The displacement vectors on the north face are not quite as strong as those at 13 000 cycles, so the failure is slowing. By 20 000 cycles, the displacement vectors indicate that the sliding failure on the north face has almost stabilised (Figure 8.24d). On the south face, a threshold has been reached and the ductile behaviour of the rock mass has changed to a brittle failure, indicated by the large-scale detachment of rock blocks from the south face. Ductile, flexural toppling is still occurring towards the crest of the slope due to an unloading effect in the detached zone.

The development of displacement zones shows the nature of deformation as failures develop. After consolidation no organisation of displacement zones has occurred. By 13 000 cycles, the contoured strain plots show three displacement zones associated with the flexural topple on the south face and two associated with the sliding failure on the north face (Figure 8.25a). The maximum displacement in the zone of flexural toppling is 30 m and in the zone of sliding 20 m. The deformation of the rock mass is deep-seated and so displacements have developed throughout the landform. By 21 000 cycles, clear zones of displacement have developed on the south face in response to the transition from ductile to brittle deformation (Figure 8.25b). Although the toppling failure is deep-seated, the development of displacement zones associated with the sliding failure on the north face shows that the sliding failure is shallow, involving relatively little material.

The second mesh simulates the behaviour of the east-west profile of the landform. The initial mesh at 10 000 cycles is plotted in Figure 8.26a. The displacement vector plot taken at 20 000 cycles shows flexural toppling of the east face and indicates that the zone of active failure is deep-seated (Figure 8.26b). Away from the active failure, the upward displacement vectors show that the stability of the

landform increases towards the west. There has been virtually no further displacement of the flexural topple by 150 000 cycles, showing self-stabilisation (Figure 8.26c).

The contoured plots show 7 zones of displacement associated with the flexural topple at 20 000 cycles, producing a maximum displacement of 35 m (Figure 8.27a). The magnitude of displacement away from the zone of failure is less than 5 m, showing that the west face of the rock mass is stable. By 150 000 cycles, the number of displacement zones associated with the failure of the east face is only 3; the depth of significant deformation is marked by the development of a shear surface (Figure 8.27b). The maximum displacement in the flexural topple is 40 m; so very little additional strain has accumulated in 130 000 cycles. This confirms that the flexural toppling failure of the east face has self-stabilised. Towards the west face, the rock mass is stable, as indicated by the large area of zero displacement.

The total history of unbalanced forces at 150 000 cycles shows that the failure is characterised by an initial period of high activity as the flexural topple propagates (Figure 8.28). However, the reduction in activity shows self-stabilisation. The continued spikes in the unbalanced forces are related to small creep movements occurring in the flexural topple as it reaches equilibrium with respect to the model boundary conditions.

The fourth model simulating the evolution of the inselbergs in the 100 to 500 m outcrop scale was AL2. The first mesh simulates the geomorphological evolution of the north-south profile, with the initial geometry of the inselberg plotted in Figure 8.29a. The displacement vector plot shows the development of a sliding failure on the north face by 20 000 cycles (Figure 8.29b). The displacement vectors are parallel to joint set 1, dipping at –63° on the mesh. On the south face, the displacement vectors are pointing out of the face, indicating that the rock mass is failing through toppling, which is controlled by joint set 1. Here the same joint set can produce different failure mechanisms, depending upon the orientation of the free face. The toppling failure on the south face has been enhanced by a notch produced by slope sapping and is one of block toppling rather than flexural toppling. By the end of the simulation at 68 502 cycles, the sliding failure on the north face has almost stabilised, and the accumulation of failed debris at the toe of the slope is preventing further failures (Figure 8.29c). The block toppling failure on the south face has also been slowed by the accumulation of basal debris. The accumulation

of debris at the toe of the south face has prevented the block toppling failure becoming deep-seated.

The contoured horizontal displacement plot shows that by 20 000 cycles, two displacement zones have developed in the sliding failure on the north face (Figure 8.30a). The maximum displacement of the failure is 40 m and the boundary between the 2 and 4 m contours represents the shear surface of the sliding zone. Three main zones of displacement have developed on the south face in response to block toppling and the maximum displacement in the toppling zone is 60 m. By 68 502 cycles, there are only two displacement zones associated with the block toppling failure, producing a maximum displacement of 100 m (Figure 8.30b). On the south face, the sliding failure has a maximum run-out distance of 50 m. Stability of the rock mass is shown by the large area of zero strain, indicating that most of the blocks in the rock mass have not undergone significant displacement.

The total history of unbalanced forces shows that initially the geomorphic activity in the rock mass is high, but that this gradually decreases (Figure 8.31). At a model time of 100 seconds, the activity in the rock mass increases and this can be related to movements of the failed blocks on the south face; after this point, the activity in the rock mass decreases rapidly. The unbalanced forces do not reach zero, but the rock mass is in equilibrium with respect to the stress acting upon it.

A second mesh was constructed to simulate the geomorphological behaviour of the east-west profile of the landform. The initial mesh at 10 000 cycles is plotted in Figure 8.32a. By 100 000 cycles the orientation of the displacement vectors indicate no failures; the rock mass is in equilibrium (Figure 8.32b). Although the east and west faces are in equilibrium, the contoured displacement plot at 100 000 cycles shows some movement has occurred on the west face (Figure 8.33). Although displacement magnitudes are < 1 m, if slope sapping were to occur, this would lead to increased risk of failure, as this area is already more highly stressed than the east face.

The final site selected to investigate the behaviour of the 100 to 500 m inselbergs is AL7. The first model simulates the north-south profile and is plotted at equilibrium in Figure 8.34a. At 15 403 cycles, the displacement vector plot indicates a flexural toppling failure on the north face and a sliding failure on the south face (Figure 8.34b). The development of the flexural topple is controlled by joint sets 1 and 3,

dipping on the mesh at 58° and 60°, respectively. The sliding failure on the south face is also controlled by joint sets 1 and 3. By 17 403 cycles, the flexural toppling and sliding failures are more advanced (Figure 8.34c). Limited anti-scarp development has occurred on the north face of the toppling tower, although this is not clear from the displacement vector plots. The flexural toppling failure on the north tower has stabilised by 30 403 cycles, apart from the detachment of a few intact rock blocks (Figure 8.34d). Creep movements are still occurring in the zone of sliding on the south face, as the failed blocks approach an equilibrium slope angle.

Two main areas of movement have developed in the sliding mass by 15 403 cycles, producing a maximum displacement of 20 m (Figure 8.35a). In the flexural toppling zone, three main displacement zones have developed, producing a maximum displacement of 30 m. At 17 403 cycles, three displacement zones have developed on the zone of sliding, resulting in a maximum displacement of 40 m. The flexural toppling zone has also developed three main displacement zones, producing a maximum displacement of 40 m. In both failures, the magnitude of deformation decreases with depth. It is difficult to compare the depths of deformation of the two failures, because the flexural toppling failure originates from a tower, which has a limited volume of material. If the flexural topple occurred in the main rock mass, previous models suggest that the depth of deformation would be much larger than for the sliding failure. By 30 403 cycles, the number of displacement zones on the northern tower is only two, indicating stabilisation of the flexural topple (Figure 8.35b). The sliding failure shows evidence of secondary rotation of displacements, as material flows over previously failed material on the bedrock ramp.

The second mesh constructed for AL7 simulates the evolution of the east-west profile. The initial mesh plotted at equilibrium is plotted in Figure 8.36a. The displacement vector plot shows that by 13 000 cycles buckling has developed in the tower, which is failing by flexural toppling (Figure 8.36b). The orientation of the vectors also indicates some sliding movement. It is unclear whether the sliding failure is initiating the flexural topple, or is a response to it. The development of the flexural topple is principally controlled by joint set 3, dipping at 81° to the west, and joint set 2, dipping at 76° on the mesh. Limited sliding failures have occurred on the west face of the tower, controlled by the 60° dip of joint set 1. Anti-scarp formation has occurred on the east face, although this is difficult to resolve on the plot presented. By 20 000 cycles, the failure mode has changed from ductile flexural toppling to brittle block toppling as blocks become detached from the east face of

the tower (Figure 8.36c). A zone of secondary toppling has developed on the west face in response to block sliding over previously failed material. At 25 056 cycles the failure of the east face is well advanced: a large amount of material has become detached from the free face and is in free-fall (Figure 8.36d).

The development of displacement zones in the rock mass shows that by 13 000 cycles, five main displacement zones have developed in the eastern tower (Figure 8.37a). The maximum magnitude of displacement within the zone of active toppling is 15 m. On the west face, a displacement of 5 m has developed in response to the onset of sliding. By 20 000 cycles, seven displacement zones have developed, with the maximum magnitude of displacement occurring on the east face (Figure 8.37b). The displacement zones are produced by the differential magnitude of block toppling on the east face. The maximum displacement on the east face is 60 m, compared with only 10 m on the west face. By 25 056 cycles, the number of displacement zones in the rock mass is fewer, because the tower has failed and many blocks are in free-fall, limiting the development of differential displacement (Figure 8.37c). As material is toppling to the east, this has limited the sliding failure on the west face, as indicated by the zero displacement contour within the sliding zone.

8.3.3 Simulation of inselbergs at the ≥ 500 m scale

The final model constructed to simulate the behaviour of the sandstone inselbergs in the Al-Quwayra-Wadi Rum region was the east-west profile of AL17, located in the Barra Canyon. Only the east-west cross-section was modelled due to the extensive longitudinal outcrop of the landform. The initial mesh at 10 000 cycles is plotted in Figure 8.38a. The west face is plotted on the right-hand side of the model and the east face on the left-hand side. By 34 360 cycles, the displacement vector plots show that a flexural topple has developed on the west face (Figure 8.38b). This is in response to oversteepening of the free face by fluvial incision within the Barra Canyon. The flexural topple is principally controlled by joint sets 1 and 3, dipping at 76° and 81°, respectively. The UDEC model output shows evidence for anti-scarp formation associated with the flexural topple. The model then self-stabilises until 334 360 cycles; the onset of further flexural toppling increases the depth of deformation in the slope, as indicated by the displacement vector plot at 334 360 cycles (Figure 8.38c). By 404 360 cycles, the failure of the west face has continued and the depth of deformation increased (Figure 8.38d). However, the plot of the

total history of unbalanced forces suggests that the model has self-stabilised again (Figure 8.39). By 404 360 cycles, the displacement vector plot indicates that tension cracks have opened up along some of the joint surfaces represented by sets 1 and 3, showing that the model is failing under a tensile stress regime, as would be expected for a flexural toppling failure (Figure 8.38d).

The development of horizontal displacement zones in the rock mass during the flexural topple is plotted in Figures 8.40a to 8.40c. At 34 360 cycles, three main displacement zones have developed within the flexural topple (Figure 8.40a). The maximum magnitude of displacement is 80 m at the surface and 40 m at depth. The 40 m contour marks the main shear surface over which deformation is occurring. On the west face, the depth of deformation in the rock slope is approximately 400 m, so the flexural toppling failure is deep-seated. By 334 360 cycles, five main displacement zones have developed on the west face as a result of continuing failure, although there has not been much increase in the depth of deformation (Figure 8.40b). The maximum surface displacement in the rock mass is 100 m, indicating 20 m of displacement has occurred over 300 000 model cycles. This reinforces the contention that flexural failures are time-dependent. By 404 630 cycles, the number of displacement zones associated with the flexural topple is just three, indicating that increased failure has occurred, as the flexural topple begins to move at a more constant rate of displacement (Figure 8.40c). The maximum surface displacement in the failure at the end of the simulation is 160 m on the west face. The zero horizontal displacement contour shows that the east face is stable, consistent with field observations, which found no geomorphological evidence for past failures on the face.

8.4 Comparison of numerical simulations

Numerical simulations have shown that toppling dominates the failure of the sandstone inselbergs in the Al-Quwayra Wadi Rum desert of southern Jordan. A summary of the failure mechanisms for each model is presented in Table 8.3. The dominant failure mechanism of all inselbergs is toppling, with sliding also occurring at some sites. This is caused by the almost vertical dip of the joint set and the near-horizontal dip of the bedding. The surfaces controlling the sliding failures are steeply dipping and occur on opposite faces to the toppling failures. The UDEC modelling confirms the kinematic analysis that toppling is the dominant failure mechanism (Chapter 6).

To compare model output from various sites a smoothing function can be applied to the output of total unbalanced forces. This reduces data noise, allowing general trends in the pattern of unbalanced forces to be identified for particular failure mechanisms. A lowess smoothing function (Cleveland, 1979; Cleveland and Devlin, 1988), with first degree polynomial and 0.01 sampling proportion was applied to the out of balance forces for all model outputs. The lowess smoothing applies a tricubic weight function to weight the data:

$$\left(1-|u|^3\right)^3, \qquad \textbf{Equation 8.1}$$

where u = unbalanced force.

The unbalanced forces, in kg m s^{-2}, represent an inertial force acting over each model cycle. As failure propagates, the out of balance forces, i.e. the inertial forces, are greatest. When the rock mass moves towards an equilibrium *in situ* stress state, the inertial forces reduce and stability is reached. The smoothed curves for all models which experienced failure are presented in Figure 8.41.

The number of model cycles over which the inertial forces are at their maximum, as failure is occurring, can be related to the failure mechanism. Sliding failures are characterised by a sharp, relatively short-lived, high magnitude peak in the inertial force indicating that propagation of failure is relatively rapid (Figure 8.42). Toppling failures tend to occur over a much longer period of time, being characterised by a gradual increase in the inertial force at a lower magnitude than the sliding failure (Figure 8.42). Flexural topples have a similar signature to block topples, but the inertial force is less and the increase and reduction in force occur over greater number of model cycles. Where self-stabilisation of the flexural topple occurs because of block inter-locking, the reduction of inertial out of balance force tends to be relatively rapid (Figure 8.42).

UDEC modelling has provided a detailed insight in to the failure mechanisms and landform behaviour of the sandstone inselbergs. However, a more general approach of summarising the failures is useful in comparing the evolution of failures in each model. The same approach of plotting the failure patterns, as outlined in Chapter 7, was therefore used. For each model, $\lambda = 1/\rho$, where ρ is displacement

was plotted against model time and an exponential asymptotic curve fitted to the data. Fitting the curve gives information on the initial condition y_1, the final condition y_2 and the relative speed of failure. Further details on the model can be found in Chapter 7, section 7.4, where the basis of the model is fully explained. Summary statistics for each model are presented in Table 8.4.

Site	Profile	Dominant failure mechanism	Joint sets responsible
AL9a	North-south	Block toppling	Joint set 3
AL9b	East-west	Stable	Stable
AL12a	North-south	Sliding and toppling	Sliding surface controlled by joint set 1
AL12b	East-west	Stable	Stable
AL10a	North-south	Sliding	Joint set 1
		Flexural toppling	Joint set 4
AL10b	East-west	Stable	Stable
AL11a	North-south	Stable	Stable
AL11b	East-west	Block toppling	Joint sets 3 and 5
AL3a	North-south	Flexural toppling	Joint set 6
AL3b	East-west	Flexural toppling	Joint set 1
AL2a	North-south	Sliding	Joint set 1
		Block toppling	Joint set 1
AL2b	East-west	Stable	Stable
AL7a	North-south	Flexural toppling	Joint sets 1 and 5
		Sliding	Joint sets 1 and 5
AL7b	East-west	Flexural toppling	Joint sets 1 and 3
AL17	East-west	Self-stabilising flexural topple	Joint sets 1 and 5

Table 8.3: Summary of the dominant failure mechanisms determined from the UDEC model output. The joint set numbers are those defined in chapter 6, and do not correspond to the UDEC input file joint set notation.

Site	y_1	y_2	ω	R^2	rmse	half-way
AL9a	459.549	0.047	1944	1.000	0.007	1347
AL12a	1785.365	0.050	1457	0.999	0.011	1010
AL10	30475.060	0.031	927	0.999	0.007	643
AL11a	10871.870	0.026	1181	0.996	0.022	819
AL3a	3.95E+07	0.021	571	0.999	0.012	395
AL3b	26156.700	0.011	965	0.996	0.017	668
AL2a	4673.038	0.014	1183	0.995	0.028	820
AL2b	53200000	0.008	561	0.990	0.025	389
AL7a	17.247	0.110	3371	0.976	0.061	2336
AL7b	7803264	0.031	628	0.993	0.019	435
AL7b2	2576.677	0.020	1265	0.976	0.040	877
AL17	64000000	0.007	610	0.976	0.022	423

Table 8.4: Summary statistics for all model runs. Models that did not fail have not been included in the table.

All values of y_2 are close to zero, indicating that the failure signature is almost an exponential decline. Large values of y_1 occur because the fitted model involves extrapolation outside the data region, and in the direction in which y is varying most rapidly. Therefore, estimates of y_1 should not be taken very seriously. The results of most interest are R^2, which should be close to 1, and the root mean square error (rmse), which should be close to zero. The halfway time is taken as $\omega \ln 2$, and gives a relative sense of the speed of failure. Higher values of halfway time indicate the failure takes a longer period of time to propagate. The sliding failure on the south face of AL2 is the most rapid failure with a halfway time of 389 model cycles. The toppling failure on the north face of AL2 has a halfway time of 820, and is much larger than the sliding failure. AL7a has the largest halfway time at 2336 model cycles, and this corresponds to the total failure of the large central tower through flexural toppling. The size of the failure on AL17 is deep-seated and involves a large volume of material due to the outcrop scale of the inselberg. However, the halfway time of 423 model cycles indicates that failure is relatively rapid and the flexural topple self-stabilises. The halfway time suggests that displacements heading towards deep-seated catastrophic failure are characterised by long periods of active failure. Toppling events are more time-dependent than sliding failures which tend to involve sudden, brittle failure, rather than time-dependent deformations associated with toppling failures. There does not seem to be any scale-dependency in the speed of failure between the sandstone inselbergs.

The halfway time can be considered as analogous to the geomorphological concept of relaxation time (Brunsden and Thornes, 1979; Brunsden, 1980, 1986). The half-way time gives an approximation of the time taken for the slope to move from an initial equilibrium to a new state of equilibrium after the failure event. Out-of-balance forces and an unstable slope geometry cause the slopes to fail. This initial condition of instability is followed by failure and the time taken for the failure/instability to propagate through the landform and reach a new equilibrium is equivalent to relaxation time indicated by the half-way time. Once the failure has stabilised, the landform has reached characteristic form time (Brunsden, 1986). The magnitude-frequency of the out-of-balance forces, or reaction time, of the landform influences the relaxation time. Models with higher magnitudes of unbalanced forces typically head towards catastrophic failures, which are characterised by a greater half-way time.

The summary measures for the modelled failures are useful in comparing the timespan over which failure is occurring. It is also instructive to examine the graphs from which the summary data were derived, so that the pattern of failure can be examined. Results presented in Chapter 7 confirmed that failures in rock masses with pre-existing discontinuities are characterised by a non-linear failure signature. The failure patterns for the inselberg models are presented in Figures 8.43 to 8.50.

The toppling failure on the north face of AL9 has an asymptotic failure signature when plotted in λ-t space (Figure 8.43). The graph shows that failure did not begin until 13 000 cycles and continues to accelerate until 21 000 cycles, when constant velocity has been reached. The slope of the fitted curve is not vertical, indicating that displacements in the toppling mass are gradual and increase as the centre of gravity falls further outside each block as the failure develops.

AL12 fails through a combination of sliding and toppling, with accelerations increasing at 12 000 model cycles, indicating that failure has begun (Figure 8.44). The extrapolated value of y_1 forces the curve above the initial data point. The shape of the curve is asymptotic and is slightly steeper than that presented for AL9. This is caused by an increase in the amount of sliding in the model. The halfway time indicates that because sliding failures are brittle they tend to produce rapid displacements once catastrophic movements have begun. It is no surprise, therefore, that a composite sliding / toppling failure produces a steeper curve than a

toppling failure. This is reflected in the halfway times, 1347 for AL9 and 1010 for AL12.

The failure occurring on AL10 is a catastrophic topple. The form of the curve is non-linear, and initially very steep (Figure 8.45). The failure begins at 10 000 cycles, immediately following the release of the constrained boundaries. Infinite velocity is reached in less than 3000 model cycles showing that this deep-seated toppling failure is rapid. This is reflected in the halfway time for the failure of 643 model cycles. Although the model fails by toppling, the pattern differs from other topples. This may be due to sliding above the zone of toppling increasing the magnitude of displacements in the topple (Figures 8.13b to 8.13d).

An asymptotic failure signature is produced by the toppling failure on AL11 (Figure 8.46). The failure begins at 11 000 model cycles and reaches a constant rate of displacement at 14 000 cycles, indicating that catastrophic failure has been initiated. Although the initial condition is over estimated, the curve summarises the data well, with little scatter. The halfway time is relatively large at 819 model cycles, because of the relatively long tail produced by the deceleration as the model approaches infinite velocity.

AL3a fails by rapid toppling controlled by the natural variability of joint spacing. The failure signature is asymptotic and the initial form of the curve is steep, indicating rapid displacements (Figure 8.47a). This is recorded by a halfway time of 395. The failure is characterised by a rapid and displacements, culminating in a catastrophic failure. The toppling failure is promoted by a zone of secondary sliding above and in response to the topple (Figures 8.24b to 8.24d). The toppling failure on the east face of AL3 shows gradual development of displacements, which begins at 10 000 cycles (Figure 8.47b). Acceleration increases as the centre of gravity falls further outside each block. There is a more gradual approach to infinite velocity, reflected in the halfway time of 668.

Toppling occurs on the south face of AL2 and this failure produces an asymptotic signature (Figure 8.48a). The pattern of failure is characterised by an increase in the magnitude of displacements over a halfway time of 820 model cycles. Displacements are more gradual due to the more progressive nature of toppling failures as blocks begin to 'free-fall', than in the sliding failure on the north face (Figure 8.48b). Here the failure signature is characterised by very rapid

displacements as joint friction is overcome. The displacements reaches a constant value very quickly, with a halfway time of 389. This is caused to some extent by the accumulation of slide debris at the toe of the slope preventing further movements (Figures 8.29b to 8.29c).

A number of failures occur at AL7, with characteristic failure signatures (Figure 8.49). The toppling failure of the central tower shows a gradual increase in the magnitude of displacements, with a halfway time of 2336 model cycles (Figure 8.49a). The displacements gradually increase as the degree of toppling increases. The final condition of y_2 is of interest because this shows that the value of constant displacement is much lower at 0.11 than other failures. This is caused by gradual creep movements in the topple which is beginning to self-stabilise by the end of the simulation at 30 000 cycles. In contrast, the sliding failure on the south face shows rapid displacements, reflected in the halfway value of 435 (Figure 8.49b). The slide is able to overcome the limiting joint friction quickly, and reach a constant rate of displacement, propagating rapidly. The fitted curve departs from the model data between 11 000 and 15 000 cycles. This is a result of a decrease in the rate of displacement as the slide begins to undergo translation as it begins to flow over the slope toe, which has a lower angle.

The west face undergoes catastrophic flexural toppling, producing an asymptotic failure signature and a halfway time of 877 (Figure 8.49c). The failure reaches a constant rate of displacement relatively quickly as a large number of blocks enter free-fall as they detach from the main zone of toppling (Figure 8.36d). Once the blocks are in free-fall the displacements are gravitational and therefore constant. The flexural topple does not reach a constant rate of displacement as quickly as the slide on the south face due to the progressive rotation of blocks as the failure begins. Only once the centre of gravity of the blocks falls outside the free-face does the catastrophic failure occur.

The largest inselberg, AL17, undergoes a short phase of displacement and the results are characterised by an asymptotic increase in the magnitude of displacements, with a halfway time of 423 (Figure 8.50). The period of displacement is short because the model self-stabilises with little change occurring after 12 000 cycles. Self-stabilising failures are, therefore, characterised by short phases of movement before stabilisation or gradual creep occurs.

The scale of the rock mass appears to exert little influence on the time taken for failures to propagate once initiated. The major influence is failure mechanism, as governed by the discontinuity and slope geometry. Sliding and self-stabilising topples are characterised by relatively short periods of movement. Topples undergo gradual displacements caused by rotation of the blocks, until catastrophic failure occurs.

8.4.1 Scale effects and slope behaviour

The failure signature for the rock masses is consistent across all outcrop scales and is characterised by an asymptotic pattern. However, block size can influence the deformation characteristics of the rock mass and the failure mechanism occurring. Inselbergs with an outcrop scale ≤ 50 m have a large block size compared with the outcrop scale of the rock mass, whereas rock masses between 100 and 500 m have a small block size distribution compared with outcrop scale. Joint spacing is relatively consistent across the study region, so the size of structural elements in the larger rock masses is smaller relative to the outcrop scale of the rock mass.

Theoretical modelling indicated that smaller elements deform in a more ductile way than large elements, which behave in a brittle manner. The deformation characteristics of sandstone inselbergs of the Al-Quwayra-Wadi Rum region seem to depend on the average element size. AL9 and AL12 failed by block toppling and this has been shown to represent a brittle failure mechanism (Nichol *et al.*, 2002). As the scale of the rock mass increases, failures become more ductile and are dominated by flexural topples and slope buckling because the element size decreases compared with the outcrop scale. As the relative element size decreases, the rock mass exhibits more elastic deformation. The ductile-brittle transition and its scale dependency is a major area of research in the field of engineering fracture mechanics; it is well established that for intact materials, scale effects can lead to a transition between ductile and brittle behaviour (Carpinteri and Karihaloo, 2003). As the scale increases from the ≤ 50 m outcrop scale to the 100-500 m scale in the sandstone inselbergs, a threshold is passed, which represents the ductile to brittle transition in the rock mass. If flexural toppling continues and tensile stresses increase, the behaviour changes from ductile to brittle as blocks detach from the free face.

An additional scale effect in the rock mass is produced by variations in the consistency of block (element) size caused by variations in the joint spacing. Although the joint spacing is fairly consistent across the Al-Quwayra-Wadi Rum study area, natural variability is represented in the models by including the standard deviation of spacing. Previous work concluded that the variation in joint spacing has little influence on the failure mechanism (Kimber, 1998). However, this research suggests that natural variability in joint spacing can affect the deformation and failure mechanism of the rock mass. The natural variability in spacing causes block size to be reduced in some areas of the models. This has the effect of producing more ductile zones in the rock mass, increasing the elastic deformation the rock mass can sustain before brittle failure and large-scale block detachment.

The two main types of failure have distinct failure signatures. Brittle, sliding failures and self-stabilising failures show a short periods of displacement while ductile, flexural failures undergo displacements over a much longer period of time. This initial work has major implications for the prediction of whether slope movements in high-risk areas are tending towards catastrophic failure. For many of the sandstone inselbergs, self-stabilisation would not occur indefinitely, because the extra stress exerted by blocks sliding above and on to the zone of flexural toppling increases the deformation and eventually produces brittle failure. Many of the plots show a complex form with periods of very little displacement, even once movements have occurred and failure is beginning. As outlined in Chapter 7, the implication of this for the interpretation of monitoring results is the misidentification of the cessation of movement within the failure. If displacement plots indicate that no further displacements are occurring, it may be incorrectly assumed that the failure has occurred and stabilised. However, the modelling results presented here suggest that caution must be exercised in the interpretation of monitoring data.

It is difficult to assess how model time compares with the field situation, and how long each failure would take to develop in the natural environment. An attempt to provide a temporal framework of failure is given in section 8.5. However, some features of the models can be identified in the field. As topples occur, this enlarges joint apertures, accentuating the pillar form of some of the inselbergs. There is also some evidence for rotational shear surfaces. On AL7, the rotational shear surface on the south face is represented in the model output. Processes which are absent from the model include slope sapping, which undercuts the toe of the slope promoting tension failure. This was not included because it is difficult to assess the

rate of undercutting and UDEC does not include any means of simulating chemical processes; it is meant to simulate joint-controlled failure. Despite this, undercuts were included if they existed at the site. This indicated that slope sapping is a contributory factor promoting failure of the inselbergs. However, the dominant control is the discontinuity geometry.

8.5 Temporal evolution of the inselbergs

In an attempt to improve understanding of the temporal evolution of the sandstone inselbergs in Wadi Rum, ^{10}Be cosmogenic dating was carried out on samples extracted from large failures. An assumption inherent in this approach is that past failure events can be used predict future events and that failure conforms to a steady state model (as opposed to the exhaustion model described for the Picos de Europa). While there are errors associated with this technique, it is not intended to be used as a predictive tool – the approach is designed to increase our understanding of timescales over which the sandstone inselbergs are likely to experience formative events. Since model time (in cycles) is unrelated to real time, cosmogenic dates may help to constrain numerical output, providing a broad temporal framework through which model output can be related to landscape evolution over geomorphic timescales.

8.5.1 Sampling and Methods

Cosmogenic exposure age dating, which relies on the measurement of rare isotopes produced in near surface rocks by cosmic-ray bombardment can be used to date bare rock surfaces (Cerling and Craig, 1994). Cosmogenic dating was chosen because organic debris is absent from the deposition zone of failed material. The lack of organic material means that conventional dating methods such as ^{14}C cannot be used to date the timing of failure. The intention of this research is to use cosmogenic isotopes in an applied sense, not to provide a full theoretical background to the use of cosmogenic nuclides for dating exposure surfaces. For detailed theoretical background information, the reader is directed to Gosse and Phillips (2001), and references therein.

Originally the intention was to use two isotopes, ^{26}Al and ^{10}Be, to provide age estimates for failures of selected sites in Wadi Rum. The advantage of using paired

isotopes is that the errors associated with using a single isotope are reduced. In addition, using two isotopes can give clues as to the complexity of the exposure history of the landform, based on the $^{26}Al/^{10}Be$ production ratio of 6.1 (Balco *et al.*, 2002). The two isotopes are usually measured together because the physical and chemical sample preparations are similar for both isotopes and the reported age is an average weighted mean of the ^{26}Al and ^{10}Be ages.

However, due to analytical delays, the results of only one isotope, ^{10}Be, are presented here. Single isotope dating using ^{10}Be has been applied to a range of geomorphic conditions, including fluvial incision rates (Brocard *et al.*, 2003), and constraining glacial chronologies (Tschudi *et al.*, 2003). ^{10}Be has a half-life of 1.5 Ma and is produced almost entirely by spallation in quartz (silica) with limited production through muon reactions (Gosse and Phillips, 2001). The main sources of error using ^{10}Be are atmospheric contamination by modern ^{10}Be during AMS measurement and errors in the production rates. Contamination can be removed through chemical techniques. Production rate estimates for ^{10}Be in quartz vary from 4.74 atoms g^{-1} a^{-1} (Clark *et al.*, 1996) to 6.4 atoms g^{-1} a^{-1} (Brown *et al*, 1991), a 40 % range. Stone (1999) found that the discrepancy between published production rates could be accounted for by a 3 % muon production contribution, yielding a scaled production rate of 5.1 $\pm$ 0.3 g^{-1} a^{-1} for ^{10}Be. This is considered to be the most appropriate production rate at present.

Samples for cosmogenic dating were collected from three sites: AL2, AL7 and AL10 (Plate 8.10). At each site two boulders were sampled. Samples were taken from boulders which showed minimal erosion on the sampled surface. Only large boulders (> 2 m diameter) were sampled to reduce the risk of post-exposure burial by wind blown-sands. Above this size, the acceleration of air over the top of the boulder will prevent the accumulation of surficial material. To correct for topographic shielding, horizon geometries were collected for each boulder so that the shielding factor could be calculated. It is important to account for topographic shielding because surrounding topography can block incoming cosmic rays, reducing the production rate of cosmogenic nuclides at a particular location (Dunne *et al.*, 2000).

Each sample was trimmed in the laboratory to a standard 5 cm thickness, reducing between sample error caused by variations in sample thickness. It is necessary to correct for sample thickness because cosmic rays are attenuated with depth. Production rates of ^{10}Be are greatest at the surface, but reduce with depth. The age

estimate is an average nuclide concentration over the sample depth range. Once trimmed, samples were crushed and sieved. Only the 100-500 μm size range was used for analysis. Chemical preparation of the samples followed the procedure used by the Australian Nuclear Science and Technology Organisation (ANSTO). External contamination was removed by washing in water and acid. The quartz mineral fraction was separated from other minerals by heavy liquid separation, magnetic separation and HF etching. The cleaned quartz was dissolved in hydrofluoric acid at a low temperature (~60 °C). Once dissolved, all silica (>99.9 % of quartz) and fluorides are fumed off at 150 °C with $HClO_4$. Contaminants are removed from the dissolved sample by collection using Ion Exchange columns. Cosmogenic isotopes are then selectively precipitated from solution. ^{10}Be contamination is removed by dissolution in ammonia and beryllium and aluminium salts are converted to BeO and Al_2O_3 suitable for AMS analysis. Nuclide concentration measurement was carried out at the Accelerator Mass Spectrometry facility at ANSTO, Australia.

Ages were calculated from measured isotope abundances in the sampled boulders using a ^{10}Be production rate of 5.1 ± 0.3 atoms/g^{-1}/a^{-1}. (Table 8.5). Production rate corrections were made for latitude, altitude and magnetic field variation using geomagnetic scaling factors from Stone (2000). Topographic shielding was significant (10^{-2}) in all samples due to proximity to the cliff free face (Table 8.5). The effect of variations in surface erosion rate on the exposure age estimate was modelled for each boulder (Figure 8.51). As erosion rate increases, the exposure age increases. This is the result of the applied correction for surface erosion. For AL2-B1, erosion rate decreases at a critical erosion rate of 18 mm Ka^{-1}. However, on all sampled boulders, geomorphic evidence indicated limited surface erosion since exposure. Therefore, sample thickness was corrected for assuming a rock density of 2500 kg cm^{-3} and for an assumed steady surface erosion rate of 1 μm / a^{-1} (i.e. 2.5 cm in the last 25 000 yrs). The selected erosion rate gives a minimum exposure age. Recent research has indicated that production rates of cosmogenic nuclides on boulders may be 10-12% lower than on large flat surfaces and that boulder size and shape may have to be corrected for (Masarik and Wieler, 2003). At present no scaling factor exists for boulder size and shape and it is not accounted for in the calculation of exposure ages used in this study.

Sample ID	N Latitude (DD)	E Longitude (DD)	Elevation (m)	Thickness (cm)	Thickness correction[a]	Shielding factor	Geographic Scaling factor[b]	^{10}Be production rate (atoms/g)	[^{10}Be] (10^4 atoms/g)	^{10}Be age (a)[c] and 1σ error	^{10}Be age (a) and 1σ error including paleomagnetic correction[d]
AL2-B1	22.7591	35.4800	877	5	0.9619	0.9020	1.3941	6.17 ± 0.363	21.00 ± 3.2	35272 ± 5972	------
AL2-B2	22.7608	35.4794	800	5	0.9619	0.8909	1.3163	5.75 ± 0.338	7.21 ± 0.3	12695 ± 927	------
AL7-B1	29.7433	35.4288	805	5	0.9619	0.8705	1.5354	7.25 ± 0.426	6.94 ± 0.3	10699 ± 790	10481 ± 733
AL7-B2	29.7433	35.4280	815	5	0.9619	0.8833	1.5466	6.70 ± 0.394	3.78 ± 0.2	5672 ± 451	5868 ± 467
AL10-B1	29.7225	35.4516	819	5	0.9619	0.8871	1.5505	6.75 ± 0.397	14.00 ± 0.5	21196 ± 1490	19485 ± 1368
AL10-B2	29.7227	35.4516	852	5	0.9619	0.8705	1.5883	6.78 ± 0.399	7.79 ± 0.4	11620 ± 918	11302 ± 893

[a] Assuming a rock density of 2500 kg m^{-3}.

[b] The geographic scaling factor, taken from Stone (2000), corrects the ^{10}Be production rate for altitude, latitude and atmospheric pressure.

[c] Ages calculated using a ^{10}Be production rate of 5.1 ± 0.3 atoms/gram/SiO_2/a, corrected for latitude and altitude and assuming a constant erosion rate of 0.001 cm/Ka^{-1}.

[d] Corrected age for paleomagnetic variation according to Nishiizumi *et al.* (1989). A limitation of the correction is that it cannot be applied to latitudes below 25 degrees.

Table 8.5: Sample information, scaling factors, site-specific nuclide production rates, analytical data and age estimates for ^{10}Be data from Wadi Rum, Jordan.

8.5.2 Results and Discussion

Boulder ages from Wadi Rum range between 35272 ± 5972 a for AL2 and 5868 ± 467 a on the south face of AL7 (Table 8.5). However, there is a distinct clustering of ages ranging from 12 695 ± 927 for the second boulder sampled at AL2 to 10 481 ± 733 for AL7-B1. Half the sampled boulders fall within this age range (Figure 8.52).

At all sites sampled, there appear to be two distinct phases of slope instabilities from the limited data presented. At AL2, the first failure event occurred 35 272 ± 5972 a, followed by a period of equilibrium until 12695 ± 927 a when the most recent failure event occurred (Table 8.5; Figure 8.52). For AL7, the oldest failure event sampled occurred 10 481 ± 733 a, with a more recent one occurring 5868 ± 467 a (Figure 8.52). This confirms geomorphic evidence that the last major failure event on the face happened relatively recently – the free face was not as weathered as those faces from other sites where the failures have been dated to be older. At AL10, the cosmogenic ages show at least two periods of slope failure; the oldest occurring 19 485 ± 1368 a and the most recent 11 302 ± 893 a.

^{10}Be exposure ages for the failure events show a marked correlation with prevailing climatic conditions (Figure 8.52). A tentative suggestion of climatic change and geomorphic activity during the Pleistocene and Holocene is made by synthesising work from around the region (Table 8.6).

The oldest failure events at AL2 and AL10, dated to 35 272 ± 5972 and 21 196 ± 1490 a, respectively, seem to correlate well with the increased period of precipitation that occurred in the region between 30 000 and 20 000 years ago. Similarly the failures dated between 12 695 ± 927 a at AL2 and 10 481 ± 733 a at AL7 appear to correlate to a period of increased precipitation between 12 000 and 10 000 a. The most recent failure at AL7, dated to 5868 ± 467 a falls within the Neolithic wet period, when rainfalls were much higher than at present. Since then, there have been very few periods of increased rainfall, which may help explain why there have been very few recent failures in the Wadi Rum region.

Table 8.6: Climate change and relative geomorphic activity.

Years B.P	Climatic description	Geomorphological activity
30000 - 20000	Period before the Last Glacial Maximum with significantly wetter conditions than present.	Greater
16000	Period following the close of the Pleistocene wet period. Aeolian processes dominant. Temperatures and rainfall lower than at present, reaching a minimum around 14000 B.P.	Lower
12000-10000	A period of increased precipitation. Lower temperatures as far south as at least 30 °N.	Greater
10000 - 8800	A less humid phase associated with the last glacial advance. Increased temperatures. Rainfall typically less than at present.	Lower
8800 - 7000	Markedly increased rainfall than present during this period.	Greater
7000 - 4400	The Neolithic moist period. Higher rainfall than at present, with increased temperatures. If evaporation was higher then conditions may have been pluvial. Notable decrease in rainfall after 5000 B.P.	Greater
4400 - 2850	Decrease in precipitation in 5th millennium B.P. led to a long period of variable climatic conditions. Average rainfall slightly less than today, interrupted by a moist spell around 3200 B.P.	Lower
2850 - 1300	Similar rainfall as today, but characterised by marked fluctuations. Periods higher humidity around 1800 and 1500 B.P, but opposed by drought conditions, notably around 1400 B.P.	Lower
1300 - present	Short term climatic fluctuations with average rainfall higher than present. Cold spells cause the Black Sea and Nile to freeze (1000 B.P). Last century has seen a marked climatic deterioration, with a rainfall decrease of between 1 and 15 %, a fall in lake levels and a decrease in the volume of the Nile	Greater

Although the modelling approach adopted in this thesis assumes dry rock mass conditions, there is much evidence relating the instability of rock slopes to groundwater levels in the rock mass and fluid flow through the joints. For topples, Kakani and Piteau (1976) demonstrated that the tensile stress region reflects real conditions only when a high groundwater condition is accounted for. In the Delabole Slate Quarry, Cornwall, modelling has confirmed the detrimental effect that a raised water table can have on the stability of a slope (Coggan and Pine, 1996). The sandstone inselbergs of Jordan act as local aquifers and during periods of increased rainfall would have experienced elevated groundwater conditions. In addition, the unit weight of the rock would be increased, producing greater tensile stresses. This would significantly reduce the shear strength of the rock mass and could promote failure. Slope sapping processes would also be increased under a wetter climatic regime, undermining the toe of the slope and decreasing the stability.

8.5.3 Temporal constraint of UDEC model output

The ^{10}Be dates suggest that past failures have been influenced by prevailing climatic conditions. Since the dates represent past events under different climatic regimes, it is not possible to directly use the results to predict the timescale of future change based on the UDEC modelling results. The modelling of the rock mass under dry conditions shows that the inselbergs are inherently unstable because of the discontinuity geometry and *in situ* stresses. A groundwater table was not included in any of the models because of the difficulty in estimating joint apertures, hydraulic pressures, flow rates and groundwater levels. Any inclusion of a groundwater table would have introduced unquantifiable errors.

Relating the cosmogenic ^{10}Be ages to model output involves a number of assumptions and associated errors. First, it is assumed that the ages are correct and represent the temporal distribution of slope failure at the site. Second, the UDEC model assumes that the landform reaches an equilibrium stress state and that stability is imparted both by toe support, provided by collapsed material and that the equilibrium slope angle remains stable. Over geomorphic timescales, the toe material is likely to become weathered, especially because a significant proportion of that material would have disintegrated on impact after detachment from the free face, resulting in loss of support. Second, the slope angle is not likely to remain constant because of weathering.

Despite this, the ^{10}Be dates may be tentatively used to provide a broad chronological constraint on the UDEC model output, so that the timescales over which failures occur may be better understood. For AL2, the UDEC model output shows a sliding failure on the south face and a toppling failure on the north face (Figures 8.29a to 8.29c). Cosmogenic samples were taken from the south face.

A smoothing function applied to the total history of unbalanced forces in the model shows two main periods of activity (Figure 8.53. The first is centred on 20 000 model cycles and the second on 55 000 cycles. In terms of providing a very tentative temporal framework, the oldest exposure age of 35 272 ± 5972 a may be correlated to the failure event around 55 000 cycles. The most recent failure event, centred on 20 000 model cycles may be considered analogous to the exposure age of 12 695 ± 927 a.

If the ^{10}Be data are crudely used to compute in years the timescale represented by each model cycle, then 1.5 model cycles represents approximately 1 year. The period of time represented by each model cycle can be overlaid on the smoothed plot of unbalanced forces and a very tentative temporal framework may be used to constrain the model output (Figure 8.53). Based on the assumption that the cosmogenic ages represent some sort of return period of rock slope failure, it could be tentatively suggested that the next failure event on the inselberg may occur between 11768 and 13622 years from now. A second failure event predicted by the UDEC model may occur between 29300 and 41244 years from now, or between 17532 and 27622 years after the first event.

The second site from which cosmogenic samples were taken was AL7. Model output shows a sliding failure on the south face, from where the cosmogenic samples were taken, and a self-stabilising flexural topple on the north face (Figures 8.34a to 8.34d). Smoothed unbalanced forces for the north-south profile of AL7 are presented in Figure 8.54. Seven main periods of activity can be identified at approximately 15 000, 20 000, 22 500, 25000, 27 500, 30 000 and 33 500 model cycles. In the UDEC model, the magnitude of unbalanced forces represents an inertial force. Comparing the sliding failure of the south face with the toppling failure of north face in λ-t space shows that the sliding failure reaches infinite velocity, i.e. maximum inertial force, much quicker than the flexural topple (Figure 8.49). This is represented on the plot of unbalanced forces by a sharp peak, over fewer model cycles. Therefore, on the smoothed plot of total history of unbalanced forces, the

first peak at 15 000 cycles is considered to represent the sliding failure, alternating with the flexural topple that lags slightly behind the slide.

Now that the slide has been identified on the plot of unbalanced forces, it is possible to use the ^{10}Be ages from the south face to tentatively constrain model output. The two exposure ages obtained from the south face of AL7 range from 5868 ± 467 a to 10 481 ± 733 a. By 15 000 cycles, vector displacement plots indicate that block detachment has occurred. If the ^{10}Be exposure age of 5868 ± 467 a is tentatively assigned to the first slide failure peak and the age of 10481 ± 733 a is assigned to the last peak, each model cycle represents 1.5 years. This is based on the assumption that the first failure occurred in 5000 model cycles and the second within 23 500 cycles because model boundaries remained fixed until 10 000 cycles. The number of model cycles represented by each failure event is plotted on Figure 8.54. It may be tentatively suggested that the next failure event, represented by the first slide peak, may occur 7500 ± 700 a from now and the second event 35 250 ± 1099 a from present.

The final site for which ^{10}Be exposure ages are available is AL10. Two boulders were sampled from debris representing past rock slope failures. The exposure ages suggest there are two main periods of rock slope failure at 19 485 ± 1368 and 11 302 ± 893 a. Applying a smoothing function to the total history of unbalanced forces suggests two main periods of activity in the model (Figure 8.55). The first peak is centred on 14 500 model cycles and the second on 19 000 cycles. Since failure of the north and south faces occurs simultaneously, it is not possible to distinguish between the failures on the plot on unbalanced forces. The peaks can, therefore, be taken to represent failure on either the north or the south face.

To temporally constrain model output, it is assumed that the youngest age of 11302 ± 893 years represents the first period of failure at 14 500 cycles and the oldest age of 19485 ± 1368 years the second failure event at 19 000 cycles. Displacement vector plots indicate that block detachment has occurred by 14 000 cycles (Figure 8.13c). Since model boundaries remained fixed until 10 000 cycles, the first failure event occurred within 4500 cycles, and the second within 9000 model cycles. If the errors associated with the ^{10}Be ages are considered, then the age of the second failure is approximately twice that of the first. This trend is also represented in the model output.

Based on the above assumptions, each model cycle can be assumed to represent 2.3 years. For the first failure, which occurred within 4500 cycles, it may be tentatively suggested that the time period represented is 10 350 years. Using the same assumption, the second failure event shown in the UDEC model output may be assigned a tentative age of 20 700 years. The number of model cycles represented by the ^{10}Be ages can be superimposed on the plot of unbalanced forces in an attempt to temporally constrain the model output (Figure 8.55).

8.5.4 Implications for landscape evolution

The approach of dating past rock slope failures to constrain evolutionary models of landform behaviour has never been attempted before. While the limitations of the adopted approach are recognised, important information regarding the temporal framework of landform development can be gained. The approach is unique in that it attempts to combine a rock mechanics modelling approach with a Quaternary dating method.

Climate appears to be a major control influencing the timing of past rock slope failures in the Wadi Rum region. All the past failures under climatic conditions which were significantly wetter than present. Slope sapping and the reduction in shear strength of the rock mass combine to promote rock slope failure. Although water flow has not been included in UDEC models due to difficulties in estimating relevant parameters, it can be argued that the cosmogenic dates do help in providing a very general indication of timescales involved in the evolution of the sandstone inselbergs of Wadi Rum. The dates are significant in providing a broad framework for understanding the temporal distribution of formative events. If the approach is accepted, then the average time, based on a combination of the ^{10}Be and UDEC model output, the recurrence interval for failures on the sandstone inselbergs is between 10 000 and 15 000 years.

The UDEC models are run until the inselbergs reach equilibrium stress conditions. Changes in slope form after equilibrium has been reached may promote further failures. The inselbergs chosen for dating have all experienced past failure events, which are the result of stresses being out of equilibrium. At present, weathering will be acting to reduce the shear strength of the rock mass, promoting failure and stress disequilibrium. The cosmogenic dates and model output can be used to examine the failures which occur during the establishment of equilibrium / stable slope

conditions. Temporary stabilisation of the rock mass during the establishment of equilibrium stress conditions is indicated by the peaked nature of unbalanced forces, even thought the vector plots may indicate continuous failure.

The scale of landforms has been used to examine the behaviour of the sandstone inselbergs. However, from the limited dates available, no evidence of scale effects can be found in the age of the failures. It was suggested that larger failures may take longer to propagate through a rock mass. Geomorphologically, larger failures are thought to have longer return intervals. AL10 was the smallest landform dated, while AL7 was the largest. No trend can be identified in age of failure compared with landform scale. In addition, there is no relationship between age of the failure and its volume from the modeled sites. Many more dates would be needed to examine such relationships.

Goudie *et al.* (2002) suggested that many of the rockfalls in the Wadi Rum were pre-Holocene in age. This was based on the highly weathered nature of some of the deposits and also because the deposits were overlain by Epipalaeolithic and Early Neolithic tools. According to Henry (1988), Epipalaeolithic tools in the Wadi Rum region can be dated to around 20 000 to 8000 years B.P. The ^{10}Be data collected as part of this research confirms this suggestion, with all rockfall being either Pleistocene or Holocene in age.

The long-term evolution of the inselbergs can be related to the classical theory of slope development proposed by King (1953), who argued that inselberg landscapes in arid and semi-arid regions were produced through parallel retreat. Many of the inselbergs show evidence of all the major components of King's (1953) model. Pediments, debris slopes, free-faces and crests are all present.

The modelling results, combined with cosmogenic dating, suggests that parallel retreat is occurring on the inselbergs of Wadi Rum. Numerical modelling has indicated that the discontinuity geometry leads to preferential development of failures on the south and north faces. The cosmogenic dates indicate that at each face where there is failure, it occurs over time - the rock slope failures are not one off events. Geomorphologically, this may be expressed by the elongate planform of many of the inselbergs.

Although it may appear that some of the inselbergs are undergoing parallel retreat, the geomorphological and UDEC model output indicate that this is not the case. The UDEC model output also indicates that there is a general reduction in the angle of the slopes through time as failures occur – the models do not indicate that a constant gradient is maintained on those faces undergoing constant failure.

Failures on the inselbergs tend to be isolated: the whole slope length does not show evidence for active failure. In addition, many inselbergs do not show an elongate planform. Episodic failure on the north and south faces gives the impression of parallel retreat, but most of the planform of the inselbergs is structurally controlled by the jointing pattern, which leads to instability on the north and south faces. Ultimately, the jointing pattern in Wadi Rum is tectonically controlled. Indeed, graben formation due to down-thrown blocks probably first resulted in exposure of the inselberg faces.

8.6 Conclusions

An initial understanding of the differences in the development of the sandstone inselbergs of the Al-Quwayra-Wadi Rum region has been gained through computer simulation of the behaviour of slopes at different scales. The UDEC simulations from characteristic field sites have led to an increased understanding of the development of slopes in jointed rock masses. The UDEC methodology adopted provides a further insight into the behaviour of rock slopes by considering more than just differences in individual joint properties such as mean joint spacing.

Scale effects are crucial in controlling the type of failure occurring in the sandstone inselbergs. The scale effects can be related to the outcrop scale of the inselberg and the element or block size distribution. As the scale of the slope increases deformations become increasingly ductile because relative block size decreases. The principal failure mechanisms operating are flexural toppling in the inselbergs greater than 100 m in height and block toppling in those less than 50 m in height. Analysis of strain zone development as the failure propagates has shown that this is related to the depth of failure and the variation in joint spacing through the creation of quasi-ductile zones in the rock masses.

The two principal failure mechanisms have distinct failure signatures. Flexural topples which show quasi-ductile behaviour are characterised by a long period of acceleration to infinite velocity. Flexural topples show a gradual increase in acceleration as the rotation of blocks increases. Sliding failures and self-stabilising topples are more rapid and show a short period of acceleration as the shear strength is overcome.

Cosmogenic dating, combined with UDEC model output, has provided a very tentative temporal framework for understanding the evolution of the sandstone inselbergs of the Wadi Rum region. The dates show that rock slope failures may occur at 10 000 and 15 000 year intervals on the sandstone inselbergs. It has also been suggested that many of the failures sampled as part of this research occur during periods when the climate was much wetter than at present. It would be useful to intensively sample one or two sites to confirm whether the return intervals calculated as part of this research are real, or just the product of two sampling locations.

Chapter 9: Conclusions

Chapter 9: Conclusions

This study uses a numerical modelling approach to simulate the failure mechanisms of jointed rock masses and the behaviour of steep slopes using the UDEC rock mass simulation code. Theoretical modelling results have identified block size and outcrop scale of the rock mass to be important controls on the geomorphological behaviour of landforms in jointed rock masses (Chapter 4). Particular attention has been paid to limestone rock slopes in the Picos de Europa (Chapters 5 and 7) and sandstone Inselbergs of the Al Quwayra-Wadi Rum area of southern Jordan (Chapters 6 and 8). *In situ* cosmogenic nuclide dating of rock slope failures has been used to provide a temporal framework for the evolution of slopes in the Picos de Europa and Al Quwayra-Wadi Rum. An attempt has also been made to provide a temporal framework for constraining UDEC model output.

9.1 Original contribution to Knowledge

This study includes the following work that makes an original contribution to knowledge.

The UDEC software has been used as a geomorphological research tool in the study of landforms in jointed rock masses. UDEC works by linking the forces acting upon individual blocks in a pre-defined mesh with displacement for successive model time-steps. The advantage of the code is that it can combine geological, geomorphological and rock geotechnical properties, such as joint geometrical, cliff morphometric and intact rock strength data, in a scientific manner. The code allows a multidisciplinary study of landform behaviour and forms the link between engineering studies of slope behaviour and geomorphological investigations of slope evolution. Examples throughout this study have demonstrated the use of UDEC and the increased geomorphological understanding of rock slope processes that can be gained from it.

Comparison of UDEC model output from sites in the Picos de Europa indicated that sliding and toppling failures are the most common failure mechanisms in the Picos de Europa. Slope deformations tend to occur over time and are a response to the elastic redistribution of stress within the rock mass. Many of the slopes in the Picos de Europa are oversteepened and UDEC modelling indicated that the slopes are still undergoing paraglacial stress redistribution.

In Wadi Rum, landform scale was shown to influence the behaviour of the landform. As landform scale increased, the relative size of the blocks decreased and slope deformations become increasingly ductile. Where block size is large compared with the landform scale, failures are brittle and occur rapidly. Flexural topples dominate landforms above the 100 m outcrop scale, whereas brittle block topples dominate at outcrop scales below 50 m. The two principal failure mechanisms have distinct failure signatures. Flexural topples which show quasi-ductile behaviour are characterised by a long period of acceleration to infinite velocity. Flexural topples show a gradual increase in acceleration as the rotation of blocks increases. Sliding failures and self-stabilising topples are more rapid and show a short period of acceleration as the shear strength is overcome.

A significant original contribution to knowledge has been provided by using *in situ* cosmogenic dating in an attempt to temporally constrain the evolution of rock slopes in Spain and Jordan and also to constrain the UDEC model output of future failures. Previous geomorphic models have been limited because the model time is unrelated to real time. The application of cosmogenic nuclide dating of rock slope failures in two contrasting environments and constraining UDEC model output has been demonstrated.

Cosmogenic ^{36}Cl dating has provided important information on the triggering mechanisms of slope failure. Rock slope failures in the Picos de Europa are the result of delayed paraglacial rock slope adjustment, climate and renewed paraglacial slope activity. Failures in the Picos de Europa have an average age of 7202 ± 324 years, indicating failure occurred approximately 8000 years after deglaciation. Cosmogenic dating and UDEC modelling has indicated that the paraglacial exhaustion model of Cruden and Hu (1993) is a useful tool for assessing the temporal frequency of slope failures in the Picos de Europa. The exhaustion model indicates that approximately 33 000 years, from the time of deglaciation, are required, for full paraglacial adjustment of slopes in the Picos de Europa. It was not considered appropriate to attempt to temporally constrain UDEC model output using the cosmogenic dates. This is because the dates only refer to one failure event; therefore it is difficult to provide an accurate assessment of rock slope failure frequency. Also, the paraglacial exhaustion model indicates failure frequency exponentially declines through time. Predicting the temporal occurrence of future failures indicated by the UDEC models would have required the application of a steady state erosion model.

Cosmogenic ^{10}Be dating of rock slope failures in Jordan indicate slope evolution is associated with climate; all rock slope failures occurred during wetter climatic periods between 35-20 ka BP, 12-10 ka BP and 7-4.4 ka BP. At each site investigated, at least two rock slope failure events were identified from the cosmogenic dating results. Assuming a steady state erosion model for the sandstone inselbergs, the average return period of failure was estimated to be 10-15 ka. Given that a range of age estimates were available, a tentative attempt was made to constrain UDEC model output of future rock slope failures in Wadi Rum. Based on past dates, the average number of model cycles corresponding to one year was approximated. Peaks in the unbalanced forces were assumed to represent a failure event. From this it was possible to place future failures in a very broad temporal context. Although there are many errors and assumptions associated with using the dates of past failure to predict future change, the approach of attempting to link numerical model output to cosmogenic dates of past failures represents an advance towards understanding the broad timescales of landscape evolution in Wadi Rum.

Cosmogenic dating of rock slope failures in the Picos de Europa and Wadi Rum has provided more detailed information on the mechanism of rock slope failure than would have been gained simply from the UDEC models. In particular, it has been possible to identify additional triggering mechanisms for the rock slope failures. In the Picos de Europa, the triggering mechanism for rock slope failure is a combination of deglaciation and delayed paraglacial slope adjustment and a wetter climatic period. In Wadi Rum, rock slope failures appeared to correspond to wetter climatic periods. Understanding the temporal context can provide more detailed information regarding rock slope failures than that gained from a pure modelling approach, such as adopted by Kimber (1998).

This research has indicated that using cosmogenic dates to constrain UDEC model output is most useful in environments where failures have developed over long time periods, such as Wadi Rum. In recently glaciated environments, such as the Picos de Europa, failures are clustered because the principal mechanism initiating failure is paraglacial slope adjustment. In recently glaciated environments, there has not been a long enough period of time for further failures to develop. In recently glaciated environments, the cosmogenic dates are most useful in constraining paraglacial exhaustion models.

Cosmogenic dates are most useful in constraining UDEC model output from sites such as Wadi Rum, where the dates show a number of discrete failure events distributed through time. Where failures of different ages are dated from a particular rock slope, this allows inferences to be made regarding the frequency of failures, which may be used to constrain UDEC model output.

The cosmogenic dates aid interpretation of rock slope failures at the field sites, particularly in explaining the speed of failure in λ-t space (Chapters 6 and 7). Gradual slope deformation leading to catastrophic failure is typical paraglacial slope behaviour where failures are controlled by oversteepening, truncation and stress redistribution. Paraglacial slope deformations caused by stress redistribution involve elastic deformations of the rock mass that occur over much longer timescales than sudden, brittle failures caused by preferential orientation of discontinuities, as in Wadi Rum. Combining engineering models of slope stability with Quaternary dating methods has much potential to increase understanding of rock slope failures.

In situ cosmogenic nuclides are most suitable for dating large, instantaneous rock slope failures. The application for dating creeping motions of slowly toppling blocks would be limited because local geometries and exposure to the cosmic ray flux would change through time. This would make it very difficult to calculate nuclide production rates and could lead to unacceptably large errors when computing exposure ages.

Theoretical modelling has shown that block size affects the stress-strain response of landforms in jointed rock masses (Chapter 4). Stress-strain relationships are considered fundamental in understanding landform behaviour (for example, Allison, 1996a). Geomorphological understanding of the stress-strain response of landforms in jointed rock masses has previously been limited to triaxial investigations of the stress-strain response of intact material (for example, Allison, 1993). Numerical modelling has shown that the stress-strain response of jointed rock masses is non-linear. The non-linear behaviour is caused by shear displacements and block rotations.

The effects of block size distribution on rock mass behaviour have been defined through analysing the deformation modulus of the landform (Chapter 4). Block size has found to be an important control on the geomorphological behaviour of the

landform. As block size is reduced, the deformation modulus of the rock mass decreases. The stiffness of the rock mass is therefore dependent on block size. Slopes in well jointed rock masses are likely to undergo much more deformation before failure than slopes in massively jointed rock masses. The decrease in stiffness with block size is caused by the increase in joint normal closure of the rock mass. Well jointed rock masses have a greater number of surfaces over which joint closure can occur, before failure occurs. The geomorphological effect of this is to produce slopes which are less steep in well jointed rock masses.

UDEC simulations also showed that as block size decreases, the maximum deviatoric stress at which failure occurs is higher for the well-jointed rock masses. This shows that the shear strength of well-jointed rock masses is greater than for slopes in more massive rock. The geomorphological implication of this is that catastrophic failures are less likely to occur on slopes in well-jointed rock masses. The geomorphological response of the slope is more likely to involve gradual time-dependent deformations which reduce slope angle through time, rather than large-scale, brittle failure. The effects of block size on the deformation properties of rock masses have never been simulated before in a geomorphological context.

Block size also affects the failure mechanism of the rock mass. As block size decreases, the magnitude of block rotation increases, while shear displacements decrease. Well-jointed models fail through toppling, while models containing few joints fail through translational shear. There has been no previous geomorphological study into the effects of block size on the failure mechanism of the rock mass.

Linking theoretical modelling to the evolution of natural slopes has been gained through modelling rock slopes in the Picos de Europa, northern Spain and Al Quwayra-Wadi Rum region, southern Jordan. Block size has a major influence on the failure mechanism. Where block sizes are large in relation to the outcrop scale of the rock mass, brittle catastrophic failures occur. These failures are dominated by slides and block topples. As relative block size decreases compared with outcrop scale, failures become more ductile and exhibit time-dependent deformation. Failures are characterised by self-stabilising topples and rotational slides.

9.2 Extension to previous studies

The work presented in this thesis has extended previous studies in the following respects.

Previous geomorphic studies using UDEC to simulate the evolution of landforms in jointed rock masses were limited because they did not provide any temporal framework through which model output could be interpreted (e.g. Allison and Kimber, 1998; Kimber *et al.*, 2002). This thesis redresses this issue and provides a tentative temporal framework for understanding the simulation of landform evolution using UDEC. The usefulness of the approach suggests that future studies of rock slope evolution would benefit greatly from the approach adopted in this thesis.

Osborne (1985), Osborne and Duford (1981) and Goudie *et al.* (2002) note that the sandstone inselbergs of the Al Quwayra-Wadi Rum region of southern Jordan are the best example of this unique environment anywhere in the world. Although Osborne (1985) and Goudie *et al.* (2002) have conducted research into the general geomorphology of the inselberg landscape, there has been little research conducted into the specific evolution of the sandstone inselbergs. This study has enhanced knowledge on the spatial effects of specific landform development evident in the Al Quwayra-Wadi Rum region and the relation to geological structure. For example, the scale of landforms increases towards the south and east; because joint spacing is constant, this leads to a change in the block size distribution of the rock mass relative to the outcrop scale. The scale of the inselbergs is affected by the development of a down-thrown graben feature centred on Al Quwayra (Heimbach and Meiser, 1971). By modelling landforms at different outcrop scales, it can be seen that the failure mechanism is dependent upon the relative block size distribution of the sandstone inselbergs.

This study represents a significant extension to previous studies in the Picos de Europa and Wadi Rum because it provides, for the first time, a temporal framework for the evolution of landforms in jointed rock masses in these areas. This work has extended previous studies which have used cosmogenic isotopes to date rock slope failures (e.g. Ballantyne *et al.*, 1998). The applicability of cosmogenic isotopes to recently glaciated and arid environments has been demonstrated. The research has demonstrated that cosmogenic isotopes can be used to establish a chronology of rock slope failures throughout a region.

Previous studies have argued that natural variability of joint spacing has little influence on the failure mechanism of natural slopes (Kimber, 1988; Allison and Kimber, 1998; Kimber *et al.*, 1998). Modelling of slopes in the Picos de Europa and Wadi Rum have shown that the natural variability in joint spacing can exert an important control on the failure mechanism. In some regions of the rock mass, natural variability in joint spacing can cause a more dense discontinuity network. Decreased joint spacing produces zones of reduced block size in the rock mass, which behave in a more ductile way than surrounding blocks. The effect is to produce a slower, less catastrophic failure.

The work presented here has demonstrated that the UDEC rock mass computer simulation software has wider application than being used as an engineering rock mass stability analysis tool. An important part of justifying the geomorphological use of UDEC has been the theoretical consideration of input parameters and the associated link between engineering input parameters and those relevant to geomorphology (Chapter 2). Hsu and Nelson (1995) demonstrated the control of cliff height for assessing slope stability in soft rock. The influence of slope height in affecting the stability of slopes in large open pit mines has also been noted (Sjöberg, 1996; 1998). The significance of slope height has been noted from both theoretical modelling and the simulation of natural slopes in jointed rock masses in the Picos de Europa and Wadi Rum. The effect of slope height on the failure of natural slopes in jointed rock masses has not been previously studied using numerical modelling in geomorphology. The change in behaviour of slopes as the height increases is partly in response to the decrease in relative block size and the increase in deviatoric stresses in larger rock slopes.

Statistical analysis of discontinuity data from a range of sites in northern Spain and southern Jordan has indicated that joint spacing does not follow a normal distribution. For UDEC to gain wider use in the geomorphological modelling of rock masses, it should be able to account for lognormal, Weibull and gamma distributions of joint spacing. At present UDEC represents joint spacing as a normal distribution and the joint cutting model should be revised to relate more directly to the geological conditions of the rock mass. Research in this thesis has indicated that variations in joint spacing can lead to more ductile zones within the rock mass. Therefore, it is suggested that improved models of joint spacing be developed to account more fully for joint spacing affecting the deformation properties of the rock mass.

Previous research has examined the mechanics of failure in natural slopes by plotting velocity data in λ-t space (Petley *et al.*, 2002; Kilburn and Petley, 2003). Most previous work has concentrated on failures in soft sediments. This study plots 1/displacement against model cycles to show the development of movement within the rock mass. All failures showed non-linear failure signatures. Plotting the data in this way to analyse the failure of UDEC modelling output has not been attempted before. Fitting a statistical model to the data helped to provide an estimate of the relative timespan over which failure occurred. The time period over which failure occurs can be considered as analogous to relaxation time in geomorphology. Significantly, the models showed that displacements are not continuous during failure events and periods of stabilisation can occur under dynamic equilibrium. The fact that displacements are not continuous through time has implications for the interpretation of monitoring data for particular failures.

9.3 Recommendations for further research

It is possible to make recommendations for future work based upon the findings of this research.

An obvious direction to pursue would be to extend the application of cosmogenic dating to construct a more detailed temporal framework of rock slope failures in a particular area. In Jordan and Spain, only three sites were investigated. There were many more potential sites that were suitable for the application of cosmogenic nuclide dating of rock slope failures. This would help provide a more robust temporal framework. More samples from each site are also required to increase the temporal constraint on the frequency of rock slope failures. This would increase the robustness of the temporal framework established for an area.

There is much scope for using cosmogenic isotopes to constrain models of rock slope evolution. Dating of a large number of sites would help place temporal constraints on the paraglacial exhaustion model. A greater number of dates would also increase the ability to provide temporal frameworks for understanding future landform change. Future research should be directed towards increasing understanding of the temporal nature of rock slope failures through cosmogenic dating.

In the Picos de Europa and Wadi Rum field sites it was assumed that weathering occurs evenly within the modelled sites. In the Wadi Rum field sites, aspect appears to be important in the evolution of slopes, with most failures occurring on the north or south faces. North and south faces were associated with the development of basal undercuts formed through slope sapping and weathering of the intact material. In the Picos de Europa, much of the development of cliff form may have occurred in past climates when freeze-thaw weathering processes may have affected some slopes more than others (Ahnert, 1960). The weathering of the sandstones in Wadi Rum showed preferential development of weathering features on north and south faces (Goudie *et al.*, 2002). It would be useful for further work to investigate the rate of weathering of the Ishrin and Disi sandstones. In the Picos de Europa, solution of the limestones and the opening of joint surfaces were not accounted for. Although it would be very difficult to incorporate the effects of weathering into the UDEC models, studies of the rates of solution would determine its importance for examining slope evolution. Incorporation of material removal could be incorporated into UDEC.

More instructive would be to develop a detailed material testing program to look at the stress-strain behaviour of material as weathering occurs. For example, blocks of sandstone could be prepared, strain gauged and then subjected to different environmental cycles in a climatic chamber. Differences in salinity, humidity and temperature could all be used to investigate material behaviour. Once the detailed behaviour of the material is known as weathering occurs, it may be possible to include the weathering effects into the properties of a strain softening or ubiquitous joint zone and intact material plasticity model. This could be achieved by defining constitutive models using the FISH programming language inside UDEC. Such research would also improve the geomorphological understanding of weathering process and material breakdown (Viles, 2000).

The modelling of landforms in the Picos de Europa and Al Quwayra-Wadi Rum areas has been achieved by the consideration of two perpendicular profile sections. Future research into the numerical modelling of landforms in jointed rock masses could make use of new three-dimensional hybrid codes, which not only allow for failure along pre-existing discontinuities but also simulate the fracture of intact material. Codes such as ELFEN (Rockfield, 2003) could used to investigate the development of flexural topples, where the failure of intact material is critical in controlling catastrophic failures. Such codes could be used to investigate the

development of landforms where the tensile and shear failure of the intact rock is important. A further understanding of landform development could be provided by using three-dimensional codes. This will allow for the analysis of three-dimensional problems, such as wedge failures, which cannot be represented using two-dimensional modelling approaches. In addition, the stability and deformation properties gained from three-dimensional codes are likely to be more realistic than existing two-dimensional codes due to more complex block interactions.

This thesis is part of ongoing research in engineering geomorphology and the behaviour of earth surface systems. It is a first attempt to try and establish temporal linkages between computer simulation and the real-time evolution of landforms in jointed rock masses. The effects of joint spacing on the deformation and failure of rock masses is also examined. Linkages between theoretical modelling and the real world are provided through the field sites selected in northern Spain and southern Jordan. Its contribution can be assessed both in terms of the details presented for the study areas and also in the conclusions, which have much wider implications. The results raise questions that may help to define the future research direction into the geomorphological behaviour of slopes in jointed rock masses.

References

Abdelhamid, G. 1990. 'The geology of the Jabal Umm Ishrin area (Wadi Ram)', *The Hashemite Kingdom of Jordan, Ministry of Energy and Mineral Resources, Natural Resources Authority*, Geology Directorate, Geological Mapping Division, Bulletin 14. Amman.

Abed, A. M. and Yaghan, R. 2000. 'On the paleoclimate of Jordan during the last glacial maximum', *Palaeogeography, Palaeoclimatology, Palaeoecology*, 160, 23-33.

Adhikary, D. P., Dyskin, A. V. and Jewell, R. J. 1996. 'Numerical modelling of the flexural deformation of foliated rock slopes', *International Journal of Rock Mechanics and Mining Sciences & Geomechanical Abstracts*, 33, 595-606.

Aggistalis, G., Alivizatos, A., Stamoulis, D. and Stournaras, G. 1996. 'Correlating uniaxial compressive strength with Schmidt hammer hardness, point load index, Young's modulus and mineralogy of gabbros and basalts (northern Greece)', *Bulletin – International Association of Engineering Geology*, 54, 3-11.

Ahnert, F. 1960. 'The influence of Pleistocene climates upon the morphology of cuesta scarps on the Colorado Plateau', *Annals of the Association of American Geographers*, 50, 139-156.

Ahnert, F. 1988. 'Modelling landform change', in Anderson, M. G. (Ed), *Modelling Geomorphological Systems*, John Wiley and Sons, Chichester, 375-400.

Ahnert, F. 1994. 'Randomness in geomorphological process response models', in Kirkby, M. J. (Ed), *Process Models and Theoretical Geomorphology*, John Wiley and Sons, Chichester, 3-21.

Ahnert, F. 1996. 'The point of modelling geomorphological systems', in McCann, S. B. and Ford, D. C. (Eds), *Geomorphology Sans Frontières*, John Wiley and Sons, Chichester, 1-13.

Allison, R. J. 1990. 'Developments in a non-destructive method of determining rock strength', *Earth Surface Processes and Landforms*, 15, 571-577.

Allison, R. J. 1991. 'Developments in a non-destructive method of determining rock strength: a reply', *Earth Surface Processes and Landforms*, 16, 473-476.

Allison, R. J. 1993. 'Slopes and slope processes', *Progress in Physical Geography*, 20, 453-465.

Allison, R. J. 1988. 'A non-destructive method for determining rock strength', *Earth Surface Processes and Landforms*, 13, 729-736.

Allison, R. J. 1996a. 'Stress and strain in geomorphology', in Mäusbacher, R. and Schulte, A. (Eds), *Readings in Physical Geography*, Springer Verlag, Heidelberg, 169-187.

Allison, R. J. 1996b. 'Slopes and slope processes', *Progress in Physical Geography*, 20, 453-465.

Allison, R. J. and Kimber, O. G. 1998. 'Modelling failure mechanisms to explain rock slope change along the Isle of Purbeck Coast, UK', *Earth Surface Processes and Landforms*, 23, 731-750.

Allison, R. J., Goudie, A. S. and Cox, N. J. 1993. 'Geotechnical properties of rock masses: their control on slope form and mechanics of change along the Napier range, Western Australia', *Geomorphology*, 8, 65-80.

Alonso, V. and González, J. J. 1998. 'Presencia de hielo glaciar en los Picos de Europa (Cordillera Cantabrica)', *Cuat. Geomorfol.*, 35-44.

Alonso, W. 1968. 'Predicting best with imperfect data', *Journal of the American Institute of Planners*, 34, 248-255.

Amadei, B. 1996. 'Importance of anisotropy when estimating and measuring *in situ* stresses in rock', *International Journal of Rock Mechanics and Mining Sciences & Geomechanics Abstracts*, 33, 293-325.

Amaral, P. M., Guerra, L. R. and Fernandes, J. C. 1999. 'Determination of Schmidt rebound hardness consistency in granite', *International Journal of Rock Mechanics and Mining Sciences & Geomechanics Abstracts*, 36, 833-837.

Anderson, M. G. and Sambles, K. M. 1988. 'A review of the bases of geomorphological modelling', in Anderson, M. G. (Ed), *Modelling Geomorphological Systems*, John Wiley and Sons, Chichester, 1-32.

Angelier, J. 1989. 'Distribution de joints de tension dans un banc rocheux: loi théorique et espacements. (Distribution of tension joints and bed thicknesses: theoretical relationship and actual joint spacings)', *Comptes Rendus – Académie des Sciences, Série II*, 309, 2119-2125.

Arioglu, E. and Tokgoz, N. 1991. 'Estimation of rock strength: rapidly and reliably by the Schmidt hammer', *Journal of Mining and Metal Fuels*, 34, 327-330.

Asef, M. R. and Reddish, D. J. 2002. 'The impact of confining stress on the rock mass deformation modulus', *Géotechnique*, 52 (4), 235-241.

Atkinson, B. K. 1984. 'Subcritical crack growth in geological materials', *Journal of Geophysical Research*, 89, 4077-4144.

Attewell, P. B. and Farmer, I. W. 1976. *Principles of Engineering Geology*. Chapman and Hall, London.

Augustinus, P. C. 1995. 'Glacial valley cross-profile development: the influence of in situ rock stress and rock mass strength, with examples from Southern Alps, New Zealand', *Geomorphology*, 11, 87-97.

Augustinus, P. C. 1991. 'Rock resistance to erosion: some further considerations', *Earth Surface Processes and Landforms*, 16, 563-596.

Aydan, Ö. and Kawamoto, T. 1990a. 'The stability of slopes and underground openings against flexural toppling and their stabilisation', *Rock Mechanics and Rock Engineering*, 25, 143-165.

Aydan, Ö. and Kawamoto, T. 1990b. 'Discontinuities and their effect on rock mass', in Barton, N. R. and Stephansson, O. (Eds), *Rock Joints*, A. A. Balkema, Rotterdam, 149-156.

Ayday, C. A. and Goktan, R. M. 1992. 'Correlations between L and N-type Schmidt hammer rebound values obtained during field testing', in *Proceedings, ISRM Symposium*, Chester, 14-17 September 1992. 47-50.

Azzoni, A., La Barbera, G. and Zaninetti, A. 1995. 'Analysis and prediction of rockfalls using a mathematical model', *International Journal of Rock Mechanics and Mining Sciences & Geomechanical Abstracts*, 32, 709-724.

Bahamonde, J. R., Colmenero, J. R. and Vera, C. 1997. 'Growth and demise of Late Carboniferous carbonate platforms in the eastern Cantabrian Zone, Asturias, northwestern Spain', *Sedimentary Geology*, 110, 99-122.

Bahamonde, J. R., Vera, C. and Colmenero, J. R. 2000. 'A steep-fronted Carboniferous carbonate platform: clinoformal geometry and lithofacies (Picos de Europa, NW Spain)', *Sedimentology*, 47, 645-664.

Balaram, V. and Gnaneshwar Rao, T. 2003. 'Rapid determination of REE's and other trace elements in geological samples by microwave acid digestions and ICP-MS', *Atomic Spectroscopy*, 24 (6), 206-212.

Balco, G., Stone, J.O., Porter, S.C., Caffee, M. 2002. '*Cosmogenic-nuclide ages for New England coastal moraines, Martha's Vineyard and Cape Cod, Massachusetts, USA*', Quaternary Science Reviews 21, 2127-2135.

Ballantyne, C. K. 2002a. 'A general model of paraglacial landscape response', *The Holocene*, 12 (3), 371-376.

Ballantyne, C. K. 2002b. 'Paraglacial geomorphology', *Quaternary Science Reviews*, 21, 1935-2017.

Ballantyne, C. K., Stone, J. O. H. and Fifield, L. K. 1998. 'Cosmogenic Cl-36 dating of postglacial landsliding at The Storr, Isle of Skye, Scotland', *The Holocene*, 8 (3), 347-351.

Bandis, S. C. 1993. 'Engineering properties and characterisation of rock discontinuities', in Hudson, J. A. (Ed), *Comprehensive Rock Engineering*, Pergamon Press, Oxford, 155-183.

Bandis, S. C., Lumsden, A. C. and Barton, N. R. 1983. 'Fundamentals of rock joint deformation', *International Journal of Rock Mechanics and Mining Sciences & Geomechanics Abstracts*, 20, 249-268.

Bardsley, W. E., Major, T. J. and Selby, M. J. 1990. 'Note on a Weibull property for joint spacing analysis', *International Journal of Rock Mechanics and Mining Sciences & Geomechanical Abstracts*, 27, 133-134.

Barla, G. and Chiriotti, E. 1995. 'Insights into the behaviour of the large deep seated gravitational slope deformation of Rosone, in the Piedmont Region (Italy)', *Felsbau*, 13 (6), 425-432.

Barnard, P. L., Owen, L. A., Sharma, M. C. and Finkel, R. C. 2001. 'Natural and human induced landsliding in the Garhwal Himalaya of northern India', *Geomorphology*, 40 (1-2), 21-35.

Barton, C. C. and Larson, E. 1985. 'Fractal geometry of two-dimensional fracture networks at Yucca mountain, south-western Nevada', in Stephansson, O. (Ed), *Proceedings of the International Symposium on Fundamentals of Rock Joints*, Björkliden, Centek Publishers, 77-84.

Barton, C. C., Samuel, J. K. and Page, W. R. 1988. 'Fractal scaling of fracture networks, trace lengths and apertures', *Geological Society of America Abstracts Programs*, 20, A299.

Barton, N. R. and Bandis, S. 1990. 'Review of predictive capabilities of JRC-JCS model in engineering practice', in Barton, N. R. and Stephansson, O. (Eds), *Rock Joints*, A. A. Balkema, Rotterdam, 603-610.

Barton, N. R., By, T. L., Chryssanthakis, P., Tunbridge, L., Kristiansen, J', Loset, F., Bhasin, R. K., Westerdahl, H. and Vik, G. 1994. 'Predicted and measured performance of the 62 m span Norwegian Olympic Ice Hockey Cavern at Gjovik', *International Journal of Rock Mechanics and Mining Sciences & Geomechanical Abstracts*, 31, 617-641.

Barton, N. R., Lien, R. and Lunde, J. 1974. 'Engineering classification of rock masses for the design of tunnel support', *Rock Mechanics*, 6, 189-236.

Barton, N. R., Loset, F., Smallwood, A., Vik, G., Rawlings, C., Chryssanthakis, P., Hansteen, H. and Ireland, T. 1992. 'Radioactive waste repository design using Q and UDEC-BB', in *Proceedings, Conference on Fractured and Jointed Rock Masses*, Lake Tahoe, 3-5 June 1992. Lawrence Berkeley Laboratory, California, 735-742.

Beicip, P. 1981. *Structural Study of Jordan*. Geology Directorate, Natural Resources Authority, Amman, Jordan.

Bell, F. G. 2000. *Engineering properties of soil and rock*. Blackwell Science, Oxford.

Bell, F. G. and Culshaw, M. G. 1993. 'A survey of the geomechanical properties of some relatively weak Triassic sandstones', in Cripps, J. C., Coulthard, J. M., Culshaw, M. G., Forster, A., Hencher, S. R. and Moon, C. F. (Eds), *The Engineering Geology of Weak Rock*, Engineering Geology Special Publication, No. 8, Geological Society, A. A. Balkema, Rotterdam, 139-148.

Bell, F. G. and Culshaw, M. G. 1998. 'Petrographic and engineering properties of sandstones from the Sneinton Formation, Nottinghamshire, England', *Quarterly Journal of Engineering Geology*, 31, 5-19.

Bell, F. G. and Lindsay, P. 1999. 'The petrographic and geomechanical properties of some sandstones from the Newspaper Member of the Natal Group, near Durban, South Africa', *Engineering Geology*, 53, 57-81.

Bell, J. W., Brune, J. N., Lui, T., Zreda, M. and Yount, J. C. 1998. 'Dating precariously balanced rocks in seismically active parts of California and Nevada', *Geology*, 26, 495-498.

Bender, F. 1969. 'Ergebnisse erdölgeologischer Untersuchungen in Jordanien' *Erdöl u. Kohle*, 22 (9), 510-515.

Bender, F. 1974. *Geology of Jordan*. Gebrüder Borntraeger, Berlin-Stuttgart.

Bender, F. 1975. 'Geology of the Arabian Peninsula', *USGS Professional Paper*, 560-561, 1-36.

Benko, B. and Stead, D. 1998. 'The Frank slide: a re-examination of the failure mechanism', *Canadian Geotechnical Journal*, 35, 299-311.

Bentley, H. W., Phillips, F. M. and Davis, S. N. 1986. 'Chlorine-36 in the terrestrial environment', in Fritz, P., and Fontes, J.-C. (Eds), *Handbook of Environmental Isotope Geochemistry*, Elsevier, Amsterdam, 427-480.

Bergerat, F., Angelier, J. and Bouroz, C. 1991. 'L'analyse des diaclases dans le Plateau du Colorado (USA): une clé pour la reconstruction des paleo-contraintes (Jointing analysis in the Colorado Plateau (USA) as a key to paleostress reconstruction), *Comptes Rendus – Académie des Sciences, Serie II,* 312, 309-316.

Bergerat, F., Bouroz-Weil, C. and Angelier, J. 1992. 'Palaeostresses inferred from microfractures, Colorado Plateau, Western USA', *Tectonophysics*, 206, 219-243.

Bhasin, R. and Kaynia, A. M. 2004. Static and dynamic simulation of a 700 m high rock slope in western Norway', *Engineering Geology*, 71 (3-4), 213-226.

Bhasin, R. K. and Hoeg, K. 1998. 'Parametric study for a large cavern in jointed rock using a distinct element model (UDEC-BB)', *International Journal of Rock Mechanics and Mining Sciences & Geomechanical Abstracts*, 35, 17-30.

Bhasin, R. K., Barton, N., Grimstad, E., Chryssanthakis, P. and Shende, F. P. 1996. 'Comparison of predicted and measured performance of a large cavern in the Himalayas', *International Journal of Rock Mechanics and Mining Sciences & Geomechanical Abstracts*, 33, 607-626.

Bieniawski, Z. T. 1973. 'Engineering classification of jointed rock masses', *Transactions of the South African Institute of Civil Engineering*, 15, 335-343.

Bieniawski, Z. T. 1978. 'Determining rock mass deformability: experience for case histories', *International Journal of Rock Mechanics and Mining Sciences and Geomechanics Abstracts*, 15, 237-247.

Blöschl, G. and Sivapalan, M. 1995. 'Scale issues in hydrological modelling – A review', *Hydrological Processes*, 9, (3-4), 251-290.

Bögli, A. 1961. 'Karrentische ein beitrag sur Karstmorphologie', *Zeitschrift für Geomorphologie*, 5, 185-193.

Boillot, G., Dupeuble, P. A. and Malod, J. 1979. 'Subduction and tectonics on the continental margin off northern Spain', *Marine Geology*, 32, 53-70.

Bovis, M. J. 1982. 'Uphill-facing (antislope) scarps in the coast mountains, southwest British Columbia', *Geological Society of America Bulletin*, 93, 804-812.

Bovis, M. J. 1990. 'Rock-slope deformation at Affliction Creek, southern Coast Mountains, British Columbia', *Canadian Journal of Earth Sciences*, 27, 243-254.

Bovis, M. J. and Evans, S. G. 1996. 'Extensive deformations of rock slopes in southern Coast Mountains, south-west British Columbia, Canada', *Engineering Geology*, 44, 163-182.

Bowman, D. 1990. 'Climatically triggered Gilbert-type lacustrine fan deltas, the Dead Sea area, Israel', *SEPM Special Publications*, 10, 273-280.

Brady, B. H. G., Cramer, M. L. and Hart, R. D. 1985. 'Preliminary analysis of a loading test on a large basalt block', *International Journal of Rock Mechanics and Mining Sciences & Geomechanical Abstracts*, 22, 345-348.

Brady, B. H. G., Hsiung, S. H., Chowdhury, A. H. and Philip, J. 1990. 'Verification studies on the UDEC computational model of jointed rock', in Rossmanith, H. P. (Ed), *Mechanics of Jointed and Faulted Rock*, A. A. Balkema, Rotterdam, 551-558.

Bray, J. W. and Goodman, R. E. 1981. 'The theory of base friction models', *International Journal of Rock Mechanics and Mining Sciences & Geomechanics Abstracts*, 18, 453-468.

Brocard, G. Y., van der Beek, P. A., Bourlès, D.L., Siame, L.L. and Mugnier, J.-L. 2003. 'Long-Term Fluvial Incision Rates and Postglacial River Relaxation Time in the French Western Alps from ^{10}Be Dating of Alluvial Terraces with Assessment of Inheritance, Soil Development and Wind Ablation Effects', *Earth and Planetary Science Letters 209*, 197-214.

Brook, M., Ibrahim, K. and McCourt, W. J. 1988. 'New geochronological data from the Arabian Shield area of southwest Jordan', *3rd Jordanian Geological Conference*, Amman.

Brown, E. T. 1987. 'Introduction', in Brown, E. T. (Ed), *Analytical and Computational Methods in Engineering Rock Mechanics*, Allen and Unwin, London, 1-31.

Brown, E. T. 1981. *Rock Characterisation Testing and Monitoring. ISRM Suggested Methods.* Pergamon Press, Oxford.

Brown, E.T., Edmond, J.M., Raisbeck, G.M., Yiou, F., Kurz, M.D., Brook, E.J. 1991. 'Examination of surface exposure ages of Antarctic moraines using in situ produced ^{10}Be and ^{26}Al', *Geochimica et Cosmochimica Acta*, 55, 2269-2283.

Bruce, I. G., Cruden, D. M. and Eaton, T. M. 1989. 'Use of a tilting table to determine the base friction of hard rock sample', *Canadian Geotechnical Journal*, 26, 474-479.

Brunsden, D. 1980. 'Applicable models of landform evolution', *Zeitschrift für Geomorphologie*, 36, 16-26.

Brunsden, D. 1993. 'The persistence of landforms', *Zeitschrift für Geomorphologie*, 93, 13-28.

Brunsden, D. and Thornes, J. B. 1979. 'Landscape sensitivity and change', *Transactions of the Institute of British Geographers*, 4, 463-484.

Brunsden, D., Jones, D. K. C. and Goudie, A. S. 1984. 'Particle size distribution on the debris slopes of the Hunza Valley', in Miller, K. J. (Ed), *The International Karakoram Project*, Cambridge University Press, Cambridge, 536-580.

Caine, N. 1982. 'Toppling failures from alpine cliffs on Ben Lomond, Tasmania', *Earth Surface Processes and Landforms*, 7, 133-152.

Cameron-Clarke, I. S. and Budvari, S. 1981. 'Correlation of rock mass classification parameters obtained from borecore and *in situ* observations', *Engineering Geology*, 17, 19-53.

Campbell, I. A. 1991. 'Comments on Allison's (1990) developments in a non-destructive method of determining rock strength', *Earth Surface Processes and Landforms*, 16, 471-472.

Cargill, J. S. and Shakoor, A. 1990. 'Evaluation of empirical methods for measuring the uniaxial compressive strength of rock', *International Journal of Rock Mechanics and Mining Sciences & Geomechanics Abstracts*, 27, 495-503.

Carpinteri, A. and Karihaloo, B. L. 2003. 'Size-scale effects', *Engineering Fracture Mechanics*, 70, 1.

Carson, M. A. and Kirkby, M. J. 1972. *Hillslope Form and Process*. Cambridge University Press, Cambridge.

Carter, B. J. and Lajtai, E. Z. 1992. 'Rock slope stability and distributed joint systems', *Canadian Geotechnical Journal*, 29, 53-60.

Carvalho, J. L. 2002 'Slope stability analysis for open pits', *Golder Associates Ltd.* Mississauga, Canada.

Cerling, T.E. and Craig, H. 1994. 'Geomorphology and *in situ* cosmogenic isotopes', *Annual Review of Earth and Planetary Sciences*, 22, 273-317.

Chappell, B. A. 1974. 'Load distribution and deformational response in discontinua', *Géotechnique*, 24 (4), 641-654.

Chen, F. H. 2000. *Soil Engineering: Testing Design and Remediation*. CRC Press: Boca Raton.

Chigira, M. 1992. 'Long-term gravitational deformation of rocks by mass creep', *Engineering Geology*, 32, 167-185.

Chorley, R. J. 1964. 'The nodal position and anomalous character of slope studies in geomorphological research', *Geographical Journal*, 130, 70-73.

Chryssanthakis, P. and Grimstad, E. 1996. 'Landslide simulation by using the distinct element method', in Aubertin, M., Hassani, F. and Mitri, H (Eds.), *Rock Mechanics: Tools and Techniques*, Proceedings of the 2nd North American Rock Mechanics Symposium, NARMS '96, Montreal, Quebec, 19-21 June 1996, 1921-1928.

Chryssanthakis, P., Monsen, K. and Barton, N. 1991. 'Verification of UDEC-BB against the CSM test and large scale application to glacier loading of jointed rock masses', in *Proceedings 7th ISRM International Congress on Rock Mechanics*, Aachen, 16-20 September, 1991. Volume 1. A. A. Balkema, Rotterdam, 693-698.

Clark, D. H., Bierman, P. and Gillespie, A. R. 1996. '^{10}Be and ^{26}Al production rates and a revised glacial chronology for the Sierra Nevada', *Radiocarbon*, 38 (1), 152.

Clark, R. 1981. 'Cold climate features of the Cordillera Cantabrica, northern Spain', *Biuletyn Peryglacjalny*, 28, 5-13.

Cleveland, W. S. 1979. 'Robust Locally Weighted Regression and Smoothing Scatterplots', *Journal of the American Statistical Association*, 74, 829-836.

Cleveland, W. S. and Devlin, S. J. 1988. 'Locally Weighted Regression: An Approach to Regression Analysis by Local Fitting,' *Journal of the American Statistical Association*, 83, 596-610.

Cockburn, H. A. P. and Summerfield, M. A. 2004. 'Geomorphological applications of cosmogenic isotope analysis', *Progress in Physical Geography*, 28 (1), 1-42.

Coggan, J. S. and Pine, R. J. 1996. 'Application of distinct-element modelling to assess slope stability at Delabole Slate Quarry, Cornwall, England', *Transactions of the Institution of Mining and Metallurgy Section A-Mining Industry*, 105, 22-30.

Coggan, J. S., Stead, D. and Eyre, J. M. 1998. 'Evaluation of techniques for quarry slope stability assessment', *Transactions of the Institution of Mining and Metallurgy – Section B*, 107, B139-B147.

Colmenero, J. R., Fern Ández, L. P., Moreno, C., Bahamonde, J. R., Barba, P., Heredia, N. and González, F. 2002. 'Carboniferous', in Gibbons, W. and Moreno, T. (Eds). *The Geology of Spain*, The Geological Society, London, 93-116.

Cook, N. G. W., Hood, M. and Tsai, F. 1984. 'Observations of crack growth in hard rock loaded by an indenter', *International Journal of Rock Mechanics and Mining Sciences & Geomechanical Abstracts*, 21, 97-107.

Cooks, J. 1981. 'Rock quality measured by seismic wave velocity as a factor in landform development', *South African Journal of Science*, 77, 517-521.

Cooks, J. 1983. 'Geomorphic response to rock strength and elasticity', *Zeitschrift für Geomorphologie*, 27, 483-493.

Coulthard, M. A., Journet, N. C. and Swindells, C. F. 1992. 'Integration of stress analysis into mine excavation design', in Tillerson, J. R. and Wawersik, W. R. (eds), *Rock Mechanics, Proceedings of the 33rd U.S. Symposium, Santa Fe NM 3 - 5 June 1992*, 451-460, A. A. Balkema, Rotterdam.

Cox, N. J. 2003. '*L-moments Stata Module*', University of Durham.

Cramer, M. L., Cunningham, J. P. and Kunsoo, K. 1994. 'Rock mass deformation properties from a large-scale block test', *Bulletin of the Association of Engineering Geologists*, 21 (1) 47-54.

Crïsescu, N. 1989. *Rock Rheology*. Kluwer Academic Publishers, Dordrecht, The Netherlands.

Crompton, J. W. 1964. 'The geomorphology of the Picos de Europa', *Proceedings of the Bristol Speleological Association*, 2, 39-47.

Crozier, M. J. and Glade, T. 1999. 'Frequency and magnitude of landsliding: fundamental research issues', *Zeitschrift für Geomorphologie*, S.B. 115, 141-155.

Cruden, D. M. 1985. 'Rock slope movements in the Canadian Cordillera', *Canadian Geotechnical Journal*, 22, 528-540.

Cruden, D. M. 1988. 'Thresholds for catastrophic instabilities in sedimentary rock slopes, some examples from the Canadian Rockies', *Zeitschrift für Geomorphologie*, 67, 67-76.

Cruden, D. M. 2003. 'The shapes of cold, high mountains in sedimentary rocks', *Geomorphology*, 55 (1-4), 249-261.

Cruden, D. M. and Charlesworth, H. A. K. 1976. 'Errors in strike and dip measurements', *Geological Society of America Bulletin*, 87, 977-980.

Cruden, D. M. and Eaton, T. M. 1987. 'Reconnaissance of rockslide hazards in Kananaskis County, Alberta', *Canadian Geotechnical Journal*, 24, 414-429.

Cruden, D. M. and Hu, X. Q. 1993. 'Exhaustion and steady state models for predicting landslide hazards in the Canadian Rocky Mountains', *Geomorphology*, 8, 279-285.

Cruden, D. M. and Hu, X.-Q. 1994. 'Topples on underdip slopes in the Highwood Pass, Alberta, Canada', *Quarterly Journal of Engineering Geology*, 27, 57-68.

Cuhna, A. P. 1990. 'Scale effects in rock mechanics', in *Proceedings 1st International Workshop on Scale Effects in Rock Masses*, Leon, 7-8 June 1990. A. A. Balkema, Rotterdam, 3-27.

Cundall, P. A. 1971. 'A computer model for simulating progressive, large-scale movements in blocky rock systems', in *Proceedings, International Symposium on Rock Fractures*, Nancy, France, II-8, 1-12.

Cundall, P. A. 1987. 'Distinct element models of rock and soil structure', in Brown, E. T. (Ed), *Analytical and Computational Methods in Engineering Rock Mechanics*, Allen and Unwin, London, 129-163.

Cundall, P. A. 1990. 'Numerical modelling of discontinua', *Engineering Computing*, 9, 101-113.

Cundall, P. A. and Hart, R. D. 1984. 'Analysis of block test No. 1. Inelastic rock mass behaviour: Phase 2 – A characterisation of joint behaviour (final report)', *Itasca Consulting Group Report, Rockwell Hanford Operations, Subcontract SA-957.*

Cundall, P. A. and Hart, R. D. 1992. 'Numerical modelling of discontinua', *Engineering Computations: International Journal for Computer-Aided Engineering*, 9 (2), 101-113.

Cundall, P. A. and Hart, R. D. 1993. 'Numerical modelling of discontinua', in Hudson, J. A. (Ed), *Comprehensive Rock Engineering*, Pergamon Press, Oxford, Volume 2, 155-183.

Cundall, P. A. and Lemos, J. V. 1990. 'Numerical simulation of fault instabilities with a continuously yielding joint model' in Fairhurst, C. (Ed), *Rockbursts and Seismicity in Mines*, A. A. Balkema, Rotterdam, 147-152.

Cundall, P. A. and Strack, O. D. L. 1979. 'A discrete numerical method for granular assemblies', *Géotechnique*, 29, 47-65.

Dafalias, Y. F. and Herrmann, L. R. 1982. 'Bounding surface formulation of soil plasticity' in Pande, G. N. and Zienkiewicz, O. C. (Eds) *Soil Mechanics – Transient and Cyclic Loads*, John Wiley and Sons, Chichester, 253-282.

Davies, P., Williams, A. T. and Bomboe, P. 1998. 'Numerical analysis of coastal cliff failure along the Pembrokeshire Coast National Park, Wales, UK', *Earth Surface Processes and Landforms*, 23 (12), 1123-1134.

Davis, R. O. and Selvadurai, A. P. S. 1996. *Elasticity and Geomechanics.* Cambridge University Press, Cambridge.

Davis, W. M. 1892. 'The convex profile of bad-land divides', *Science*, 20, 245.

Davis, W. M. 1899. 'The geographical cycle', *Geographical Journal*, 14, 481-504.

Davis, W. M. 1930. 'Rock floors in arid and humid climates', *Journal of Geology*, 38, 1-27 and 136-158.

Day, M. J. and Goudie, A. S. 1977. 'Field assessment of rock hardness using the Schmidt rest hammer', *BGRG Technical Bulletin*, 18, Geo. Abstracts, Norwich, 19-23.

De Sitter, L. 1962. 'Structural development of the Arabian Shield in Palestine', *Geol. en Mijnbouw*, 41, 116-124.

Deere, D. U. 1966. 'Engineering Classification and Index Properties for Intact Rock', *Technical Report*, AFWL-TR-65-116. Air Force Weapons Laboratory, Research and Technology Division, Kirtland Air Force Base, New Mexico.

Deere, D. U., Hendron, A. J., Patton, F. D. and Cording, E. J. 1967. 'Design of Surface and Near-Surface Construction in Rock', *Proceedings of the 8th Symposium Rock Mechanics*, AIME, 1967, 237-302.

Deere, D. U., Merrit, A. H. and Coon, R. F. 1969. 'Engineering Classification of *in situ* Rock', *Technical Report*, AWFL-TR-67-144, Air Force Weapons Laboratory, Kirtland Air Force Base, New Mexico.

DeFreitas, M. H. and Watters, R. J. 1973. 'Some field examples of toppling failure', *Géotechnique*, 23, 495-514.

DeToledo, P. E. C. and DeFreitas, M. H. 1993. 'Laboratory testing and parameters controlling the shear strength of filled rock joints', *Géotechnique*, 43, 1-19.

Donath, F. A., Faill, R. T. and Tobin, D. G. 1971. 'Deformational mode fields in experimentally deformed rock', *Geological Society of America Bulletin*, 82, 1441-1462.

Douglas, G. R., Whalley, W. B. and McGreevy, J. P. 1991. 'Rock properties as controls on free-face debris fall activity', *Permafrost and Periglacial Processes*, 2, 311-319.

Douglas, I. 1988. 'Restrictions on hillslope modelling', in Anderson, M. G. (Ed), *Modelling Geomorphological Systems*, John Wiley and Sons, Chichester, 401-420.

Duffaut, P. 1968. 'Deformations in rock mechanics', *Proceedings of International Symposium on Rock Mechanics*, 3-12. Editorial Blume, Madrid.

Dunne, J., Elmore, D. and Muzikar, P. 1999. 'Scaling factors for the rates of production of cosmogenic nuclides for geometric shielding and attenuation at depth on sloped surfaces', *Geomorphology*, 27 (1-2), 3-12.

Dyke, D. G. and Dobereiner, L. 1991. 'Evaluating the strength and deformability of sandstones', *Quarterly Journal of Engineering Geology*, 24, 12-34.

Eberhardt, E, Stead, D. and Coggan, J. S. 2004. 'Numerical analysis of initiation and progressive failure in natural rock slopes–the 1991 Randa rockslide', *International Journal of Rock Mechanics and Mining Sciences & Geomechanical Abstracts*, 41, 69-87.

Eberhardt, E., Stead, D. and Stimpson, B. 1999. 'Effects of sample disturbance on the stress-induced microfracturing characteristics of brittle rock', *Canadian Geotechnical Journal*, 36, 239-250.

Eberhardt, E., Stead, D., Coggan, J. S. and Wallenberg, H. 2002. 'An integrated numerical analysis approach to the Randa rockslide', in Rybár, J. and Stemberk, J. (Eds), *Landslides: Proceedings of the First European Conference on Landslides, Prague, Czech Republic, 24-26 June 2002*, Sewts and Zeitinger, The Netherlands.

Ehlen, J. 2000. 'Fractal analysis of joint patterns in granite', *International Journal of Rock Mechanics and Mining Sciences & Geomechanical Abstracts*, 37, 909-922.

Ehlen, J. and Wohl, E. 2002. 'Joints and landform evolution in bedrock canyons', in Suzuki, T., Matsukura, Y., Ehlen, J. and Tanaka, Y., (eds.), *Rock Control in Geomorphological Processes*. Transactions, Japanese Geomorphological Union, 23, (2), 237-256.

Einstein, H. H. 1993. 'Modern developments in discontinuity analysis – the persistence-connectivity problem', in Hudson, J. A. (Ed), *Comprehensive Rock Engineering*. Pergamon Press, Oxford, 193-213.

Einstein, H. H. and Hirschfeld, R. C. 1973. 'Model studies on mechanics of jointed rock', *Journal of Soil Mechanics and Foundations*, 99(SM3), 229-248.

Einstein, H. H., Veneziano, D., Baecher, G. B. and O'Reilly, K. J. 1983. 'The effect of discontinuity persistence on rock slope stability', *International Journal of Rock Mechanics and Mining Sciences & Geomechanics Abstracts*, 20, 227-236.

Evans, R. S. 1981. 'An analysis of secondary toppling rock failures – the stress redistribution method', *Quarterly Journal of Engineering Geology*, 14, 77-76.

Fabryka-Martin, J. T. 1998. 'Production of radionuclides in the Earth and their hydrogeologic significance, with emphasis on Chlorine-36 and Iodine-129', *Unpublished Ph.D. dissertation*, University of Arizona.

Fairhurst, C. 2003. 'Stress estimation in rocks: a brief history and review', *International Journal of Rock Mechanics and Mining Sciences & Geomechanics Abstracts*, 40, 957-973.

Farias, P. 1982. 'La estructura del sector Central de los Picos de Europa', *Trab. Geol.*, University of Oviedo, 63-72.

Fookes, P. G. and Vaughan, P. R. 1986. *'A handbook of engineering geomorphology'*, Surrey University Press: Chapman and Hall, *USA*.

Ford, D. C. and Williams, P. W. 1989. *Karst Geomorphology and Hydrology*, Chapman and Hall, London.

Franklin, J. A. and Dusseault, M. B. 1989. *Rock Engineering*, McGraw-Hill, New York, U.S.A.

Freund, R., Garfunkel, Z., Zak, I., Goldberg, M., Weissbord, T. and Derin, B. 1970. 'The shear along the Dead Sea rift', *Philosophical Transactions of the Royal Society of London*, Series A, 267, 107-130.

Gabrielsen, R. H. 1990. 'Characteristics of joints and faults', in Barton, N. R. and Stephansson, O. (Eds), *Rock joints*, A. A. Balkema, Rotterdam, 11-17.

Gale, S. J. and Hoare, P. G. 1997. 'The glacial history of the northwest Picos de Europa of northern Spain', *Zeitschrift für Geomorphologie*, 41 (1), 81-96.

Galli, P. 1999. 'Active tectonics along the Wadi Araba Jordan valley transform fault', *Journal of Geophysical Research – Solid Earth*, 104 (B2), 2777-2796.

García-Ruiz, M. J. C., Miriam, D. V., Rodríguez, A. V. and Zapata, M. B. R. 2002. 'Late Glacial and Holocene palaeoclimatic record from Sierra de Cebollera (northern Iberian Range, Spain)', *Quaternary International*, 93, 13-18.

Gardner, J. S. 1977. 'High magnitude rockfall-rockslide frequency and geomorphic significance in the Highwood Pass area, Alberta' *Great Plains Rocky-Mountains Geographical Journal*, 6, 228-238.

Gardner, J. S. 1980. 'Frequency, magnitude and spatial distribution of mountain rockfalls and rockslides in Highwood Pass area, Alberta, Canada', in Coates, D. R. and Vitek, J. D. (Eds), *Thresholds in Geomorphology*. London, Allen and Unwin, 267-295.

Gardner, J. S. 1982. 'Alpine mass wasting in contemporary time: some examples from the Canadian Rocky Mountains', in Thorn, C. E. (Ed), *Space and Time in Geomorphology*. Allen and Unwin, London, 171-192.

Gardner, J. S. 1993. 'Accretion rates on some debris slopes in the Mt. Rae area, Canadian Rocky Mountains', *Earth Surface Processes and Landforms*, 8, 347-355.

Gasparrini, M., Bakker, R. J., Bechstadt, T. and Boni, M. 2003. 'Hot dolomites in a Variscan foreland belt: hydrothermal flow in the Cantabrian Zone (NW Spain)', *Journal of Geochemical Exploration*, 78-9, 501-507.

Gerrard, C. M. 1982. 'Elastic models of rock masses having one, two and three sets of joints', *International Journal of Rock Mechanics and Mining Sciences & Geomechanics Abstracts*, 19, 15-23.

Gerrard, J. 1988. '*Rocks and Landforms*'. Kluwer Academic Publishers, Amsterdam,

Girdler, R. W. 1985. 'Problems concerning the evaluation of oceanic lithosphere in the Northern Red Sea', *Tectonophysics*, 116, 109-122.

Girdler, R. W. and Styles, P. 1974. 'Two stage Red Sea floor spreading', *Nature*, 247, 7-11.

Gleick, J. 1987. *Chaos: Making a New Science.* Viking, New York.

Gökçeoglu, C., Sonmez, H. and Kayabasi, A. 2003. 'Predicting the deformation moduli of rock masses', *International Journal of Rock Mechanics and Mining Sciences & Geomechanics Abstracts*, 40, 701-710.

Goktan, R. M. and Ayday, C. A. 1993. 'Suggested improvement to the Schmidt rebound hardness ISRM suggested methods with particular reference to rock machineability', *International Journal of Rock Mechanics and Mining Sciences & Geomechanics Abstracts*, 30, 321-322.

Gomez-Fernandez, F. 2000. 'Metallogenesis of Zn-Pb carbonate-hosted mineralization in the southeastern region of the Picos de Europa (central northern Spain) province: Geologic, fluid inclusion, and stable isotope studies', *Economic Geology and the Bulletin of the Society of Economic Geologists*, 95 (1), 19-39.

González-Díaz, I., Remondo, A., Díaz de Terán, J. R. and Cendrero, A. 1999. 'A methodological approach for the analysis of the temporal occurrence and triggering factors of landslides', *Geomorphology*, 30, 95-114.

Goodman, R. E. 1995. 'Block theory and its application', *Géotechnique*, 45, 383-423.

Goodman, R. E. 1980. *Introduction to rock mechanics.* John Wiley and Sons, New York.

Goodman, R. E. 1989. *Introduction to rock mechanics.* Second Edition. John Wiley and Sons, New York.

Goodman, R. E. and Bray, J. W. 1976. 'Toppling of rock slopes', in *Proceedings of the Speciality Conference on Rock Engineering for Foundations and Slopes*, ASCE (Boulder, Colorado), 2, 201-234.

Goodman, R. E. and Kieffer, D. S. 2000. 'Behaviour of rock in slopes', *Journal of Geotechnical and Geoenvironmental Engineering*, 126 (8), 675-684.

Goodman, R. E. and Shi, G.-H. 1982. 'Geology and rock slope stability - application of a keyblock concept for rock slopes', *Proceedings of the International Conference on Stability in Surface Mining, SME*, 347-374.

Goodman, R. E. and Shi, G.-H. 1995. *Block Theory and its Application to Rock Engineering*. Prentice-Hall, London.

Gosse, J. C. and Phillips, F. M. 2001. 'Terrestrial *in situ* cosmogenic nuclides: theory and application', *Quaternary Science Reviews*, 20, 1475-1560.

Goudie, A. S., Migoń, P., Allison, R. J. and Rosser, N. J. 2002. 'Sandstone geomorphology of the Al-Quwayra area of south Jordan', *Zeitschrift für Geomorphologie*, 46 (3), 365-390.

Grandia, F., Canals, A., Cardellach, E., Banks, D. A. and Perona, J. 2003. 'Origin of ore-forming brines in sediment-hosted Zn-Pb deposits of the Basque-Cantabrian basin, northern Spain', *Economic Geology and the Bulletin of the Society of Economic Geologists*, 98 (7), 1397-1411.

Guessous, Z., Ladanyi, B. and Gill, D. E. 1984. 'Effect of sampling disturbance on laboratory determined properties of rock salt', in Hardy, H. R. and Langer, M. (Eds.), *The Mechanical behaviour of Salt, Proceedings of the 2nd Conference*, Hanover, Trans Tech Publications, Clausthal-Zellerfied, Germany, 137-158.

Gutiérrez-Elorza, M., Garcia-Ruiz, J. M., Goy, J. L., Gracia, J., Gutierrez-Santolalla, F., Marti, C., Martin-Serrano, A., Perez-Gonzalez, A. and Zazo, C. 2002. 'Quaternary', in Gibbons, W. and Moreno, T. (Eds.) *The Geology of Spain*, The Geological Society, London, 336-366.

Hall, D. B. 1996. 'Modelling the failure of natural rock columns', *Geomorphology*, 15, 123-134.

Hardin, E., Barton, N., Voegele, M., Board, M., Lingle, H., Pratt, H. R., and Unnes, W. 1981. 'Measuring the thermo-mechanical and transport properties of a rock mass using the heated block test', in Goodman, R. E. and Heuze, F. E. (Eds), *23rd Symposium on Rock Mechanics*, U.S. National Committee for Rock Mechanics and the University of California, Berkeley, 802-813.

Hart, R. D. 1993. 'An introduction to distinct element modelling for rock engineering', in Hudson, J. A. (Ed), *Comprehensive Rock Engineering*, Pergamon Press, Oxford, Volume 2, 245-261.

Hart, R. D. 2003. 'Enhancing rock stress understanding through numerical analysis', *International Journal of Rock Mechanics and Mining Sciences & Geomechanics Abstracts*, 40, 1089-1097.

Hatcher, R., Zeitz, I., Regan, R. and Abu-Ajamieh, M. 1981. 'Sinistral strike-slope motion in the Dead Sea rift: confirmation from new magnetic data', *Geology*, 9, 458-462.

Hawkins, A. B. and McConnell, B. J. 1992. 'Sensitivity of sandstone strength and deformability to changes in moisture content', *Quarterly Journal of Engineering Geology*, 25, 115-129.

Heimbach, W. and Meiser, P. 1971. 'Beispiele zur geoelektrischen Widerstandmessung und ihrer geologischen Interpretation in Jordanian', *Geol. Jahrb.*, 89, 419-428.

Hencher, S. R. 1987. 'The implication of joints and structures for slope stability', in Anderson, M. G. and Richards, K. S. (Eds), *Slope Stability: Geotechnical Engineering and Geomorphology*, John Wiley and Sons, Chichester, 145-186.

Henry, D. O. 1988. 'The epipalaeolithic sequence within the Ras En Naqb – Al-Quweira area, southern Jordan', *Paléorient*, 14, 245-256.

Herget, G. 1988. *Stresses in Rock*. A. A. Balkema, Rotterdam.

Hermanns, R. L. and Strecker, M. R. 1999. 'Structural and lithological controls on large Quaternary rock avalanches (sturzstroms) in arid northwestern Argentina', *Geological Society of America Bulletin*, 111 (6), 934-948.

Hermanns, R. L., Niedermann, S., Villanueva Garcia, A., Sosa Gomez, J. and Strecker, M. R. 2001. 'Neotectonics and catastrophic failure of mountain fronts in the southern intra-Andean Puna Plateau, Argentina', *Geology* 29, 619–23.

Hermanns, R. L., Trauth, M. H., Niedermann, S., McWilliams, M. and Strecker, M. R. 2000. 'Tephrochronologic constraints on temporal distribution of large landslides in northwest Argentina', *Journal of Geology*, 108, 35-52.

Hinchcliffe, S. and Ballantyne, C. K. 1999. 'Talus accumulation and rockwall retreat, Trotternish, Isle of Skye' *Scottish Geographical Journal*, 115, 53-70.

Hoek, E. 1983. 'Strength of jointed rock masses', *Géotechnique*, 33, 187-223.

Hoek, E. and Bray, J. W. 1981. *Rock Slope Engineering*. The Institution of Mining and Metallurgy, London.

Holcombe, R. J. 2003. *Geocalculator 4.5*. Department of Earth Sciences, University of Queensland. http://www.earth.uq.edu.au/~rodh/software/ Date last accessed: 25/02/2003.

Holmes, G. and Jarvis, J. J. 1985. 'Large-scale toppling within a Sackũng type deformation at Ben Attow, Scotland', *Quarterly Journal of Engineering Geology*, 18, 287-289.

Homand-Eitenne, F., Rode, N. and Schwartzmann, R. 1990. 'Block modelling of jointed cliffs', in Rossmanith, H. P. (Ed), *Mechanics of Jointed and Faulted Rock*, A. A. Balkema, Rotterdam, 819-825.

Horowitz, A. 1979. *The Quaternary of Israel*, Academic Press, London.

Horowitz, A. 1992. *Palynology of Arid Lands*. Elsiever, Amsterdam.

Hosking, J. R. M. 1986. 'The theory of probability weighted moments' *Research Report RC12210*, IBM Research Division, Yorktown Heights, N.Y.

Hosking, J. R. M. 1990. 'L-moments: analysis and estimation of distributions using linear combinations of order statistics', *Journal of the Royal Statistical Society, Series B*, 52, 105-124.

Hosking, J. R. M. 1992. 'Moments or *L*-moments? An example comparing two measures of distributional shape', *The American Statistician*, 46, 186-189.

Hosking, J. R. M. and Wallis, J. R. 1997. *Regional frequency analysis: an approach based on L-moments*, Cambridge University Press, Cambridge, U.K.

Howard, A. D. 1988. 'Equilibrium models in geomorphology', in Anderson, M. G. (Ed), *Modelling Geomorphological Systems*, John Wiley and Sons, Chichester, 49-72.

Howard, A. D. and Selby, M. J. 1994. 'Rock slopes', in Abrahams, A. D. and Parsons, A. J. (Eds), *Geomorphology of Desert Environments*, Chapman and Hall, London, 421-440.

Howes, S. and Anderson, M. G. 1988. 'Computer simulation in geomorphology', in Anderson, M. G. (Ed), *Modelling Geomorphological Systems*, John Wiley and Sons, Chichester, 421-440.

Hsu, S. C. and Nelson, P. P. 1995. 'Analyses of slopes in jointed rock masses using the distinct element method', in Rossmanith, H. P. (Ed), *Mechanics of Jointed and Faulted Rock*, A. A. Balkema, Rotterdam, 589-594.

Huang, Q. and Angelier, J. 1989. 'Fracture spacing and its relation to bed thickness', *Geological Magazine*, 126, 355-362.

Huang, T. H., Chang, C. S. and Yang, Z. Y. 1995. 'Elastic moduli for fractured rock mass', *Rock Mechanics and Rock Engineering*, 28 (3), 135-144.

Hucka, V. 1965. 'A rapid method for determining the strength of rocks *in situ*', *International Journal of Rock Mechanics and Mining Sciences & Geomechanics Abstracts*, 2, 127-134.

Huckriede, R. and Wiesemann, G. 1968. 'Der Jungpleistozäne Pluvial-See von El-Jafr und weitere Daten zum Quartär Jordaniens', *Geologica et Paleontologica*, 2, 73-95.

Hungr, O., Evans, S. G. and Harzard, J. 1999. 'Magnitude and frequency of rock falls and rock slides along the main transportation corridors of south-western British Columbia', *Canadian Geotechnical Journal*, 36 (2), 224-238.

Ibrahim, K. M. and McCourt, W. J. 1995. 'Neoproterozoic magnetism and tectonic evolution of the northern Arabian Shield: evidence from southwest Jordan', *Journal of African Earth Sciences*, 20, 103-118.

International Society for Rock Mechanics (ISRM) Commission on Computer Programs. 1988. 'List of computer programs in rock mechanics', *International Journal of Rock Mechanics and Mining Sciences & Geomechanics Abstracts*, 25, 183-252.

Iofis, I. M., Maksimov, A. V. and Mironov, V. V. 1990. 'Some practical aspects of numerical simulation of jointed rock mass by distinct element method', in *Proceedings, International Conference on Mechanics of Jointed and Faulted Rock*, Vienna, 18-20 April 1990. A. A. Balkema, Rotterdam, 479-486.

Itasca Consulting Group Inc. 2000. *Universal Distinct Element Code: Manual, Version ICG3.0.* Itasca Consulting Group Inc., Minneapolis.

Itasca Consulting Group Inc. 2003. *PFC2D: Particle Flow Code in 2-dimensions.* Itasca Consulting Group Inc., Minneapolis.

Itasca Consulting Group Inc. 2003. *PFC3D: Particle Flow Code in 3-dimesions.* Itasca Consulting Group Inc., Minneapolis.

Ivy-Ochs, S., Heuberger, H., Kubik, P. W., Kerschner, H., Bonani, G., Frank, M. and Schlüchter, C. 1998. 'The age of the Köfelsevent. Relative ^{14}C and cosmogenic isotope dating of an early Holocene landslide in the central Alps (Tyrol, Austria)', *Zeitschrift für Gletscherkunde und Glazialgeologie* 34, 57–68.

Jaeger, J. C. and Cook, N. G. W. 1979. *Fundamentals of Rock Mechanics*, Methuen and Co. Ltd., London.

Jiang, Y., Negatomi, M. and Okada, T. 1995. 'Studies on toppling failure mechanism of slope in discontinuous rockmass', in Rossmanith, H. P. (Ed), *Mechanics of Jointed and Faulted Rock*, A. A. Balkema, Rotterdam, 605-610.

Jing, L. and Hudson, J. A. 2002. 'Numerical methods in rock mechanics', *International Journal of Rock Mechanics and Mining Sciences & Geomechanics Abstracts*, 39, 409-427.

Jing, L. and Stephansson, O. 1994. 'Topological identification of block assemblages for jointed rock masses', *International Journal of Rock Mechanics and Mining Sciences & Geomechanics Abstracts*, 31, 163-172.

Jones, D. G. and Williams, A. T. 1991. 'Statistical analysis of factors influencing cliff erosion along a section of the West Wales coast, U. K.', *Earth Surface Processes and Landforms*, 16, 95-111.

Kakani, D. L. and Piteau, D. R. 1976. 'Finite element analysis of toppling at Hell's Gate Bluffs, British Columbia', *Bulletin of the Association of Engineering Geologists*, 13, 315-327.

Kenter, J. A. M., Van Hoeflaken, F., Bahamode, J. R., Bracco Gartner, G. L. and Kleim, L. 2002. 'Anatomy and lithofacies of an intact and seismic scale Carboniferous carbonate platform (Asturias, NW Spain)', in Zemplolich, W. and Cook, H. E. (Eds) *Paleozoic Carbonates of the Commonwealth of Independent States (CIS): Subsurface Reservoirs and Outcrop Analogues*, SEPM, Special Publication, 74, 185-207.

Kieffer, D. S. 1998. *Rock Slumping – a compound failure mode of jointed hard rock slopes*, Ph.D. Thesis, Department of Civil and Environmental Engineering, University of California, Berkeley.

Kilburn, C. R. J. and Petley, D. N. 2003. 'Forecasting giant, catastrophic slope collapse: lessons from Vajont, Northern Italy', *Geomorphology*, 54, 21-32.

Kimber, O. G. 1998. *Mechanisms of Failure of Jointed Rock Masses and the Behaviour of Steep Slopes*. PhD. Thesis, University of Durham.

Kimber, O. G., Allison, R. J. and Cox, N. J. 2002. 'Rates and Mechanisms of Change of Hard Rock Steep Slopes on the Colorado Plateau, USA', in Allison, R. J. (Ed), *Applied Geomorphology*, John Wiley and Sons, Chichester, 65-90.

King, L. C. 1953. 'Canons of landscape evolution', *Geological Society of America Bulletin*, 64, 721-752.

King, L. C. 1957. 'The uniformitarian nature of hillslopes', *Transactions of the Edinburgh Geological Society*, 17, 81-102.

Kirkby, M. J. 1994. *Process Models and Theoretical Geomorphology*, John Wiley and Sons, Chichester.

Klinger, Y., Avouac, J. P., Abou Karaki, N., Dorbath, L., Bourles, D. and Reyss, J. L. 2000. 'Slip rate on the Dead Sea transform fault in northern Araba valley (Jordan)', *Geophysical Journal International*, 142 (3), 755-768.

Koenke, C., Harte, R., Krätzig, W. B. and Rosenstein, O. 1998. 'On adaptive remeshing techniques for crack simulation problems', *Engineering Computations: International Journal for Computer-Aided Engineering*, 15, 74-88.

Kolaiti, E. and Papadopoulos, Z. 1993. 'Evaluation of Schmidt hammer rebound testing: a critical approach', *Bulletin – International Association of Engineering Geology*, 48, 69-76.

Koons, D. 1955. 'Cliff retreat in the south-western United States', *American Journal of Science*, 253, 44-52.

Korients, A. and Alehossein, H. 2002. 'On the initial non-linearity of compressive stress-strain curves for intact rock', *Rock Mechanics and Rock Engineering*, 35 (4), 319-328.

Kubik, P. W., Ivy-Ochs, S., Schlüchter, C., Masarik, J. and Frank, M. 1998. '^{10}Be and ^{26}Al production rates deduced from an instantaneous event within the dendro-calibration curve, the landslide of the Köfels Otz Valley Austria', *Earth and Planetary Science Letters*, 161, 231–41.

Kulatilake, P. H. S. W. and Ucpirti, H. 1994. 'Effects of finite-size joints on the deformability of jointed rock at the two-dimensional level', *Canadian Geotechnical Journal*, 31, 364-374.

Kulatilake, P. H. S. W. and Wu, T. H. 1984. 'Sampling bias on the orientation of discontinuities', *Rock Mechanics and Rock Engineering*, 17, 243-253.

Kulatilake, P. H. S. W., Ucpirti, H. and Stephansson, O. 1994. 'Effects of finite-size joints on the deformability of jointed rock at the two-dimensional level', *Canadian Geotechnical Journal*, 31, 364-374.

Kulatilake, P. H. S. W., Ucpirti, H., Wang, S., Radberg, G. and Stephansson, O. 1992. 'Use of the distinct element method to perform stress-analysis in rock with non-persistent joints and to study the effect of joint geometry parameters on the strength and deformability of rock masses', *Rock Mechanics and Rock Engineering*, 25 (4), 253-274.

Kulatilake, P. H. S. W., Wathugala, D. N. and Stephansson, O. 1993. 'Joint network modelling with a validation exercise in Stripa Mine, Sweden', *International Journal of Rock Mechanics and Mining Sciences & Geomechanical Abstracts*, 30, 503-526.

Kulhawy, F. H. 1975. 'Stress deformation properties of rock and rock discontinuities', *Engineering Geology*, 9, 327-350.

La Pointe, P. R. 1988. 'A method to characterise fracture density and connectivity through fractal geometry', *International Journal of Rock Mechanics and Mining Sciences & Geomechanical Abstracts*, 25, 421-429.

Laity, J. E. and Malin, M. C. 1985. 'Sapping processes and the development of theatre-headed valley networks on the Colorado Plateau', *Geological Society of America Bulletin*, 96, 203-217.

Lal, D. 1991. 'Cosmic ray labelling of erosion surface: *in situ* nuclide production rates and erosion rates', *Earth and Planetary Science Letters*, 104, 424-439.

Lana, M. S. and Gripp, M. F. A. 2003. 'The use of inclined hemisphere projections for analyzing failure mechanisms in discontinuous rocks', *Engineering Geology*, 67, 321-330.

Lemos, J. V. 1990. 'A comparison of numerical and physical models of a blocky medium', in Rossmanith, H. P. (Ed), *Mechanics of Jointed and Faulted Rock*, A. A. Balkema, Rotterdam, 509-514.

Lemos, J. V. 1994. 'Computational topics in discrete element modelling' in Vargas, E. A. (Ed), *Applications of Computational Mechanics in Geotechnical Engineering*, A. A. Balkema, Rotterdam, 371-384.

Lemos, J. V., Hart, R. D. and Cundall, P. A. 1985. 'A generalised distinct element program for modelling jointed rock masses. A keynote lecture', in *Proceedings of the International Symposium on Fundamentals of Rock Joints. Björkliden, Sweden,* 335-343.

Leung, C. F. and Kheok, S. C. 1987. 'Computer aided analysis of rock slope stability', *Rock Mechanics and Rock Engineering*, 20, 111-122.

Leung, C. F. and Quek, S. T. 1995. 'Probabilistic stability analysis of excavations in jointed rock', *Canadian Geotechnical Journal*, 32, 397-407.

Liu, B., Phillips, F. M., Fabryka-Martin, J. T., Fowler, M. M., Biddle, R. S. and Stone, W. D. 1994. 'Cosmogenic ^{36}Cl accumulation in unstable landforms, I. Effects of the thermal neutron distribution', *Water Resources Research*, 30, 1071-1074.

Lorenz, E. N. 1976. 'Nondeterministic theories of climate change', *Quaternary Research*, 6, 495-506.

Maas, K. 1974. 'The Geology of Liebana. Cantabrian Mountains, Spain. Deposition and deformation in a Flysch area', *Leidse Geologische Mededelingen*, 49, 379-465.

Maharaj, R. J. 1994. 'The morphology, geometry and kinematics of Judgement Cliff rock avalanche, Blue Mountains, Jamaica, West Indies', *Quarterly Journal of Engineering Geology*, 27, 243-256.

Makhlouf, I. M. and Abed, A. M. 1991. 'Depositional facies and environments in the Umm Ishrin Sandstone Formation, Dead Sea area, Jordan', *Sedimentary Geology*, 71, 177-187.

Makurat, A., Barton, N. R., Vik, G., Chryssanthakis, P., and Monsen, K. 1990. 'Jointed and rock mass modelling', in Barton, N. R. and Stephansson, O. (Eds), *Rock Joints*, A. A. Balkema, Rotterdam, 647-656.

Marquínez, J. 1978. 'Estudio geologico del sector SE de los Picos de Europa (Cordillera Cantabrica, NW Spain)', *Trab. Geol.*, 10, 295-315.

Marquínez, J. and Adrados, L. 2000. 'La Geologíca y el relieve de los Picos de Europa', *INDUROT, Universidad de Oviedo*, 1-18.

Marrett, R., Ortega, O. J. and Kelsey, C. M. 1999. 'Extent of power-law scaling for natural fractures in rock', *Geology*, 27, 799-802.

Martin, C. D. and Stimpson, B. 1994. 'The effect of sample disturbance on laboratory properties of Lac du Bonnet granite', *Canadian Geotechnical Journal*, 31 (5), 692-702.

Martinez Garcia, E. 1981. 'El Paleozoico de la zona Cantabrica oriental (NW de Españia)', *Trab. Geol.*, 12, 95-127.

Martín-Serrano, A. 1994. 'Macizo Hespérico Septentional', in Gutiérrez, M. (Ed), *Geomorfología de España*. Rueda, Madrid, 25-62.

Masarik, J. and Reedy, R. C. 1995. 'Terrestrial cosmogenic nuclide production systematics calculated from numerical simulations', *Earth and Planetary Science Letters*, 136, 381-395.

Masarik, J. and Wieler, R. 2003. 'Production rates of cosmogenic nuclides in boulders', *Earth and Planetary Science Letters*, 216 (1-2), 201-208.

Matsuoka, N. and Sakai, H. 1999. 'Rockfall activity from an alpine cliff during thawing periods', *Geomorphology*, 28, 309-328.

Mauldon, M. and Goodman, R. E. 1996. 'Vector analysis of key-block rotations', *Journal of Geotechnical Engineering*, 122, 976-987.

McClusky, S., Reilinger, R., Mahmoud, S., Ben Sari, D., and Tealeb, A. 2003. 'GPS constraints on Africa (Nubia) and Arabia plate motions', *Geophysical Journal International*, 155 (1), 126-138.

Mitoke, F. D. 1968. 'Karstmorphologische Studien in der glazial-überformten Höhenstufe der Picos de Europa, Nordspanien', *Jb. Geogr. Ges. Hannover*, 4, 161.

Mohajerani, A. 1989. 'Rock discontinuity spacing statistics: log-normal distribution versus exponential', *Australian Geomechanics*, 17, 20-21.

Moon, B. P. 1984. 'Refinement of a technique for determining rock mass strength for geomorphological purposes', *Earth Surface Processes and Landforms*, 9, 189-193.

Müller, L. 1974. 'Rock mass behaviour-determination and application in engineering practice', *Proceedings 3rd Congress on Rock Mechanics*, Volume 1, 205-215. International Society of Rock Mechanics, Denver.

Mustoe, G. E. 1983. 'Cavernous weathering in the Capitol Reef Desert, Utah', *Earth Surface Processes and Landforms*, 8, 517-526.

Narr, W. and Suppe, J. 1991. 'Joint spacing in sedimentary rocks', *Journal of Structural Geology*, 13, 1037-1048.

Nash, D. 1987. 'A comparative review of limit equilibrium methods of stability analysis', in Anderson, M. G. and Richards, K. S. (Eds), *Slope Stability*, John Wiley and Sons, Chichester, 11-75.

Neev, E. and Emery, K. 1995. *The Destruction of Sodom, Gomorah and Jericho*. Oxford University Press, New York.

Nichol, S., Hungr, O. and Evans, S. G. 2002. 'Large-scale brittle and ductile toppling of rock slopes', *Canadian Geotechnical Journal*, 39, 773-788.

Nishiizumi, K., Winterer, E. L., Kohl, C. P. Klein, J., Middleton, R., Lal, D. and Arnold, J. R. 1989. 'Cosmic ray production rates of ^{10}Be and ^{26}Al in quartz from glacially polished rocks', *Journal of Geophysical Research*, 94, 17907-17915.

Odling, N. E. 1997. 'Scaling and connectivity of joint systems in sandstones from western Norway', *Journal of Structural Geology*, 19, 1257-1271.

Ofoegbu, G. I. and Curran, J. H. 1991. 'Yielding and damage of intact rock', *Canadian Geotechnical Journal*, 28, 503-516.

Osborne, G. 1985. 'Evolution of the Late Cenozoic inselberg landscape of southwestern Jordan', *Palaeogeography, Palaeoclimatology, Palaeoecology*, 49, 1-23.

Osborne, G. and Duford, J. M. 1981. 'Geomorphological processes in the inselberg region of southwest Jordan', *Palestine Exploration Quarterly*, 1-17.

Palmström, A. 1995. *RMi – a rock mass characterisation system for rock engineering purposes*, Ph.D. thesis, University of Oslo, Norway.

Palmström, A. 2000. 'Block size and block size distribution', *Workshop on Reliability of classification systems – GeoEng2000 conference*, 18-24 November, Melbourne Australia.

Palmström, A. and Singh, R. 2001. 'The deformation modulus of rock masses – comparisons between *in situ* tests and indirect estimates', *Tunnelling and Underground Space Technology*, 16, 115-131.

Pande, G. N., Beer, G. and Williams, J. R. 1990. *Numerical methods in rock mechanics*. John Wiley and Sons, Chichester.

Park, H. J. and West, T. R. 2002. 'Sampling bias of discontinuity orientation caused by linear sampling technique', *Engineering Geology*, 66, 99-110.

Pascal, C., Angelier, J. and Hancock, P. L. 1997. 'Distribution of joints: probabilistic modelling and case study near Cardiff (Wales, U. K.)', *Journal of Structural Geology*, 19, 1273-1284.

Pastor, M. and Tamagnini, C. 2003. *Numerical Modelling in Geomechanics*. Kogan Page Science, London.

Pavlović, N. 1996. *Methodology of geotechnical modelling*. PhD. Thesis, Belgrade University, Belgrade.

Pavlović, N. 1998. 'Principles of numerical modelling of jointed rock masses', in Rossmanith, H. P. (Ed), *Mechanics of Jointed and Faulted Rock: Proceedings of the Third International Conference on Mechanics of Jointed and Faulted Rock, Mjfr-3, Vienna, Austria, 6-9 April, 1998*, A. A. Balkema, Rotterdam, 311-316.

Penck, W. 1925. *Die piedmontflachen des sudlichen Schwarzwaldes*. Z. Ges. Erdlk, Berlin.

Penck, W. 1953. '*Morphological analysis of landforms*', MacMillan, London.

Perez-Estúan, A., Bastida, F. and Alonso, J. L. 1988. 'A thin-skinned tectonics model for an arcuate fold and thrust belt: The Cantabrian Zone (Variscan Ibero-Armorican Arc)', *Tectonics*, 7, 517-537.

Petley, D. N., Bulmer, M. H. K. and Murphy, W. 2002. 'Patterns of movement in rotational and translational landslides', *Geology*, 30 (8), 719-722.

Phillips, F. C. 1971. *The Use of Stereographic Projection in Structural Geology*. 3rd edition. Edward Arnold, London.

Phillips, F. M. and Plummer, M. A. 1996. 'CHLOE – a program for interpreting in situ cosmogenic nuclide dating studies erosion studies', *Radiocarbon*, 38, 98.

Phillips, F. M., Leavy, B. D., Jannik, N. O., Elmore, D. and Kubik, P. W. 1986. 'The accumulation of Chlorine-36 in rocks: a method for surface exposure dating', *Science*, 231, 41-43.

Phillips, F. M., Stone, W. D. and Fabryka-Martin, J. T. 2000. 'An improved approach to calculating low-energy cosmic-ray neutron fluxes near the land/atmosphere interface', *Chemical Geology*, 175, 689-701.

Phillips, F. M., Zreda, M. G., Flinsch, M. R., Elmore, D. and Sharma, P. 1996. 'A re-evaluation of cosmogenic ^{36}Cl production rates in terrestrial rocks', *Geophysical Research Letters*, 23, 949-952.

Phillips, J. D. 1988. 'The role of Spatial Scale in Geomorphic Systems', *Geographical Analysis*, 20 (4), 308-317.

Phillips, J.D . 1993. 'Instability and chaos in hillslope evolution', *American Journal of Science*, 293, 25-48.

Piteau, D. R. 1973. 'Characterising and extrapolating rock joint properties in engineering practice', *Rock Mechanics Supplement*, 2, 5-31.

Poole, R. W. and Farmer, I. W. 1980. 'Consistency and repeatability of Schmidt hammer rebound data during field testing: Technical note', *International Journal of Rock Mechanics and Mining Sciences & Geomechanics Abstracts*, 17, 167-171.

Powell, J. H. 1988. *The geology of Karak.* Bulletin 8, Geology Directorate, Natural Resources Authority, Jordan.

Powell, J. H. 1989. *Stratigraphy and sedimentation of the Phanerozoic rocks in Central and South Jordan: Part A – Ram and Khreim Groups.* Bulletin 11, Geology Directorate, Natural Resources Authority, Jordan, Amman.

Pratt, H. R., Swolfs, H. S., Brace, W. F., Black, A. D. and Handin, J. W. 1977. 'Elastic and transport properties of an *in situ* jointed granite', *International Journal of Rock Mechanics and Mining Sciences & Geomechanical Abstracts*, 14, 35-45.

Price, D. G. 1993. 'A suggested method for the classification of rock mass weathering by a ratings system', *Quarterly Journal of Engineering Geology*, 26, 69-76.

Priest, S. D. 1995. *Hemispherical Projection Methods in Rock Mechanics*. George Allen and Unwin, London.

Priest, S. D. 1993. 'The collection and analysis of discontinuity orientation data for engineering design, with examples', in Hudson, J. A. (Ed), *Comprehensive Rock Engineering*, Pergamon Press. 167-192.

Priest, S. D. and Hudson, J. A. 1981. 'Estimation of discontinuity spacing and trace length using scan line surveys', *International Journal of Rock Mechanics and Mining Sciences & Geomechanics Abstracts*, 18, 183-197.

Pritchard, M. A. and Savigny, K. W. 1990. 'Numerical modelling of toppling', *Canadian Geotechnical Journal*, 27, 823-834.

Pritchard, M. A. and Savigny, K. W. 1991. 'The Heather Hill landslide: an example of a large scale toppling failure in a natural slope', *Canadian Geotechnical Journal*, 28, 410-422.

Pritchard, M. A., Savigny, K. W. and Evans, S. G. 1990. 'Toppling and deep-seated landslides in natural slopes', in Rossmanith, H. P. (Ed), *Mechanics of Jointed and Faulted Rock*, A. A. Balkema, Rotterdam, 937-943.

Purrer, W. 1997. 'Geotechnical based procedures in tunnelling', *Felsbau*, 15, 222-224.

Qin Huang and Angelier, J. 1989. 'Fracture spacing and its relation to bed thickness', *Geological Magazine*, 126, 355-362.

Quennell, A. M. 1951. 'The geology and mineral resources of (former) Transjordan', *Colonial Geology and Mineral Resources*, 2 (2), 85-115.

Quennell, A. M. 1958. 'The structural and geomorphic evolution of the Dead Sea rift', *Quarterly Journal of the Geological Society of London*, 114, 1-24.

Quennell, A. M. 1984. 'The Western Arabian Rift System', in Dixon, J. E. and Robertson, H. E. (Eds.), *Geological Society of London Special Publications*, 17, 775-778.

Rabba, I. 1991. 'The Geology of the Al Quwayra Area', *The Hashemite Kingdom of Jordan, Ministry of Energy and Mineral Resources, Natural Resources Authority*, Geology Directorate, Geological Mapping Division, Bulletin 16. Amman.

Ramamurthy, T. and Arora, V. K. 1994. 'Strength predictions for jointed rocks in confined and unconfined states', *International Journal of Rock Mechanics and Mining Sciences & Geomechanical Abstracts*, 31, 9-22.

Rashdan, M. 1988. *The regional geology of the Aqaba-Wadi Araba area*. Map sheets 3049 III and 2949 II. Bulletin 7, Geology Directorate, Natural Resources Authority, Jordan.

Rathore, J. S., Holt, R. M. and Fjaer, E. 1989. 'Effects of stress history on petrophysical properties of granular rocks', in Khair, A. W. (Ed.), *Rock Mechanics as a Guide for Efficient Utilisation of Natural Resources: Proceedings of the 30th U.S. Symposium on Rock Mechanics*, Morgantown, A. A. Balkema, Rotterdam, 765-772.

Reuther, C. D. 1980. 'Das Namur im sudlichen Kantabrischen Gebirge (Nord-spanien)-Krustenbewegungen und Faziesdifferenzierung in Übergang Geosynklinale-Orogen', *Clausthaler Geologische Abhandlungen, Clausthal-Zellerfeld*, 28, 1-122.

Rives, T., Razack, M., Petit, J-P. and Rawnsley, K. D. 1992. 'Joint spacing: analogue and numerical simulations', *Journal of Structural Geology*, 14, 925-937.

Roach, D. E., Fowler, A. D. and Fyson, W. K. 1993. 'Fractal fingerprinting of joint and shattercone surfaces', *Geology*, 21, 759-762.

Rocha, M. and Da Silva, J. N. 1970. 'A new method for the determination of deformability of rock masses', *Proceedings 2nd Congress on Rock Mechanics*, paper 2-21. International Society of Rock Mechanics, Belgrade.

Rockfield Software. 2003. *ELFEN 2.8: The Finite Element / Discrete Element System.* Rockfield Software, Swansea, Wales, U.K.

Rocscience – DIPS V. 5.0. 2002. *Dips: Plotting, analysis and presentation of structural data using spherical projection techniques: Manual.* Rocscience geomechanics software and research, Toronto.

Rosso, R. S. 1976. 'A comparison of joint stiffness measurements in direct shear, triaxial compression and *in situ*', *International Journal of Rock Mechanics and Mining Sciences & Geomechanics Abstracts*, 13, 167-172.

Royston, P. 1992. 'Which measures of skewness and kurtosis are best?', *Statistics in Medicine*, 11, 333-343.

Sánchez de la Torre, L., Águeda, J., Colmenero-Navarro, J. R. and González Lastra, J. 1983. 'Evolución sedimentaria y paleogeográica del Carbonifero en la Cordillera Cantabrica', in Martinez Daiz, C. (Ed), *Carbonifero y Pérmico de España.* IGME, Madrid, 133-150.

Sánchez, M. J. and Arquer, P. F. 2001. 'New radiometric and geomorphologic evidences of a last glacial maximum older than 19 ka in SW European mountains: the example of Redes National Park (Cantabrian Mountains, NW Spain)', *Geodinamica Acta*, 15, 93-101.

Sauchyn, D. J., Cruden, D. M. and Hu, X. Q. 1998. 'Structural control on the morphometry of open rock basin, Kananaskis region, Canadian Rocky Mountains', *Geomorphology*, 22, 313-324.

Schultz, R. A. 1996. 'Relative scale and the strength and deformability of rock masses', *Journal of Structural Geology*, 18, 1139-1149.

Schumm, S. A. 1991. *To interpret the Earth: Ten ways to go wrong*, Cambridge University Press, Cambridge.

Selby, M. J. 1980. 'A rock mass strength classification for geomorphic purposes: with tests from Antarctica and New Zealand', *Zeitschrift für Geomorphologie*, 24, 489-497.

Selby, M. J. 1993. *Hillslope Materials and Processes*. Oxford University Press, Oxford.

Selby, M. J. 1987. 'Rock slopes', in Anderson, M. G. and Richards, K. S. (Eds), *Slope Stability: Geotechnical Engineering and Geomorphology*, John Wiley and Sons, Chichester, 475-504.

Selby, M. J., Augustinus, P., Moon, V. G. and Stevenson, R. J. 1988. 'Slopes on strong rock masses: modelling and influences of stress distributions and geomechanical properties', in Anderson, M. G. (Ed), *Modelling Geomorphological Systems*, John Wiley and Sons, Chichester, 341-374.

Selley, R. C. 1972. 'Diagnosis of marine and non-marine environments from the Cambro-Ordovician sandstones of Jordan', *Journal of the Geological Society of London*, 128, 135-150.

Sen, Z. 1993. 'RQD-fracture frequency chart based on a Weibull distribution', *International Journal of Rock Mechanics and Mining Sciences & Geomechanical Abstracts*, 30 (5), 555-557.

Sen, Z. and Kazai, A. 1984. 'Discontinuity spacing and RQD estimates from finite length scanlines', *International Journal of Rock Mechanics and Mining Sciences & Geomechanics Abstracts*, 21, 203-212.

Sen, Z. and Sadahah, B. H. 2003. 'Modified rock mass classification system by continuous rating', *Engineering Geology*, 67, 269-280.

Senior, K. J. 1987. 'Geology and Speleogenesis of the M2 Cave System, Western Massif, Picos de Europa, Northern Spain', *Cave Science, Transactions of the British Cave Research Association*, 14 (3), 93-103.

Senseny, P. E. and Pučik, T. A. 1999. 'Development and validation of computer models for structures in jointed rock', *International Journal for Numerical and Analytical Methods in Geomechanics*, 23, 751-778.

Senseny, P. E. and Simons, D. A. 1994. 'Comparison of calculational approaches for structural deformation in jointed rock', *International Journal for Numerical and Analytical Methods in Geomechanics*, 18, 327-344.

Sharma, S., Raghuvanshi, T. K. and Anbalagan, R. 1995. 'Plane failure analysis of rock slopes', *Geotechnical and Geological Engineering*, 13, 105-111.

Shi, G.-H. and Goodman, R. E. 1981. 'A new concept for support of underground and surface excavations in discontinuous rocks based on a keystone principle', *22nd U.S. Symposium on Rock Mechanics, MIT*, 290-296.

Singh, M. 2000. 'Applicability of a constitutive model to jointed block mass, *Rock Mechanics and Rock Engineering*, 33 (2), 141-147.

Singh, M., Rao, K. S. and Ramamurthy, T. 2002. 'Strength and Deformational Behaviour of a Jointed Rock Mass', *Rock Mechanics and Rock Engineering*, 35 (1), 45-64.

Sjöberg, J. 1996. 'Large scale slope stability in open pit mining – a review' *Division of Rock Mechanics – Technical Report 1996:10T, Luleå University of Technology, Luleå.*

Sjöberg, J. 1999. *Analysis of Large Scale Rock Slopes*, Ph.D. Thesis, Department of Civil and Mining Engineering, Rock Mechanics Division, *Luleå University of Technology, Luleå.*

Smart, P. L. 1984. 'The geology, geomorphology and speleogenesis of the eastern massif, Picos de Europa, Spain', *Cave Science, Transactions of the British Cave Research Association*, 11 (4), 238-245.

Smart, P. L. 1986. 'Origin and development of glacio-karst closed depressions in the Picos de Europa, Spain', *Zeitschrift für Geomorphologie*, N.F. 30 (4), 423-443.

Souley, M. and Homand, F. 1996. 'Stability of jointed rock masses evaluated by UDEC with an extended Saeb-Amadei constitutive law', *International Journal of Rock Mechanics and Mining Sciences & Geomechanical Abstracts*, 33. 233-244.

Spink, T. 2003. *Geotechnical and Geoenvironmental Software Directory*. Internet URL: www.ggsd.com. Date last accessed: 11/12/2003.

Sridevi, J. and Sitharam, T. G. 2000. 'Analysis of strength and moduli of jointed rocks', *International Journal of Geotechnical and Geological Engineering*, 18, 1-19.

Starfield, A. M. and Cundall, P. A. 1988. 'Towards a methodology for rock mechanics modelling', *International Journal of Rock Mechanics and Mining Sciences & Geomechanical Abstracts*, 25, 99-106.

Starfield, A. M., Smith, K. A. and Bleloch, A. C. 1990. *How to Model it: Problem Solving for the Computer Age*. McGraw-Hill, New York.

Stone, J. O. H. 2000. 'Air pressure and cosmogenic isotope production', *Journal of Geophysical Research*, 105, 23753-23759.

Stone, J. O. H., Ballantyne, C. K. and Fifield, L. K. 1998. 'Exposure dating and validation of periglacial weathering limits, northwest Scotland', *Geology*, 26, 587-590.

Stone, J. O., Allan, G. L., Fifield, L. K. and Cresswell, R. G. 1996. 'Cosmogenic chlorine-36 from calcium spallation', *Geochimica et Cosmochimica Acta*, 60 (4), 679-692.

Stone, J.O., 1999. 'A consistent Be-10 production rate in quartz – muons and altitude scaling', AMS-8 Proceedings Abstract Volume, Vienna, Austria.

Suárez, J. J. G. and Alonso, V. 1996. 'Glaciers in the Picos de Europa, NW Spain', *Journal of Glaciology*, 42 (141), 386-389.

Swan, A. R. H. and Sandilands, M. 1995. *Introduction to geological data analysis*. Blackwell Science, Oxford.

Swan, G. 1983. *The Stiffness of Joints.* Lulea University, Division of Rock Mechanics, Sweden.

Swanson, T. 1996. 'Determination of ^{36}Cl production rates from the deglaciation history of Whidbey and Fidalgo Islands, Washington', *Radiocarbon*, 38 (1), 172.

Swanson, T. W. and Caffee, M. L. 2001. 'Determination of ^{36}Cl production rates derived from the well-dated deglaciation surfaces of Whidbey and Fidalgo Islands, Washington', *Quaternary Research*, 56, 366-382.

Terzaghi, K. 1950. 'Mechanism of Landslides', *Berkey Vol.*, Geological Society of America, 83-123.

Terzaghi, R. D. 1965. 'Sources of error in joint surveys', *Géotechnique*, 15, 289-304.

Thompson, J. M. T. and Stewart, H. B. 1988. *Nonlinear Dynamics and Chaos.* John Wiley and Sons, New York.

Thornes, J. B. and Brunsden, D. 1977. *Geomorphology and Time*, Methuen, London.

Tindall, S. E. and Davis, G. H. 2003. 'Joint spacing and distribution in deformation band shear zones', *Geological Magazine*, 140, 1-9.

Truyols, J., Gonzalez Lastra, J., Marquínez, J., Martinez Diaz, C., Medez Fernandez, C., Menendez Aluarez, J. R. and Sanchez de Posada, L. 1980. Preliminary note on two marine sections (Tournaisian-Kasimovian) in the Picos de Europa area (Cantabrian Mountains, NW Spain)', *C. R. III Cong. Int. Strat. Geol. Carb. Urbana 1979.*

Tschudi, S., Ivy-Ochs, S., Schlüchter, C., Kubik, P.W., Raino, H. 2000. '^{10}Be dating of Younger Dryas Salpausselkä I Formation in Finland', *Boreas*, 29, 287-293.

Tuan, Y. F. 1958. 'The misleading antithesis of Penckian and Davisian concepts of slope retreat in waning development', *Indiana Academy of Science, Proceedings*, 67, 212-241.

Varley, P. M., Parkin R. J. H, Taylor D. and Patel R. 1999. 'Design of the power caverns for Pergau hydroelectric project, Malaysia' *Transactions of the Institution of Mining and Metallurgy Section A-Mining Industry*, 108, A1-A7.

Vegas, R. and Banda, E. 1982. 'Tectonic framework and Pyrenean evolution of the Iberian Peninsula', *Earth Evolution Sciences*, 4, 320-343.

Viles, H. A. (ed.) 2000. 'Recent advances in field and experimental studies of rock weathering', *Zeitschrift für Geomorphologie Supplement Band*, 120.

Villa, E. and Bahamonde, J. R. 2001. 'Accumulations of Ferganites (Fusculinacea) in shallow turbidite deposits from the Carboniferous of Spain', *Journal of Foraminferal Research*, 31, 173-190.

Vogel, R. M. and Fennessy, N. M. 1993. '*L*-moment diagrams should replace product-moment diagrams', *Water Resources Research*, 29, 1745-1752.

Wagner, E. H. and Winkler Prins, C. F. 1999. 'Carboniferous stratigraphy of the Sierra del Brezo in northern Palencia: evidence of major uplifts', *Trabajos de Geología, Universidad de Oviedo*, 21, 385-403.

Wagner, E. H., Winkler Prins, C. F. and Riding, R. E. 1971. 'Lithostratigraphic units of the lower part of the Carboniferous in Northern Leon, Spain', *Trabajos de Geologia*, 4, Department of Geology, University of Oviedo.

Walker, R. 1989. *Walks and Climbs in the Picos de Europa*, Cicerone Press, Milnthorpe, Cumbria.

Warburton, P. M. 1980. 'Stereological interpretation of joint trace data: influence of joint shape and implications for geological surveys', *International Journal of Rock Mechanics and Mining Sciences & Geomechanical Abstracts*, 17, 305-316.

Weissel, J. K. and Seidl, M. A. 1997. 'Influence of rock strength properties on escarpment retreat across passive continental margins', *Geology*, 25, 631-634.

Whalley, W. B. 1984. 'Rockfalls', in Brunsden, D. and Prior, D. B. (Eds), *Slope Instability*, John Wiley and Sons, Chichester, 217-256.

Whalley, W. B., Douglas, G. R. and McGreevy, J. P. 1982. 'Crack propagation and associated weathering in igneous rocks', *Zeitschrift für Geomorphologie*, 26, 33-54.

Xu, S., Grasso, P. and Mahtab, A. 1990. 'Use of Schmidt hammer for estimating mechanical properties of weak rocks', *6th International IAEG Congress*. A. A. Balkema, Rotterdam. 511-519.

Yilmaz, I. and Sendir, H. 2002. 'Correlation of Schmidt hardness with unconfined compressive strength and Young's modulus in Gypsum from Sivas (Turkey)', *Engineering Geology*, 66, 211-219.

Yokoyama, Y., Reyess, J.-L. and Guichard, F. 1977. 'Production of radionuclides by cosmic rays at mountain altitudes', *Earth and Planetary Science Letters*, 36, 44-50.

Yoon, W. S., Jeong, U. J. and Kim, J. H. 2002. 'Kinematic analysis for sliding failure of multi-faced rock slopes', *Engineering Geology*, 67, 51-61.

Yoshinaka, R. and Yamabe, T. 1986. 'Joint stiffness and the deformation behaviour of discontinuous rock', *International Journal of Rock Mechanics and Mining Sciences & Geomechanical Abstracts*, 23, 19-24.

Zak, I. and Freund, R. 1981. 'Asymmetry and basin migration in the Dead Sea Rift', *Tectonophysics*, 80 (1-4), 27-38.

Zreda, M. G., Phillips, F. M., Elmore, D., Kubik, P.W., Sharma, P. and Dorn, R. I. 1991. 'Cosmogenic ^{36}Cl production in terrestrial rocks', *Earth and Planetary Science Letters*, 105, 94-109.